

THE UNIVERSITY OF CHICAGO

SECONDARY SPHERE EFFECTS ON THE REACTIVITY OF TRANSITION METAL COMPLEXES

A DISSERTATION SUBMITTED TO
THE FACULTY OF THE DIVISION OF THE PHYSICAL SCIENCES
IN CANDIDACY FOR THE DEGREE OF
DOCTOR OF PHILOSOPHY

DEPARTMENT OF CHEMISTRY

BY

ANDREW JOHN MCNEECE

CHICAGO, ILLINOIS

DECEMBER 2020

TABLE OF CONTENTS

List of Figures	vi
List of Tables.....	xvi
List of Schemes	xviii
List of Abbreviations.....	xx
Acknowledgements	xxiv
Abstract	xxvi
Preface.....	xxix
Introduction.....	1
Redox Active Ligands.....	3
Hydrogen Donor Ligands	4
Oriented Electric Field Effects.....	5
Combined Hydrogen and Redox Activity.....	6
References	9
Chapter 1. Diiminopyrrole Ligands	14
Introduction	14
Results and Discussion.....	14
Synthesis of Palladium Complexes with ^{Tol,Cy} DIPy.....	14
First-Row Transition Metals with ^{Tol,Cy} DIPy	21
Conclusion.....	24

Experimental Section	24
References	32
Chapter 2: Dihydrazonepyrrole Ligands	34
Introduction	34
Results and Discussion.....	35
Synthesis and Intramolecular Oxidation with Fluorinated DHP.	35
Oxidative Reactivity of (^t Bu, ^{Tol} DHP)Ni	39
Characterization of a Ni Superoxo Complex	42
Oxidative Reactivity	46
Metalation to (^t Bu, ^{Tol} DHPH ₂)NiCl.	48
Conclusions	53
Experimental Section	54
References	62
Chapter 3: Charged Phosphines for Studying Electric Field Effects.....	65
Introduction	65
Results and Discussion.....	67
Determination of Phosphine Donor Strength.....	68
Effect of Charged Phosphine on Cross-Coupling Reactivity	72
Conclusion.....	73
Experimental Section	73

References	76
Appendix 1. Supporting Data for Chapter 1	78
NMR Spectra.....	78
UV-visible Spectra	87
IR Spectra.....	88
Computations	91
Electrochemistry.....	97
GC Data.....	99
X-Ray Structure Determination	100
Appendix 2. Supporting Data for Chapter 2.	103
NMR spectra	103
EPR Spectra.....	112
UV-visible Spectra	116
Electrochemistry.....	122
IR Spectra.....	124
GC/MS	128
DFT Calculations.	131
X-Ray Absorption Studies	155
X-ray Crystallography.....	159
Appendix 3. Supporting Data for Chapter 3.	161

NMR spectra	161
GC/MS	168
IR Spectra	171
X-Ray Structure Determination	172
Appendix 4. Further H ₂ Donor Ligand Research.....	173
Titanium Templated Condensation with Hydrazides	173

List of Figures

Chapter 1

Figure 1 - 1. Solid state structure of 1	15
Figure 1 - 2. Solid state structure of 2	16
Figure 1 - 3. Solid state structure of 4	17
Figure 1 - 4. EPR of 5 in frozen THF at 15 K.	18
Figure 1 - 5. Solid state structure of 6	22

Chapter 2

Figure 2 - 1 Solid state structure of 2	36
Figure 2 - 2. Solid state structure of 2	38
Figure 2 - 3. CV of 1 mM 2 in THF with 0.1 M nBu ₄ PF ₆ . Scan rate = 100 mV/sec.....	40
Figure 2 - 4. Solid state structure of 4 with triflate bridging (right).	41
Figure 2 - 5. Left: K-Edge X-ray absorption data for 2 and 4 showing no change in edge energy upon reaction of 2 with O ₂ . Right: XAFS fitting of 4 , with K-space inset.	44
Figure 2 - 6. Solid state structure of 5	50
Figure 2 - 7. H ₂ splitting by 3 to give 6 . Peaks at 3.5 ppm and 1.5 ppm are from residual THF, and the peak at 5 ppm is due to dissolved H ₂	51
Figure 2 - 8. ¹ H NMR of H ₂ transfer to benzoquinone, starting from 3 , H ₂ , and benzoquinone and resulting in 6 and hydroquinone.	52

Chapter 3

Figure 3 - 1. Structure of 2 (left), and structure of 2 showing PPh ₄ (right).	68
Figure 3 - 2. Solvent dependence of J_{P-Se} of PPh ₄ 1 ^{Se} , fit to asymptotic fit with $R^2 = 0.99$. Intermediate points were achieved with solvent mixtures, assuming a linear relationship.	70

Figure 3 - 3. Correlation of TEP and J_{P-Se} for 1 and typical phosphines for comparison, showing change based on through-space effects.....	71
--	----

Appendix 1

Figure 1A - 1. 1H NMR of ditoylacylpyrrole in $CDCl_3$	78
Figure 1A - 2. $^{13}C\{^1H\}$ NMR of ditoylacylpyrrole in $CDCl_3$	78
Figure 1A - 3. 1H NMR of $^{Tol,Cy}DIPy$ in $CDCl_3$	79
Figure 1A - 4. $^{13}C\{^1H\}$ NMR of $^{Tol,Cy}DIPy$ in $CDCl_3$	79
Figure 1A - 5. 1H NMR of 1 in C_6D_6	80
Figure 1A - 6. $^{13}C\{^1H\}$ NMR of 1 in C_6D_6 , low signal intensity is due to low solubility of 1	80
Figure 1A - 7. 1H NMR of 2 in C_6D_6	81
Figure 1A - 8. $^{13}C\{^1H\}$ NMR of 2 in C_6D_6	81
Figure 1A - 9. 1H NMR of 3 in C_6D_6	82
Figure 1A - 10. 1H NMR of 4 in C_6D_6	82
Figure 1A - 11. $^{31}P\{^1H\}$ NMR of 4 in C_6D_6	83
Figure 1A - 12. $^{13}C\{^1H\}$ NMR of 4 in C_6D_6	83
Figure 1A - 13. $^{31}P\{^1H\}$ NMR of 4 in THF (bottom), reduction of 4 with Na (middle), and reduction of 4 with Na with an added spike of PMe_3 (top).	84
Figure 1A - 14. $^{31}P\{^1H\}$ NMR of vacuum distillates from reduction reaction.	84
Figure 1A - 15. 1H NMR of $(^{Tol,Cy}DIPyH)NiCl_2$ (6) in C_6D_6	85
Figure 1A - 16. 1H NMR of $(^{Tol,Cy}DIPyH)CoBr_2$ (7) in C_6D_6	85
Figure 1A - 17. 1H NMR of $(^{Tol,Cy}DIPy)_2Co$ (8) in C_6D_6	86
Figure 1A - 18. UV-vis trace for decomposition of 5 in THF with linear fit to model first order kinetics.	87

Figure 1A - 19. UV-vis trace of decomposition of 5 in benzene. Note that decomposition was too fast for accurate kinetic data.	87
Figure 1A - 20. IR (KBr Pellet) of ^{Tol,Cy} DIPyH. The residual broadness at 3500 cm ⁻¹ is due to water in the KBr.....	88
Figure 1A - 21. IR (KBr Pellet) of (^{Tol,Cy} DIPy)PdCl. Residual water causes the features at 3200 cm ⁻¹	88
Figure 1A - 22. IR (KBr Pellet) of 2	89
Figure 1A - 23. IR (KBr Pellet) of (^{Tol,Cy} DIPy)(PMe ₃) ₂ PdCl. Residual water causes the features at 3200 cm ⁻¹	89
Figure 1A - 24. IR (THF solution) of 7	90
Figure 1A - 25. Calculated lowest energy structure of 5	92
Figure 1A - 26. CV of 4 THF with 0.1 M NBu ₄ PF ₆ electrolyte. Scan rate = 100mV/sec.	97
Figure 1A - 27. CV of 1 in THF with 0.1 M NBu ₄ PF ₆ electrolyte. Scan rate = 100mV/sec.....	97
Figure 1A - 28. CV of 5 in THF with a Pt working electrode, scan rate 100 mV/sec, 0.1 M NBu ₄ PF ₆	98
Figure 1A - 29. CV of 5 in THF with a glassy carbon working electrode, scan rate 100 mV/sec, 0.1 M NBu ₄ PF ₆	98
Figure 1A - 30. GC of the headspace of a sealed solution of 5 before and after addition of HBF ₄ . The peak observed is due to gaseous H ₂	99
Figure 1A - 31. SXR structure of 2	100
Figure 1A - 32. SXR structure of 8	100

Appendix 2

Figure 2A - 1. ¹ H NMR of ^{Tol,FPh} DHP in CDCl ₃	103
--	-----

Figure 2A - 2. $^{13}\text{C}\{^1\text{H}\}$ NMR of $^{\text{Tol,FPPh}}\text{DHP}$ in CDCl_3	103
Figure 2A - 3. $^{19}\text{F}\{^1\text{H}\}$ NMR of symmetrical $^{\text{Tol,FPPh}}\text{DHP}$ in CDCl_3 Small impurities result from a small amount of mono-condensed product.	104
Figure 2A - 4 ^1H NMR of $^{\text{Tol,FPPh}}\text{DHP}$ in CDCl_3 after sitting at RT for 2 days, leading to appearance of isomerized DHP.....	104
Figure 2A - 5 $^{19}\text{F}\{^1\text{H}\}$ NMR of $^{\text{Tol,FPPh}}\text{DHP}$ in CDCl_3 after sitting at RT for 2 days, leading to appearance of isomerized DHP.....	105
Figure 2A - 6. ^1H NMR of 1 in C_6D_6	105
Figure 2A - 7. $^{19}\text{F}\{^1\text{H}\}$ NMR of 1 in C_6D_6	106
Figure 2A - 8. $^{19}\text{F}\{^1\text{H}\}$ NMR in C_6D_6 of reaction to form 1 , showing appearance of fluorosilicates at -79 ppm.....	106
Figure 2A - 9. ^1H NMR of $^{\text{tBuTol}}\text{DHP}\cdot 2\text{HCl}$ in CDCl_3	107
Figure 2A - 10. ^1H NMR of $^{\text{tBu,Tol}}\text{DHP}\cdot 2\text{HCl}$ in CDCl_3	107
Figure 2A - 11. ^1H NMR of $(^{\text{tBu,Tol}}\text{DHP})\text{NiOTf}$ in C_6D_6	108
Figure 2A - 12. ^1H NMR of $(^{\text{tBu,Tol}}\text{DHP})\text{Ni}$ (2) in C_6D_6	108
Figure 2A - 13. $^{19}\text{F}\{^1\text{H}\}$ NMR of $(^{\text{tBu,Tol}}\text{DHP})\text{NiOTf}$ in C_6D_6	109
Figure 2A - 14. ^1H NMR of $(^{\text{tBu,Tol}}\text{DHPH}_2)\text{NiCl}$ in C_6D_6	109
Figure 2A - 15. $^{13}\text{C}\{^1\text{H}\}$ NMR of $(^{\text{tBu,Tol}}\text{DHPH}_2)\text{NiCl}$ (5) in C_6D_6	110
Figure 2A - 16. ^1H NMR of $[(^{\text{tBu,Tol}}\text{DHPH}_2)\text{Ni}]\text{OTf}$ (6) in C_6D_6	110
Figure 2A - 17. $^{19}\text{F}\{^1\text{H}\}$ NMR of $[(^{\text{tBu,Tol}}\text{DHPH}_2)\text{Ni}]\text{OTf}$ (6) in C_6D_6	111
Figure 2A - 18. X-band EPR of 1 mM 2 in toluene/petroleum ether at 15 K, MW frequency = 9.628 GHz, MW power = 2.0 mW. Simulation parameters: $g_{x,y,z} = 2.24, 2.12, 2.12$, HStrain = 400, 275, 275 Hz.	112

Figure 2A - 19. X-band EPR of 1 mM **2** in frozen THF at 15 K. MW power = 2 mW, MW freq = 9.630 GHz. 112

Figure 2A - 20. X-Band EPR of 10 mM **4** in THF at 15 K, MW frequency = 9.631 GHz, MW power = 0.06 mW. Simulation parameters: $g_{x,y,z} = 2.23, 2.10, 2.07$. HStrain = 125, 70, 130 Hz. *S = $\frac{1}{2}$ impurity. 113

Figure 2A - 21. X-Band EPR of 1 mM **4** in benzene at 15 K. MW frequency = 9.629 GHz, MW power = 2.0 mW. Simulation parameters: $g_{x,y,z} = 2.23, 2.10, 2.07$. HStrain = 125, 70, 130 Hz. *S = $\frac{1}{2}$ impurity. 113

Figure 2A - 22. Comparison of the EPR of **2** and **4** in THF. Intensities have been normalized for comparison. 114

Figure 2A - 23. Comparison of the EPR of **2** and **4** in benzene. Intensities have been normalized for comparison. 114

Figure 2A - 24. X-band EPR of **3** in frozen THF compared with EPR of **3** generated from **2** at 15 K. MW power = 0.002 mW, MW freq = 9.630 GHz. *S = $\frac{1}{2}$ impurity. Intensities have been normalized for comparison. 115

Figure 2A - 25. UV-visible spectrum of 0.5 mM **2** in benzene at room temperature, with an inset of the low energy feature. 116

Figure 2A - 26. UV-visible spectra of 0.25 mM **3** in THF at room temperature. 116

Figure 2A - 27. UV-visible spectra of conversion of 0.5 mM **2** to **4** in benzene after injection of an excess of ambient air, with scans taken every 52 seconds. The feature at 400 nm is cut off due to overloading the detector. 117

Figure 2A - 28. UV-visible spectrum **3** (1 mM in Ni) in benzene at room temperature. 117

Figure 2A - 29. Conversion of 0.5 mM **1** to **3** by exposure of **1** to O₂ at room temperature in THF, with an inset showing isosbestic conversion at the low energy feature, with scans every 15 seconds. Note that the low energy feature exhibits some solvent dependence..... 118

Figure 2A - 30. Conversion of **3** (0.5 mM in Ni) to **2** by addition of AgOTf at room temperature in THF..... 118

Figure 2A - 31. UV-Vis comparison of **4** generated via two different methods. The presence of residual **2** is responsible for the extra features in the orange spectrum. 119

Figure 2A - 32. Conversion of 0.1 mM **3** to **4** with KO₂ at room temperature in THF. *The feature at 650 nm is residual **2** that has not fully reacted..... 119

Figure 2A - 33. UV-visible spectra of the reaction of **4** with benzyl alcohol (30 eq) in benzene at 50 °C in C₆H₆ with scans every 2 minutes..... 120

Figure 2A - 34. Linear fit to 1/[**4**] (left) and non-linear fit of absorbance vs. time (right). Rate constant from non-linear fit: -0.0011 sec⁻¹ The data was fit to $A = A_{inf} + (A_0 - A_{inf})/(1+kT)$. R² of Fit: 0.99..... 120

Figure 2A - 35. UV-visible spectra of decay of **4** at 50° C in benzene, with scans taken every 2 minutes..... 121

Figure 2A - 36. Linear fit to 1/[**4**] (left) and non-linear fit of absorbance vs. time (right) Rate constant from non-linear fit: 6.9 x 10⁻⁴. The data was fit to $A = A_{inf} + (A_0 - A_{inf})/(1+kT)$. R² of fit: 0.97..... 121

Figure 2A - 37. Cyclic voltammogram of 1 mM **2** in 0.1 M NBu₄PF₆ in THF with 100 mV/sec scan rate. 122

Figure 2A - 38. Cyclic voltammogram of 1 mM **4** in 0.1 M NBu₄PF₆ in THF with 100 mV/sec scan rate. 122

Figure 2A - 39. CV of 2 mM 5 in THF with 0.1 M NBu ₄ PF ₆ electrolyte, and 100 mV/sec scan rate.....	123
Figure 2A - 40. IR (THF solution) of ^{Tol,FPh} DHP.....	124
Figure 2A - 41. IR (nujol mull) of ^{tBu,Tol} DHP•2HCl. The intense features from 3000-2500 and 1500 cm ⁻¹ are from the nujol.....	124
Figure 2A - 42. IR (KBr Pellet) of 2 . The broad feature at 3500 cm ⁻¹ is due to residual water in the KBr.....	125
Figure 2A - 43. IR (KBr Pellet) of 3 . The broad feature at 3500 cm ⁻¹ is due to residual water in the KBr.....	125
Figure 2A - 44. IR (KBr Pellet) of 4 . The broad feature at 3500 cm ⁻¹ is due to residual water in the KBr.....	126
Figure 2A - 45. IR (THF solution) of (^{tBu,Tol} DHPH ₂)NiCl (5).....	126
Figure 2A - 46. IR (KBr Pellet) of 4 with ¹⁶ O (dotted line) overlaid with the IR (KBr Pellet) of 4 with ¹⁸ O (solid line). Predicted shift: 64 cm ⁻¹ Actual: 60 cm ⁻¹	127
Figure 2A - 47. IR (C ₆ H ₆ solution) of 4 , with ¹⁶ O in blue (top), ¹⁸ O in red (middle), and the subtraction in black (bottom).....	127
Figure 2A - 48. GC trace of oxidation of toluene with 4 showing appearance of benzaldehyde at 4.7 minutes. Inset: Calibration curve for benzaldehyde.	128
Figure 2A - 49. MS of benzaldehyde from oxidation of toluene by 4	128
Figure 2A - 50. MS comparison between ¹⁶ O benzaldehyde and ¹⁸ O enriched benzaldehyde from toluene oxidation. Residual ¹⁶ O benzaldehyde is from exchange with natural abundance water in the reaction.....	129
Figure 2A - 51. GC trace of reaction of 4 with toluene under ¹⁸ O ₂	129

Figure 2A - 52. GC trace of the control reaction of toluene heated to 70 °C in air for 3 hours.	130
Figure 2A - 53. Calculated Structure of 2 .	131
Figure 2A - 54. Spin density map of 2 .	132
Figure 2A - 55. Calculated Structure of 4 .	135
Figure 2A - 56. Spin density map of 4 , with isovalues set to 0.005.	136
Figure 2A - 57. Calculated structure of hydroperoxo.	140
Figure 2A - 58. TD-DFT predicted UV-vis spectrum of 4 . 2000 cm ⁻¹ line broadening was applied. Inset shows the low-energy feature.	145
Figure 2A - 59. TD-DFT calculated UV-vis transitions of and the experimental collected UV-vis of 4 (red).	147
Figure 2A - 60. Calculated structure of 6 .	147
Figure 2A - 61. Coordinates of the calculated structure of 3 .	151
Figure 2A - 62. Calculated structure of 4 with atom labels.	155
Figure 2A - 63. EXAFS spectrum (black) and fits (red) in k-space at the Ni K-edge absorption of 4 .	157
Figure 2A - 64. EXAFS spectrum (black) and fits (red) in k-space at the Ni K-edge absorption of 4 .	157

Appendix 3

Figure 3A - 1. ¹ H NMR of K1 in DMSO-d ₆ .	161
Figure 3A - 2. ³¹ P{ ¹ H} NMR of K1 in DMSO-d ₆ .	161
Figure 3A - 3. ¹¹ B{ ¹ H} NMR of K1 in DMSO-d ₆ .	162
Figure 3A - 4. ³¹ P{ ¹ H} NMR of PPh ₄ 1 ^{Se} in CDCl ₃ .	162
Figure 3A - 5. ¹⁹ F{ ¹ H} NMR of PPh ₄ 1 ^{Se} in CDCl ₃ .	163

Figure 3A - 6. ^1H NMR of $\text{PPh}_4\mathbf{1}^{\text{Se}}$ in CDCl_3 .	163
Figure 3A - 7. $^{11}\text{B}\{^1\text{H}\}$ NMR of $\text{PPh}_4\mathbf{1}^{\text{Se}}$ in CDCl_3 .	164
Figure 3A - 8. $^{13}\text{C}\{^1\text{H}\}$ NMR of $\text{PPh}_4\mathbf{1}^{\text{Se}}$ in CDCl_3 .	164
Figure 3A - 9. ^1H NMR of $\mathbf{2}$ in CDCl_3 . Peaks at 3-4 and 1.2 are from THF and Et_2O .	165
Figure 3A - 10. $^{31}\text{P}\{^1\text{H}\}$ NMR of $\mathbf{2}$ in CDCl_3 .	165
Figure 3A - 12. $^{13}\text{C}\{^1\text{H}\}$ NMR of $\mathbf{2}$ in CDCl_3 .	166
Figure 3A - 11. $^{19}\text{F}\{^1\text{H}\}$ NMR of $\mathbf{2}$ in CDCl_3 .	166
Figure 3A - 13. $^{31}\text{P}\{^1\text{H}\}$ NMR of the reaction mixture of the Heck coupling of styrene and chlorobenzene with $\text{PPh}_4\mathbf{1}$ and $\text{Pd}(\text{dba})_2$.	167
Figure 3A - 14. Representative GCMS trace for the Heck Coupling of styrene and chlorobenzene.	168
Figure 3A - 15. Comparison of GCMS trace for the Heck coupling of 1-hexene and chlorobenzene for PCy_3 and $\mathbf{1}$. Additional peaks are various dba degradation products.	168
Figure 3A - 16. Comparison of GCMS trace of Heck coupling of styrene and chlorobenzene with PCy_3 or $\mathbf{1}$.	169
Figure 3A - 17. IR (DCM solution) of $\mathbf{2}$.	171
Figure 3A - 18. IR (DCM solution) of $\text{PPh}_4\mathbf{1}^{\text{Se}}$.	171

Appendix 4

Figure 4A- 1. SXRDR Structure of $\mathbf{1}$.	173
Figure 4A- 2. Symmetrization of ^1H NMR of $\mathbf{1}$ upon switching from CDCl_3 (bottom) to CDCl_3 with a drop of CD_3CN (middle) to only CD_3CN (top).	174
Figure 4A- 3. CV of 5 mM $\mathbf{1}$ in THF with 0.1 M NBu_4PF_6 electrolyte, at variable scan rates.	175
Figure 4A- 4. SXRDR Structure of $\mathbf{4}$.	176

Figure 4A- 5. ^1H NMR of ($^{t\text{Bu,Tol}}\text{DHZPH}$) TiCl_2 in CDCl_3	177
Figure 4A- 6. ^1H NMR of ($^{t\text{Bu,Tol}}\text{DHZP}$) $\text{Ti}(\text{Py})_2\text{O}$ in C_6D_6	178

List of Tables

Appendix 1

Table 1A - 1. Tabulated results of calculations for energy and EPR parameters for proposed structures of 5 . Geometry Optimization: Gaussian 09, B3LYP, Functional: LANL2DZ (Pd), 6-31G(d,p) (C,N,H,P)EPR Calculation: ORCA B3LYP, Functional: ZORA-def2TZVP (Pd), def2-TZVP (P), EPR-II (C,H,N).	91
Table 1A - 2. Coordinates of calculated structure of 5	93
Table 1A - 3. Structural refinement parameters of structures.	101

Appendix 2

Table 2A - 1. Coordinates of calculated structure of 2	132
Table 2A - 2. Coordinates of calculated Structure of 4	136
Table 2A - 3. Orbital Contributions in 2 and 4	139
Table 2A - 4. Coordinates of calculated structure of hydroperoxide.	141
Table 2A - 5. Tabulated Energies for the calculation of O–H BDE.	144
Table 2A - 6. Wavelength and intensities of transitions of 4 calculated by TD-DFT.	145
Table 2A - 7. Coordinates of the calculated structure of 6	148
Table 2A - 8. Coordinates of the calculated structure of 3	152
Table 2A - 9. EXAFS Fit Parameters for 4	155
Table 2A - 10. Comparison of EXAFS and DFT calculated bond lengths of 4	156
Table 2A - 11. EXAFS fit parameters of pathways with or without O40 (second O).	158
Table 2A - 12. Crystal structure and refinement data.	159

Appendix 3

Table 3A - 1. Percent conversion of Heck reaction of chlorobenzene and styrene at different timepoints.	169
--	-----

Table 3A - 2. Conversion of chlorobenzene and 1-hexene.....	170
Table 3A - 3. Refinement data for X-ray structures.	172

Appendix 4

Table 4A - 1. Refinement data for	178
---	-----

List of Schemes

Introduction

Scheme i. Reaction using a redox-active pyridine diimine (PDI) ligand, where reduction of the PDI scaffold allows a 4-electron transformation without needing to access Fe(IV).	3
Scheme ii. H ⁺ -donor/acceptor activity of pendant acetate groups in a water oxidation catalyst....	4
Scheme iii. Ligand-based H ₂ transfer using an incorporated quinone for O ₂ reduction to H ₂ O.....	6
Scheme iv. H ₂ and H-atom addition across a generic DHP scaffold.	7

Chapter 1

Scheme 1 - 1. Synthesis of ^{Tol,Cy} DIPy and metalation to Pd.	14
Scheme 1 - 2. Protonation and reduction of 1	15
Scheme 1 - 3. Addition of phosphines to 1 and subsequent reduction to form 5	17
Scheme 1 - 4. Cobalt reactivity with ^{Tol,Cy} DIPy.....	22

Chapter 2

Scheme 2 - 1. Reactivity in the ^{Ph,Tol} DHPNi system.....	34
Scheme 2 - 2. Synthesis of 1 via C-F oxidation using ^{FPh,Tol} DHP.	35
Scheme 2 - 3. Metalation of ^{tBu,Tol} DHP to Ni to form 2 , and oxidation to form 3	37
Scheme 2 - 4. Reaction of 2 with O ₂ to form 4 , and interconversion of 3 and 4	41
Scheme 2 - 5. Oxidative Reactivity of 4	47
Scheme 2 - 6. Metalation of ^{tBuTol} DHP to form (^{tBu,Tol} DHPH ₂)NiCl.....	49
Scheme 2 - 7. Halide abstraction and reversible H ₂ splitting and transfer.	50

Chapter 3

Scheme 3 - 1. Anionic phosphines that have been previously synthesized.	67
Scheme 3 - 2. Synthesis of K1	67
Scheme 3 - 3. Synthesis of PPh ₄ 1 ^{Sc} and 2 from K1	68

Appendix 3

Scheme 3A - 1. Heck coupling of styrene and chlorobenzene.	169
Scheme 3A - 2. Heck coupling of chlorobenzene and 1-hexene.	170

List of Abbreviations

acac	Acetylacetonate
Avg	Average
br	Broad
Bu	Butyl
calcd	Calculated
cm	Centimeter
cm ⁻¹	Wavenumber
CSD	Cambridge Structural Database
CV	Cyclic voltammogram
Cy	Cyclohexyl
d	Doublet or deuterium
dba	Dibenzylideneacetone
DCM	Dichloromethane
dd	Doublet of doublets
<i>d_x</i>	Compound with x deuterium atoms
DFT	Density Functional Theory
DHP	Dihydrasonopyrrole
DIPy	Diiminopyrrole
DME	1,2-dimethoxyethane
DMSO	Dimethylsulfoxide
e	Electron
EPR	Electron paramagnetic Resonance

eq	Equivalents
equiv	Equivalents
EXAFS	X-ray Absorption Fine Structure
eV	Electron Volt
Fc	Ferrocene
G	Gauss
g	Gram
<i>g</i>	Electron <i>g</i> -factor
GC	Gas Chromatography
GHz	Gigahertz
Hz	Herzt
iPr	Isopropyl
IR	Infrared
<i>J</i>	NMR Coupling Constant
<i>k</i>	Rate constant
kcal	Kilocalorie
m	Multiplet
M	Concentration in molarity
mg	milligram
MHz	Megahertz
mM	Millimolar
mm	millimeter
MS	Mass Spectrometry

mV	Millivolt
mmol	Millimole
mol	Mole
nm	Nanometer
NMR	Nuclear Magnetic Resonance
PDI	Pyridine diimine
Ph	Phenyl
q	Quartet
R	Generic organic group or R-factor
RT	Room temperature
<i>S</i>	Spin quantum number
s	Singlet or second
t	Triplet or time
<i>t</i> Bu	<i>Tert</i> -butyl
TEP	Tolman Electronic Parameter
Tf	SO ₂ CF ₃
THF	Tetrahydrofuran
TMS	Trimethylsilyl
UV	Ultraviolet
V	Volt
Vis	Visible
wR	Weighted R-factor
XAS	X-ray absorption spectroscopy

XRD	X-ray Diffraction
δ	Chemical Shift
$^{\circ}$	Degree
$^{\circ}\text{C}$	Degrees Celsius
ε	Extinction Coefficient
η^x	Hapticity of order x
λ	Wavelength
μA	Microamps
μB	Bohr magneton
μ_{eff}	Effective magnetic moment
\AA	Angstrom
^1H	Hydrogen-1
^{11}B	Boron-11
^{19}F	Fluorine-19
^{13}C	Carbon-13
^{31}P	Phosphorous-31
$\{^1\text{H}\}$	Proton decoupled
Def2-TZVP, etc	Basis sets for DFT
B3P, etc	DFT functionals

Acknowledgements

Firstly I would like express my gratitude towards my advisor, Prof. John Anderson, for taking me into his newly-formed lab and for all his guidance over my graduate career. His helpful discussions and encouragement to pursue a wide variety of systems and reactivity were invaluable in my growth as a scientist through graduate school, and I always appreciated his availability and willingness to talk about different ideas or proposals that I had, despite the fact that many of them were highly impractical. I also thank the other members of my committee, Prof. Michael Hopkins and Prof. Guangbin Dong for their helpful discussions. Also I very much appreciate the other members of the bifunctional project for sharing materials, advice, and glovebox space over the last five years. Prof. Mu-Chieh Chang, Kate A. Jesse, and Sophie Whitmeyer have all contributed to the collective growth of this project and I look forward to the exciting new discoveries that the future holds. I hope the other citizens of Glovebox A enjoy the newfound cleanliness once I am no longer in the lab. I thank Sophie for her work as a summer REU student as well, though the project that I gave her turned out to be a bit of a dead-end, I appreciate the work she did on it to determine whether or not it would work (it did not). I thank Kate for her help with DFT calculations, Dr. Ethan Hill for his help with EPR spectroscopy, and Jiaze for his help with XAS and EXAFS fitting. I would also like to thank all of the instrument and administrative staff at the University of Chicago, especially Dr. Alex Filatov for teaching me X-ray crystallography and having me as a part time graduate assistant for the past two years. Additionally, I would like to thank Prof. Joshua Figueroa for allowing me to work in his lab as an undergraduate. He had a huge effect on stoking my enthusiasm for organometallic chemistry, and I very much appreciate the help and guidance he gave me as an undergraduate in his lab.

I would like to thank my friends for helping me stay sane, most notably those involved in my two favorite parts of the last five years: Beer and The Seamen. I would like show my gratitude to Dr. Chris Hansen for inviting me to play on Beer, which I started only hours after moving to Chicago and have continued for the past 5 years. I would also like to thank Dr. Surrey Walton for the many rounds of margaritas that he supplied during our end-of-season celebrations, and Huw Rees for taking over captaincy of the team after I abdicated my position. Our two championship runs are some of the highlights of my graduate school experience. For The Seamen, once I convinced the my classmates that innertube water polo is in fact (1) fun and (2) not as strenuous as real water polo, we established a four year intramural dynasty, becoming a well-oiled, infamous machine for kicking ass and taking names while floating around in our innertubes, swim caps, and team-mandated jorts. I appreciate everyone who played in the games and who helped in our many brainstorming sessions during happy hour or at the pub for our uniforms, logo, and Facebook page.

For other sports, I would like to thank all the members of the baseball, flag football, and basketball teams that I played on at various times, which is how I learned that flag football in sub-freezing temperatures sucks, but I still had a great time playing on those teams.

Abstract

Transition metal catalysis is an important tool for chemical synthesis and industrial transformations. Utilizing secondary sphere effects and metal-ligand cooperativity has led to greatly improved catalysis in many different reactions, such as CO₂ reduction or H₂ evolution. There are generally two major strategies for these cooperative effects: redox activity and pendant acidic/basic sites. In order to expand strategies for secondary sphere effects, ligands were targeted that could transfer both protons and electrons as either H-atoms or H₂ equivalents or exert an electric field over a substrate complex via distal charged groups. A 2,5-pyrrole pincer scaffold was particularly attractive for the former strategy, as it could be protonated on both arms and the central pyrrole ring can undergo two-electron reduction and oxidation to facilitate H₂ gain and loss by the ligand. To study and quantify electric field effects, a distally anionic phosphine was synthesized, and the through-space and through-bond contributions of the charge were quantified through the Tolman Electronic Parameter and phosphorus-selenium coupling.

Chapter 1 discusses the synthesis and metalation of a diimino pyrrole ligand, ^{Tol,Cy}DIPy, to palladium. ^{Tol,Cy}DIPy supports three different binding modes, κ^1 , κ^2 , and κ^3 , and can be protonated and reduced on the ligand. Further reactivity with the reduced ligand led to intractable mixtures, but this system does reduce H⁺ to H₂, suggesting that the ligand is supporting H-atom transfer to form the H–H bond. Metalation of ^{Tol,Cy}DIPy with first-row transition metals via addition of ^{Tol,Cy}DIPyH to Ni or Co formed identical tetrahedral metal dihalides with the ligand bound in a bidentate manner. Upon further reaction, all cases led to a very stable, homoleptic bis-^{Tol,Cy}DIPy complexes, showing that the wide bite angle of the DIPy scaffold does not coordinate well to small, first row metal ions.

Chapter 2 describes synthesis and reactivity of a dihydrazonopyrrole (DHP) ligand with Ni. The DHP scaffold binds significantly better to first row metals by coordinating through the beta-nitrogen of the hydrazone, leading to stable 6-membered ring coordination. Previous studies in the group indicated that C–H oxidation of phenyl group of ^{Ph,Tol}DHP was a major decomposition pathway, so a more stable system was targeted. First, the fluorinated version, ^{Tol,FPh}DHP was synthesized, but was still sensitive to oxidation, so the alkyl variant ^{tBu,Tol}DHP was synthesized. The large change in electron donation precluded similar reactivity as the ^{Tol,Ph}DHP system, but reaction with oxygen formed a novel superoxide complex from ligand-based electron transfer that was characterized by FTIR, EXAFS, and EPR. The superoxo complex was competent for some oxidative reactivity, but was less reactive and oxidizing than many other superoxo complexes, likely due to the mildness of the ligand-based oxidation. The ^{tBu,Tol}DHP ligand also allowed isolation of the hydrogenated ligand form in the complex (^{tBu,Tol}DHPH₂)NiOTf by hydrogen splitting across the ligand. This was competent for hydrogenation of benzoquinone but had limited reactivity with other H₂ acceptors.

Chapter 3 discusses the synthesis of phosphine ligands substituted with a CH₂BF₃⁻ group to give the phosphine a distal charge that could exert an electric field upon the phosphorus center, a metal center, or a substrate. Measurement of the electron-donation of the phosphine based on Tolman parameter and phosphine-selenium coupling of the phosphine selenide indicated that the phosphine was much more donating than an analogous non-charged derivative. The phosphine selenium coupling was also solvent dependent, indicating a through-space electric field effect that could be masked by solvents of a high enough dielectric constant. Quantification of the through-space effect by variation of the solvent shows that the through-space effect of the charge can effectively double the electron donation of the phosphine, as both through-bond and through-space

effects contribute ~ 30 Hz each to the J_{P-Se} . Studies on the effects of the electric field on catalytic activity for cross-coupling are ongoing, but preliminary results suggest that the charge is beneficial for this reactivity, as the distally charged phosphine outperforms even more donating phosphines such as PCy_3 in its catalytic reactivity.

This thesis also contains multiple appendices which contain supporting data for the previous chapters, or additional projects that did not proceed to a point where full publication-quality data was collected.

Appendix 4 discusses attempts to synthesize ligand with more metal-binding and protonation sites by condensation of hydrazides with the 2,5-ditolyacylpyrrole. Direct condensation was not effective, so $TiCl_4$ was used as a strong Lewis acid to promote the reaction. Surprisingly, the Ti was bound in the binding pocket of the resulting ligand in a seven-coordinate dichloride complex and could not be removed even under forcing conditions. Modified Ti complexes were made by substituting the chlorides for phenolate ligands, by reduction to give a cobaltocenium salt, and deprotonation and reaction with H_2O to give an oxo-bridged dimer structure. Some of these complexes were explored for H_2 reduction and showed high current in CV but poor efficiency in bulk electrolysis measurements.

Preface

All chapters have an independent compound numbering system. Characterization spectra are provided in the corresponding appendix for each chapter.

Introduction

Transition metal catalysis is a ubiquitous process spanning many different industries and applications. In commodity chemical synthesis, many precursors are synthesized via metal-catalyzed pathways, including hydroformylation catalyzed by rhodium phosphines and oxidation reactions catalyzed by a heterogenous silver catalyst.¹ Among the most widely used catalytic reaction is the polymerization to make polyolefins and many other polymers and plastics through insertion polymerization with early transition metal Ziegler-Natta catalysts, or olefin metathesis with ruthenium catalysts.² In the pharmaceutical industry, carbon-carbon bond formation via palladium or nickel catalyzed cross-coupling has greatly enhanced the toolbox of organic chemists for drug discovery and total synthesis.³ Finally, in the energy industry, fuel cells require transition metal electrodes to catalyze the electrochemical reactions that regenerate or power the cell, such as water oxidation and hydrogen or oxygen reduction.⁴ These catalysts can be homogeneous or heterogenous, but often work using either very expensive precious metals, such as platinum or rhodium, or requiring extremely high temperature or pressure conditions to function efficiently.

While these important catalytic processes either are already or are nearly commercially viable, there are many additional reactions that could have environmental benefits for carbon-neutral fuel synthesis. Closing the carbon cycle would require widespread catalytic CO₂ conversion back to useful products such as fuels. Molecular complexes have been shown to electrochemically reduce CO₂ to CO and H₂O, where the CO can then be used in the water-gas shift reaction for H₂ production or directed into the Fischer-Tropsch process to synthesize liquid fuels.⁵ Another potential pathway could electrochemically reduce CO₂ directly with C–C bond formation to make longer carbon chain products such as ethylene, acetic acid, or alkanes directly, but thus far has only been successful using heterogeneous copper catalysts.⁶ Alternatively,

transitioning to a hydrogen economy would require widespread metal catalyzed electrolysis of water or acid to make H₂ or the use of the water-gas shift reaction from electrochemically produced CO, as current synthesis of H₂ from crude oil by steam reforming releases huge quantities of CO₂. Many metal catalysts can effectively mediate this transformation, but efforts are still ongoing to provide scalable, economically viable examples.⁷

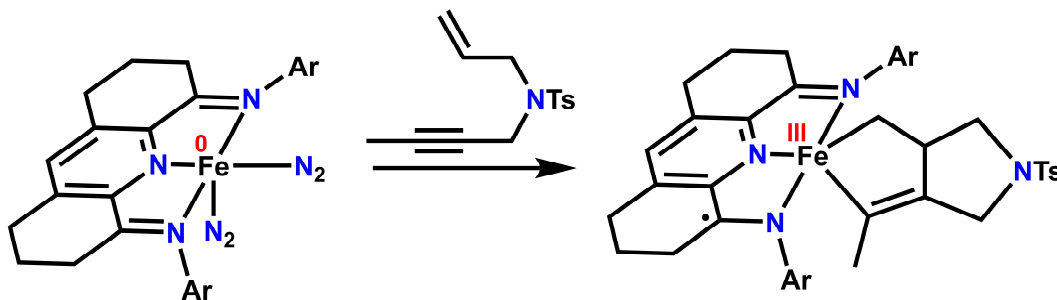
Because transition metal catalysis is so widespread, methods to improve selectivity, catalytic efficiency, and stability are extensive areas of research. Many different strategies for improving catalysis exist and are often inspired by enzymes. Enzymes catalyze extremely difficult processes such as N₂ cleavage and CO₂ fixation using naturally abundant metals at comparatively mild temperatures and pressures.⁸ What allows them to be this effective is an exact control of the active site environment, especially precise control of both the metal's primary and secondary coordination sphere.⁹ The "primary coordination sphere" refers to the environment at the metal center, typically dictated by the ligands that are bound to the metal. Enzymes exert control over the primary sphere using specific ligand groups, such as thiols, to modulate the redox potentials of the metal center, a strategy that can also be effectively employed in synthetic systems. Extensive research has led to a wide array of ligands featuring specific donor properties or steric properties, such as N-Heterocyclic carbenes (NHCs) that have very strong σ -donation to the metal.¹⁰ What especially separates enzymes is their control over the "secondary coordination sphere," or the environment surrounding the active metal site. Three major motifs that have arisen in the study of secondary coordination sphere effects within enzymes are external reducing or oxidizing equivalents, hydrogen bond-donors or external protons, and electric fields mediated by electrostatic charges within the enzyme. With the identification of these motifs, great synthetic effort has been put forward to mimic this reactivity in synthetic systems using redox active ligands,

ligands with pendant protons, and ligands that can exert an external electric field over the metal complex.

Redox Active Ligands: Redox active ligands have become prevalent in a variety of transition-metal catalyzed reactions.¹¹ These ligands typically have extensive π -conjugation, which allow the ligand to have a milder reduction potential than a metal-based redox couple. One application of this is to enable transformations to be performed at a lower redox potential with less overpotential. One of the most efficient examples of this process is in the electrochemical reduction of CO_2 to CO by rhenium or manganese bipyridine complexes.¹² The low overpotential in this system is assigned to an initial ligand-based reduction, which leads to CO_2 binding to start the catalytic cycle. Bipyridine ligands are a prototypical example of bidentate N-donor ligands, but others have been extensively studied as well.¹³

Redox active ligands are also typically coupled with first-row transition metals to encourage two-electron reactivity steps.¹⁴ While expensive precious metals such as platinum, palladium, or rhodium typically undergo two-electron redox couples, first row transition metals are more prone to one-electron pathways. Redox active ligands allow for two-electron reactivity by coupling a one-electron metal-based electron transfer with a ligand-based single electron transfer. One such example is shown in Scheme i, where the ability of the pyridine diimine (PDI) ligand to accept an electron allows a 4-electron process to occur, but with only a three-electron oxidation state change

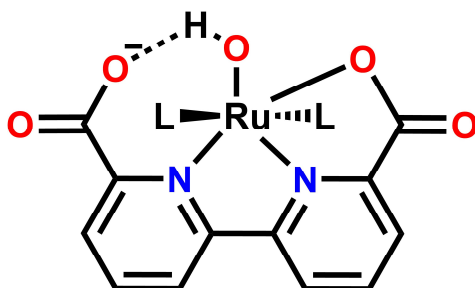
Scheme i. Reaction using a redox-active pyridine diimine (PDI) ligand, where reduction of the PDI scaffold allows a 4-electron transformation without needing to access Fe(IV).



on the metal from Fe(0) to Fe(III), as Fe(IV) is comparatively unstable.¹⁵ PDI ligands are a common class of redox active ligands that have been explored in a variety of these two electron transformations, including hydroboration, polymerization, and bond-forming coupling reactions among others.¹⁶

Hydrogen Donor Ligands: Ligands with hydrogen bond donors or acidic/basic groups in the secondary coordination sphere have been extensively used to enhance the efficiency and speed of proton transfer catalysis or stabilize reactive intermediates using hydrogen bonding. A prototypical example of this are phosphine ligands with a pendant amine used in nickel complexes to achieve extremely rapid proton reduction catalysis.¹⁷ The phosphines bind to the metal center, leaving the basic nitrogen group in the secondary sphere. The proposed bond-forming step to form H₂ in this system is the protonated amine in the ligand scaffold interacting with a metal-hydride to eliminate H₂. The specific positioning of the basic group allows for a much more efficient transition state for bond formation than would be possible if the hydride needed to be protonated by external acidic protons. Similarly, ruthenium complexes with a tethered carboxylate group on the ligand have been studied for water oxidation reactivity where the negatively charged oxygen of the carboxylate assists in the removal of protons from a bound aquo or hydroxide ligand to facilitate O–O bond formation (Scheme ii).¹⁸ Although closer to a primary sphere effect, another noteworthy example is in transfer hydrogenation using Noyori-type catalysts, where H₂ splitting across a M–N bond

Scheme ii. H⁺-donor/acceptor activity of pendant acetate groups in a water oxidation catalyst.



leads to effective transfer hydrogenation.¹⁹ Secondary sphere protons have been used extensively in CO₂ reduction as well to facilitate faster catalytic rates or affect the selectivity of the reaction.²⁰

Another powerful application of secondary sphere acidic or basic groups is the ability of these groups to hydrogen bond to a substrate to stabilize a reactive intermediate. This concept has been illustrated in multiple transition-metal oxo complexes, where pendant N–H groups hydrogen bond to the oxo ligand, stabilizing a lower bond-order to the metal.²¹ All of these applications prove how powerful a pendant acidic/basic group can be in facilitating and stabilizing catalytic reactivity.

Oriented Electric Field Effects: Electric field effects have been significantly less explored than redox activity or pendant protons, but are considered to be a potential future “green reagent”.²² Computational studies have shown that oriented electric fields can have large effects on reaction barriers or rates, and this has been especially well explored within protein architectures.²³ The selectivity of cytochrome P450 was computationally examined to suggest that reversing the polarity of the electric field changes the selectivity of the enzymes from epoxide formation to alcohol formation.²⁴ The lack of broad application of electric fields for molecular catalytic reactivity is partially due to the difficulty in applying them in a controlled orientation, and experimentally quantifying their effects.

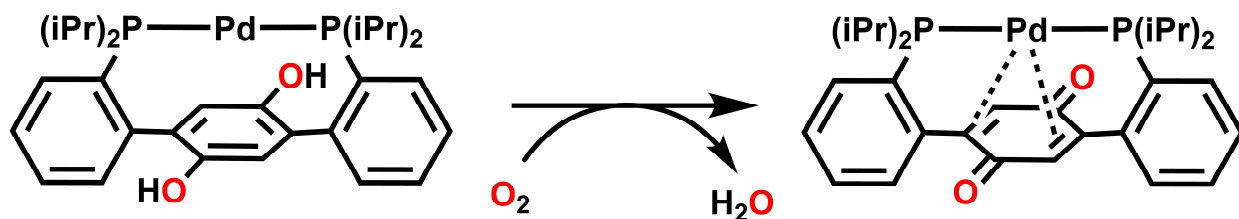
Controlling electric field without the benefit of a large protein architecture is significantly more challenging. Initial studies which use an STM tip to catalyze a Diels-Alder reaction show the utility of electric fields towards effectively catalyzing reactions without the need for additives, but this example would not be amenable to a preparative scale.²⁵ Covalently attaching catalysts to an electrode is another viable strategy, and has shown success in polarizing pi-manifolds to increase pi-stacking for catalysis, but the effect of the electric field can be very difficult to study on an electrode surface.²⁶ Recent reports studying CO₂ reduction catalysts on electrode surfaces depend

on highly specialized spectroscopic techniques. In contrast, studying the electric field effects in single molecules could be significantly simpler.²⁷

In order to study these effects in single molecules, molecules featuring point charges have been synthesized to study the effect the electric field generated from the point charge has on the molecular properties. While this has been extensively explored computationally, there are significantly fewer synthetic studies. In one example, a crown-ether group was appended to a ligand framework to trap a positively charged alkali or alkaline earth metal, to study the electric field exerted by the positive charge.²⁸ Other porphyrin systems with distal charges have also been studied, but both of these examples lack a quantitative understanding of the competition between through-space effects of the charge and through-bond inductive effects. This ambiguity makes this a very intriguing field for study.²⁹ Here we present a distally charged phosphine ligand that allows quantification of the through-space and through-bond effects of the electric field on the phosphine donor properties.

Combined Hydrogen and Redox Activity: An emerging field in transition metal catalysis is to use groups that transfer not just H^+ and e^- , but H-atoms or full H_2 equivalents.³⁰ This could engender greater reactivity on less reactive metals, and also potentially encourage a greater number of H_2 equivalents to be transferred to a substrate, such as reduction of O_2 to H_2O rather than H_2O_2 . This strategy has been tested by using external H atom sources or abstractors during standard catalysis or electrocatalysis. Many studies on alcohol oxidation incorporate TEMPO or similar

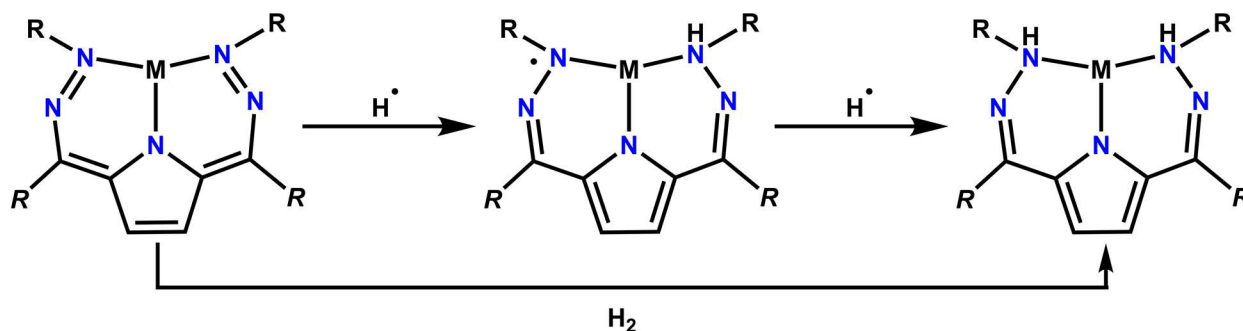
Scheme iii. Ligand-based H_2 transfer using an incorporated quinone for O_2 reduction to H_2O .



radicals to accept H-atoms and accelerate the reaction rates.³¹ Nitrogen reduction catalysis has also been achieved using a combination of SmI₂ and H₂O to transfer H-atoms rather than going through separate proton and electron transfer steps.³² Progress has been made in synthesizing ligands that can mimic this external reactivity through a variety of strategies, but this is still an underexplored area. One example incorporates a quinone moiety into the ligand scaffold, allowing access to the H₂ couple of the quinone during O₂ reduction, but this strategy is poorly tunable and could be mimicked by addition of external benzoquinone (Scheme iii).³³ Other systems have begun using cobaltocene derivatives as H-atom donors by protonation of one of the Cp rings in cobaltocene.³⁴ Finally, systems have been used to electrocatalytically reduce H⁺ to H₂ using redox inactive metals, such as aluminum or zinc, where both the proton and electron transfer must be happening on the ligand.³⁵

With this interest in synthesizing new ligands that can donate both protons and electrons to explore new catalytic chemistry, here I report a 2,5-pyrrole pincer ligand framework that can store a full H₂ equivalent across the ligand scaffold. Though related to the PDI systems, the change from pyridine to pyrrole can give many beneficial improvements for this chemistry. The pyrrole, once deprotonated, can serve as an anionic “anchor” on the metal center while the protonation states of the other nitrogen binding systems changes. Additionally, the resonance of the 2,5-pyrrole system

Scheme iv. H₂ and H-atom addition across a generic DHP scaffold.



allows for two-electron reduction of the pyrrole ring that allows H₂ addition across the ligand framework without making charged zwitterionic species that would likely constitute a significant barrier to H₂ activation (Scheme iv).

Outside of the ubiquitous porphyrins and related systems, ligands featuring pyrroles have not been commonly used. The few examples that are related to this strategy, such as 2,5-diiminopyrrole ligands, show some of the primary differences between using a central pyrrole ring versus the related PDI systems. The main change is the bite angle of the pincer arms of the ligands is much wider in the pyrrole system, leading to challenges in binding all three arms to a metal center, especially smaller, first row transition metals. In some examples, the ligand binds tridentate and the third arm of the pincer rotates away from the metal center.³⁶

References

-
- ¹ (a) Evans, D.; Osborn, J. A.; Wilkinson, G., Hydroformylation of alkenes by use of rhodium complex catalysts. *J. Chem. Soc. A* **1968**, (12), 3133-42. (b) Franke, R.; Selent, D.; Boerner, A., Applied Hydroformylation. *Chem. Rev.* **2012**, *112* (11), 5675-5732.
- ² (a) Brintzinger, H. H.; Fischer, D.; Muelhaupt, R.; Rieger, B.; Waymouth, R. M., Stereospecific olefin polymerization with chiral metallocene catalysts. *Angew. Chem., Int. Ed. Engl.* **1995**, *34* (11), 1143-70. (b) Ittel, S. D.; Johnson, L. K.; Brookhart, M., Late-Metal Catalysts for Ethylene Homo- and Copolymerization. *Chem. Rev.* **2000**, *100* (4), 1169-1203. (c) Grubbs, R. H., Olefin metathesis. *Tetrahedron* **2004**, *60* (34), 7117-7140.
- ³ (a) Miyaura, N.; Suzuki, A., Palladium-Catalyzed Cross-Coupling Reactions of Organoboron Compounds. *Chem. Rev.* **1995**, *95* (7), 2457-83. (b) Lyons, T. W.; Sanford, M. S., Palladium-Catalyzed Ligand-Directed C-H Functionalization Reactions. *Chem. Rev.* **2010**, *110* (2), 1147-1169.
- ⁴ (a) Debe, M. K., Electrocatalyst approaches and challenges for automotive fuel cells. *Nature* **2012**, *486* (7401), 43-51. (b) Gasteiger, H. A.; Kocha, S. S.; Sompalli, B.; Wagner, F. T., Activity benchmarks and requirements for Pt, Pt-alloy, and non-Pt oxygen reduction catalysts for PEMFCs. *Appl. Catal., B* **2005**, *56* (1-2), 9-35.
- ⁵ Benson, E. E.; Kubiak, C. P.; Sathrum, A. J.; Smieja, J. M., Electrocatalytic and homogeneous approaches to conversion of CO₂ to liquid fuels. *Chem. Soc. Rev.* **2009**, *38* (1), 89-99.
- ⁶ (a) Montoya, J. H.; Peterson, A. A.; Norskov, J. K., Insights into C-C Coupling in CO₂ Electroreduction on Copper Electrodes. *ChemCatChem* **2013**, *5* (3), 737-742. (b) Peterson, A. A.; Abild-Pedersen, F.; Studt, F.; Rossmeisl, J.; Norskov, J. K., How copper catalyzes the electroreduction of carbon dioxide into hydrocarbon fuels. *Energy Environ. Sci.* **2010**, *3* (9), 1311-1315.
- ⁷ Rakowski Dubois, M.; Dubois, D. L., Development of Molecular Electrocatalysts for CO₂ Reduction and H₂ Production/Oxidation. *Acc. Chem. Res.* **2009**, *42* (12), 1974-1982.
- ⁸ (a) Stec, B., Structural mechanism of RuBisCO activation by carbamylation of the active site lysine. *Proc. Natl. Acad. Sci. U. S. A.* **2012**, *109* (46), 18785-18790, S18785/1-S18785/6. (b) Einsle, O.; Rees, D. C., Structural Enzymology of Nitrogenase Enzymes. *Chem. Rev.* **2020**, *120* (12), 4969-5004.
- ⁹ (a) Cleland, W. W.; Andrews, T. J.; Gutteridge, S.; Hartman, F. C.; Lorimer, G. H., Mechanism of Rubisco: The Carbamate as General Base. *Chem. Rev.* **1998**, *98* (2), 549-561. (b) Van Stappen, C.; Decamps, L.; Cutsail, G. E.; Bjornsson, R.; Henthorn, J. T.; Birrell, J. A.; DeBeer, S., The Spectroscopy of Nitrogenases. *Chem. Rev.* **2020**, *120* (12), 5005-5081.

¹⁰ (a) Fortman, G. C.; Nolan, S. P., N-Heterocyclic carbene (NHC) ligands and palladium in homogeneous cross-coupling catalysis: a perfect union. *Chem. Soc. Rev.* **2011**, *40* (10), 5151-5169. (b) Hopkinson, M. N.; Richter, C.; Schedler, M.; Glorius, F., An overview of N-heterocyclic carbenes. *Nature* **2014**, *510* (7506), 485-496.

¹¹ (a) Luca, O. R.; Crabtree, R. H., Redox-Active Ligands in Catalysis. *Chem. Soc. Rev.*, **2013**, *42*, 1440-1459. (b) Chirik, P. J., Iron- and Cobalt-Catalyzed Alkene Hydrogenation: Catalysis with Both Redox-Active and Strong Field Ligands. *Acc. Chem. Res.* **2015**, *48* (6), 1687-1695.

¹² a. Riplinger, C.; Sampson, M. D.; Ritzmann, A. M.; Kubiak, C. P.; Carter, E. A., Mechanistic Contrasts between Manganese and Rhenium Bipyridine Electrocatalysts for the Reduction of Carbon Dioxide. *J. Am. Chem. Soc.* **2014**, *136* (46), 16285-16298.

¹³ (a) Bhutto, S. M.; Holland, P. L., Dinitrogen Activation and Functionalization Using β -Diketiminato Iron Complexes. *Eur. J. Inorg. Chem.* **2019**, *2019* (14), 1861-1869. (b) Nguyen, A. I.; Blackmore, K. J.; Carter, S. M.; Zarkesh, R. A.; Heyduk, A. F., One- and Two-Electron Reactivity of a Tantalum(V) Complex with a Redox-Active Tris(amido) Ligand. *J. Am. Chem. Soc.* **2009**, *131* (9), 3307-3316.

¹⁴ (a) Chirik, P. J., Modern alchemy: replacing precious metals with iron in catalytic alkene and carbonyl hydrogenation reactions. *Catal. Precious Met.* **2010**, 83-110. (b) Chirik, P. J.; Wieghardt, K., Radical Ligands Confer Nobility on Base-Metal Catalysts. *Science*, **2010**, *327*, 794-795.

¹⁵ Hoyt, J. M.; Sylvester, K. T.; Semproni, S. P.; Chirik, P. J., Synthesis and Electronic Structure of Bis(imino)pyridine Iron Metallacyclic Intermediates in Iron-Catalyzed Cyclization Reactions. *J. Am. Chem. Soc.* **2013**, *135* (12), 4862-4877.

¹⁶ (a). Bart, S. C.; Chlopek, K.; Bill, E.; Bouwkamp, M. W.; Lobkovsky, E.; Neese, F.; Wieghardt, K.; Chirik, P. J., Electronic Structure of Bis(imino)pyridine Iron Dichloride, Monochloride, and Neutral Ligand Complexes: A Combined Structural, Spectroscopic, and Computational Study. *J. Am. Chem. Soc.* **2006**, *128* (42), 13901-13912 (b) Tondreau, A. M.; Milsman, C.; Patrick, A. D.; Hoyt, H. M.; Lobkovsky, E.; Wieghardt, K.; Chirik, P. J., Synthesis and Electronic Structure of Cationic, Neutral, and Anionic Bis(imino)pyridine Iron Alkyl Complexes: Evaluation of Redox Activity in Single-Component Ethylene Polymerization Catalysts. *J. Am. Chem. Soc.* **2010**, *132* (42), 15046-15059. (c) Atienza Crisita Carmen, H.; Diao, T.; Weller Keith, J.; Nye Susan, A.; Lewis Kenrick, M.; Delis Johannes, G. P.; Boyer Julie, L.; Roy Aroop, K.; Chirik Paul, J., Bis(imino)pyridine cobalt-catalyzed dehydrogenative silylation of alkenes: scope, mechanism, and origins of selective allylsilane formation. *J Am Chem Soc* **2014**, *136* (34), 12108-18.

¹⁷ (a) Helm, M. L.; Stewart, M. P.; Bullock, R. M.; DuBois, M. R.; DuBois, D. L., A Synthetic Nickel Electrocatalyst with a Turnover Frequency Above 100,000 s⁻¹ for H₂ Production. *Science (Washington, DC, U. S.)* **2011**, *333* (6044), 863-866. (b) DuBois, D. L.; Bullock, R. M., Molecular Electrocatalysts for the Oxidation of Hydrogen and the Production of Hydrogen - The Role of Pendant Amines as Proton Relays. *Eur. J. Inorg. Chem.* **2011**, (7), 1017-1027.

¹⁸ Wada, T.; Tanaka, K.; Muckerman, J. T.; Fujita, E., Water oxidation by ruthenium catalysts with non-innocent ligands. *Mol. Water Oxid. Catal.* **2014**, 77-111.

¹⁹ (a) Ikariya, T.; Murata, K.; Noyori, R., Bifunctional transition metal-based molecular catalysts for asymmetric syntheses. *Org. Biomol. Chem.* **2006**, 4 (3), 393-406. (b) Noyori, R.; Hashiguchi, S., Asymmetric Transfer Hydrogenation Catalyzed by Chiral Ruthenium Complexes. *Acc. Chem. Res.* **1997**, 30 (2), 97-102

²⁰ (a) Zee, D. Z.; Nippe, M.; King, A. E.; Chang, C. J.; Long, J. R., Tuning Second Coordination Sphere Interactions in Polypyridyl-Iron Complexes to Achieve Selective Electrocatalytic Reduction of Carbon Dioxide to Carbon Monoxide. *Inorg. Chem.* **2020**, 59 (7), 5206-5217. (b) Queyriaux, N.; Sun, D.; Fize, J.; Pecaut, J.; Field, M. J.; Chavarot-Kerlidou, M.; Artero, V., Electrocatalytic Hydrogen Evolution with a Cobalt Complex Bearing Pendant Proton Relays: Acid Strength and Applied Potential Govern Mechanism and Stability. *J. Am. Chem. Soc.* **2020**, 142 (1), 274-282. (c) Costentin, C.; Drouet, S.; Robert, M.; Saveant, J.-M., A Local Proton Source Enhances CO₂ Electroreduction to CO by a Molecular Fe Catalyst. *Science* **2012**, 338 (6103), 90-94. (d) Costentin, C.; Passard, G.; Robert, M.; Saveant, J.-M., Pendant Acid-Base Groups in Molecular Catalysts: H-Bond Promoters or Proton Relays? Mechanisms of the Conversion of CO₂ to CO by Electrogenerated Iron(0)Porphyrins Bearing Prepositioned Phenol Functionalities. *J. Am. Chem. Soc.* **2014**, 136 (33), 11821-11829. (e) Sinha, S., Warren J. J. "Electrocatalytic CO₂-to-CO conversion by Metalloporphyrins: Catalytic Improvement from One Phenolic Proton Relay" *Inorg. Chem.* **2018**, 57, 12650-12656.

²¹ (a) Ford, C. L.; Park, Y. J.; Matson, E. M.; Gordon, Z.; Fout, A. R., A bioinspired iron catalyst for nitrate and perchlorate reduction. *Science* **2016**, 354 (6313), 741-743. (b) MacBeth, C. E.; Golombek, A. P.; Young, V. G. Jr.; Yang, C.; Kuczera, K.; Hendrich, M. P.; Borovik, A. S. O₂ activation by nonheme iron complexes: a monomeric Fe(III)-oxo complex derived from O₂. *Science*, **2000**, 289, 938-941.

²² Shaik, S.; Mandal, D.; Ramanan, R., Oriented electric fields as future smart reagents in chemistry. *Nat. Chem.* **2016**, 8 (12), 1091-1098.

²³ (a) Warshel, A.; Sharma, P. K.; Kato, M.; Xiang, Y.; Liu, H.; Olsson, M. H. M., Electrostatic basis for enzyme catalysis. *Chem. Rev.* **2006**, 106 (8), 3210-3235. (b) Warshel, A., Electrostatic origin of the catalytic power of enzymes and the role of preorganized active sites. *J. Biol. Chem.* **1998**, 273 (42), 27035-27038. (c) Fried, S. D.; Boxer, S. G., Electric Fields and Enzyme Catalysis. *Annu. Rev. Biochem.* **2017**, 86, 387-415.

²⁴ Schyman, P.; Lai, W.; Chen, H.; Wang, Y.; Shaik, S., The Directive of the Protein: How Does Cytochrome P450 Select the Mechanism of Dopamine Formation? *J. Am. Chem. Soc.* **2011**, 133 (20), 7977-7984.

²⁵ Aragones, A. C.; Haworth, N. L.; Darwish, N.; Ciampi, S.; Bloomfield, N. J.; Wallace, G. G.; Diez-Perez, I.; Coote, M. L., Electrostatic catalysis of a Diels-Alder reaction. *Nature* **2016**, 531 (7592), 88-91

-
- ²⁶ Akamatsu, M.; Sakai, N.; Matile, S., Electric-Field-Assisted Anion- π Catalysis. *J. Am. Chem. Soc.* **2017**, *139* (19), 6558-6561.
- ²⁷ Clark, M. L.; Ge, A.; Videla, P. E.; Rudshiteyn, B.; Miller, C. J.; Song, J.; Batista, V. S.; Lian, T.; Kubiak, C. P., CO₂ Reduction Catalysts on Gold Electrode Surfaces Influenced by Large Electric Fields. *J. Am. Chem. Soc.* **2018**, *140* (50), 17643-17655.
- ²⁸ (a) Chantarojsiri, T.; Ziller, J. W.; Yang, J. Y., Incorporation of redox-inactive cations promotes iron catalyzed aerobic C-H oxidation at mild potentials. *Chem. Sci.* **2018**, *9* (9), 2567-2574. (b) Kang, K.; Fuller, J.; Reath, A. H.; Ziller, J. W.; Alexandrova, A. N.; Yang, J. Y., Installation of internal electric fields by non-redox active cations in transition metal complexes. *Chem. Sci.* **2019**, *10* (43), 10135-10142.
- ²⁹ (a) Bell, S. R.; Groves, J. T., A Highly Reactive P450 Model Compound I. *J. Am. Chem. Soc.* **2009**, *131* (28), 9640-9641. (b) Azcarate, I.; Costentin, C.; Robert, M.; Saveant, J.-M., Through-Space Charge Interaction Substituent Effects in Molecular Catalysis Leading to the Design of the Most Efficient Catalyst of CO₂-to-CO Electrochemical Conversion. *J. Am. Chem. Soc.* **2016**, *138* (51), 16639-16644.
- ³⁰ (a) Lindley, B. M.; Bruch, Q. J.; White, P. S.; Hasanayn, F.; Miller, A. J. M., Ammonia Synthesis from a Pincer Ruthenium Nitride via Metal-Ligand Cooperative Proton-Coupled Electron Transfer. *J. Am. Chem. Soc.* **2017**, *139* (15), 5305-5308.
- ³¹ (a) Hoover, J. M.; Ryland, B. L.; Stahl, S. S., Mechanism of Copper(I)/TEMPO-Catalyzed Aerobic Alcohol Oxidation. *J. Am. Chem. Soc.* **2013**, *135* (6), 2357-2367. (b) Hoover, J. M.; Stahl, S. S., Highly Practical Copper(I)/TEMPO Catalyst System for Chemoselective Aerobic Oxidation of Primary Alcohols. *J. Am. Chem. Soc.* **2011**, *133* (42), 16901-16910.
- ³² Ashida, Y.; Arashiba, K.; Nakajima, K.; Nishibayashi, Y., Molybdenum-catalysed ammonia production with samarium diiodide and alcohols or water. *Nature* **2019**, *568* (7753), 536-540.
- ³³ Horak, K. T.; Agapie, T., Dioxygen Reduction by a Pd(0)-Hydroquinone Diphosphine Complex. *J. Am. Chem. Soc.* **2016**, *138* (10), 3443-3452
- ³⁴ Chalkley, M. J.; Oyala, P. H.; Peters, J. C., Cp* Noninnocence Leads to a Remarkably Weak C-H Bond via Metallocene Protonation. *J. Am. Chem. Soc.* **2019**, *141* (11), 4721-4729.
- ³⁵ (a) Sherbow, T. J.; Fettinger, J. C.; Berben, L. A., Control of Ligand pK_a Values Tunes the Electrocatalytic Dihydrogen Evolution Mechanism in a Redox-Active Aluminum(III) Complex. *Inorg. Chem.* **2017**, *56* (15), 8651-8660. (b) Sherbow, T. J.; Thompson, E. J.; Arnold, A.; Sayler, R. I.; Britt, R. D.; Berben, L. A., Electrochemical Reduction of N₂ to NH₃ at Low Potential by a Molecular Aluminum Complex. *Chem. - Eur. J.* **2019**, *25* (2), 454-458 (c) Thompson, E. J.; Berben, L. A., Electrocatalytic Hydrogen Production by an Aluminum(III) Complex: Ligand-Based Proton and Electron Transfer. *Angew. Chem., Int. Ed.* **2015**, *54* (40), 11642-11646. (d)

³⁶ Fortun, S.; Daneshmand, P.; Schaper, F., Isotactic rac-Lactide Polymerization with Copper Complexes: The Influence of Complex Nuclearity. *Angew. Chem., Int. Ed.* **2015**, *54* (46), 13669-13672.

Chapter 1. Diiminopyrrole Ligands

Introduction

Due to the ready comparison with the well-studied pyridine diimine ligands, diimino pyrrole (DIPy) ligands were first targeted for combining redox-activity and pendant protonation sites within a pyrrole-pincer scaffold.¹ Derivatives of these ligands had been previously studied for their reactivity in polymerization systems, but never for their redox-activity or proton transfer abilities.² In these prior cases, the wider bite angle of the pyrrole-based ligand led to solely bidentate coordination to smaller first-row metals. Two strategies were targeted to solve this problem: (1) synthesizing a ditolylacyl pyrrole complex as a ligand precursor so the sterically bulky *p*-tol substituents would any arm rotation away from the metal center and (2) beginning work with larger, second row metals such as palladium in order to study the ligand with a metal that may fit better into the binding pocket.³ Working with palladium was also beneficial due to its propensity for square planar, diamagnetic complexes that can be readily accessed and studied.

Results and Discussion

Synthesis of Palladium Complexes with ^{Tol,Cy}DIPy Acylation of pyrrole at the 2 and 5 positions was achieved via synthesis and substitution with a benzoxathiolium salt, which could then be oxidatively cleaved using H₂O₂ and acetic acid, giving a ditolylacyl pyrrole in good yield. Condensation of the ditolylacyl pyrrole with neat cyclohexylamine at high temperature gave ^{Tol,Cy}DIPyH in 75% yield. The metalation of ^{Tol,Cy}DIPyH to palladium proceeds smoothly via Scheme 1 - 1. Synthesis of ^{Tol,Cy}DIPy and metalation to Pd.

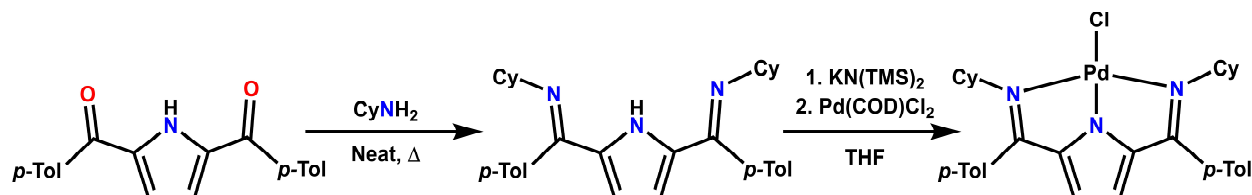
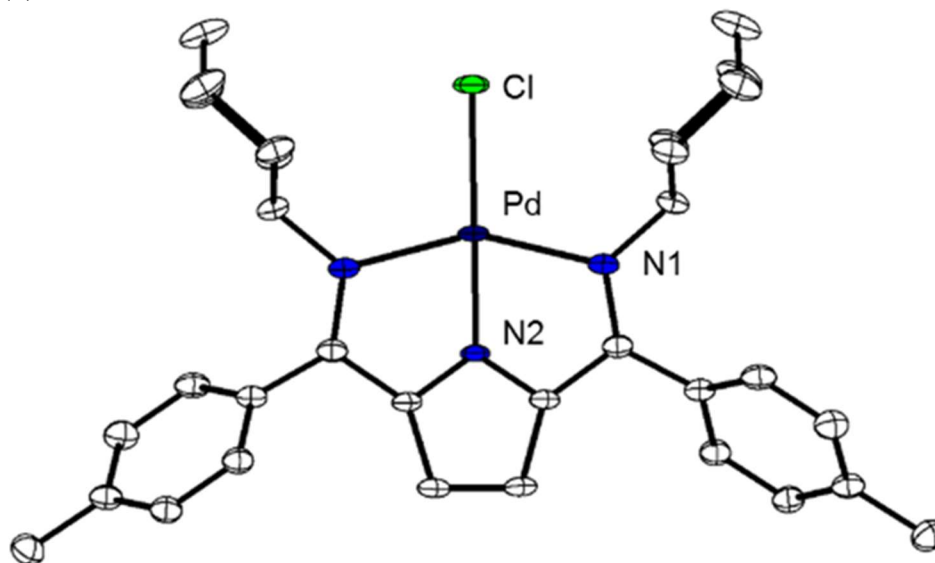


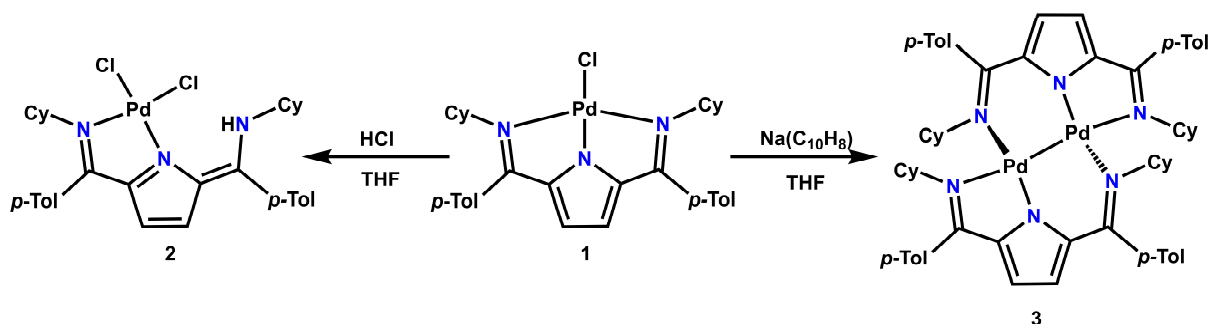
Figure 1 - 1. Solid state structure of **1**.

Ellipsoids are set to 50% probability. Hydrogen atoms have been omitted for clarity. Selected bond lengths and angles: Pd–Cl1 2.318(9) Å, Pd–N1 2.150(2) Å, Pd–N2 1.878(2) Å, N1–Pd–N2: 76.32(4)°.



initial deprotonation with $\text{KN}(\text{TMS})_2$ followed by dropwise addition to a stirred solution of $(\text{COD})\text{PdCl}_2$ (COD = 1,5-cyclooctadiene), resulting in $(^{\text{Tot,Cy}}\text{DIPy})\text{PdCl}$ (**1**) as an orange solid in good yield (Scheme 1 - 1). The ^1H NMR spectrum of **1** is consistent with a symmetric diamagnetic product, suggestive of a planar κ^3 binding mode for the $^{\text{Tot,Cy}}\text{DIPy}$ ligand (Figure 1A - 5). Single-crystal X-ray diffraction (XRD) of **1** corroborates this assignment and reveals a distorted square planar geometry around Pd, with an $\text{N}_{\text{imine}}\text{--Pd--N}_{\text{imine}}$ angle of 152° (Figure 1 - 1). The $\text{N}_{\text{pyrrole}}\text{--Pd}$ bond length is also very short, at 1.87 Å, among the shortest reported for N–Pd.⁴ Both of these

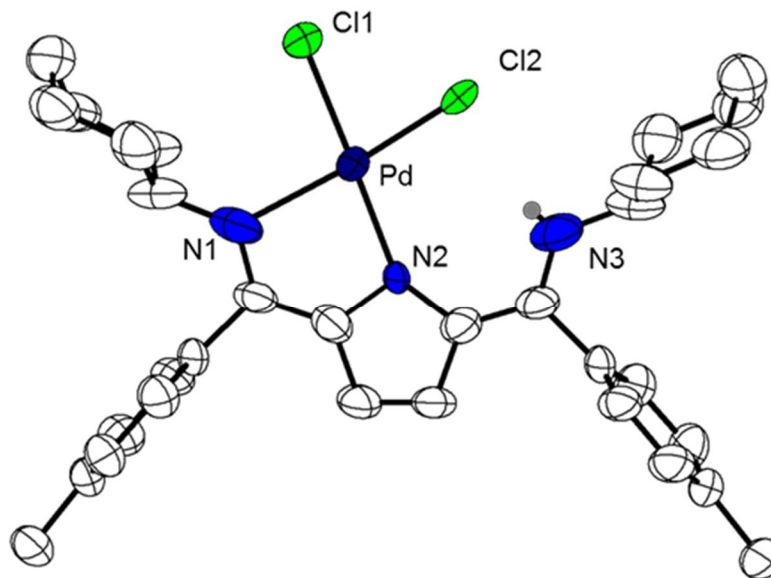
Scheme 1 - 2. Protonation and reduction of **1**.



structural parameters reflect the strained metallacycle formed by planar chelation in **1** and likely

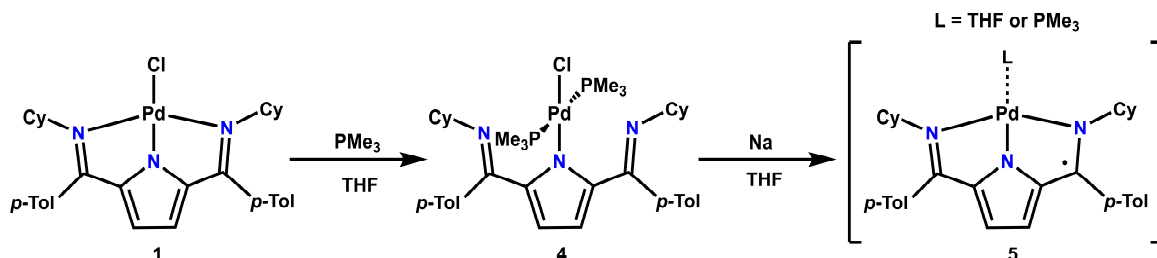
Figure 1 - 2. Solid state structure of **2**.

Ellipsoids are set to 50% probability. Hydrogen atoms other than the N-H have been omitted for clarity. The Pd center was modeled for two-component disorder across both binding sites. Selected bond lengths and angles: Pd–N1 2.250(5) Å, Pd–N2: 2.080(5) Å.



arise from the larger bite angle enforced by the pyrrole backbone. This apparently strained binding mode prompted us to investigate the ability of the imine arms of ^{Tol,Cy}DIPy to behave as protonation sites. Addition of HCl·Et₂O to **1** results in conversion to (^{Tol,Cy}DIPyH)PdCl₂ (**2**) (Scheme 1 - 1). Unlike **1**, complex **2** shows signals consistent with an asymmetric ligand environment in its ¹H NMR spectrum, suggesting that the ligand is no longer tridentate (Figure 1A - 7). Single-crystal XRD confirms that the ligand binds to Pd in a κ² fashion through the pyrrole N and one imine N while two Cl atoms complete the expected square-planar geometry (Figure 1 - 2). The structure shows lengthening of the N_{pyrrole}–Pd bond and shortening of the N_{imine}–Pd bond to accommodate the new binding mode and allow for the extra chlorine atom bound to Pd. Despite the protonation on the ligand arm, rotation around the N–C–C–N dihedral angle is not observed, which illustrates the steric protection the tolyl group provides in preventing this isomerization. Indeed, the protonated imine arm is still positioned near the Pd center which could be suitable for

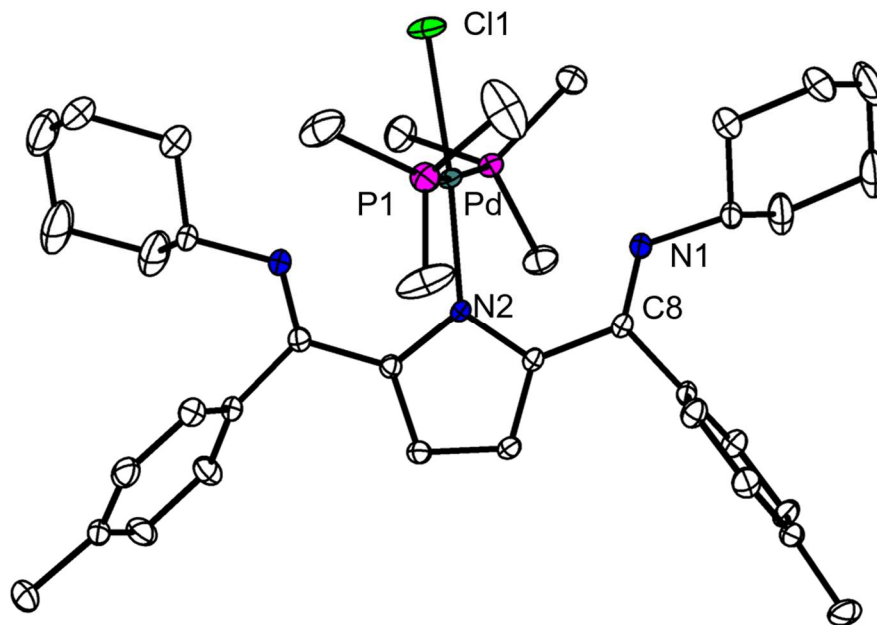
Scheme 1 - 3. Addition of phosphines to **1** and subsequent reduction to form **5**.



proton-transfer reactivity. The structure is disordered with each Pd half-occupied in both bidentate binding pockets. Nevertheless, the structure provides sufficient accuracy that bond lengths within the conjugated system can be used to analyze the resonance structure of the complex. These bond lengths support the resonance structure shown in Scheme 1 - 2, as the C8–C9 bond contracts from 1.44 to 1.38 Å and the C10–C11 bond at the pyrrole 3,4-positions contracts from 1.38 to 1.28 Å, consistent with greater double-bond character. This form of tautomeric amine–azafulvene structure is reminiscent of that recently reported in related pyrrole-based ligands.⁵ Finally, we note that complex **2** can also be accessed in good yield (97%) by the direct reaction of free ToI,CyDIPyH with

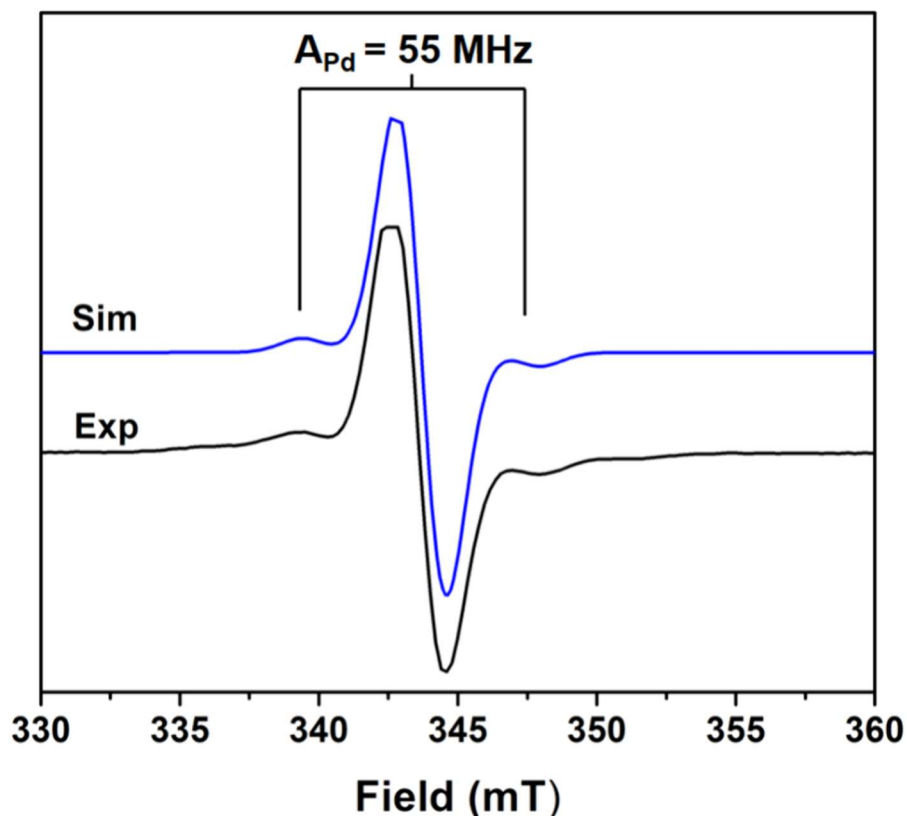
Figure 1 - 3. Solid state structure of **4**.

Ellipsoids are set to 50% probability. Hydrogen atoms have been omitted for clarity. Pd–Cl1 2.314(5) Å, Pd–P1 2.291(5) Å, Pd–N2 2.030(1) Å, N1–C8: 1.285(1) Å, N2–Pd–Cl1 175.69(3)°.



(COD)PdCl₂. The protonation of **2** is also reversible, as reaction with KO^tBu results in clean conversion to **1**. Complexes **1** and **2** show that ^{Tol,Cy}DIPy complexes can react with acid to protonate on the imines of the ligand and that this chelate supports both κ³ and κ² binding modes. With evidence for at least two coordination modes and ligand protonation, we began to probe the potential redox activity of this system. Several reductions of **1** were attempted, but a mixture of products was invariably obtained. While these mixtures have been difficult to characterize, at least one product obtained by reduction with 1 equiv of sodium naphthalenide is a Pd(I)–Pd(I) dimer (**3**), as determined by single-crystal XRD and ¹H NMR spectroscopy (Scheme 1 - 2, Figure 1A - 9, Figure 1A - 31). Complex **3** could not be isolated in large enough quantities for thorough characterization, but the crystal structure exhibits a bridging coordination mode of ^{Tol,Cy}DIPy and a short Pd–Pd bond of 2.47 Å, a distance similar to that observed in many examples of Pd(I)–Pd(I)

Figure 1 - 4. EPR of **5** in frozen THF at 15 K.



dimers.⁶ The other imine of the ^{Tol,Cy}DIPy ligand bridges to the second Pd atom of the dimer with a bond length of 2.049(3) Å, illustrating an additional bridging binding mode for this system. The bond lengths in the ^{Tol,Cy}DIPy ligands of **3** suggest a pyrrolide structure similar to that of **1**, rather than an amine–azafulvene resonance structure similar to **2**.

Given this observation, the addition of an exogenous ligand was targeted to prevent formation of dimeric species and lead to either monomeric Pd(I) or a ligand-based radical. Addition of 2 equiv of PMe₃ to **1** results in clean conversion to (^{Tol,Cy}DIPy)Pd(PMe₃)₂Cl (**4**) (Scheme 1 - 3). The XRD structure of **4** shows a square-planar Pd center where the imine arms of the ^{Tol,Cy}DIPy have been displaced by two PMe₃ ligands such that the PdP₂N_{pyrrole} square plane is orthogonal to the conjugated system of the ^{Tol,Cy}DIPy ligand (Figure 1 - 3). The N_{pyrrole}–Pd bond is substantially lengthened in comparison with **1**, reflecting the release of the strain from the metallacycle, and the average N_{imine}–Pd distance is 3.02 Å, suggesting minimal interaction with the Pd center. This observation further demonstrates the lability of the imine arm of the ligand, going from κ³ to κ¹ upon addition of external ligands. It is still noteworthy that arm rotation is not observed and that the imine arms remain poised near the Pd center.

Unlike attempts with **1**, reduction of **4** with sodium metal results in the formation of a new species which displays a deep blue color in solution. This newly formed species is silent by ¹H NMR spectroscopy, suggesting the formation of a paramagnetic product. Analysis of solutions of **5** by EPR spectroscopy shows an intense signal at *g* = 2.003, attributed to a radical species (Figure 1 - 4). This signal is strongly suggestive of an organic radical, and simulations of this spectrum support this assignment. The broadness of the main peak obscures any phosphorus or nitrogen coupling, but there is resolved coupling to ¹⁰⁵Pd which results in small but significant satellite peaks as shown. The ¹⁰⁵Pd coupling is 55 MHz, which is large for a ligand-based radical

Pd(II) species, but still significantly smaller than would be observed in a *bona fide* Pd(I) species.⁷ Complex **5** is unstable at room temperature, and its half-life depends on the solvent utilized, varying from 240 min in THF to under 10 min in benzene or petroleum ether (Figure 1A - 18, Figure 1A - 19). This observation suggests that the coordinating ability of the solvent may play a role in the stability of **5**.

The decomposition of **5** has precluded structural characterization; therefore, DFT calculations were used to model potential structures. The most stable structure is the four-coordinate complex (^{Tol,Cy}DIPy)Pd(THF) with ^{Tol,Cy}DIPy bound in a κ^3 fashion similar to that for compound **1** and a THF filling the fourth coordination site on Pd (Figure 1A - 25). The computationally predicted electronic structure shows that the majority of the spin density is ligand centered but that there is a Mulliken spin population of ~ 0.35 on Pd. Other structures featuring a bound PMe_3 , or one vacant coordination site, are also energetically reasonable and have comparable spin localization (Table 1A - 1). These computational results are consistent with our assignment of an organic radical but also suggest that Pd(I) resonance structures are also important contributors to the electronic structure of **5**.

Even with these calculations, the structure of **5** depicted in Scheme 1 - 3 is speculative, and other potential assignments cannot be excluded. It is likely that the exact nature of **5** depends strongly on the potential ligands in solution and that a ligand equilibrium is possible in this species. To test this hypothesis, the possible fluxionality of PMe_3 binding was examined by ³¹P NMR spectroscopy. No ³¹P signal is observed in freshly prepared solutions of **5**, presumably due to paramagnetic broadening via interaction with the radical species (Figure 1A - 13). Further addition of excess PMe_3 does not result in any observable signal, supporting exchange of the PMe_3 ligands in solution. Vacuum transfer of the volatiles from a freshly prepared solution of **5** indicates that all

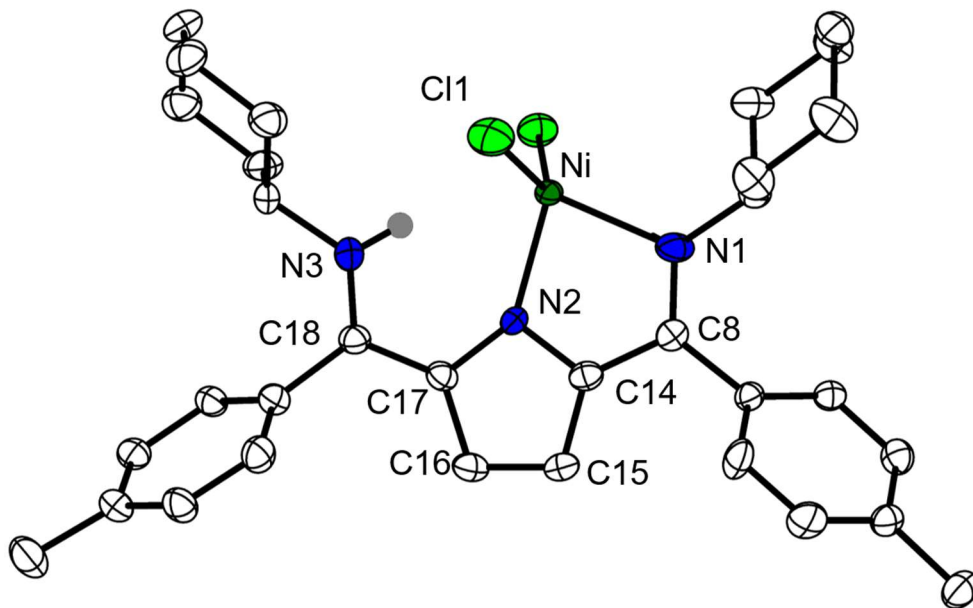
the PMe_3 can be removed, as monitored by ^{31}P NMR integration (Figure 1A - 14). These studies are consistent with a weakly coordinating, potentially fluxionally bound, PMe_3 ligand in solution. In sum, we cannot concretely assign the structure of **5**, but its properties are consistent with the depiction in Scheme 1 - 3.

As a final probe of the properties of **5**, its redox chemistry was examined electrochemically. Cyclic voltammetry (CV) shows a quasi-reversible redox couple at approximately -0.8 V vs Fc/Fc^+ . This is significantly more positive and reversible than the couples observed in both **1** and **4**, which show only irreversible features in the CV at substantially more negative potentials (<-1.8 V) (Figure 1A - 27, Figure 1A - 26). This relatively mild redox couple led us to perform initial studies on the reactivity of this reduced complex. Complex **5** rapidly reacts with acids such as HBF_4 to generate H_2 and a complicated mixture of products (Figure 1A - 30). The measured redox potential of **5** is not reducing enough to perform an outer-sphere reduction of a proton, and so combined reactivity where the complex is protonated before generating H_2 is likely.

First-Row Transition Metals with $^{\text{Tol,Cy}}\text{DIPy}$ After showing that $^{\text{Tol,Cy}}\text{DIPy}$ can mediate both proton and electron storage with palladium, analogous reactivity with first row metals was targeted. Initial attempts focused on Ni as a group 10 analog to palladium. Metalation by addition of $^{\text{Tol,Cy}}\text{DIPyH}$ to NiCl_2dme to form a nickel analog of **2** resulted in $(^{\text{Tol,Cy}}\text{DIPyH})\text{NiCl}_2$ (**6**). The ^1H NMR of **6** was paramagnetic, the large number of paramagnetically shifted ^1H NMR resonances which also suggest an asymmetric binding mode of $^{\text{Tol,Cy}}\text{DIPy}$. Crystallization by vapor diffusion of petroleum ether into benzene resulted in single crystals of **6**, and showed a tetrahedral structure at nickel. The nickel atom is disordered across both potential bidentate binding spots of the DIPy , though the disorder was not symmetric, so the bond lengths differences assigned to the amine-azafulvene resonance structure could be observed in the single crystal XRD structure, such as

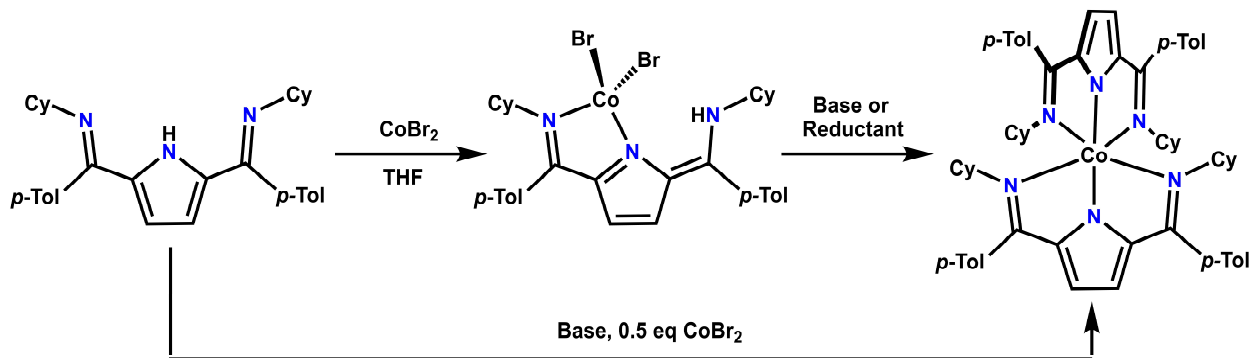
Figure 1 - 5. Solid state structure of **6**.

Ellipsoids are set to 50% probability. Hydrogen atoms except for the N–H are omitted for clarity. The Ni was modeled for two site disorder, with the 75% contributor shown. Selected bond lengths and angles: Ni–Cl1: 2.181(14) Å, Ni–N1 2.039(3) Å, Ni–N2 1.982(3) Å, N1–C8 1.294(5) Å, N3–C18 1.301(5) Å, C18–C17 1.427(6) Å, C16–C15 1.378(6) Å, C14–C8 1.447(5) Å, N1–Ni–N2 82.89(1)°, C11–Ni–N2 112.66(3)°.



lengthening of one C–N bond by 0.1 Å. The N–H proton was located in the difference map, and was additionally confirmed via solution IR, showing a N–H stretch at 3157 cm^{-1} . A similar binding of a diiminopyrrole has been seen previously in the literature as well.⁸ Further reactivity with this species did not result in any tractable products, so metalation with cobalt was targeted to incorporate more potential binding sites and metal-based redox.

Scheme 1 - 4. Cobalt reactivity with ^{Tol,Cy}DIPy.



Metalation with cobalt by addition of the ^{Tol,Cy}DIPyH to CoBr₂ in THF at room temperature immediately gave a dark green colored solution, and ¹H NMR showed an asymmetric ^{Tol,Cy}DIPy environment (Figure 1A - 16). This was assigned as (^{Tol,Cy}DIPyH)CoBr₂, (**7**), a complex analogous to **6**. Single crystals were obtained by diffusion of petroleum ether into a benzene solution, and SXRDR showed the expected structure, with the Co disordered across the two binding sites. The ligand bond metrics match well with **6**, though the disorder is approximately 1:1 in the Co case, giving a more symmetric solid-state structure. Further reactions of **7**, via either deprotonation or reduction, resulted in either intractable mixtures, or conversion to a new, symmetric paramagnetic product, assigned as ((^{Tol,Cy}DIPy)₂Co) (**8**). The SXRDR structure shows short Co-N_{pyrrole} distances and long Co-N_{imine} distances which are barely within the Van der Waals radius for bonding interactions (Figure 1A - 32). This suggests that the complex may best be thought of as a linear, two coordinate Co complex with weak interactions with the imine nitrogens. Compound **8** is highly stable, showing no reaction with either ambient air or strong reductants, such as sodium/mercury amalgam. The high stability is likely due to the coordinative saturation of the cobalt center and the large steric protection afforded by the 4 cyclohexyl groups surrounding the metal center.

Metalation of ^{Tol,Cy}DIPy with first-row transition metals via deprotonation was significantly more challenging. In many reactions, the protonated product, **6** or **7** was observed, likely through reaction of the pyrrolide ligand with adventitious water during the metalation. Metalation of deprotonated ^{Tol,Cy}DIPy with Co often resulted in **8**, showing that tridentate binding in a manner analogous to **1** may not be possible with small, first row metal ions. These studies indicated that different ligand designs were necessary to improve stability with first-row metal centers.

Conclusion

Diimino-pyrrole systems have been shown to effectively store both protons and electrons and to unexpectedly bind in multiple different geometries. The wider bite angle of the central pyrrole is likely the most important factor for the lack of strong, tridentate binding to first-row transition metals, but with palladium the ligand could form a strained square-planar type geometry to allow for effective study. These ligands are a proof of concept for 2,5-substituted pyrroles storing both protons and electrons, but a different binding geometry is necessary for stabilizing transition metal binding, especially to small, first row metals where hydrogen transfer is likely to be more necessary, as protonation of the DIPy scaffold makes it much more labile and subject to decomposition.

Experimental Section

General Considerations. All reagents were purchased from commercial suppliers and used without further purification. All manipulations were carried out under an atmosphere of N₂ using standard Schlenk and glovebox techniques. Glassware was dried at 180 °C for a minimum of two hours and cooled under vacuum prior to use. Solvents were dried on a solvent purification system from Pure Process Technology and stored over 4 Å molecular sieves under N₂. Tetrahydrofuran was stirred over NaK alloy and run through an additional alumina column prior to use to ensure dryness. Solvents were tested for H₂O and O₂ using a standard solution of sodium-benzophenone ketyl radical anion. C₆D₆ was dried by passage over a column of activated alumina and stored over 4 Å molecular sieves in the glovebox. ¹H, ¹³C{¹H}, and ³¹P NMR spectra were recorded on Bruker DRX 400 or 500 spectrometers. Chemical shifts are reported in ppm units referenced to residual solvent resonances for ¹H and ¹³C{¹H} spectra, and referenced to external H₃PO₄ for ³¹P. UV-Visible spectra were recorded on a Thermo Evolution 300 spectrometer, and IR was recorded on

a Bruker Tensor II. EPR spectra were recorded on a Elexsys E500 Spectrometer with an Oxford ESR 900 X-band cryostat and a Bruker Cold-Edge Stinger and were simulated using Easyspin suite in Matlab software.¹ Gas chromatography was recorded on an Agilent 7890B GC equipped with FID and TCD detectors. Elemental analysis was performed by Midwest Microlabs. Electrochemical Measurements Electrochemical measurements were performed using a BAS Epsilon potentiostat and analyzed using BAS Epsilon software version 1.40.67NT. Cyclic voltammetry measurements were made using a glassy carbon working electrode, platinum wire counter electrode, and silver wire pseudo-reference electrode, and referenced to internal Fc/Fc⁺.

Synthesis of 2,5-ditolylacetylpyrrole.³ 2-Hydroxythiophenol (10 mL, 0.063 mol) and *p*-toluic acid (8.6 g, 0.063 mol, 1 eq) were dissolved in POCl₃ (100 mL) in a 250 mL round-bottom flask and heated with stirring to 110 °C for 10 min, turning a deep red color. The reaction was cooled to room temperature and HBF₄•Et₂O (30 mL) was added, followed by dry ether (200 mL), resulting in precipitation of the benzoxathiolium salt as a yellow powder. The powder was collected by vacuum filtration and used without further purification or characterization (yield: 18 g). All of the benzoxathiolium salt was added with stirring to a 250 mL round-bottom flask containing pyrrole (1.7 mL, 0.0245 mol), pyridine (5.4 mL, 0.067 mol), and acetonitrile (100 mL). The salt dissolved immediately upon addition and the solution become hot and turned dark yellow. The reaction was stirred for 45 min and then CHCl₃ (200 mL) and H₂O (100 mL) were added. The aqueous and organic layers were separated, and the aqueous layer was extracted with CHCl₃ (3 x 150 mL). The combined organic layers were washed with 5% NaOH (aq) (100 mL) and water (100 mL), then dried with MgSO₄ and the solvent was evaporated to give a dark brown oil. The oil was suspended in acetic acid (150 mL) and 30% H₂O₂ (aq) (10 mL) was added. The mixture was stirred and heated to 110 °C for 30 min, gradually turning a deep red color. After cooling to room temperature, H₂O

(100 mL) and CHCl_3 (200 mL) were added and the aqueous and organic layers were separated. The aqueous layer was washed with CHCl_3 (4 x 100 mL), and the combined organic layers were washed with 10% NaOH (aq) (2 x 100 mL) until the red color no longer persisted in the organic layer. The yellow organic layer was washed with H_2O (100 mL), dried with MgSO_4 , and solvent was removed to leave a yellow solid. The solid was washed with MeOH (100 mL) resulting in ditolylacetylpyrrole as a white solid. Analytical quality crystals were grown from concentrated MeOH solution at $-78\text{ }^\circ\text{C}$. Yield: 5.5 g (0.018 mmol, 74%). ^1H NMR (400 MHz, CDCl_3 , $25\text{ }^\circ\text{C}$) δ = 7.85 (d, 4H, J = 8 Hz, Tol C-H), 7.31 (d, 4H, J = 8 Hz, Tol C-H), 6.89 (s, 2H, Pyrrole), 2.45 (s, 6H, Tol- CH_3). ^{13}C $\{^1\text{H}\}$ NMR (100 MHz, CDCl_3 , $25\text{ }^\circ\text{C}$) δ = 185.1 (C=O), also 143.5, 134.9, 134.1, 129.3, 129.2, 118.0, 21.7. IR (KBr Pellet, cm^{-1}) 3429 (N-H, s) 1633 (C=O, vs), also 3130 (w), 2919 (w), 1568 (s) 1527 (s), 1419 (m), 1277 (vs), 1207 (m), 1130 (s), 1011 (m), 880 (m), 835 (m), 749 (s). Anal. Calc. C, 79.19; H, 5.65; N, 4.62; Found: C, 78.89; H, 5.67; N, 4.34.

Synthesis of $^{\text{Tol,Cy}}\text{DIPyH}$. Ditolylacetylpyrrole (2.035 g, 6.7 mmol) was slurried in neat cyclohexylamine (15 mL) and three drops of acetic acid were added. The mixture was heated to $140\text{ }^\circ\text{C}$ with stirring for two days. After cooling to room temperature, the solution was poured out into hexanes (200 mL) and water (100 mL) and the aqueous and organic layers were separated. The aqueous layer was then extracted with hexanes (2 x 100 mL) and the combined organic layers were dried with MgSO_4 and evaporated to give a yellow residue. The yellow residue was slurried in 50 mL hexanes and filtered, resulting in pure $^{\text{Tol,Cy}}\text{DIPyH}$ (2.458 g, 5.3 mmol, 79%). ^1H NMR (400 MHz, CDCl_3 , $25\text{ }^\circ\text{C}$) δ = 7.21 (d, 4H, J = 8 Hz, Tol C-H), 7.10 (d, 4H, J = 8 Hz, Tol C-H), 5.75 (s, 2H, Pyrrole), 3.23 (pentet, 2H, J = 4 Hz, CH methine), 2.41 (s, 6H, Tol- CH_3), 1.74, 1.59, 1.17 (m, 20H, Cy). ^{13}C $\{^1\text{H}\}$ NMR (100 MHz, CDCl_3 , $25\text{ }^\circ\text{C}$) 157 S5 (C=N), 138.0, 135.5, 133.4, 128.8, 127.8, 60.5, 34.4, 25.8, 24.7, 21.5 IR (KBr Pellet, cm^{-1}) 3449 (N-H, m), 1601 (C=N, m),

also 2925 (m), 2852(w) 1516 (w) 1447 (w), 1293(s), 1132(w), 1070(w), 789(m), 736(w). Anal. Calc. C, 82.5; H, 9.0; N, 8.5; Found: C, 82.47; H, 8.55; N, 8.98.

Synthesis of [^{Tol,Cy}DIPy]PdCl (1). To a stirring THF solution of the ^{Tol,Cy}DIPyH (0.167 g, 0.361 mmol, 10 mL) was added 0.5 M KN(TMS)₂ (0.73 mL, 0.361 mmol, 1 eq) via syringe, resulting in a yellow solution. The deprotonated ligand solution was then added dropwise to a stirring THF slurry of dichloro(1,5-cyclooctadiene)palladium(II) (0.110 g, 0.385 mmol, 5 mL, 1.06 eq) and let stir for 30 min, resulting in a color change from yellow to red. The resulting red solution was filtered through Celite and all volatiles were removed in vacuo. The resulting orange residue was slurried in petroleum ether and filtered, resulting in pure [^{Tol,Cy}DIPy]PdCl (0.133 g, 0.219 mmol, 61%) as an orange solid. Diffraction quality crystals were obtained from a concentrated 2:1 solution of diethyl ether and benzene at -35°C. ¹H NMR (400 MHz, C₆D₆, 25 °C) δ = 7.05 (d, 4H, *J* = 8 Hz, Tol C-H), 6.83 (d, 4H, *J* = 8 Hz, Tol C-H), 5.86 (s, 2H, Pyrrole), 3.42 (m, 2H, C-H methine), 1.98 (s, 6H, Tol-CH₃) 1.7-1.1 (m, 20H, Cy) ¹³C {¹H} NMR (100 MHz, C₆D₆, 25 °C) δ = 171.1 (C=N) 144.9, 140.1, 129.6, 129.4, 127.3, 113.8, 109.8, 64.1, 31.8, 25.0, 24.5, and 20.9. IR (KBr Pellet, cm⁻¹) 2927 (m), 2855 (m), 1610 (C=N, s), 1476 (s), 1400 (m), 1385 (m), 1328 (m), 1299 (m), 1067 (w) Anal. Calc. C, 63.37; H, 6.37; N, 6.93 Found: C, 63.48; H, 6.37; N, 6.63.

Synthesis of (^{Tol,Cy}DIPyH)PdCl₂ (2). To a stirring benzene solution of **1** (0.043 g, 0.07 mmol, 5 mL) was added 2.2 M HCl•Et₂O (0.03 mL, 1 eq) via syringe. The reaction was stirred for 5 min then all volatiles were removed in vacuo. Analytical quality crystals of **2** were obtained from diffusion of petroleum ether into a saturated THF solution. Yield: 0.03 g, 0.04 mmol, 66%. ¹H NMR (400 MHz, 25 °C, CDCl₃) δ = 12.12 (s, 1H, N-H), 7.29 (d, 2H, *J* = 8 Hz, Tol C-H), 7.23 (d, 2H, *J* = 8 Hz, Tol C-H), 7.18 (d, 2H, *J* = 8 Hz, Tol C-H), 7.09 (d, 2H, *J* = 8 Hz, Tol C-H), 6.00 (d, 1H, *J* = 4 Hz, Pyrrole), 5.76 (d, 1H, *J* = 4 Hz, Pyrrole) 3.43 (m, 1H, Cy Methine), 2.42 (m, 1H,

Cy Methine), 2.41 (s, 3H, Tol-CH₃) 2.39 (s, 3H, Tol-CH₃) 1-2 (m, 20H, Cy) ¹³C{¹H} NMR (100 MHz, CDCl₃, 25 °C) δ = 173.2 (C=N), also 164.3, 157.5 141.1, 139.9, 138.5, 130.7, 130.0, 129.2, 127.6, 127.2, 118.5, 67.2, 58.1, 32.2, 31.7, 25.3, 24.7, 24.5, 24.5, 21.4. . IR (KBr Pellet, cm⁻¹) 3211 (N-H, w), 2929 (s) 2854 (s) 1607 (C=N, vs), 1513 (m), 1473 (w), 1329 (s), 1299 (s), 1067 (m), 822 (m). Anal Calc. C, 59.77; H 6.11; N, 6.54 Found C, 59.81; H, 6.15; N, 6.44.

Alternate Synthesis of 2. To a stirring THF suspension of dichloro(1,5-cyclooctadiene)palladium(II) (0.077 g, 0.27 mmol, 5 mL) was added a THF solution of Tol,CyDIPyH (0.120 g, 0.25 mmol, 10 mL, 0.9 eq). The resulting mixture was stirred overnight at room temperature, gradually turning from yellow to bright orange. The mixture was concentrated to 3 mL in vacuo, filtered, and crystallized by vapor diffusion with petroleum ether, resulting in orange/red crystals of **2**. Yield: 0.156 g, 0.24 mmol, 97 %.

Synthesis of [Tol,CyDIPy]₂Pd₂ (3). Naphthalene (0.003 g, 0.03 mmol, 1 eq) was stirred over freshly cut Na in THF (2 mL) for 15 min, turning dark green. The sodium naphthalenide solution was filtered into a stirring solution of **1** (0.016 g, 0.03 mmol, 4 mL) and let stir for 1 hr. All volatiles were removed in vacuo and the mixture was dissolved in petroleum ether and let stand for 1 day, resulting in dimer [Tol,CyDIPy]₂Pd₂ as diffraction quality dark-red crystals. Note that co-crystallization of impurities precluded full characterization, but peaks corresponding to [Tol,CyDIPy]₂Pd₂ could be identified in the proton NMR. ¹H NMR (400 MHz, 25 °C, C₆D₆) δ = 6.22 (d, *J* = 4 Hz, 2H, pyrrole), 6.12 (d, *J* = 4 Hz, 2H, pyrrole), 3.91 (m, 2H, C-H methine), 3.47 (m, 2H, C-H methine), 2.02 (s, 6H, Tol-CH₃), 1.99 (s, 6H, TolCH₃).

Synthesis of [Tol,CyDIPy]Pd(PMe₃)₂Cl (4). To a stirring THF solution of **1** (0.0583 g, 0.09 mmol, 5 mL) was added via syringe 1.0 M PMe₃ in THF (0.07 mL, 2 eq). The color changed immediately from orange to yellow. After stirring for 10 min, all volatiles were removed in vacuo. The yellow

residue was washed with petroleum ether, giving **4** as a yellow powder. (0.062 g, 0.08 mmol, 80%)
Diffraction quality crystals were obtained from a concentrated solution of **4** in petroleum ether sitting overnight at room temperature. ^1H NMR (400 MHz, 25 °C, C_6D_6) δ = 7.17 (d, 4H, J = 8 Hz, Tol C–H) 7.02 (d, 4H, J = 8 Hz, Tol C–H), 6.20 (s, 2H, pyrrole), 3.51 (pentet, 2H, J = 4 Hz, C–H methine), 2.10 (s, 6H, Tol- CH_3), 1.195 (d, 18H, J = 4 Hz, P- CH_3), 1-2 (m, 20H, Cy) $^{13}\text{C}\{^1\text{H}\}$ NMR (100 MHz, C_6D_6 , 25 °C) δ = 162.5 (C=N), also 141.8, 137.1, 128.5, 127.8, 127.7, 119.0, 61.9, 35.6, 25.9, 25.3, 21.0, 13.5. ^{31}P NMR (162 MHz, C_6D_6 , 25 °C) δ = -15.1 (s, PMe_3). IR (KBr Pellet, cm^{-1}) 2928 (s), 2853 (s), 1588 (C=N, s) 1509 (w), 1449 (w), 1322 (s), 1066 (w), 848 (s).
Anal. Calc. C, 60.16; H, 7.44; N, 5.54 Found: C, 59.91; H, 7.24; N, 5.38.

Synthesis of 5. To a THF solution of **2** (0.062 g, 0.08 mmol, 8 mL) was added an excess of freshly cut metallic sodium (0.050 g) and stirred for 60 min, resulting in **5** as a deep blue solution. This solution was filtered and characterized by EPR and UV-Visible spectroscopy. EPR (frozen THF solution, 15K) g = 2.003, A_{Pd} = 55 MHz. UV-Vis (Et_2O Solution) (Wavelength, Extinction Coefficient) 580 nm, 59000 $\text{M}^{-1}\text{cm}^{-1}$.

Generation of H_2 from 5. A freshly prepared solution of **5** was filtered to ensure removal of any sodium metal, then placed in Schlenk tube with a septum over the end. The atmosphere was initially sampled to get the background, then HBF_4 etherate was added via syringe, the reaction was stirred for 1 min, and the atmosphere was sampled again via gas-tight syringe for GC analysis.

Synthesis of $(^{\text{Tol,Cy}}\text{DIPyH})\text{NiCl}_2$ (6**).** To a stirring THF solution of NiCl_2dme (0.022 g, 0.10 mmol, 3 mL) was added a THF solution of $^{\text{Tol,Cy}}\text{DIPyH}$ (0.045 g, 0.096 mmol, 1 eq, 5 mL). The solution gradually changed to a deep red, and was stirred overnight. After evaporation of all volatiles, the resulting red residue was crystallized from diffusion of petroleum ether into benzene, giving $(^{\text{Tol,Cy}}\text{DIPyH})\text{NiCl}_2$ as red crystals (0.015 g, 0.025 mmol, 25 %). ^1H NMR (C_6D_6 , 400 MHz, 25°

C) $\delta = 76.35, 59.25, 53.41, 18.97, 16.98, 15.76, 13.43, 13.24, 10.26, 10.01, 9.51, 8.14, 7.06, 6.73, 4.01, 1.42$. IR (THF solution, CaF₂ windows, cm⁻¹) 3197 (w, N-H), 1577 (s, C=N)

Synthesis of (Tol,CyDIPyH)CoBr₂ (7). To a stirring THF solution of CoBr₂ (0.017 g, 0.077 mmol, 2 mL) was added a THF solution of Tol,CyDIPyH (0.035 g, 0.077 mmol, 1 eq, 4 mL). turning green immediately. The reaction was stirred overnight, resulting in a dark green solution which was evaporated to dryness. Crystallization from vapor diffusion of petroleum ether into benzene resulted in green crystals of (Tol,CyDIPyH)CoBr₂ (0.021 g, 0.030 mmol, 40 %). ¹H NMR (C₆D₆, 400 MHz, 25° C) $\delta = 27.89, 18.31, 15.61, 4.03, 2.70, 2.42, 1.33, 0.80, 0.6, -1.88, -4.74, -8.22, -8.63, -12.78, -17.08, -22.36$. IR (THF solution, CaF₂ windows, cm⁻¹) 3202 (w, br, N-H), 1590 (s, C=N) also 2793 (m), 2677 (w), 1494 (m), 1317 (s), 1293 (s), 1257 (m).

Synthesis of (Tol,CyDIPy)₂Co (8). To a stirring THF solution of Tol,CyDIPyH (0.121 g, 0.26 mmol, 10 mL) was added a THF solution of KN(TMS)₂ (0.050 g, 0.26 mmol, 2 mL, 1 eq), turning immediately from pale yellow to bright red. This solution was added in one portion to a stirring THF solution of CoBr₂ (0.058 g, 0.26 mmol, 1 eq, 5 mL), turning a darker red color. The solution was stirred for 2 hours, then all volatiles were removed *in vacuo*, and the resulting red residue was washed with 10 mL petroleum ether, giving (Tol,CyDIPy)₂Co as a red solid. ¹H NMR (C₆D₆, 400 MHz, 25° C) $\delta = 19.35, 12.48, 9.77, 3.97, 3.26, 1.12, -4.93, -17.90$.

X-Ray Structure Determination The diffraction data were measured at 100 K on a Bruker D8 VENTURE with PHOTON 100 CMOS detector system equipped with a Mo-target micro-focus X-ray tube ($\lambda = 0.71073 \text{ \AA}$). Data reduction and integration were performed with the Bruker APEX3 software package (Bruker AXS, version 2015.5-2, 2015). Data were scaled and corrected for absorption effects using the multi-scan procedure as implemented in SADABS (Bruker AXS, version 2014/5, 2015, part of Bruker APEX3 software package). The structure was solved by the

dual method implemented in SHELXT2 and refined by a full-matrix least-squares procedure using OLEX23 software package (XL refinement program version 2014/74).⁹ The structure of **2**, **6**, and **7** suffered from disorder of the metal center between the two bidentate binding pockets of the ligand. This disorder was modeled as 50% occupancy at each site for **2** and **7**, and 75% in one orientation for **6**. Due to this model, the N–H of the protonated ligand could not be located in **2** in the difference map and was not affixed to the structure due to overlap with the disordered Pd center. The omission of this hydrogen from the structure causes a discrepancy in the molecular formula from the cif file and that reported for the compound. Despite this issue, the presence of the N–H in this compound is unequivocal based on other data.

References

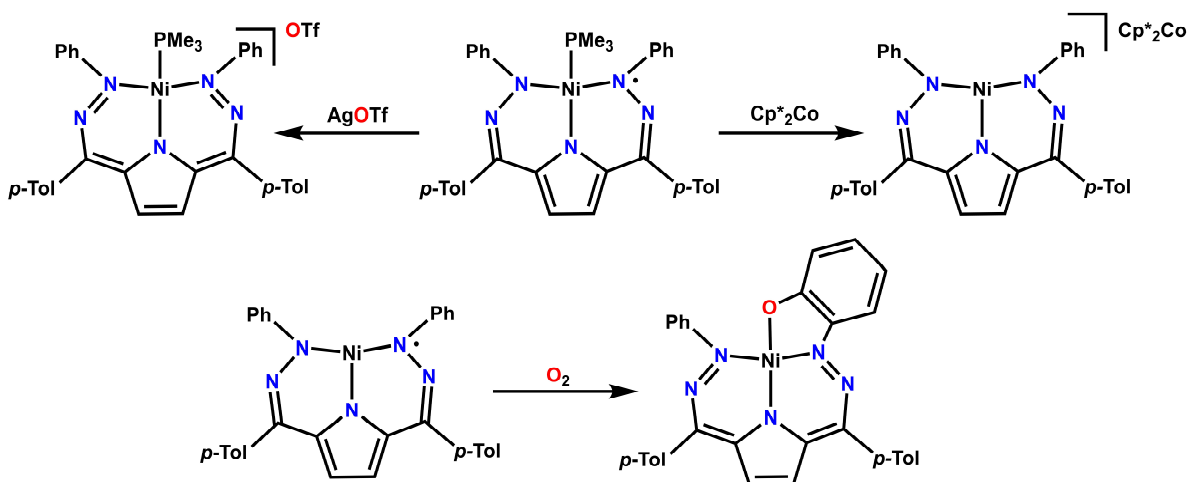
- ¹ Bowman, A. C.; Milsmann, C.; Hojilla Atienza, C. C.; Lobkovsky, E.; Wieghardt, K.; Chirik, P. J., Synthesis and Molecular and Electronic Structures of Reduced Bis(imino)pyridine Cobalt Dinitrogen Complexes: Ligand versus Metal Reduction. *J. Am. Chem. Soc.* **2010**, *132* (5), 1676-1684.
- ² Fortun, S.; Daneshmand, P.; Schaper, F., Isotactic rac-Lactide Polymerization with Copper Complexes: The Influence of Complex Nuclearity. *Angew. Chem., Int. Ed.* **2015**, *54* (46), 13669-13672.
- ³ Barbero, M.; Cadamuro, S.; Degani, I.; Fochi, R.; Gatti, A.; Regondi, V., Pentaatomic heroaromatic cations. 18. Acylation of pyrrole and N-methylpyrrole with 1,3-benzoxathiolium tetrafluoroborates. A high-yield method for the synthesis of diacylpyrroles. *J. Org. Chem.*, **1988**, *53*, 2245.
- ⁴ Based on a search of the Cambridge Structural Database
- ⁵ Ford, C. L.; Park, Y. J.; Matson, E. M.; Gordon, Z.; Fout, A. R., A bioinspired iron catalyst for nitrate and perchlorate reduction. *Science* **2016**, *354* (6313), 741-743.
- ⁶ (a) Huacuja, R.; Graham, D. J.; Fafard, C. M.; Chen, C.-H.; Foxman, B. M.; Herbert, D. E.; Alliger, G.; Thomas, C. M.; Ozerov, O. V., Reactivity of a Pd(I)-Pd(I) Dimer with O₂: Monohapto Pd Superoxide and Dipalladium Peroxide in Equilibrium. *J. Am. Chem. Soc.* **2011**, *133* (11), 3820-3823. (b) Zhang, J.; Pattacini, R.; Braunstein, P., Tridentate Assembling Ligands Based on Oxazoline and Phosphorus Donors in Dinuclear Pd(I)-Pd(I) Complexes. *Inorg. Chem.* **2009**, *48* (24), 11954-11962. (c) Murahashi, T.; Kurosawa, H., Organopalladium complexes containing palladium-palladium bonds. *Coord. Chem. Rev.* **2002**, *231* (1-2), 207-228.
- ⁷ (a) Gautam, R.; Loughrey, J. J.; Astashkin, A. V.; Shearer, J.; Tomat, E., Tripyrrindione as a Redox-Active Ligand: Palladium(II) Coordination in Three Redox States. *Angew. Chem., Int. Ed.* **2015**, *54* (49), 14894-14897. (b) Comanescu, C. C.; Vyushkova, M.; Iluc, V. M., Palladium carbene complexes as persistent radicals. *Chem. Sci.* **2015**, *6* (8), 4570-4579. (c) Zhang, J.; Pattacini, R.; Braunstein, P., Tridentate Assembling Ligands Based on Oxazoline and Phosphorus Donors in Dinuclear Pd(I)-Pd(I) Complexes. *Inorg. Chem.* **2009**, *48* (24), 11954-11962.
- ⁸ Peters, G. M.; Winegrad, J. B.; Gau, M. R.; Imler, G. H.; Xu, B.; Ren, S.; Wayland, B. B.; Zdilla, M. J. Synthesis and Structure of 2,5-Bis[N-(2,6-mesityl)iminomethyl]pyrrolylcobalt(II): Evidence for One-Electron-Oxidized, Redox Noninnocent Ligand Behavior. *Inorg. Chem.* **2017**, *56* 3377-3385.
- ⁹ (a) Sheldrick, G. M. SHELXT- Integrated space-group and crystal-structure determination. *Acta Cryst.* **2015**, *A71*, 3- 9. (b) Dolomanov, O.V.; Bourhis, L. J.; Gildea, R. J.; Howard, A. K.; and

Puschmann, H. Olex2, a complete structure solution, refinement, and analysis program. *J. Appl. Cryst.* **2009**, *42*, 339. (c) Sheldrick, G. M. A Short History of SHELX. *Acta Cryst.* **2008**, *A64*, 112-122. (d) Sheldrick, G. M. Crystal structure refinement with SHELXActa Cryst. 2015, *C71*, 3-8.

Chapter 2: Dihydrzonopyrrole Ligands

Introduction

After studying $\text{To}^{\text{l,Cy}}\text{DIPy}$ and observing the lack of stability in binding first-row metals, dihydrazonepyrrole (DHP) ligands were targeted. The DHP scaffold is beneficial as the beta-nitrogen of the hydrazone unit can also coordinate to the metal center, giving a very stable six-membered ring with the pyrrole nitrogen. The first DHP derivative synthesized was $\text{To}^{\text{l,Ph}}\text{DHP}$, synthesized through condensation of phenylhydrazine with the ditolylacetyl pyrrole. Unlike $\text{To}^{\text{l,Cy}}\text{DIPy}$, the free ligand is unstable towards oxidation, with the formation of a further cyclized system upon exposure to oxygen or benzoquinone. Previous research within the group has shown that $\text{To}^{\text{l,Ph}}\text{DHP}$ binds well to Ni through the β -nitrogens of the hydrazone and forms a T-shaped Ni complex which is competent for homolytic activation of the O–H bonds of H_2O to form a bridging hydroxide, which can then perform O-atom transfer to phosphines (Scheme 2 - 1).¹ This system did have two major pitfalls. The most significant was the propensity for C–H oxidation of the phenyl groups of the ligand to form an phenoxide which binds to the metal center, shutting down all further reactivity (Scheme 2 - 1). An identical product was also rapidly observed upon any Scheme 2 - 1. Reactivity in the $\text{Ph,To}^{\text{l}}\text{DHPNi}$ system.

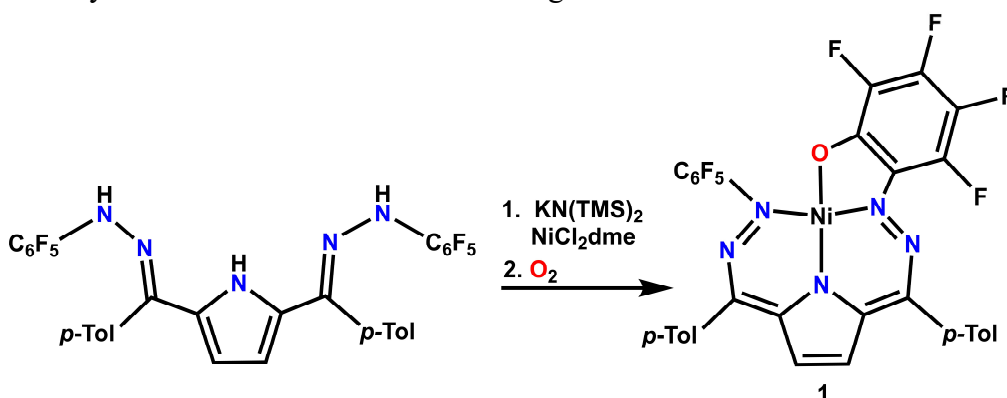


reaction with O₂ with Ni complexes featuring the ^{Tol,Ph}DHP ligand, showing the lack of stability to oxidation.

The second area where the ^{Tol,Ph}DHP scaffold did not show promise was in limited ligand-based H₂ reactivity. The nitrogens of the hydrazone could not be protonated and remain coordinated to the metal center, so full H₂ transfer across the scaffold was impossible.¹ This was likely due to the weak basicity of the aromatic hydrazone unit, so more basic nitrogens were targeted for future ligand designs.

Results and Discussion

Synthesis and Intramolecular Oxidation with Fluorinated DHP. Oxidation of aromatic C–H bonds often occurs through a highly reactive metal-oxygen species, such as a superoxide, peroxide, or oxyl-type species. These oxygen complexes typically react through a radical C–H abstraction pathway that is dictated by the BDE of the functional group that it is attacking. In order to avoid this pathway, fluorination of the phenyl groups was targeted so that the C–F BDE would be high enough to preclude oxidation by even a reactive nickel-oxygen species. Condensation of the diacylpyrrole with pentafluorophenylhydrazine was performed and the perfluorinated ligand could be purified by repeated washings with Et₂O. Unlike ^{Ph,Tol}DHP, ^{Tol,FPh}DHP is initially isolated as one isomer, though upon standing in a CDCl₃ there is appearance of an asymmetric isomer. Scheme 2 - 2. Synthesis of **1** via C–F oxidation using ^{FPh,Tol}DHP.

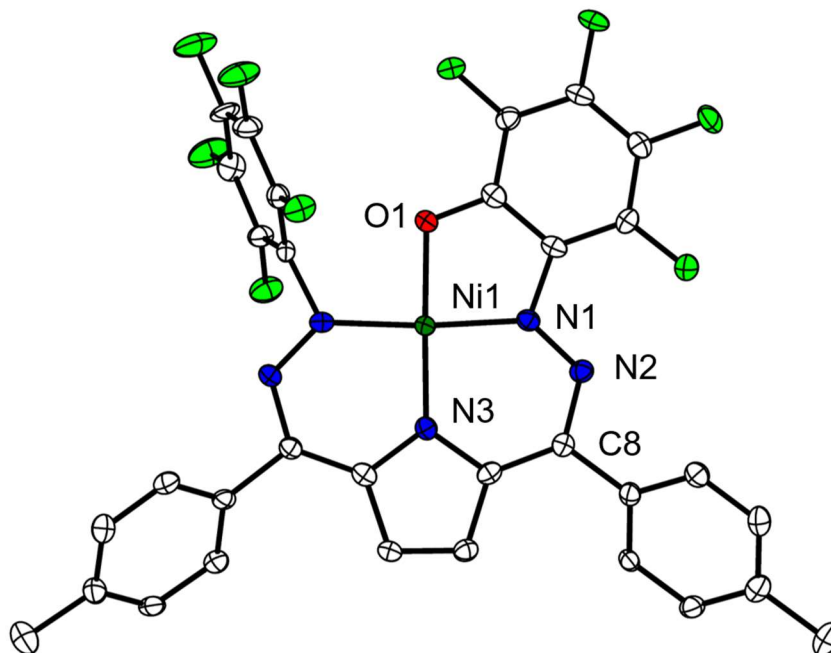


Based upon earlier studies in the $^{\text{ToI,Ph}}\text{DHP}$ system, it was reasonably assumed that this would not affect further reactivity, so the metalation with $^{\text{ToI,Ph}}\text{DHP}$ was conducted with NiCl_2dme and pyridine.

Though metal complexes with this ligand were not fully characterized, similar products and binding modes as in $^{\text{Ph,ToI}}\text{DHPNi}$ were proposed. Several of these proposed complexes were then exposed to O_2 in order to preliminarily test the stability of the $^{\text{FPh,ToI}}\text{DHP}$ system to intramolecular oxidation. Crystallization of the reaction mixture from acetonitrile allowed isolation of $(^{\text{ToI,FPh}}\text{DHPO})\text{Ni}$ (**1**), a C–F activated form of the ligand with the phenoxide bound to Ni as was previously observed in the proteo variant (Figure 2 - 1). The ^{19}F NMR of the reaction in situ showed formation of fluorosilicates by a peak at -79 ppm, likely from formation of HF during the reaction which then etches the silicates in the glass (Figure 2A - 8). The oxidized product of the $^{\text{ToI,Ph}}\text{DHP}$ system had not been previously structurally characterized, so structural

Figure 2 - 1 Solid state structure of **2**.

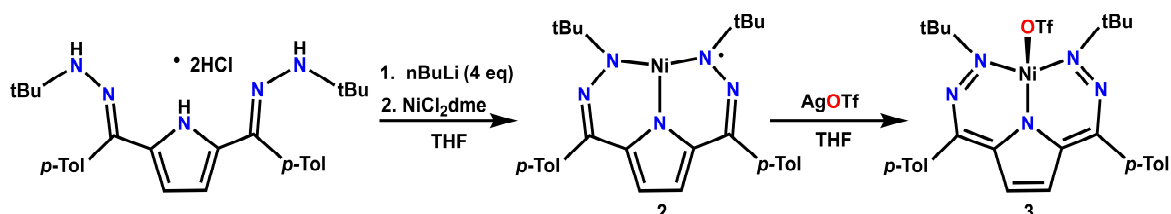
Ellipsoids are set to 50% probability and hydrogen atoms are omitted for clarity. Selected bond lengths and angles: Ni1–O1: 1.851(19) Å, Ni1–N1: 1.842(2) Å, Ni1–N3: 1.822(2) Å, N1–N2: 1.311(3) Å, 1.352(3) Å. N3–Ni1–O1 172.2(9)°



characterization of **1** confirmed both the binding mode of the ligand and ligand oxidation state. Bond lengths within the ligand, especially the contracted N–N bond lengths and lengthened C–N bond lengths indicate a fully oxidized ligand while the two beta nitrogens of the hydrazones are bound to Ni, leaving a five-membered ring chelate in the hydrazone and oxidized ligand.

Oxidation of C–F bonds is very rare in synthetic or biological systems.² The ease of activation of the very strong aryl C–F bond indicates that the likely mechanism for intramolecular oxidation is a nucleophilic aromatic substitution with the reactive oxygen species bound to Ni acting as a strong nucleophile. Because the ^{Tol,FPh}DHP ligand was still susceptible to intramolecular oxidation, *t*-butyl groups were instead targeted to remove all weak or electrophilic bonds from the ligand to access a Ni complex with greater stability to intramolecular oxidation. The *t*-butyl groups would also be significantly more basic than the aromatic hydrazones, so H₂ transfer was also targeted with this system.

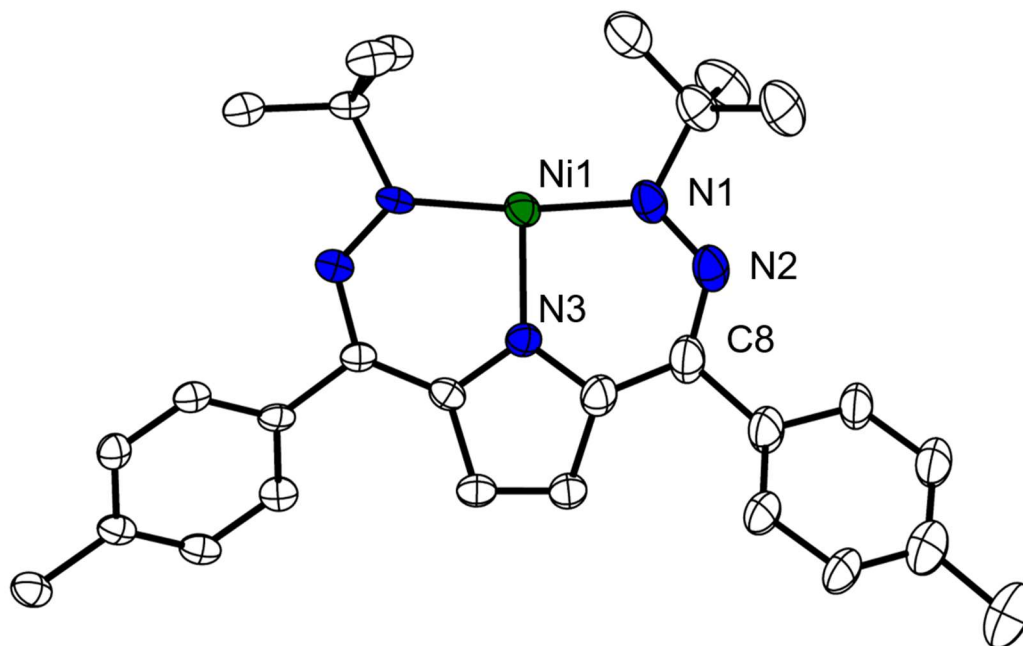
Synthesis and Metalation of ^{tBu,Tol}DHP. The dihydrazonepyrrole ligand, ^{tBu,Tol}DHP, is synthesized by condensation of excess *t*-butyl hydrazine with the previously reported ditolylacetyl pyrrole at high temperature for 5 days, after which it is isolated in 66% yield as a doubly protonated hydrochloride salt. Deprotonation with four equivalents of *n*-BuLi and subsequent addition to (DME)NiCl₂ yields a deep purple complex in 43% yield, assigned as [^{tBu,Tol}DHP[•]]Ni (**2**) which can be purified by passage through a silica plug. Complex **2** is paramagnetic, and Evan's method gives a μ_{eff} of 2.02 B.M., indicating an $S = \frac{1}{2}$ spin system. The X-band EPR spectrum of **2** in toluene is also consistent with this assignment, as a broad axial signal is observed with features at $g = 2.24$. Scheme 2 - 3. Metalation of ^{tBu,Tol}DHP to Ni to form **2**, and oxidation to form **3**.



and 2.12 (Figure 2A - 18). When the EPR spectrum was recorded in THF, a much more complicated signal arises, likely from a solvent-binding equilibrium in the fourth coordination site of the Ni center (Figure 2A - 19). Crystals of **2** were obtained to allow for more detailed structural analysis of this complex, and single crystal X-ray diffraction (SXRD) revealed a T-shaped Ni complex bound to ^tBu,^{Tol}DHP through the pyrrole nitrogen and both β -nitrogens of the hydrazone arms of the ligand (Figure 2 - 2). The structure is symmetric within the estimated standard deviation, with the two Ni–N_{hydrazone} bond lengths being 1.843(4) Å and 1.843(7) Å. The N_{pyrrole}–Ni–N_{hydrazone} angles of 93.78(1)° indicate a nearly perfect T-shaped geometry. T-shaped complexes are uncommon with Ni(II) and while the DHP scaffold may have some electronic influence in enforcing a T-shaped geometry in **3**, this coordination is likely facilitated by steric crowding from the *t*Bu groups as well.³

Figure 2 - 2. Solid state structure of **2**.

Ellipsoids are set to 50% probability and hydrogen atoms are omitted for clarity. Selected bond lengths and angles. Ni1–N1 1.843(9) Å, Ni1–N3 1.877(3) Å, N1–N2 1.302(5) Å, C8–N2 1.349(6) Å, N3–Ni1–N1 93.7(1)°



This complex is analogous to the previously published [^{Ph,Tol}DHP[•]]Ni T-shaped complex which was assigned as a high spin $S = 1$ Ni(II) center antiferromagnetically coupled to a ligand-based radical based on structural and spectroscopic data. The bond lengths in **2** are very similar to those in [^{Ph,Tol}DHP[•]]Ni with both the Ni–N bond distances and the bond lengths within the ligand backbone nearly identical between the two structures. The similarity in bond lengths within the DHP scaffold and in the Ni–N distances indicates that the ligands in both complexes have a similar electronic structure. The deviation from $g = 2$ in the EPR spectrum of **2** is similar to that of [^{Ph,Tol}DHP[•]]Ni and can be explained by a significant amount of spin density localized on Ni as would be expected for a high-spin Ni(II) center.

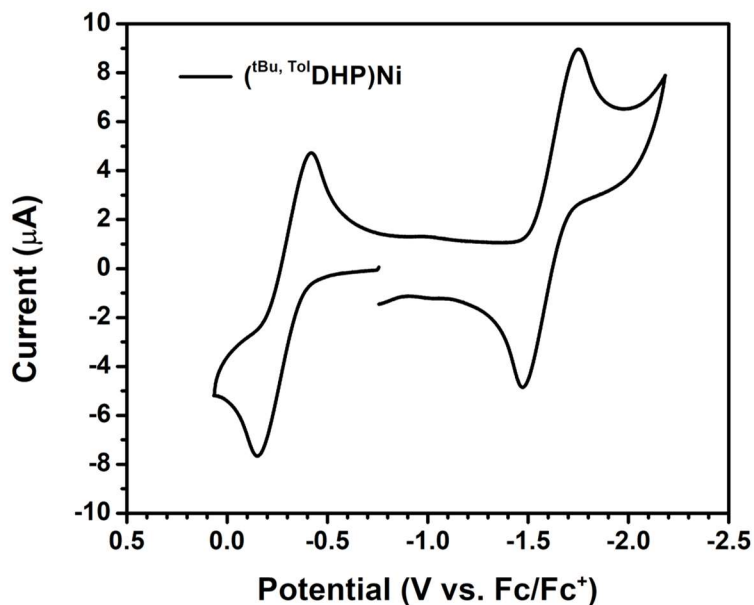
To further investigate this proposed electronic configuration, **2** was modeled with a variety of DFT calculations including broken symmetry treatments. All calculations on **2** illustrate a similar picture which is consistent with an $S = 1$ Ni center antiferromagnetically coupled to a ligand radical. The Ni center has a Mulliken spin of 1.12, with a mixture of positive and negative spin densities of -0.32 and 0.22 on the ligand backbone (Figure 2A - 54). The negative spin density is distributed on both hydrazones and through the pyrrole carbons of the ligand while the positive spin density is largely centered on the pyrrole nitrogen and is likely due to covalency between Ni and N. Here too, the spin density is qualitatively identical to that observed for the Ph-substituted system. In sum, all of these data are consistent with the assignment of **2** as a high-spin Ni(II) center coupled antiferromagnetically to a ligand-based radical, directly analogous to the electronic structure of [^{Ph,Tol}DHP[•]]Ni.

Oxidative Reactivity of (^{Bu,Tol}DHP)Ni With the concrete assignment of a ligand-based radical bound to Ni(II), we investigated the analogous reactivity to [^{Ph,Tol}DHP[•]]Ni. Unlike the Ph-substituted congener [^{Ph,Tol}DHP[•]]Ni, **2** does not show any reactivity with H₂O, even at high

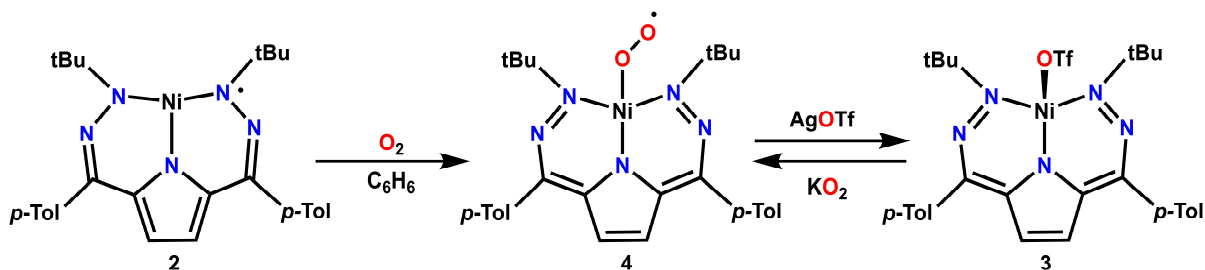
temperature. Tracking the reaction by ^1H NMR shows a sharp resonance for the proton of H_2O , indicating that there is no binding with the paramagnetic metal center. While it is possible that the steric bulk could disfavor binding, we also investigated the reduction potentials of the ligand to see how the *t*-butyl substitution alters the electronic environment.

The cyclic voltammogram (CV) of **2** shows two reversible redox events: an oxidation at -0.3 V vs. Fc/Fc^+ and a reduction at -1.7 V vs. Fc/Fc^+ , which we assign as ligand-based oxidation and reduction respectively based on comparison with similar couples in the Ph substituted system (Figure 2 - 3). These couples are shifted approximately 300 mV negative of those in $[\text{Ph, Tol}^1\text{DHP}^*]\text{Ni}$, suggesting a more reducing ligand environment due to the more donating *t*-butyl groups.

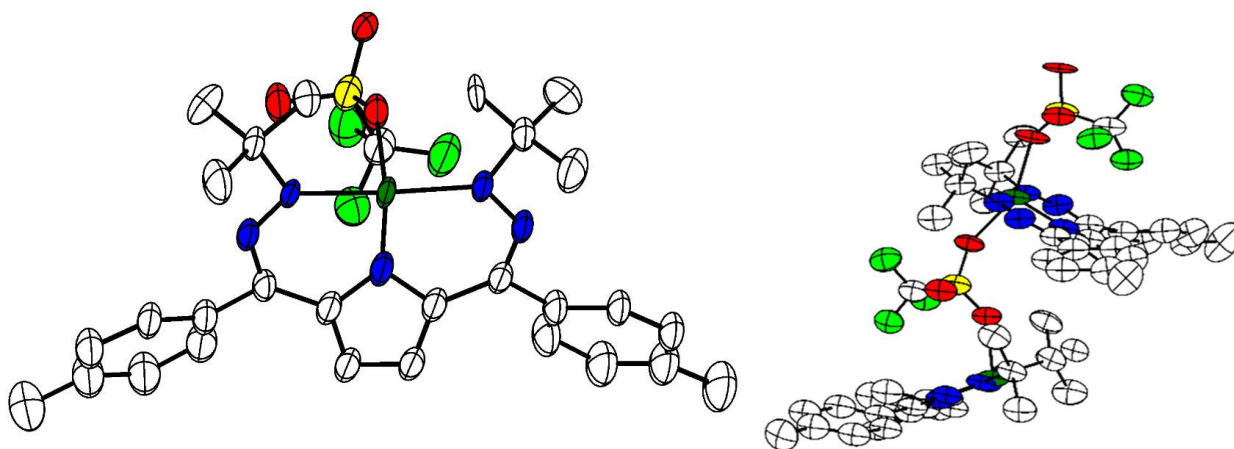
We then attempted to chemically access these ligand-based redox events. While we have been unable to isolate more reduced complexes, addition of one equivalent of AgOTf to **2** results in an immediate color change from purple to deep blue. The ^1H NMR spectrum of this reaction product shows the disappearance of the characteristic broad peaks for **2**, with new paramagnetic features growing into the spectrum, assigned as the four-coordinate triflate adduct Figure 2 - 3. CV of 1 mM **2** in THF with 0.1 M nBu_4PF_6 . Scan rate = 100 mV/sec.



Scheme 2 - 4. Reaction of **2** with O₂ to form **4**, and interconversion of **3** and **4**.



[^tBu,^{Tol}DHP]NiOTf (**3**) (Scheme 2 - 3). The ¹⁹F NMR spectrum of **3** indicates that the triflate anion remains bound to the metal center in solution, as demonstrated by the chemical shift and broadening of the triflate signal (Figure 2A - 13). Complex **3** is best assigned as a high-spin Ni center with an oxidized DHP ligand. The paramagnetism of the complex and an Evans method magnetic moment of $\mu_{\text{eff}} = 2.87$ B.M. support the assignment of an $S = 1$, high-spin Ni(II) center. The solid-state structure of **3** was obtained by SXRD and confirms the connectivity of the complex, but poor diffraction precluded analysis of specific bond lengths. The structure does show a novel chain structure where each Ni center is bridged to an adjacent Ni through the triflate ligands, leading to 1-D chains in the solid state. This binding mode is unlikely in solution due to the complex's solubility in benzene and other non-polar solvents. The chemical accessibility and Figure 2 - 4. Solid state structure of **4** with triflate bridging (right).



reasonable potentials of this ligand-based redox event suggested to us that reactivity with O₂ would be viable.

Characterization of a Ni Superoxo Complex We then turned to investigate the aerobic reactivity of **2** to determine whether the *t*-butyl groups effectively stabilize this complex towards oxidative degradation. Complex **2** undergoes a distinct color change from purple to red when exposed to air or pure O₂ in a benzene solution resulting in a ¹H NMR silent product. We have assigned this new species as a Ni superoxo complex [^{*t*}Bu,^{*o*}TolDHP]NiO₂ (**4**) based on a variety of characterization (Scheme 2 - 4). Tracking the conversion of **2** to **4** in benzene by UV-vis spectroscopy reveals an isosbestic transition suggesting a clean 1:1 transformation (Figure 2A - 29). Complex **4** has a solution magnetic moment of $\mu_{\text{eff}} = 1.65$ B.M., confirming that the complex is still an $S = \frac{1}{2}$ species despite the lack of ¹H NMR signals. X-band EPR indicates the formation of a new species that displays a rhombic $S = \frac{1}{2}$ signal with $g = 2.23, 2.10,$ and 2.07 (Figure 2A - 20). These values are consistent with other reported Ni(II) superoxo complexes.⁴

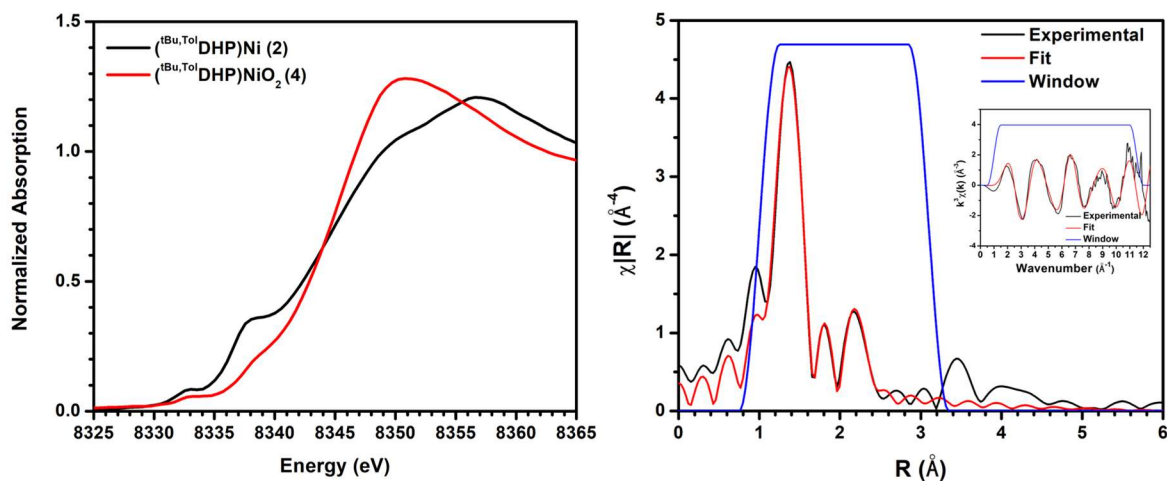
We have extensively attempted to collect Raman data on **4** with no success. We have been, however, able to record infrared (IR) spectra of **4** as a KBr pellet and in solution with both ¹⁶O₂ and ¹⁸O₂. The solid state spectrum of **4** shows a isotope sensitive feature assigned as an O–O stretch which appears at 1045 cm⁻¹ upon labeling, similar to other published vibrational data for superoxo species (Figure 2A - 47).⁴ The feature with natural abundance O₂ is difficult to directly assign due to overlap with other features in that area, but is likely underneath a feature at ~1105 cm⁻¹ to give a shift of 60 cm⁻¹ compared to an expected shift of 64 cm⁻¹. In an effort to obtain a better subtraction, the IR spectrum of **4** was also recorded as a C₆H₆ solution. An ¹⁶O₂ – ¹⁸O₂ subtraction spectrum shows the appearance of a feature at 1097 cm⁻¹ and a decrease in intensity of the features at 1170 cm⁻¹ (Figure 2A - 46). This gives a shift of 73 cm⁻¹ compared to a predicted shift of 68

cm⁻¹. Taken together, these vibrational analyses are consistent with the assignment of a superoxo complex.

Complex **4** is extremely oily and soluble which has precluded the determination of its structure via single crystal XRD analysis. To circumvent this issue Ni K-edge X-ray absorption spectroscopy (XAS) was performed to probe the geometry and electronic structure of Ni. Complexes **2** and **4** have distinct shapes in their edge regions consistent with a change in coordination number upon exposure to air (Figure 2 - 5). The intense rising edge in the spectrum of **2** at 8338.9 eV corresponds to a 1s→4p transition due to the expected non-degenerate 4p levels in a T-shaped geometry. Similar features are observed in reported XAS spectra of trigonal planar Cu(I) complexes.⁵ In contrast, this feature in **4** is assigned as a shakedown transition by comparison to similar features observed in square planar 3d transition metal complexes with ligand to metal charge transfer transitions (LMCT).⁵⁸ The lowered intensity of this feature is likely due to the deviation from ideal D_{4h} symmetry as predicted in the DFT calculated structure of **4** (Figure 2A - 55). In addition to this feature, a 1s→3d transition is observed at 8333.6 eV in both **2** and **4**. The intensity of 1s→3d pre-edge features is dependent on the degree of p-d mixing. The coordination of an O atom to the T-shaped geometry of **3** will lead to a distorted square-planar geometry. This higher coordination number should increase the energy gap between the d and p levels, effectively decreasing p-d mixing and causing a drop in the intensity of this pre-edge feature. Similar drops in intensity have been observed for other series with increasing coordination numbers.⁶ DFT calculations also support this assignment, as the p-orbital contribution to the highest lying d-orbital drops from 8% to 2% in the conversion from **2** to **4** (Table 2A - 3). Taken together, these pre-edge data support the assigned structure of **4**.

We have also examined the Extended Absorption Fine Structure (EXAFS) region of the XAS data for **4**. (Figure 2 - 5). The EXAFS data was fit for the first two shells around Ni and confirms the assignment of an end-on Ni superoxo, showing a Ni-O bond length of 2.08(1) Å. This bond length is longer than that typically found in Ni superoxo complexes, but is similar to the Ni-O bond length of another end-on Ni superoxo that has been characterized by EXAFS. The second shell fitting also distinguished the second O of the superoxo at 2.70(1) Å from the Ni, indicating there is no interaction with the metal but confirming the presence of the superoxo ligand.⁴ The second shell fit also included the nitrogen of the hydrazone and carbons of the *t*-butyl group to confirm that these signals are not interfering with the superoxo oxygen, and the C and N scatterers are distinct at longer distances of at least 0.17 Å further from Ni. The Ni-N bond lengths are slightly lengthened compared to **2**, with a Ni-N_{pyrrole} distance of 1.873(6) Å and Ni-N_{hydrazone} distances of 1.920(6) Å, suggesting ligand-based oxidation to a monoanionic ligand in **4** weakens the ligand binding to Ni compared to the dianionic ligand in **2**. Attempts to fit the second shell of **4** without the second O of the superoxo resulted in a significantly worse fit, indicating the second

Figure 2 - 5. Left: K-Edge X-ray absorption data for **2** and **4** showing no change in edge energy upon reaction of **2** with O₂. Right: XAFS fitting of **4**, with K-space inset.



O is necessary for describing the structure (Table 2A - 11). Overall, the EXAFS data and analysis verifies the structure of **4** as a Ni superoxo.

The XAS data on **2** and **4** also provide an opportunity to probe the oxidation state of the Ni center and verify the proposed ligand centered electron transfers. There is effectively no energy shift (less than the 0.4 eV resolution) for the K-edge or pre-edge features in the generation of **4** from **2** (Figure 2 - 5). Although the Ni K-edge does not show a large change with oxidation state, a 1.8 eV shift in the K-edge and 0.7 eV shift in the pre-edge energy has been observed between Ni(III) peroxy and Ni(II) superoxo complexes.^{4,7} The absence of similar shifts in the conversion from **2** to **4** indicates that no metal centered redox occurs.

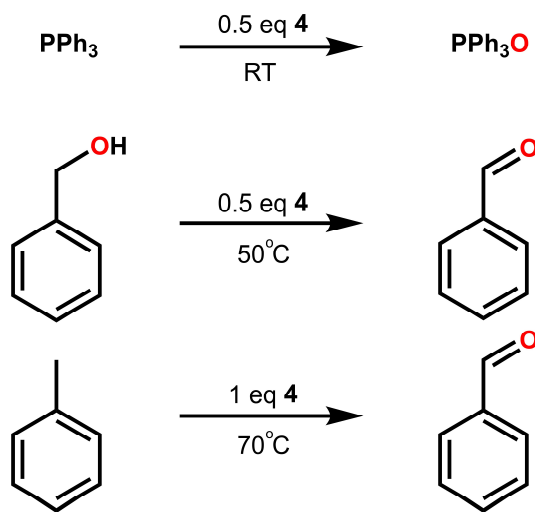
Finally, we have examined the geometry and electronic structure of **4** with DFT calculations. The geometry of **4** in the DFT computed structure is that of an end-on superoxide ligand consistent with our assignment. Attempts to minimize an η^2 structure resulted in dissociation of the second O ligand to generate an end-on structure. The computed spin density in **4** is predicted to lie nearly entirely on O₂, consistent with our spectroscopic data (Figure 2A - 56). TD-DFT was also performed to compare the calculated UV-vis data with the experimentally determined data. The shape of the UV-vis spectrum of **4** is reliably reproduced, with the peaks of the calculated spectrum within a reasonable error of those in the experimentally determined spectrum (Figure 2A - 58, Figure 2A - 59). In sum, all these data are consistent with the proposed structural assignment of **4** as an end-on Ni superoxo complex which is formed by ligand centered electron transfer with no formal oxidation state change on Ni. While several Ni superoxo complexes have been published, none have used a ligand-based redox event to reduce O₂. The only precedent for this comes from natural systems. Many enzymes use specific ligand fields to stabilize either Ni(I) or Ni(III), such as highly donating thiol groups, but a nickel-containing quercetin dioxygenase uses

an electron from the substrate to reduce O₂ to superoxide, which then binds to Ni(II) to undergo further reactivity.⁸

Oxidative Reactivity. With the characterization of **4** in hand, we then examined reactivity both to confirm its composition and to probe whether **4** can mediate oxidative conversions. Stirring **3** with one equivalent of KO₂ for one hour results in a color change from blue to dark red (Scheme 2 - 4). Analysis of this reaction mixture by UV-vis and EPR spectroscopy reveals signals consistent with conversion to **4** (Figure 2A - 24, Figure 2A - 32). These data also support the assignment of **4** as a Ni superoxo complex as using an external superoxide source produces the same product. Electrochemistry of **4** was also investigated to probe the reversibility of O₂ binding and activation. CV of **4** shows an irreversible oxidation and reduction at 0.32 and -1.7 V vs. Fc/Fc⁺ respectively (Figure 2A - 38). Chemical oxidation was targeted with the hypothesis that oxidation of **4** could convert back to **3**. Addition of one equivalent of AgOTf to a stirring THF solution of **4** indeed results in the reappearance of **3** as indicated by UV-vis spectroscopy (Figure 2A - 30). This is likely due to oxidation of the superoxide to dioxygen, which then dissociates as the triflate binds to give **3**.

We then investigated the reactivity of **4** with the H-atom donors diphenylhydrazine (DPH) and 9,10-dihydroanthracene (DHA). Complex **4** somewhat surprisingly shows little to no reactivity with DHA but does generate azobenzene within 10 minutes when reacted with DPH under N₂. We rationalize that the muted reactivity with DHA implies a very weak O–H BDE for the putative Ni hydroperoxo product of C–H abstraction. Computations support this hypothesis and suggest an O–H BDE of ~63 kcal/mol (Table 2A - 5).

Despite this muted H-atom abstraction reactivity, complex **4** still mediates oxidative reactivity with organic substrates. Complex **4** reacts with triphenylphosphine under N₂ to produce two equivalents of triphenylphosphine oxide by ³¹P NMR at room temperature (Scheme 2). Oxidation of alcohols to aldehydes was also investigated and NMR analysis indicates that complex **4** converts two equivalents of benzyl alcohol to benzaldehyde at 50 °C over three hours under air (Scheme 2 - 5). Finally, C–H activation was studied using toluene as a test substrate. At 70 °C for three hours under air, **4** produces ~ one equivalent of benzaldehyde from neat toluene, likely via C–H activation to benzyl alcohol then oxidation of the benzyl alcohol to benzaldehyde. This reaction was also performed using **4** enriched with ¹⁸O from reaction of **2** with ¹⁸O₂. GC/MS analysis indicates that the benzaldehyde product is enriched with ¹⁸O₂ as expected (Figure 2A - 50). There are very few examples of C–H oxidation reactivity with Ni, though superoxo species in general have been suggested as intermediates in C–H oxidations.^{4,9} The consistent appearance of two equivalents of oxidized products (or double oxidation in the case of toluene) suggests that the reaction is stoichiometric in oxygen equivalents. Furthermore, the fact that **4** generates two equivalents of triphenylphosphine oxide under N₂ also implies that both of the O-equivalents from Scheme 2 - 5. Oxidative Reactivity of **4**.



the superoxide ligand can be transferred to substrates. It is currently unclear why the complex cannot turn over to bind another equivalent of O₂ and enable catalytic oxidations.

The muted C–H abstraction reactivity of **4** with DHA raises interesting mechanistic questions about the oxidative activity of this complex. The resulting mixtures after the oxidation reactions are complicated and further study is needed to understand potential decomposition routes. It is possible if not likely that the elevated temperatures required for this oxidative reactivity lead to the formation of another species which is the active oxidant. Kinetic analysis of the reaction of **4** with benzyl alcohol shows a second order dependence on the concentration of **4**, indicating a more complex mechanism than direct substrate oxidation by the superoxide species (Figure 2A - 34). The low reactivity of **4** is unusual in that many other Ni(II) superoxo species are much more unstable and reactive. Because complex **4** is formed by a comparatively mild, ligand-based redox event, the resulting superoxo is not very oxidizing. Therefore, the ligand-based nature of the electron transfer may play an important role in the isolation and study of this species, suggesting the viability of ligand-based redox events for stabilizing highly reactive compounds. While still stoichiometric, the oxidative reactivity of **4** is unusual and demonstrates that the ligand-based activation of O₂ enables oxidative reactivity for Ni centers as has been proposed in quercetin dioxygenase.

Metalation to (^tBu,^{Tol}DHPH₂)NiCl. After probing the aerobic reactivity of this system, reactivity with H₂ was targeted to verify that the DHP scaffold could affect secondary sphere H₂ transfer. In order to initially probe this reactivity, a complex with a fully hydrogenated DHP scaffold was targeted.

Metalation of ${}^{t\text{Bu,Tol}}\text{DHP}\cdot\text{HCl}$ via deprotonation with 4 equiv of $n\text{-BuLi}$ furnishes **2**, but metalation via deprotonation with 3 equiv. of $n\text{-BuLi}$ gives a new diamagnetic species, assigned as $({}^{t\text{Bu,Tol}}\text{DHPH}_2)\text{NiCl}$ (**5**) (Scheme 2 - 6). The ${}^1\text{H}$ NMR shows a symmetric ligand environment with a broad singlet that integrates to 2 protons, assigned to the N–H protons on the ligand (Figure 2A - 14). Structural determination of **5** by single crystal XRD shows a square planar geometry around Ni, though the ligand is significantly twisted so that the square plane of the Ni does not align with the plane of the pyrrole ring (Figure 2 - 6). The Ni–N_{hydrazone} bonds are lengthened by 0.1 Å compared to **2**, indicating significantly weaker coordination of the protonated nitrogens. The N–N bonds are lengthened by 0.15 Å compared to **2**, indicating full conversion to a N–N single bond. This bond is also significantly longer than the N–N bond length in the fully reduced $({}^{\text{Ph,Tol}}\text{DHP})\text{Ni}$ complex, indicating that hydrogenation of the ligand alters the ligand properties distinctly from simple reduction.¹ The N–H protons are oriented towards the Cl ligand while the *t*-butyl groups are twisted almost perpendicular to the Ni square plane due to hydrogen bonding from the H to the Cl, at a distance of 2.5 Å. The isolation of a DHP ligand with a full H₂ equivalent has not been observed in the ${}^{\text{Tol,Ph}}\text{DHP}$ system, indicating that alkyl rather than aromatic substituents are preferable for this reactivity likely due to increased nitrogen basicity. Cyclic voltammetry of **5** showed that there was no accessibly redox events, showing that hydrogenation of the scaffold has a dramatic effect on the ligand properties (Figure 2A - 39).

Scheme 2 - 6. Metalation of ${}^{t\text{BuTol}}\text{DHP}$ to form $({}^{t\text{Bu,Tol}}\text{DHPH}_2)\text{NiCl}$.

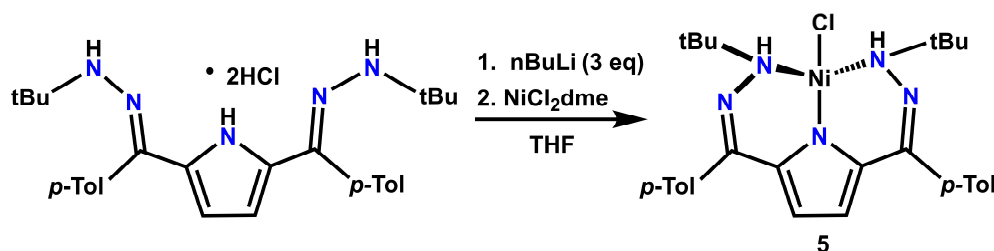
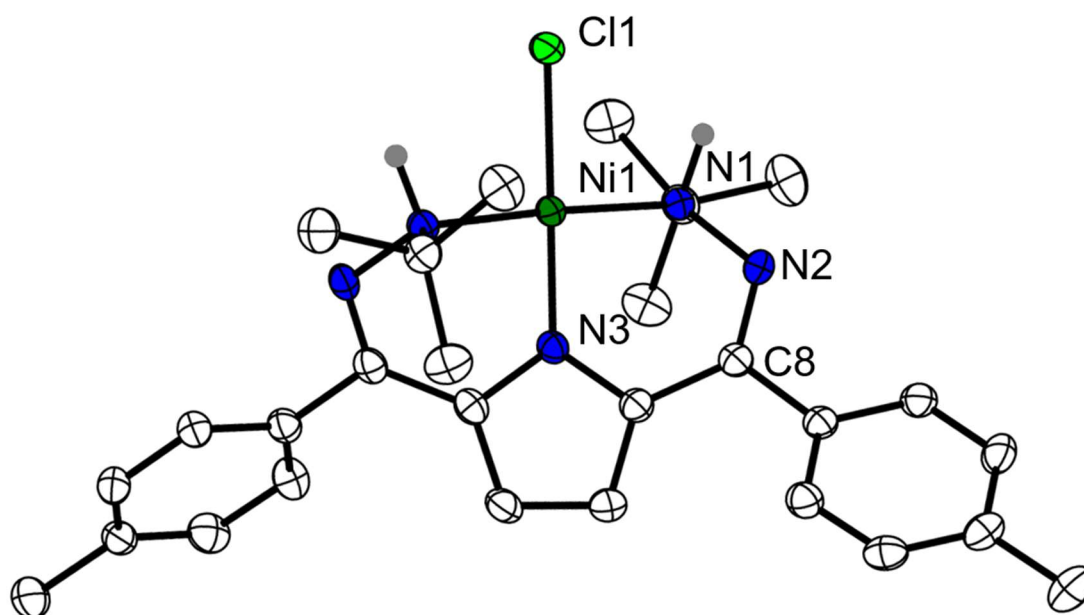


Figure 2 - 6. Solid state structure of **5**.

Ellipsoids are set to 50% probability, and all C–H hydrogens are omitted for clarity. Selected bond lengths and angles: Ni1–Cl1 2.181(8) Å, Ni1–N1 1.946(1) Å, Ni1–N3 1.824(2) Å, N1–N2 1.459(2) Å, C8–N2 1.295(3) Å, N3–Ni1–Cl1 179.47(6)°, N3–Ni1–N1 88.47(8)°.



H₂ Transfer Reactivity As **3** and **5** represent the two ligand states necessary for ligand-based H₂ transfer, the interconversion of these species was studied. To investigate whether the ligand could split H₂, **3** was reacted with H₂ gas. Degassing and addition of an atmosphere of H₂ resulted in slow conversion to a new diamagnetic species at room temperature but heating to 40° C led to significantly faster reactivity (Figure 2 - 7). This new species was assigned as (^tBu,^{Tol}DHPH₂)NiOTf (**6**) based on the proton NMR, and could also be separately accessed via halide abstraction from **5** with AgOTf (Scheme 2 - 7). To probe the catalytic H₂ transfer reactivity, Scheme 2 - 7. Halide abstraction and reversible H₂ splitting and transfer.

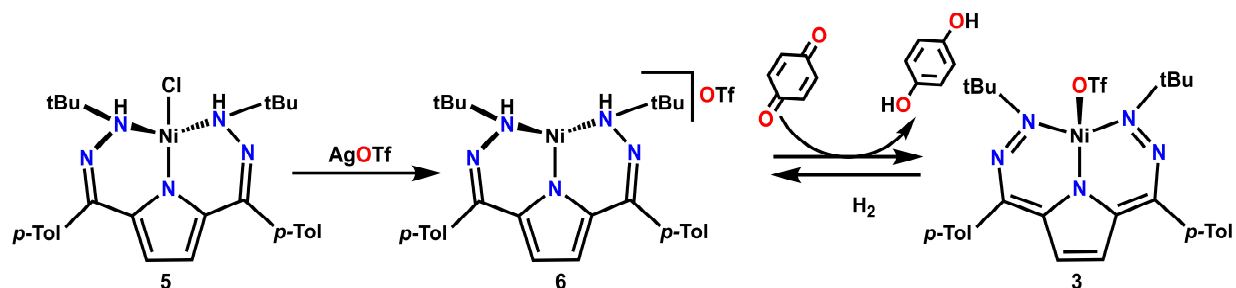
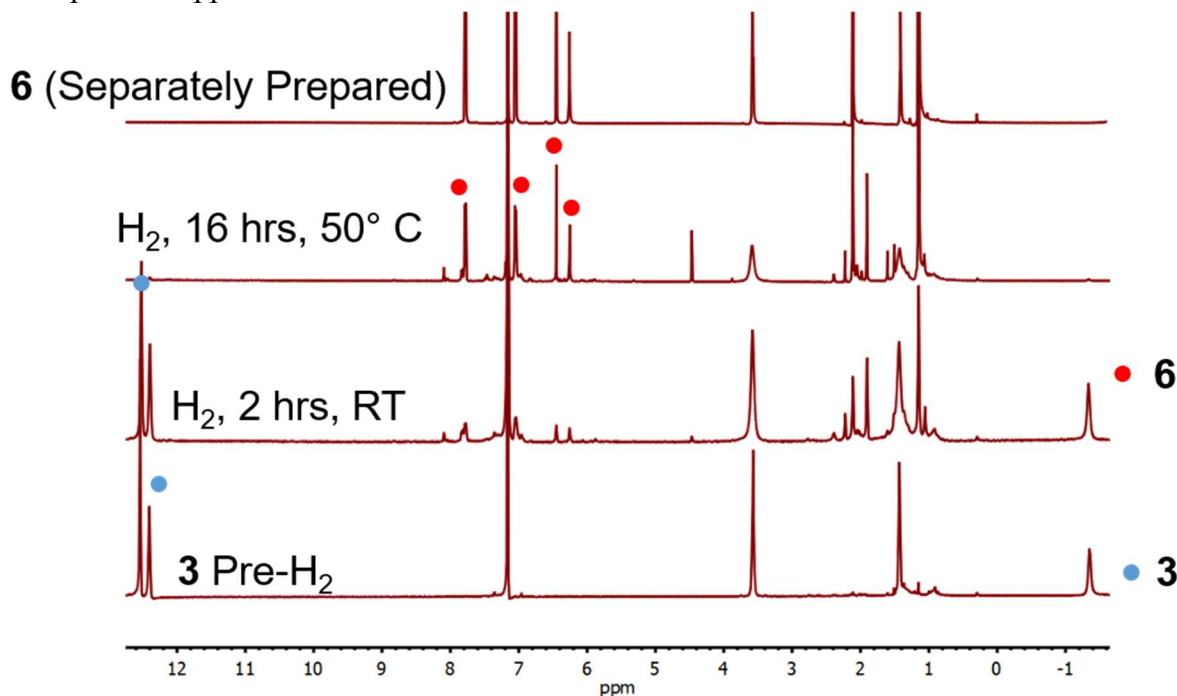


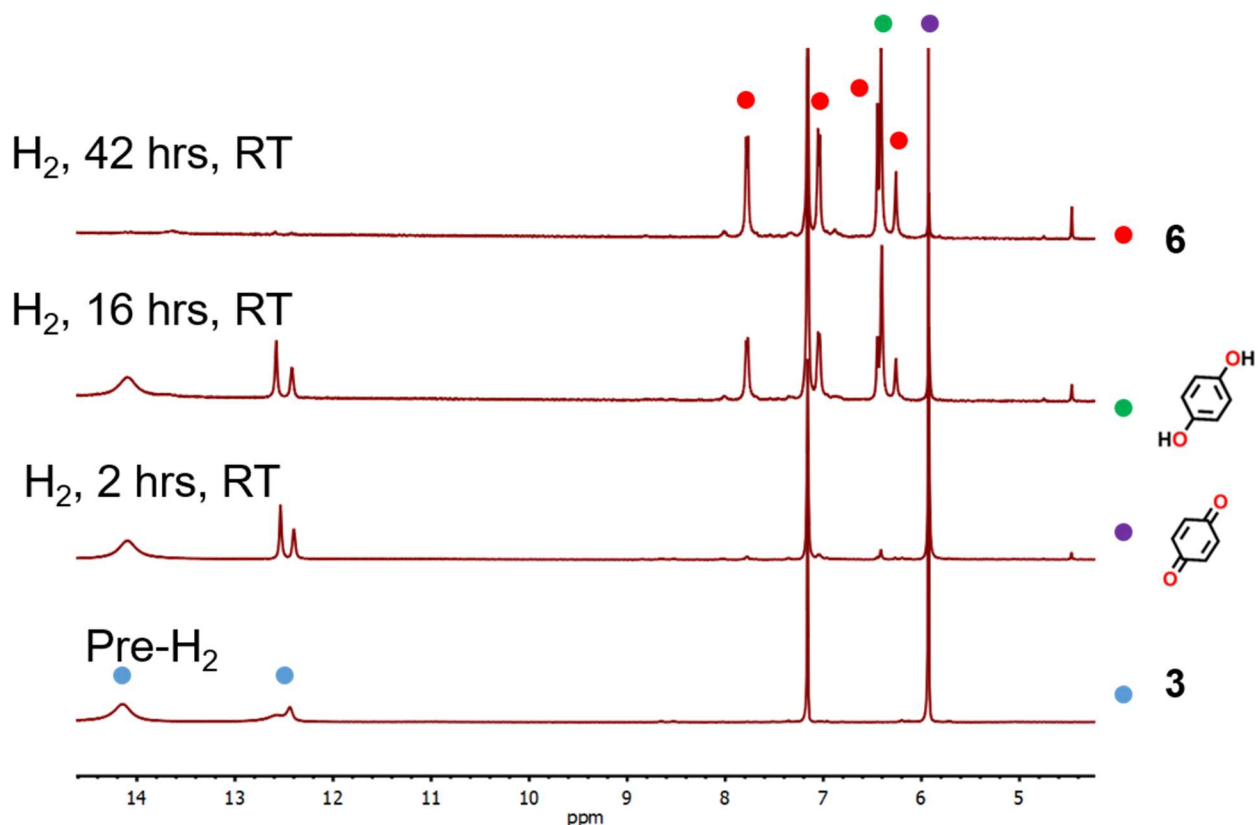
Figure 2 - 7. H₂ splitting by **3** to give **6**. Peaks at 3.5 ppm and 1.5 ppm are from residual THF, and the peak at 5 ppm is due to dissolved H₂.



3 was combined with 5 equivalents of benzoquinone, a strong H₂ acceptor, and placed under a hydrogen atmosphere at room temperature. Tracking the reaction by ¹H NMR showed slow conversion of **3** to **6** and appearance of hydroquinone, indicating that the H₂ splitting is more rapid than the hydrogenation of benzoquinone (Figure 2 - 8). The complex hydrogenated 5 equivalents of benzoquinone over 2 days, and stoichiometric reactions of **5** or **6** with benzoquinone were also successful to form hydroquinone, indicating that the isolated complexes are likely the active catalysts, rather than some hydride intermediates.

After seeing that **6** was competent for hydrogen transfer, multiple other substrates were attempted for hydrogenation or small molecule activation, but no reactivity was observed in all cases. Addition of several equivalents of 1-hexene led to no conversion of **6** to **3** or any reactivity at all with the complex. A similar lack of reactivity was observed with CO and CO₂ even at temperatures up to 90 °C. Even reactivity with O₂ was sluggish, showing appearance of a mixture of products gradually, leading to approximately 30% conversion of **6** to product over the course

Figure 2 - 8. ^1H NMR of H_2 transfer to benzoquinone, starting from **3**, H_2 , and benzoquinone and resulting in **6** and hydroquinone.



of 3 days. This reactivity was likely sluggish due to the significant steric bulk covering the fourth binding site of the nickel center, and the lack of accessible redox transformations at the nickel center to accompany the reactivity of the ligand.

To probe the energetics of this transformation, DFT calculations were used to investigate the difference in energy between the hydrogenated NiDHP complex, **6**, and the dehydrogenated complex **3**. Optimization of both structures revealed a downhill H_2 splitting reaction of 32 kcal/mol, or that **6** is favored by 32 kcal/mol over **3**. While this shows the favorability of H_2 activation, it also implies a very high barrier to potential hydrogenation reactivity. Though hydrogenation of alkenes can be a downhill process by up to 30 kcal/mol, this barrier is likely high enough that the reaction overall is not favorable. Between this barrier and the difficulty in coordinating an alkene in the sterically bulky environment, the lack of reactivity is not surprising.

Conclusions

Dihydrazonepyrrole ligands have been shown to bind strongly to first row transition metals and have multiple different stable protonation and redox states. While the early, ^{Ph,Tol}DHP system was plagued by instability resulting from C–H activation of the ligand upon reaction with H₂O or O₂, ligand modifications stabilized the ligand immensely. Fluorination to give ^{Tol, FPh}DHP led to a similar decomposition pathway to ^{Ph,Tol}DHP, but ^{*t*Bu,Tol}DHP was much more robust. Significant changes to the electrochemistry of the ligand were seen upon addition of the more electron-donating *t*-butyl group, which led to a lack of reactivity with H₂O but more tractable reactivity with O₂ leading to a novel Ni superoxo complex resulting from ligand-based electron transfer. This method of O₂ activation has only been seen biologically, specifically in quercetin dioxygenase, but never in synthetic systems to make a Ni(II) superoxo complex.⁸ The superoxo species was competent for oxidative reactivity, but required heating in most cases, likely suggesting that the superoxo complex was not the active oxidant, and it was most likely some more reactive Ni oxygen species formed during the decomposition.

The *t*-butyl substitutions also led to isolation of the hydrogenated ligand form which had not previously been seen in the ^{Ph,Tol}DHP ligand. Hydrogen splitting on the ligand and subsequent transfer to benzoquinone served as proof of concept for the reversible $2e^-/2H^+$ chemistry that the pyrrole ligand can facilitate. In the case of Ni, the barrier for H₂ transfer was calculated as 32 kcal/mol, so hydrogenation reactivity was not viable, and research is ongoing into investigating the effects of changing the metal center to incorporate more binding sites and metal-based redox.

Experimental Section

General Considerations: All reagents were purchased from commercial suppliers and used without further purification unless otherwise specified. The *t*-butyl hydrazine was synthesized by deprotonating *t*-butyl hydrazine hydrochloride. All manipulations were carried out under an atmosphere of N₂ using standard Schlenk and glovebox techniques. Glassware was dried at 180 °C for a minimum of two hours and cooled under vacuum prior to use. Solvents were dried on a solvent purification system from Pure Process Technology and stored over 4 Å molecular sieves under N₂. Tetrahydrofuran was stirred over NaK alloy and run through an additional activated alumina column prior to use to ensure dryness. Solvents were tested for H₂O and O₂ using a standard solution of sodium-benzophenone ketyl radical anion. C₆D₆ was dried by passage over a column of activated alumina and stored over 4 Å molecular sieves in the glovebox. ¹H and ¹³C{¹H} spectra were recorded on Bruker DRX 400 or 500 spectrometers. Chemical shifts are reported in ppm units referenced to residual solvent resonances for ¹H and ¹³C{¹H} spectra, UV-visible spectra were recorded on a Thermo Evolution 300 spectrometer and addition of gases was performed by injecting via syringe into a cuvette sealed with a septum. UV-visible spectra at elevated temperature were done using a Unisoku Cryostat. IR was recorded on a Bruker Tensor II. EPR spectra were recorded on an Elexsys E500 Spectrometer with an Oxford ESR 900 X-band cryostat and a Bruker Cold-Edge Stinger and were simulated using the Easyspin suite in Matlab software.¹⁰ GC/MS was collected on an Agilent SQ GCMS with 5977A single quad MS and 7890B GC. Elemental analysis was performed by Midwest Microlabs. Electrochemical measurements were performed using a BAS Epsilon potentiostat and analyzed using BAS Epsilon software version 1.40.67NT. Cyclic voltammetry measurements were made using a glassy carbon working

electrode, platinum wire counter electrode, and silver wire pseudo-reference electrode, and referenced to internal Fc/Fc⁺.

X-Ray Structure Determination. Crystal Structure Determination. The diffraction data were measured at 100 K on a Bruker D8 VENTURE with PHOTON 100 CMOS detector system equipped with a Mo-target micro-focus X-ray tube ($\lambda = 0.71073 \text{ \AA}$). Data reduction and integration were performed with the Bruker APEX3 software package (Bruker AXS, version 2015.5-2, 2015). Data were scaled and corrected for absorption effects using the multi-scan procedure as implemented in SADABS (Bruker AXS, version 2014/5, 2015, part of Bruker APEX3 software package). The structure was solved by the dual method implemented in SHELXT¹¹ and refined by a full-matrix least-squares procedure using OLEX2¹² software package (XL refinement program version 2014/7¹³). Suitable crystals were mounted on a cryo-loop and transferred into the cold nitrogen stream of the Bruker D8 Venture diffractometer. Most of the hydrogen atoms were generated by geometrical considerations and constrained to idealized geometries and allowed to ride on their carrier atoms with an isotropic displacement parameter related to the equivalent displacement parameter of their carrier atoms. Compound **2** was modeled for three component disorder of one of the *p*-tol rings. Compound **3** was modeled for two component disorder of the bridging triflate group.

X-ray Absorption Measurements. Powder samples were prepared by grinding finely. A Teflon washer (5.3 mm internal diameter) was sealed on one side with Kapton tape and powder was then transferred to the inside of this ring before compacting with a Teflon rod and sealing the remaining face with Kapton tape. All sample preparation was performed under an inert atmosphere. X-ray absorption near-edge spectra (XANES) and Extended Absorption Fine Structure (EXAFS) were employed to probe the local environment around Ni. Data were acquired

at the Advanced Photon Source at Argonne National Laboratory with a bending magnet source with ring energy at 7.00 GeV. Ni K-edge (8332.8 eV) data were acquired at the MRCAT 10-BM beam line in transmission. The incident, transmitted, and reference X-ray intensities were monitored using gas ionization chambers. A metallic nickel foil standard was used as a reference for energy calibration and was measured simultaneously with experimental samples. X-ray absorption spectra were collected at room temperature.

Data collected was processed using the Demeter software suite by extracting the EXAFS oscillations $\chi(k)$ as a function of photoelectron wavenumber k .¹⁴ The theoretical paths were generated using FEFF6 and the models were determined using the fitting program Artemis.¹⁴

Synthesis of 2,5-bis((2-pentafluorophenylhydrazono)(*p*-tolyl)methyl-pyrrole (^{Tol,FPh}DHP)). In the glovebox, a 25 mL Qorpak vial was charged with 0.3 g (0.99 mmol) of 2,5-ditolylacetylpyrrole, 0.6 g of pentafluorophenylhydrazine (2.9 mmol, 3 equivalent), catalytic (1 drop) of 2.5 M HCl etherate, molecular sieves, and 15 mL toluene. This was heated, with stirring, for 3 days at 100° C, gradually turning yellow. The solution was cooled to room temperature and filtered through Celite. The resulting yellow solution was evaporated to dryness, and the resulting yellow residue was washed with 3 x 20 mL of Et₂O, resulting in (^{Tol,FPh}DHP) as a yellow powder (0.1 g, 0.19 mmol, 20%). The Et₂O washes can be evaporated to give a mixture of mono-condensed product and ^{Tol,FPh}DHP, which can be recycled to synthesize more (^{Tol,FPh}DHP), but longer reaction times or addition of a larger excess pentafluorophenylhydrazine did not result in greater conversion. ¹H NMR (CDCl₃ 400 MHz, 25° C) δ = 9.78 (s, 1H, N–H), 7.37 (d, J = 8 Hz, 2H, Tol C–H), 7.33 (d, J = 8 Hz, 2H, Tol C–H), 5.88 (d, J = 4 Hz, 2H, Pyrrole C–H), 2.47 (s, 6H, Tol-CH₃). ¹⁹F {¹H} NMR (CDCl₃ 162 MHz, 25° C). δ = -155.85 (d, J = 8 Hz, 4F, *o*-Ph), -163.22 (t, J = 8 Hz, 4F, *m*-F) -168 (t, 2F J = 8 Hz, *p*-F). ¹³C {¹H} NMR (CDCl₃ 162 MHz, 25° C). δ = 142.75, 140.15,

132.44, 130.26, 128.41, 126.92, 125.8, 114.99, 112.13, 21.48. IR (THF solution, CaF₂ windows, cm⁻¹) 3447 (w, N–H), 3334 (w, N–H), 2686 (m), 1527 (s, C=N), 1367 (w), 1324 (w), 1117 (m).

Synthesis of (Tol,FP^hDHPO)Ni (1). To a stirring THF slurry of NiCl₂dme (0.017 g, 0.078 mmol, 3 mL) was added an excess of pyridine and stirred for 30 minutes, turning from an orange slurry into a blue slurry. Separately, a THF solution of KN(TMS)₂ (0.029 g, 0.14 mmol, 1 eq, 2 mL) was added with stirring to a THF solution of Tol,FP^hDHP (0.054 g, 0.08 mmol, 1 eq, 5 mL), resulting in a red solution. This was added dropwise to the nickel solution and stirred overnight. The resulting green solution was evaporated to dryness, extracted into 10 mL benzene, filtered, and evaporated to give a green oil. The green oil was washed with 5 mL petroleum ether, dissolved in deuterated benzene (0.5 mL), removed from the glovebox and exposed to air, turning from green to blue. After 5 min, the reaction was dried in vacuo, extracted with petroleum ether, dried in vacuo again, and crystallized from acetonitrile, resulting in (Tol,FP^hDHPO)Ni as blue crystals. Yield: 0.010 g, 0.013 mmol, 17%. ¹H NMR (C₆D₆, 400 MHz, 25° C) δ = 7.76 (d, 2H, *J* = 8 Hz, *p*-Tol C–H) 7.75 (d, 2H, *J* = 4 Hz, pyrrole C–H), 7.63 (d, 2H, *J* = 8 Hz, *p*-Tol C–H), 7.57 (d, 2H, *J* = 4 Hz Pyrrole C–H) 7.19 (d, 2H, *J* = 8 Hz, *p*-Tol C–H), 2.21 (s, 3H, *p*-Tol CH₃), 2.18 (s, 3H, *p*-Tol CH₃). ¹⁹F {¹H} NMR (C₆D₆, 162 MHz, 25° C) δ = -147.4 (t, 1F, 6 Hz) -149.67 (d, 2F, *J* = 6 Hz), -153.34 (t, 1F, *J* = 6 Hz) -157.09 (t, 1F, *J* = 6 Hz), -165.13 (t, 2F, *J* = 8 Hz), -166.40 (t, 1F, *J* = 8 Hz), -174.09 (t, 1F, *J* = 8 Hz)

Synthesis of 2,5-bis((2-*t*-butylhydrazono)(*p*-tolyl)methyl)-pyrrole) (t^{Bu},TolDHP•2HCl). In the glovebox, a 500 mL 3-neck round bottom flask equipped with two septa and a reflux condenser was charged with 2,5-ditolylacetylpyrrole¹⁵ (3.0 g 9.9 mmol), *t*-butyl hydrazine (6.1 g, 70 mmol, 7.0 eq), toluene (250 mL), molecular sieves, catalytic 2 M HCl etherate (0.01 mL) and a stir bar. This was removed from the glovebox and refluxed on the Schlenk line for 5 days at 115 °C. The

resulting yellow solution was cooled to room temperature, returned to the glovebox, and filtered through Celite to remove the molecular sieves, giving a clear yellow solution. This was evaporated to dryness to give an orange oil, which was taken up in benzene, then 2 M HCl etherate (10 mL, 2 eq) was added, resulting in precipitation of a yellow solid. The yellow solid was collected by filtration, then the benzene filtrate was evaporated to dryness, taken up in petroleum ether (100 mL) and filtered to collect more yellow solid. The two batches of solid were combined to give $^{t\text{Bu,Tol}}\text{DHP}\cdot 2\text{HCl}$ (3.4 g, 6.6 mmol, 66%). ^1H NMR (CDCl_3 , 500 MHz, 25° C) δ = 12.96 (s, 1H, N–H pyrrole), 11.46 (s, 4H, N–H hydrazone), 7.63 (d, 4H, J = 8 Hz, tol C–H), 7.27 (d, 4H, J = 8 Hz, tol C–H), 6.48 (d, 2H, J = 4 Hz, Pyrrole C–H), 2.46 (s, 6H, tol-Me), 1.71 (s, 18H, $t\text{bu}$). ^{13}C $\{^1\text{H}\}$ NMR (CDCl_3 , 125 MHz 25 °C) δ = 164.6 (C=N), also 142.6, 133.3, 129.9, 128.8, 126.9, 119.8, 62.5, 25.3, 21.3. IR (nujol mull, cm^{-1}): 3457 (m, N–H), 3131 (m, N–H), 3088 (m, N–H), 1598 (s, C=N). Anal calcd: C 65.1, H 7.6, N 13.5 Found: C 65.8, H 7.7, N 11.8

Synthesis of $^{t\text{Bu,Tol}}\text{DHP}\cdot\text{Ni}$ (2). To a stirring THF solution of $^{t\text{Bu,Tol}}\text{DHP}\cdot 2\text{HCl}$ (0.47 g, 0.92 mmol, 40 mL) was added 2.5 M $n\text{-BuLi}$ in hexanes (1.5 mL, 4 eq), turning from yellow to red. The red mixture was stirred for 5 minutes, then added to a stirring slurry of NiCl_2DME in THF, turning deep purple. After stirring overnight for 12 hours, all volatiles were removed under vacuum, and the resulting purple residue was taken up in benzene and passed through a silica plug, then evaporated to give **1** as a purple powder. Yield: 0.20 g, 0.40 mmol, 43%. Single crystals can be obtained by crystallization from concentrated Et_2O at -35°C . EPR (frozen toluene/petroleum ether, 15 K, g_z , g_y , g_x) 2.24, 2.10, 2.07. Evans method (C_6D_6 , 25 °C, μ_{B}) $\mu_{\text{eff}} = 2.02$. IR (KBr pellet, cm^{-1}) 3026 (w), 2963 (s), 2919 (s), 1905, 1797, 1521 (s, C=N), 1466, (m) 1460 (s), 1364 (s), 1011 (m), 820 (s), 719 (m) UV-vis (Benzene solution) 275 nm, 570 nm, 800 nm. Anal calc'd: C 67.3; H 6.8; N 14.0. Found: C 66.5; N 7.6; H 13.7.

Synthesis of [^tBu,^{Tol}DHP]NiOTf (3). To a stirring THF solution of **3** (0.050 g, 0.1 mmol, 5 mL) was added a THF solution of AgOTf (0.026 g, 0.1 mmol, 2 mL, 1 eq) resulting in an immediate color change from dark purple to dark blue. The reaction was stirred for 30 min, then filtered and the solvent was evaporated. The resulting blue residue was washed with petroleum ether (5 mL) then taken up in benzene (10 mL), filtered, and evaporated to give **3** as a blue powder (0.052 g, 0.08 mmol, 80%). Single crystals could be obtained by layering a toluene solution of **4** with petroleum ether at -35 °C. ¹H NMR (C₆D₆, 500 MHz, 25° C) δ = 46.06, 14.13, 12.54, 12.40, -1.36. IR (KBr Pellet, cm⁻¹) 2973 (s), 2920 (m), 2867 (w). 1614 (m), 1508 (m), 1468 (m) 1366 (s), 1261 (vs), 1174 (s) 1100 (m), 1032 (m), 822 (w). Anal Calc'd C 53.7; H 5.2; N 10.8. Found: C 53.8; H 5.6; N 10.6

Synthesis of [^tBu,^{Tol}DHP]NiO₂ (4). A solution of **2** in benzene (0.023 g, 0.046 mmol, 5 mL) was removed from the glovebox and air was bubbled through the solution for 30 seconds, resulting in a color change from purple to red. All volatiles were removed under vacuum, giving **3** as a red oil. Yield: 0.022 g, 0.041 mmol, 90%. EPR (frozen benzene, 15 K, g_z, g_y, g_x) 2.23, 2.09, 2.00. Evans method (C₆D₆, 25 °C, μ_B) μ_{eff} = 1.65. IR (KBr Pellet, cm⁻¹) 2965 (s), 2919 (m), 2861 (m), 1607 (m), 1512 (m), 1440 (s), 1361 (s), 1303 (m), 1266 (s), 1183 (m), 1115 (m), 1103 (m), 1014 (s), 833 (m), 805 (m). UV-vis (Benzene solution) 350 nm, 550 nm, 870 nm. ESI-MS: m/z = 539.2 [^tBu,^{Tol}DHP]Ni(NCMe)⁺. Due to decomposition of the material over time, satisfactory elemental analysis could not be obtained.

Synthesis of 4 by reaction of 3 with KO₂. To a stirring THF solution of **3** (0.013 g, 0.02 mmol, 3 mL) was added a THF slurry of KO₂ (0.0015 g, 0.02 mmol, 1 mL, 1 eq). This was stirred for 1 hour, slowing turning from deep blue to dark red. The solution was filtered and evaporated under vacuum to give **4** as a red oil.

Oxidation of benzyl alcohol. In a nitrogen glovebox, to a solution of **4** in C₆D₆ (0.005 g, 0.01 mmol, 0.5 mL) was added benzyl alcohol (0.002 mg, 0.02 mmol, 2 eq) and naphthalene (6 mg). This was added to an NMR tube and removed from the glovebox and exposed to air, turning from purple to red as **2** reacted to form **4**. The tube was heated to 50 °C for 5 hours and the appearance of 1.9 equivalents of benzaldehyde was observed by integration against the internal naphthalene standard.

Oxidation of toluene. To 5 mL of toluene was added **2** (0.005 g, 0.01 mmol), which was then removed from the glovebox, exposed to air to convert **2** to **4**, then heated to 70 °C for 3 hours, at which point it was tested by GC/MS and the resulting benzaldehyde peak was integrated versus a benzaldehyde standard curve and indicated the formation of 0.9 equivalents of benzaldehyde.

Oxidation of PPh₃. To a C₆D₆ solution of **2** (0.003 g, 0.006 mmol, 0.5 mL) was added PPh₃ (0.030 g, 0.012 mmol, 20 eq) and removed from the glovebox, exposed to air overnight, then tested by ³¹P NMR. The amount of PPh₃O was quantified by integration compared to the PPh₃ peak to give the percentage of the PPh₃ that had converted indicating the formation of 2.0 equivalents of PPh₃O.

Synthesis of [^{*t*Bu,Tol}DHPH₂]*Ni*Cl (5**).** To a stirring THF solution of ^{*t*Bu,Tol}DHP•2HCl (0.075g 0.14 mmol, 10 mL) was added 2.0 M *n*-BuLi in hexanes (0.15 mL, 0.40 mmol, 2.9 eq) turning immediately to clear red color. This solution was then added dropwise to a stirring THF solution of NiCl₂dme (0.035 g, 0.16 mmol, 1.1 eq) resulting in a reddish/tan solution. This was stirred for 2 hours, then filtered and all volatiles were removed in vacuo. The resulting red oil was crystallized from petroleum ether at -35°C, resulting in [^{*t*Bu,Tol}DHPH₂]*Ni*Cl as red crystals. Yield: 0.026 g, 35 %. ¹H NMR (C₆D₆, 400 MHz, 25° C) δ = 7.87 (d, *J* = 8 Hz, 4H, Tol C-H), 7.06 (d, *J* = 8 Hz, 4H, Tol C-H), 6.55 (s, 2H, Pyrrole C-H), 5.99 (s, 2H, N-H), 2.12 (s, 6H, Tol-CH₃), 1.19 (s, 18H, *t*Bu-

CH₃). ¹³C {¹H} NMR (C₆D₆, 125 MHz, 25° C) δ = 166.84, 141.15, 134.94, 130.56, 129.97, 129.49, 119.93, 64.78, 29.09, 21.67 IR (THF solution, CaF₂ windows, cm⁻¹): 3241 (w, N–H), 1618 (w), 1585 (m, C=N), 1553 (m), 1470 (s), 1364 (s), 1314 (m), 1250 (m), 1179 (s), 1131 (w).

Synthesis of [(^tBu,^{Tol}DHPH₂)Ni]OTf. To a stirring THF solution of [(^tBu,^{Tol}DHPH₂)Ni]Cl (0.023 g, 0.044 mmol, 5 mL) was added a THF solution of AgOTf (0.011 g, 0.044 mmol, 1 eq, 2 mL) resulting in immediate precipitation of a white powder. The reaction was stirred for 20 minutes, then filtered and all volatiles were removed *in vacuo*, giving [(^tBu,^{Tol}DHPH₂)Ni]OTf as an oily yellow residue (0.025 g, 0.039 mmol, 89%). ¹H NMR (C₆D₆, 400 MHz, 25° C) δ = 7.78 (d, *J* = 8 Hz, 4H, Tol C–H), 7.05 (d, *J* = 8 Hz, 4H, Tol C–H), 6.45 (s, 2H, Pyrrole C–H), 6.26 (s, 2H, N–H), 2.22 (s, 6H, Tol-CH₃), 1.26 (s, 18H, ^tBu-CH₃). ¹⁹F {¹H} NMR (162 MHz, 25 °C, CDCl₃) δ = -77.3.

References

¹ (a) Chang, M.-C.; Jesse, K. A.; Filatov, A. S.; Anderson, J. S., Reversible homolytic activation of water via metal-ligand cooperativity in a T-shaped Ni(II) complex. *Chem. Sci.* **2019**, *10* (5), 1360-1367. (b) Chang, M.-C.; McNeece, A. J.; Hill, E. A.; Filatov, A. S.; Anderson, J. S., Ligand-Based Storage of Protons and Electrons in Dihydrzonopyrrole Complexes of Nickel. *Chem. - Eur. J.* **2018**, *24* (31), 8001-8008.

² Eisenstein, O.; Milani, J.; Perutz, R. N. Selectivity of C–H Activation and Competition between C–H and C–F Bond Activation at Fluorocarbons. *Chem Rev* **2017**, *117* (13) 8710-8753. (b) Ahrens, A.; Kohlmann, J.; Ahrens, M.; Braun, T.; Functionalization of Fluorinated Molecules by Transition-Metal-Mediated C–F Bond Activation To Access Fluorinated Building Blocks. *Chem Rev* **2015**, *115* (2) , 931-972. (c) Edelbach, B. L.; Jones, W. D.; Mechanism of Carbon-Fluorine Bond Activation by (C₅Me₅)Rh(PMe₃)H₂

³ (a) Yoo, C.; Lee, A T-Shaped Nickel(I) Metalloradical Species. *Y. Angew. Chem., Int. Ed.*, **2017**, *56* , 9502 -9506. (b) Wenz, J.; Kochan, A.; Wadepohland, H.; Gade, L. H. A Readily Accessible Chiral NNN Pincer Ligand with a Pyrrole Backbone and Its Ni(II) Chemistry: Syntheses, Structural Chemistry, and Bond Activations. *Inorg. Chem.*, **2017**, *56* , 3631 -3643 (c) Rettenmeier, C. A.; Wenz, J.; Wadepohl, H.; Gade, L. H. Activation of Aryl Halides by Nickel(I) Pincer Complexes: Reaction Pathways of Stoichiometric and Catalytic Dehalogenations. *Inorg. Chem.*, **2016**, *55* , 8214 -8224 (d) Andrella, N. O.; Sicard, A. J.; Gorelsky, S. I.; Korobkov, I.; Baker, R. T. A T-shaped Ni[κ²-(CF₂)₄-] NHC complex: unusual C_{sp}³-F and M–C^F bond functionalization reactions. *Chem. Sci.*, 2015, **6** , 6392 -6397 (e) Eckert, N. A.; Dinescu, A.; Cundari, T. R.; Holland, P. L. A T-Shaped Three-Coordinate Nickel(I) Carbonyl Complex and the Geometric Preferences of Three-Coordinate d⁹ Complexes. *Inorg. Chem.*, **2005**, *44* , 7702 -7704.

⁴ (a) Noh, H.; Cho, J., Synthesis, characterization and reactivity of non-heme 1st row transition metal-superoxo intermediates. *Coord. Chem. Rev.* **2019**, *382*, 126-144. (b) Panda, C.; Chandra, A.; Corona, T.; Andris, E.; Pandey, B.; Garai, S.; Lindenmaier, N.; Kuenstner, S.; Farquhar, E. R.; Roithova, J.; Rajaraman, G.; Driess, M.; Ray, K., Nucleophilic versus Electrophilic Reactivity of Bioinspired Superoxo Nickel(II) Complexes. *Angew. Chem., Int. Ed.* **2018**, *57* (45), 14883-14887. (c) Duan, P.-C.; Manz, D.-H.; Dechert, S.; Demeshko, S.; Meyer, F., Reductive O₂ Binding at a Dihydride Complex Leading to Redox Interconvertible μ-1,2-Peroxo and μ-1,2-Superoxo Dinickel(II) Intermediates. *J. Am. Chem. Soc.* **2018**, *140* (14), 4929-4939. (d) Corona, T.; Company, A., Spectroscopically Characterized Synthetic Mononuclear Nickel-Oxygen Species. *Chem. - Eur. J.* **2016**, *22* (38), 13422-13429. (e) Jeoung, J.-H.; Nianios, D.; Fetzner, S.; Dobbek, H., Quercetin 2,4-Dioxygenase Activates Dioxygen in a Side-On O₂-Ni Complex. *Angew. Chem., Int. Ed.* **2016**, *55* (10), 3281-3284. (f) Cho, J.; Kang, H. Y.; Liu, L. V.; Sarangi, R.; Solomon, E. I.; Nam, W., Mononuclear nickel(II)-superoxo and nickel(III)-peroxo complexes bearing a common macrocyclic TMC ligand. *Chem. Sci.* **2013**, *4* (4), 1502-1508. (g) Yao, S.; Bill, E.; Milsman, C.; Wieghardt, K.; Driess, M., A "side-on" superoxonickel complex [LNi(O₂)] with a square-planar tetracoordinate nickel(II) center and its conversion into [LNi(μ-OH)₂NiL]. *Angew. Chem., Int. Ed.* **2008**, *47* (37), 7110-7113. (h) Suzuki, M., Ligand Effects on

Dioxygen Activation by Copper and Nickel Complexes: Reactivity and Intermediates. *Acc. Chem. Res.* **2007**, *40* (7), 609-617. (i) Kieber-Emmons, M. T.; Annaraj, J.; Seo, M. S.; Van Heuvelen, K. M.; Tosha, T.; Kitagawa, T.; Brunold, T. C.; Nam, W.; Riordan, C. G., Identification of an "End-on" Nickel-Superoxo Adduct, $[\text{Ni}(\text{tmc})(\text{O}_2)]^+$. *J. Am. Chem. Soc.* **2006**, *128* (44), 14230-14231. (h) Fujita, K.; Schenker, R.; Gu, W.; Brunold, T. C.; Cramer, S. P.; Riordan, C. G., A Monomeric Nickel-Dioxygen Adduct Derived from a Nickel(I) Complex and O_2 . *Inorg. Chem.* **2004**, *43* (11), 3324-3326.

⁵ (a) Sarangi, R. X-ray absorption near-edge spectroscopy in bioinorganic chemistry: Application to M– O_2 systems. *Coord. Chem. Rev.* **2013**, *257*, 459-472. (b)

⁶ (a) Mitsuru, S.; Komorita, S.; Yamatera, H. XANES spectra of copper(II) complexes: correlation of the intensity of the $1s \rightarrow 3d$ transition and the shape of the complex. *Inorg. Chem.* **1992**, *31*, 459. (b) Wirt, M. D.; Sagi, I.; Chen, E.; Frisbie, S. M.; Roxane, L.; Chance, M. R. *J. Am. Chem. Soc.* **1991**, *113*, 5299. (c) Colpas, G. J.; Maroney, M. J.; Bagyinka, C.; Kumar, M.; Willis, W. S.; Suib, S. L.; Baidya, N.; Mascharak, P. K. Geometric conformations of intermediates of B12 catalysis by x-ray edge spectroscopy: cobalt(I) B12, cobalt(II) B12, and base-off adenosylcobalamin. *Inorg. Chem.* **1991**, *30*, 920. (d) Penner-Hahn, J. E.; Fronko, R. M.; Pecraro, V. L.; Yocum, C. F.; Betts, S. D.; Bowlby, N. R. Structural characterization of the manganese sites in the photosynthetic oxygen-evolving complex using x-ray absorption spectroscopy. *J. Am. Chem. Soc.* **1990**, *112*, 2549. (e) Roe, A. L. Schneder, D. J.; Mayer, R. J.; Pyrz, J. W.; Widom, J.; Que, L. X-ray absorption spectroscopy of iron-tyrosinate proteins. *J. Am. Chem. Soc.* **1984**, *106*, 1676.

⁷ Cho, J.; Sarangi, R.; Annaraj, J.; Kim, S. Y.; Kubo, M.; Ogura, R.; Solomon, E. I.; Nam, W. Geometric and electronic structure and reactivity of a mononuclear 'side-on' nickel(III)–peroxo complex. *Nat. Chem.* **2009**, *1*, 568-572.

⁸ (a) Li, H.; Wang, X.; Tian, G.; Liu, Y., Insights into the dioxygen activation and catalytic mechanism of the nickel-containing quercetinase. *Catal. Sci. Technol.* **2018**, *8* (9), 2340-2351. (b) Maroney, M. J.; Ciurli, S., Nonredox nickel enzymes. *Chem. Rev.* **2014**, *114* (8), 4206-4228. (c) Murray, L. J.; Lippard, S. J., Substrate trafficking and dioxygen activation in bacterial multicomponent monooxygenases. *Acc. Chem. Res.* **2007**, *40* (7), 466-474. (d) Barondeau, D. P.; Kassmann, C. J.; Bruns, C. K.; Tainer, J. A.; Getzoff, E. D., Nickel Superoxide Dismutase Structure and Mechanism. *Biochemistry* **2004**, *43* (25), 8038-8047.

⁹ (a) Holze, P.; Corona, T.; Frank, N.; Braun-Cula, B.; Herwig, C.; Company, A.; Limberg, C., Activation of Dioxygen at a Lewis Acidic Nickel(II) Complex: Characterization of a Metastable Organoperoxide Complex. *Angew. Chem., Int. Ed.* **2017**, *56* (9), 2307-2311. (b) Rettenmeier, C. A.; Wadepohl, H.; Gade, L. H., Electronic structure and reactivity of nickel(I) pincer complexes: their aerobic transformation to peroxo species and site selective C-H oxygenation. *Chem. Sci.* **2016**, *7* (6), 3533-3542.

¹⁰ Stoll, S.; Schweiger, A., Easyspin, a Comprehensive Software Package for Spectral Simulation and Analysis in EPR. *J. Magn. Reson.* **2006**, *178*, 42

-
- ¹¹. Sheldrick, G. M. SHELXT- Integrated space-group and crystal-structure determination. *Acta Cryst.* **2015**, *A71*, 3- 9
- ¹². Dolomanov, O.V.; Bourhis, L. J.; Gildea, R. J.; Howard, A. K.; and Puschmann, H.,. Olex2, a complete structure solution, refinement, and analysis program. *J. Appl. Cryst.* **2009**. *42*, 339
- ¹³. (a) Sheldrick, G. M. A Short History of SHELX. *Acta Cryst.* **2008**, *A64*, 112-122; (b) Sheldrick, G. M. Crystal structure refinement with SHELX *Acta Cryst.* **2015**, *C71*, 3-8
- ¹⁴ (a) Ravel, B., Newville, M., ATHENA, ARTEMIS, HEPHAESTUS: data analysis for X-ray absorption spectroscopy using IFEFFIT. *J. Synchr. Radn.*, **2005**, *12*, 537-541 (b) Newville, M., IFEFFIT: interactive EXAFS analysis and FEFF fitting. *J. Synchr. Radn.* **2001**, *8*, 322-324; (c) Rehr, J. J.; Albers, R. C. *Rev. Mod. Phys.* **2000**, *72*, 621-654.
- ¹⁵ (a) M.-C. Chang, A. J. McNeece, E. A. Hill, A. S. Filatov, J. S. Anderson, *Chem. - Eur. J.* **2018**, *24* (31), 8001-8008. (b) A. J. McNeece, M.-C. Chang, A. S. Filatov, J. S. Anderson, *Inorg. Chem.*, **2018**, *57*, 7044-7050.

Chapter 3: Charged Phosphines for Studying Electric Field Effects

Introduction

The effect of oriented electric fields on catalysis is an emerging area of study for enzymatic and molecular systems¹. The electric field maintained by enzymes has been shown computationally to greatly accelerate the rate of reactivity and affect the selectivity of enzymatic reactions.² Enzymes can maintain and orient electric fields using charged groups in the protein superstructure built around the reactive center, but this is harder to mimic in molecular systems. Electric fields applied on electrode surfaces or through STM tips have been shown to catalyze reactions or increase catalytic rates, but measuring these effects is challenging, and these systems are often not broadly applicable.³

One strategy to study electric field effects is to synthesize molecular systems where a charged molecular functionality exerts an electric field on the molecule.⁴ Indeed, there has been an enormous interest in making simple model systems wherein electrostatic interactions can be leveraged or modeled.⁵ Computations have shown that these effects can have large, beneficial effects on catalytic reactivity, such as lowering the barriers to oxidative addition for accelerating cross coupling.⁶

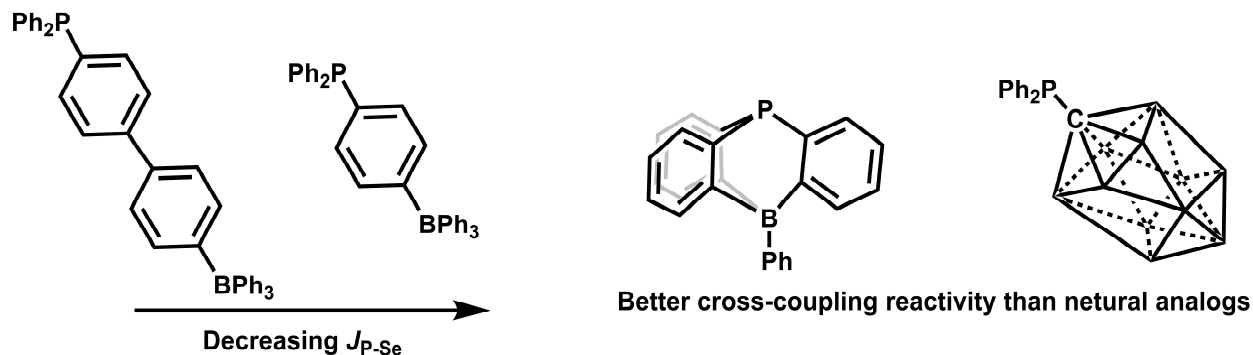
However, even in simple systems, understanding the relative inductive or electrostatic contributions from charged groups is difficult. A prime example of this is in classic Hammett literature where inductive “through bond” and electrostatic “through space” effects for charged substituents have been treated as one combined effect. There has been considerable debate on whether electrostatics or through bond electron density effects are dominant in this literature. Hammett originally considered the effect of substituents to be entirely electrostatic in nature,

which was supported by calculations by Ri, Eyring, and Westheimer, while Jaffe considered the effect only through electron density.⁷ The efficacy of both of these methods likely shows that both effects are active, and no simple method exists to separate those components. This historical discussion illustrates the difficulties associated with teasing apart the relative contributions between through space and through bond effects. However, obtaining a more detailed understanding of the relative importance of through bond or through space effects would be valuable, particularly as leveraging through space effects should serve as an ideal strategy to break free-energy relationships as has been demonstrated in some cases.⁸

As a possible scaffold to consider the effect and measurement of electrostatic effects, phosphines are ideal as there are well defined parameters and measurement techniques for the donor strength of these species such as the Tolman Electronic Parameter (TEP).⁹ Furthermore, charge effects in these ubiquitous ligands have recently been considered theoretically to provide enhanced reactivity for cross-coupling reactions.⁶ While several anionic phosphines have been synthesized and often do show enhanced cross-coupling reactivity, detailed studies aimed at understanding the relative contributions of inductive versus electrostatic effects have not been undertaken (Scheme 3 - 1).¹⁰ Furthermore, these systems all use aromatic linkers, increasing the amount of possible resonance effects on these catalysts.

As such, we targeted a new anionic phosphine where the charge is separated by only a simple aliphatic group, namely a methylene linker. Here we report 1) a new charged phosphine, 2) detailed quantification of the relative electrostatic contribution to its donor properties via NMR coupling constants, and 3) its complexes and subsequent reactivity with TM centers. These studies illustrate that electrostatic through space interactions are a major contributor even with short bridges such as a methylene spacer. Furthermore, we demonstrate that these electrostatic

Scheme 3 - 1. Anionic phosphines that have been previously synthesized.



interactions can be leveraged for improved catalysis compared to other typical phosphines, such as PCy_3 .

Results and Discussion

Synthesis of Anionic Phosphine Synthesis of the targeted anionic phosphine proceeded readily via deprotonation of Ph_2PH with $\text{KN}(\text{TMS})_2$ in THF and dropwise addition to a stirring THF solution of potassium iodomethyltrifluoroborate (Scheme 3 - 2). The reaction was tracked by proton decoupled ^{31}P NMR, and growth of a quartet peak at -15 ppm confirmed the formation of potassium diphenylphosphinomethyltrifluoroborate, (K1). After filtration, removal of all volatiles under vacuum, and washing with Et_2O , K1 was isolated as a white powder. Due to the wealth of spin-active nuclei in this system, K1 could be well characterized by a variety of NMR spectroscopies. The ^1H NMR spectrum of the complex showed the expected aromatic signals, and a complicated doublet of quartets at 0.8 ppm, indicative of coupling of the CH_2 linker to both Scheme 3 - 2. Synthesis of K1.

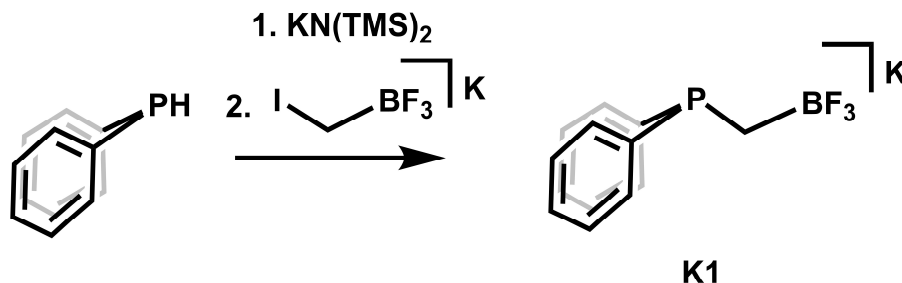
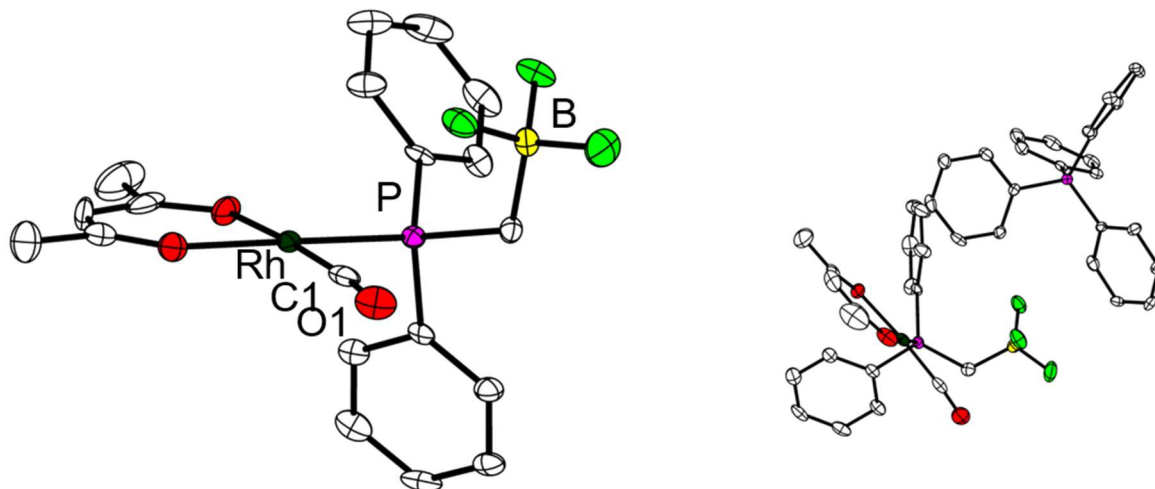
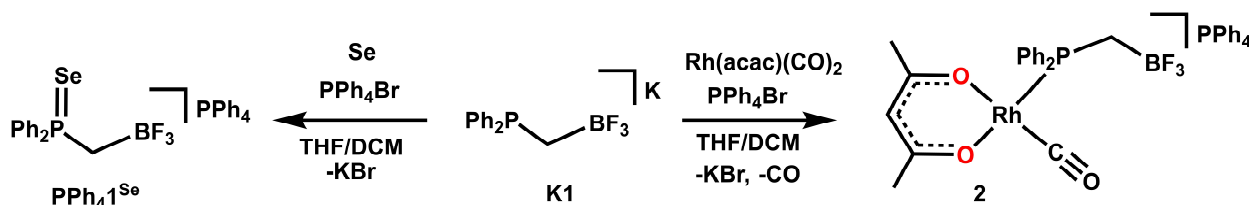


Figure 3 - 1. Structure of **2** (left), and structure of **2** showing PPh₄ (right). Ellipsoids are set to 50% probability, and all hydrogen atoms are omitted for clarity. Selected bond lengths and angles: Rh–C1 1.805(4) Å, Rh–P 2.241(1) Å, C1–O1 1.148(5) Å, C1–Rh–P 89.5(1)°, Rh–C1–O1 175.1(3)°.



phosphorus and fluorine. The ³¹P NMR showed coupling to fluorine, and the signal has an identical chemical shift to PPh₂Et, which is consistent with previous reports that the charged phosphines have similar or identical shifts to their neutral analogs.¹⁰ Analysis by ¹⁹F and ¹¹B NMR indicated the expected shifts and coupling for a BF₃ group, indicating that this functionality is maintained in **K1**. While it is unclear how closely associated the K or other alkali cations would be in solution, larger more weakly coordinating cations were targeted for future studies to minimize any possibility of ion pairing affecting the measurements.

Determination of Phosphine Donor Strength To initially assay the donor strength, the Tolman Electronic Parameter (TEP) was determined through the synthesis and IR spectroscopic characterization of Rh(acac)(CO)L which is a safer alternative to Ni(CO)₃L..¹¹ Addition of **K1** to Scheme 3 - 3. Synthesis of PPh₄**1**^{Se} and **2** from **K1**.

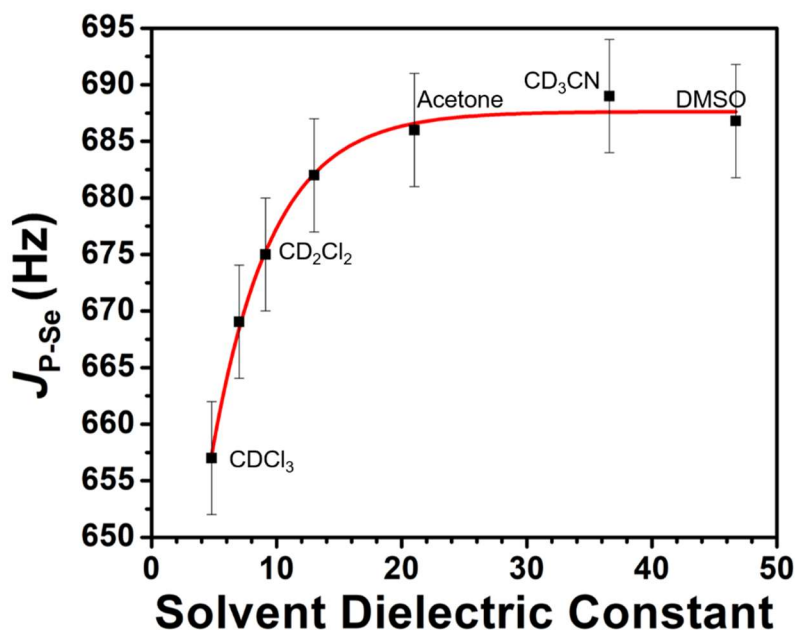


Rh(acac)(CO)₂ and PPh₄Br led to the formation of PPh₄[Rh(acac)(CO)(PPh₂(CH₂BF₃))] (**2**) (Scheme 3 - 3). Compound **2** was readily identified in the ³¹P NMR spectrum by the appearance of a doublet of quartets at 33 ppm due to coupling of the phosphorous nuclei to ¹⁰³Rh. Crystallization by diffusion of petroleum ether into a saturated CHCl₃ solution of **2** resulted in crystals suitable for SXRD. The solid-state structure confirmed the four coordinate, square planar rhodium center (Figure 3 - 1). The BF₃ is significantly above the rhodium square plane, and the PPh₄ cation is not interacting with either the BF₃ or the CO, as it is over 5 Å away from either moiety. Solution IR of **3** was recorded in CH₂Cl₂ and showed a ν_{CO} = 1965 cm⁻¹, which correlates to a TEP of 2060 cm⁻¹. This TEP matches well with P(iPr)₃, indicating that **1** is significantly more donating than would be expected for a diaryl phosphine. This observation is consistent with similar effects in previous reports of anionic phosphines.¹⁰

To further study the electron donation of **1** and what contribution electrostatic effects provide, the corresponding phosphine selenide of **1** was synthesized. The phosphine-selenium coupling (*J*_{P-Se}) correlates well with basicity of the phosphine, giving another measure of electron donation. Compound K**1** was stirred with an excess of elemental selenium and PPh₄Br, resulting in clean formation of PPh₄**1**^{Se} (Scheme 3 - 3). Analysis by ³¹P NMR spectroscopy indicated formation of PPh₄**1**^{Se} by a quartet peak at 35 ppm with selenium satellites from coupling with the ⁷⁷Se nucleus. In DMSO, *J*_{P-Se} correlates well with the TEP determined via Rh(acac)(CO)L, giving a value of 686 Hz, similarly consistent with P(iPr)₃. The TEP and *J*_{P-Se} values indicate that the anionic charge has a large effect on increasing the donor strength of the phosphine, even without a conjugated linker to the phosphine. Seeing this large effect encouraged us to investigate whether there was a reasonable experimental technique to separate the through-space component of the electron donation from the through-bond inductive effect.

We hypothesized that the through-space electrostatic effect of the charged group could be modified or screened by the solvent environment around the molecule, while the through bond interactions would only be slightly affected by solvent variations. Therefore, we determined J_{P-Se} of PPh_4^1Se as well as $PPh_2P(Se)Et$ in solvents with a variety of dielectric constants to probe the relative contribution from electrostatic interactions, assuming that the through bond interaction would be constant. The dielectric measures the ability to “shield” an electrostatic effect, so higher dielectric solvents such as MeCN or DMSO should shield the charge more effectively, giving a higher J_{P-Se} , or effectively a less electron donating phosphine (lower TEP). The observed solvent dependence of J_{P-Se} in PPh_4^1Se does follow this trend and indicates through-space electrostatic effects are a major contributor (Figure 3 - 2). Notably, the neutral congener $Ph_2P(Se)Et$ shows only a slight change in coupling constant of ~ 7 Hz over the same range, indicating that the observed shift is a direct result of the charged group and is not present in neutral compounds. While ion pairing could show similar effects depending on solvation of the counterion, the solid-state

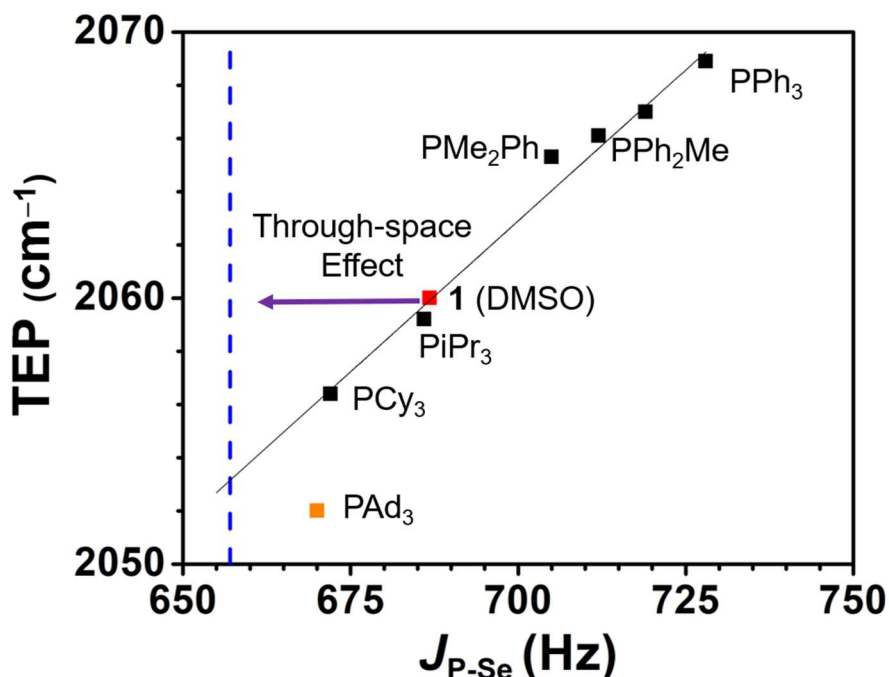
Figure 3 - 2. Solvent dependence of J_{P-Se} of PPh_4^1Se , fit to asymptotic fit with $R^2 = 0.99$. Intermediate points were achieved with solvent mixtures, assuming a linear relationship.



structure indicates there is little interaction. Furthermore, control experiments with high concentrations of PPh_4Br showed only small changes to $J_{\text{P-Se}}$ (<7 Hz).

Comparison of $J_{\text{P-Se}}$ with TEP indicates a good correlation for the $J_{\text{P-Se}}$ in DMSO, but there is large deviation when the $J_{\text{P-Se}}$ in CDCl_3 is compared (Figure 3 - 3). If we consider the $J_{\text{P-Se}}$ in DMSO to be indicative of the limit of no electrostatic interactions, indicating dominant through bond interactions, and the $J_{\text{P-Se}}$ in chloroform to be near the no-shielding limit, then we can estimate the relative magnitude of the electrostatic and through bond interactions. The observed $J_{\text{P-Se}}$ in DMSO is 687 Hz, which is shifted by 34 Hz from the neutral analog, PPh_2Et . We can therefore estimate the through bond contribution to $J_{\text{P-Se}}$ as 34 Hz, which corresponding to a 7 cm^{-1} shift in the TEP, or a change from an aryl-dialkyl phosphine to a trialkyl phosphine. This suggests then that the change in $J_{\text{P-Se}}$ on moving from DMSO to CHCl_3 of 31 Hz is due to through space effects, showing that even in an extreme case of a one-atom linker, that electrostatic contributions have a

Figure 3 - 3. Correlation of TEP and $J_{\text{P-Se}}$ for **1** and typical phosphines for comparison, showing change based on through-space effects.



roughly equal effect on donor strength as through bond interactions. This result suggests that other systems with longer linkers but short through space distances should exhibit predominant electrostatic effects.

Effect of Charged Phosphine on Cross-Coupling Reactivity After studying the effects of the charge on phosphine basicity, reactivity studies were performed to investigate the effect of the charge upon cross coupling reactivity. As a comparison, PCy₃ was also studied under the same conditions to determine how the reactivity of the charged phosphine would compare to a phosphine that is more electron donating as measured by the TEP, but less electron donating when the through-space effects (as determined by J_{P-Se}) are considered. PCy₃ is significantly more sterically hindered than **1**, but using unsubstituted aryl halides and aryl or alkyl olefins should prevent steric bulk from being a determining factor in the reactivity.

A simple Heck coupling was performed as a test reaction between 1-hexene and chlorobenzene. Addition of 2 equiv. of L (either PCy₃ or PPh₄**1**) to Pd(dba)₂ to 1-hexene and chlorobenzene in dioxane, with K₃PO₄ as a base, led to small amounts of conversion at 100°C for **1**, but no appearance of the coupled product for PCy₃ (Figure 3A - 15). The lack of high conversion indicated that the reaction was likely sluggish, but even in this case, **1** outperforms PCy₃, indicating that the through-space effects are beneficial to this reactivity.

To achieve higher conversion, styrene was used in similar reaction conditions to give a more activated and higher-boiling olefin for the cross-coupling. Though the overall conversion was still low, **1** outperformed PCy₃ and to give an increased yield of stilbene supporting that the charged phosphine has better cross-coupling reactivity. ³¹P NMR of the reaction mixture after the reaction indicated possible decomposition of **1**, as a large amount of peaks are seen and many do not show the quartet coupling pattern that is indicative of intact **1** (Figure 3A - 13). Decomposition

of **1** may be hindering overall conversion if the charged group is no longer intact and cannot provide through-space effects to encourage catalysis, so studies are ongoing to optimize this reaction and achieve higher overall turnover.

Conclusion

A distally anionic phosphine was synthesized in order to study the through-space electric field effect of the charge. The anionic charge does increase donor strength of the phosphine significantly, as measured by the TEP. Using the solvent dependence of the J_{P-Se} of the phosphine selenide analog enabled deconvolution of the through-space versus through-bond effects. Both effects contribute approximately 30 Hz of J_{P-Se} to the overall electron donation, indicating that the through space effects can have a large impact on the resulting properties of the phosphines. These effects are also beneficial in preliminary reactivity studies, showing higher conversion in a Heck reaction compared to PCy_3 , which should be more donating through analysis of the TEP alone.

Experimental Section

General Considerations: All reagents were purchased from commercial suppliers and used without further purification unless otherwise specified. All manipulations were carried out under an atmosphere of N_2 using standard Schlenk and glovebox techniques. Glassware was dried at 180 °C for a minimum of two hours and cooled under vacuum prior to use. Solvents were dried on a solvent purification system from Pure Process Technology and stored over 4 Å molecular sieves under N_2 . Tetrahydrofuran was stirred over NaK alloy and run through an additional activated alumina column prior to use to ensure dryness. Solvents were tested for H_2O and O_2 using a standard solution of sodium-benzophenone ketyl radical anion. C_6D_6 was dried by passage over a column of activated alumina and stored over 4 Å molecular sieves in the glovebox. 1H , $^{13}C\{^1H\}$, $^{19}F\{^1H\}$, $^{11}B\{^1H\}$, and $^{31}P\{^1H\}$ spectra were recorded on Bruker DRX 400 or 500 spectrometers.

Chemical shifts are reported in ppm units referenced to residual solvent resonances for ^1H and $^{13}\text{C}\{^1\text{H}\}$ spectra, and external standards for ^{31}P , ^{11}B , and ^{19}F . IR was recorded on a Bruker Tensor II. GC/MS was collected on an Agilent SQ GCMS with 5977A single quad MS and 7890B GC. Elemental analysis was performed by Midwest Microlabs.

Synthesis of $\text{K}[\text{Ph}_2\text{P}(\text{CH}_2\text{BF}_3)]$ (K1**).** To a stirring THF solution of PPh_2 (0.184 g, 0.99 mmol, 3 mL) was added a THF solution of $\text{KN}(\text{TMS})_2$ (0.199 g, 1 mmol, 1 eq 3 mL) resulting in a bright red solution. This was added dropwise over 1 hour to a stirring THF slurry of potassium iodomethyltrifluoroborate (0.285 g, 1 mmol, 1 eq, 15 mL), then the resulting slurry was stirred for 12 hours, filtered through Celite, and all volatiles were removed in vacuo. Washing with Et_2O (2 x 10 mL) afforded $\text{K}[\text{Ph}_2\text{P}(\text{CH}_2\text{BF}_3)]$ as a white powder (0.205 g, 0.68 mmol, 68%). ^1H NMR (400 MHz, 25 °C, $\text{DMSO-}d_6$) $\delta = 7.33$ (t, $J = 8$ Hz, 4H, *o*-Ph-H), 7.24-7.17 (m, 6H, *o*- and *p*-Ph-H), 0.8 (dq, $J_{\text{P-H}} = 14$ Hz, $J_{\text{F-H}} = 4$ Hz, 2H, CH_2). $^{31}\text{P}\{^1\text{H}\}$ NMR (162 MHz, 25 °C, $\text{DMSO-}d_6$) $\delta = -15.9$ (q, $J = 13$ Hz). $^{11}\text{B}\{^1\text{H}\}$ NMR (162 MHz, 25 °C, $\text{DMSO-}d_6$) $\delta = 4$ (broad s).

Synthesis of $\text{PPh}_4[\text{Se}=\text{PPh}_2(\text{CH}_2\text{BF}_3)]$ (PPh₄1^{Se}**).** To a stirring THF solution of **1** (0.050 g, 0.016 mmol, 10 mL) was added an excess of solid selenium powder, then a DCM solution of PPh_4Br (0.075 g, 0.017 mmol, 1.05 eq, 5 mL). This mixture was stirred overnight, then filtered through Celite and all volatiles were removed in vacuo. Crystallization by vapor diffusion of Et_2O into a CDCl_3 solution of **1^{Se}** gave **1^{Se}** as clear crystals (0.060 g, 0.085 mmol, 53%). ^1H NMR (400 MHz, 25 °C, CDCl_3) $\delta = 8.01$ -7.95 (m, 4H), 7.91-7.86 (m, 4H), 7.78-7.73 (m, 8H), 7.65-7.60 (m, 8H), 7.31-7.20 (m, 6H) 1.94 (dq, $J_{\text{P-H}} = 10$ Hz, $J_{\text{F-H}} = 4$ Hz, 2H, CH_2) $^{31}\text{P}\{^1\text{H}\}$ NMR (162 MHz, 25 °C, CDCl_3) $\delta = 33.59$ (q, $J = 10$ Hz, 1P, $\text{Se}=\text{PPh}_2(\text{CH}_2\text{BF}_3)$), 22.08 (s, 1P, PPh_4). $^{11}\text{B}\{^1\text{H}\}$ NMR (162 MHz, 25 °C, CDCl_3) $\delta = 5.2$ (broad s). $^{19}\text{F}\{^1\text{H}\}$ NMR (162 MHz, 25 °C, CDCl_3) $\delta = -132.93$

(d, $J = 10$ Hz). IR (CDCl₃ solution): 3058 (m), 2258 (m), 2202 (m), 1978 (w), 1907 (w), 1814 (w), 1590 (m), 1487 (m), 1438 (s), 1310 (w), 1144 (m), 1103 (s), 1023 (s).

Synthesis of PPh₄[Rh(acac)(CO)(PPh₂(CH₂BF₃))] To a stirring THF solution of Rh(acac)(CO)₂ (0.067 g, 0.26 mmol, 3 mL) was added a THF solution of K1 (0.080 g, 0.26 mmol, 5 mL, 1 eq) and a DCM solution of PPh₄Br (0.115 g, 0.26 mmol, 4 mL, 1 eq), resulting in a color change from light yellow to brown. The reaction was stirred at room temperature for 1 hour, then filtered and evacuated to dryness, leaving PPh₄[Rh(acac)(CO)(PPh₂(CH₂BF₃))] as a brown oil, which was crystallized by vapor diffusion of Et₂O into CHCl₃ solution at room temperature. ¹H NMR (400 MHz, 25 °C, CDCl₃) $\delta = 7.85$ (m, 8H, Ph) 7.73 (m, 16H, Ph), 7.57 (m, 6H, Ph) 7.19 (5.30 (s, 1 H, acac), 1.92 (s, 3H, acac),) 1.62 (m, 2H, CH₂-BF₃), 1.56 (s, 3H, acac). ³¹P{¹H} NMR (162 MHz, 25 °C, CDCl₃) $\delta = 40.35$ (dq, $J_{Rh} = 166$ Hz, $J_F = 10$ Hz, 1P, PPh₂(CH₂BF₃)), 25.58 (s, 1P, PPh₄). ¹⁹F {¹H} NMR (162 MHz, 25 °C, CDCl₃) $\delta = -131.59$ (broad s, 3F, BF₃). ¹³C {¹H} NMR (100 MHz, 25 °C, CDCl₃) $\delta = 185.47, 135.70, 134.48, 130.72, 128.31, 126.84, 117.93, 117.04, 26.85$ IR (DCM solution, CaF₂ windows, cm⁻¹) 3068 (m), 2969 (s), 2859 (m), 1962 (s, C≡O), 1574 (s, C=O), 1514 (s), 1487 (m), 1434 (m), 1383 (m), 1167 (m), 1104 (s). Elem. Anal: Calc'd (2 + Et₂O) C 62.5, H 5.2, N 0. Found: C 63.4 H 4.9 N 0

General Cross Coupling Reaction. Dioxane solutions of chlorobenzene (0.250 g, 2.23 mmol, 1 mL), styrene (0.225 g, 2.16 mmol, 1 mL), Pd(dba)₂ (0.011 g, 0.02 mmol, 0.5 mL, 1%), a dioxane slurry of PPh₄1 (prepared by addition of PPh₄Br to K1, 0.024 g, 0.04 mmol, 1 mL, 2 %), and solid K₃PO₄ (0.500 g, 2.3 mmol) were added to a vial with a new Teflon stir bar, and heated to 100 °C overnight. The reaction was monitored by product formation by removing 0.5 mL aliquots, diluting to a total volume of 4 mL with Et₂O, filtering through silica, and analyzing by GC/MS by comparing to a standard curve of stilbene.

References

- ¹ (a) Fried, S. D.; Boxer, S. G., Electric Fields and Enzyme Catalysis. *Annu. Rev. Biochem.* **2017**, *86*, 387-415. (b) Warshel, A.; Sharma, P. K.; Kato, M.; Xiang, Y.; Liu, H.; Olsson, M. H. M., Electrostatic basis for enzyme catalysis. *Chem. Rev.* **2006**, *106* (8), 3210-3235. (c) Warshel, A., Electrostatic origin of the catalytic power of enzymes and the role of preorganized active sites. *J. Biol. Chem.* **1998**, *273* (42), 27035-27038.
- ² Schyman, P.; Lai, W.; Chen, H.; Wang, Y.; Shaik, S., The Directive of the Protein: How Does Cytochrome P450 Select the Mechanism of Dopamine Formation? *J. Am. Chem. Soc.* **2011**, *133* (20), 7977-7984.
- ³ a) Aragonés, A. C.; Haworth, N. L.; Darwish, N.; Ciampi, S.; Bloomfield, N. J.; Wallace, G. G.; Diez-Perez, I.; Coote, M. L., Electrostatic catalysis of a Diels-Alder reaction. *Nature* **2016**, *531* (7592), 88-91. (b) Warshel, A., Electrostatic origin of the catalytic power of enzymes and the role of preorganized active sites. *J. Biol. Chem.* **1998**, *273* (42), 27035-27038. (c) Akamatsu, M.; Sakai, N.; Matile, S., Electric-Field-Assisted Anion- π Catalysis. *J. Am. Chem. Soc.* **2017**, *139* (19), 6558-6561. (d) Clark, M. L.; Ge, A.; Videla, P. E.; Rudshteyn, B.; Miller, C. J.; Song, J.; Batista, V. S.; Lian, T.; Kubiak, C. P., CO₂ Reduction Catalysts on Gold Electrode Surfaces Influenced by Large Electric Fields. *J. Am. Chem. Soc.* **2018**, *140* (50), 17643-17655.
- ⁴ Stuyver, T.; Ramanan, R.; Mallick, D.; Shaik, S., Oriented (Local) Electric Fields Drive the Millionfold Enhancement of the H-Abstraction Catalysis Observed for Synthetic Metalloenzyme Analogues. *Angew. Chem., Int. Ed.* **2020**, *59* (20), 7915-7920.
- ⁵ (a) Chantarojsiri, T.; Ziller, J. W.; Yang, J. Y., Incorporation of redox-inactive cations promotes iron catalyzed aerobic C-H oxidation at mild potentials. *Chem. Sci.* **2018**, *9* (9), 2567-2574. (b) Dhar, D.; Yee, G. M.; Tolman, W. B., Effects of Charged Ligand Substituents on the Properties of the Formally Copper(III)-Hydroxide ([CuOH]²⁺) Unit. *Inorg. Chem.* **2018**, *57* (16), 9794-9806. (c) Oswald, V. F.; Lee, J. L.; Biswas, S.; Weitz, A. C.; Mitra, K.; Fan, R.; Li, J.; Zhao, J.; Hu, M. Y.; Alp, E. E.; Bominaar, E. L.; Guo, Y.; Green, M. T.; Hendrich, M. P.; Borovik, A. S., Effects of Noncovalent Interactions on High-Spin Fe(IV)-Oxido Complexes. *J. Am. Chem. Soc.* **2020**, Ahead of Print. (d) Azcarate, I.; Costentin, C.; Robert, M.; Saveant, J.-M., Through-Space Charge Interaction Substituent Effects in Molecular Catalysis Leading to the Design of the Most Efficient Catalyst of CO₂-to-CO Electrochemical Conversion. *J. Am. Chem. Soc.* **2016**, *138* (51), 16639-16644. (e) Fried, S. D.; Boxer, S. G., Measuring Electric Fields and Noncovalent Interactions Using the Vibrational Stark Effect. *Acc. Chem. Res.* **2015**, *48* (4), 998-1006.
- ⁶ Joy, J.; Stuyver, T.; Shaik, S., Oriented External Electric Fields and Ionic Additives Elicit Catalysis and Mechanistic Crossover in Oxidative Addition Reactions. *J. Am. Chem. Soc.* **2020**, *142* (8), 3836
- ⁷ Ri, T.; Eyring, H. Calculation of Dipole Moments from Rates of Nitration of Substituted Benzenes and Its Significance for Organic Chemistry. *J. Chem. Phys.* **1940**, *8*, 433. (b) Jaffe, H.

H., Correlation of Hammett's σ values with electron densities calculated by molecular-orbital theory. *J. Chem. Phys.* **1952**, *20*, 279-84. (c) Jaffe, H. H., A reëxamination of the Hammett equation. *Chem. Rev.* **1953**, *53*, 191-261. (d) Westheimer, F. H., The electrostatic effect of substituents on the dissociation constants of organic acids. IV. Aromatic acids. *J. Am. Chem. Soc.* **1939**, *61*, 1977-80.

⁸ (a) Zhang, R.; Warren, J. J. Controlling the Oxygen Reduction Selectivity of Asymmetric Cobalt Porphyrins by Using Local Electrostatic Interactions. *J. Am. Chem. Soc.* **2020**. ASAP. (b) Yuan, Z.; Yang, H.; Malik, N.; Čolović, M.; Weber, D. S.; Wilson, D.; Bénard, F.; Martin, R. E.; Warren, J. J.; Schaffer, P.; et al. Electrostatic Effects Accelerate Decatungstate-Catalyzed C–H Fluorination Using [18F]- and [19F]NFSI in Small Molecules and Peptide Mimics. *ACS Catal.* **2019**, 8276–8284. (c) Azcarate, I.; Costentin, C.; Robert, M.; Saveant, J.-M., Through-Space Charge Interaction Substituent Effects in Molecular Catalysis Leading to the Design of the Most Efficient Catalyst of CO₂-to-CO Electrochemical Conversion. *J. Am. Chem. Soc.* **2016**, *138* (51), 16639-16644. (d) Pegis, M. L.; Wise, C. F.; Koronkiewicz, B.; Mayer, J. M. Identifying and Breaking Scaling Relations in Molecular Catalysis of Electrochemical reactions. *J. Am. Chem. Soc.* **2017**, *139* (32), 11000-11003.

⁹ Tolman, C. A., Steric effects of phosphorus ligands in organometallic chemistry and homogeneous catalysis. *Chem. Rev.* **1977**, *77* (3), 313-48.

¹⁰ (a) Hoic, D. A.; Davis, W. M.; Fu, G. C., Diphenylphosphidoboratabenzene: An Anionic Analog of Triphenylphosphine. *J. Am. Chem. Soc.* **1996**, *118* (34), 8176-8177. (b) Alcarazo, M., α -Cationic Phosphines: Synthesis and Applications. *Chem. - Eur. J.* **2014**, *20* (26), 7868-7877. (c) Konishi, S.; Iwai, T.; Sawamura, M., Synthesis, properties, and catalytic application of a triptycene-type borate-phosphine ligand. *Organometallics* **2018**, *37* (12), 1876. (d) Chan, A. L.; Estrada, J.; Kefalidis, C. E.; Lavallo, V., Changing the Charge: Electrostatic Effects in Pd-Catalyzed Cross-Coupling. *Organometallics* **2016**, *35* (19), 3257-3260. (e) Gott, A. L.; Piers, W. E.; Dutton, J. L.; McDonald, R.; Parvez, M., Dimerization of Ethylene by Palladium Complexes Containing Bidentate Trifluoroborate-Functionalized Phosphine Ligands. *Organometallics* **2011**, *30* (16), 4236-4249. (f) Tassone, J. P.; Mawhinney, R. C.; Spivak, G. J. An Examination of the Effects of Borate Group Proximity on Phosphine Donor Power in Anionic (Phosphino)tetraphenylborate Ligands. *J. Organomet. Chem.* **2015**, *776*, 153–156.

¹¹ Chen, L.; Ren, P.; Carrow, B. P., Tri(1-adamantyl)phosphine: Expanding the Boundary of Electron-Releasing Character Available to Organophosphorus Compounds. *J. Am. Chem. Soc.* **2016**, *138* (20), 6392-6395.

Appendix 1. Supporting Data for Chapter 1

NMR Spectra

Figure 1A - 1. ^1H NMR of ditoylacetylpyrrole in CDCl_3 .

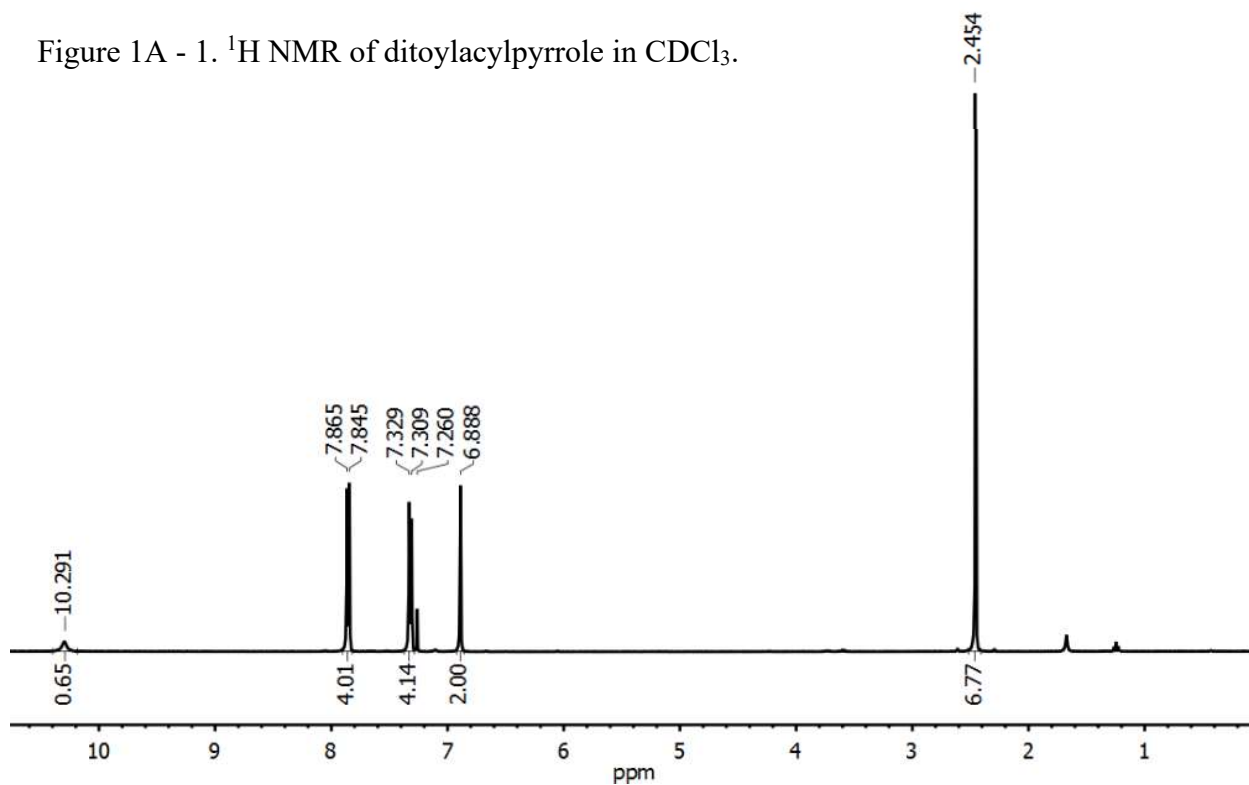


Figure 1A - 2. $^{13}\text{C}\{^1\text{H}\}$ NMR of ditoylacetylpyrrole in CDCl_3 .

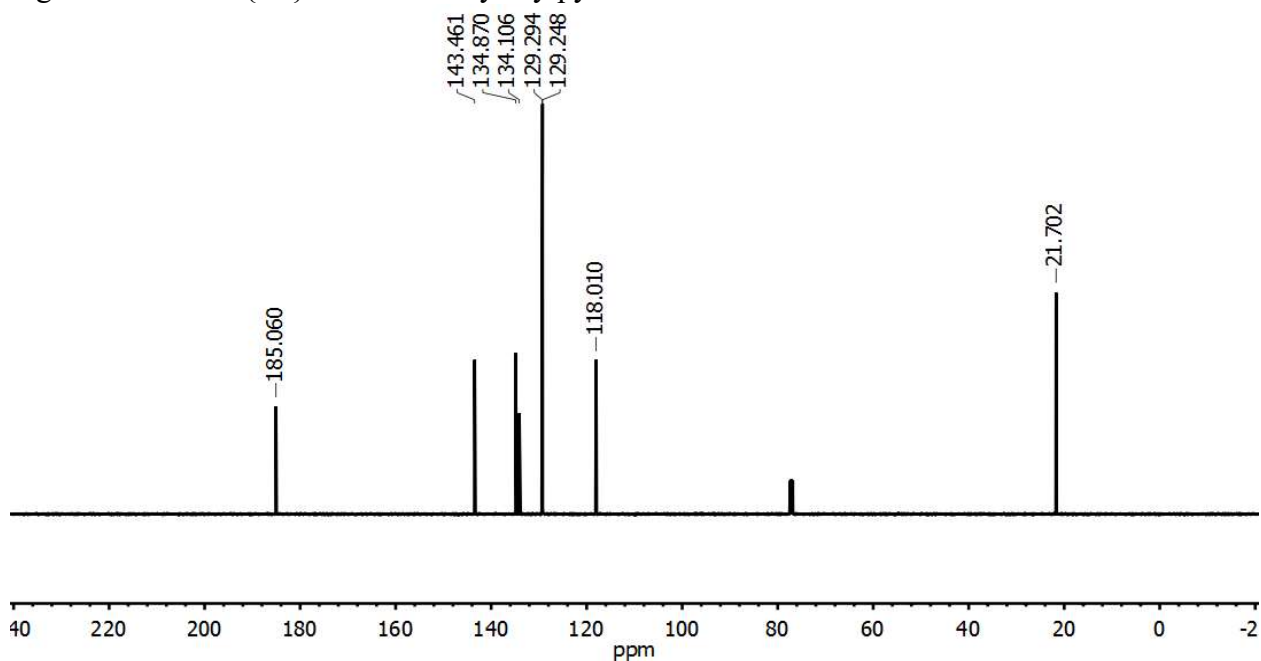


Figure 1A - 3. ^1H NMR of $^{\text{Tol,Cy}}\text{DIPy}$ in CDCl_3 .

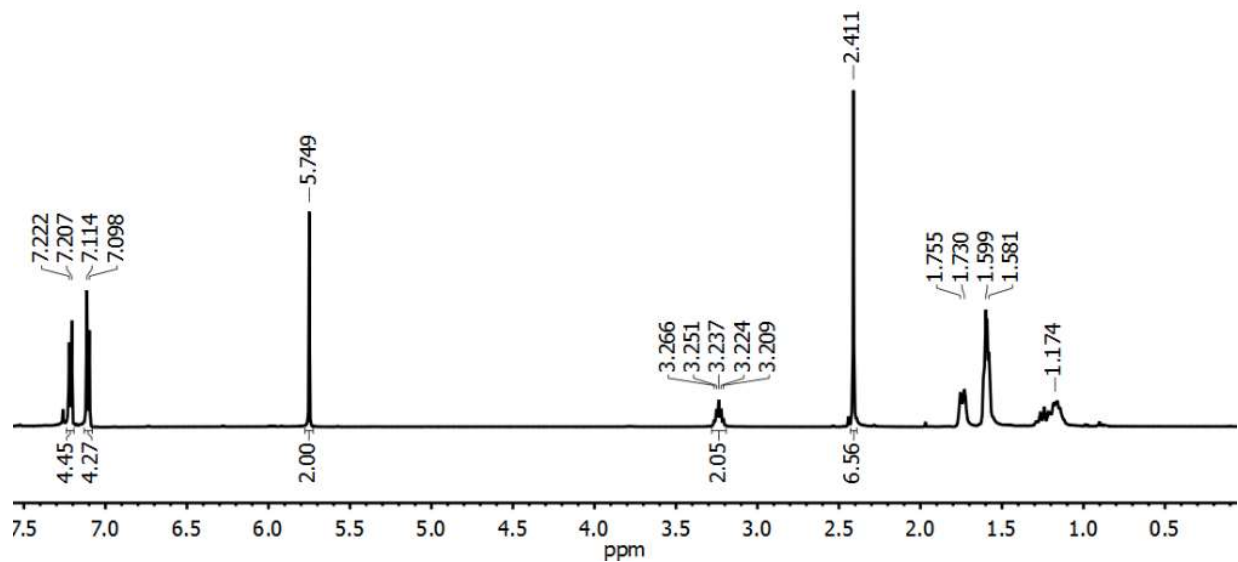


Figure 1A - 4. $^{13}\text{C}\{^1\text{H}\}$ NMR of $^{\text{Tol,Cy}}\text{DIPy}$ in CDCl_3 .

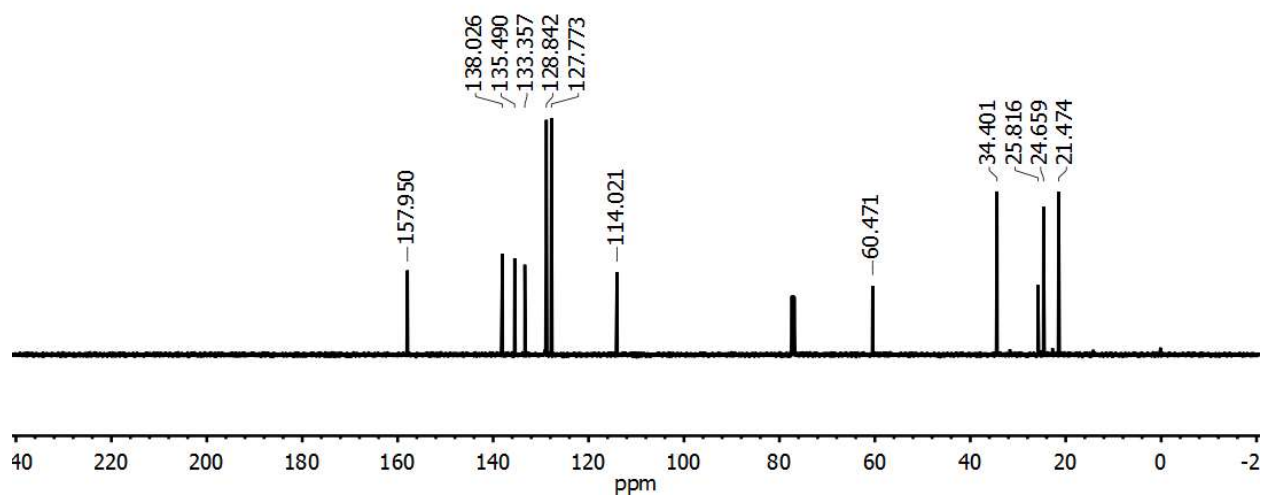


Figure 1A - 5. ^1H NMR of **1** in C_6D_6 .

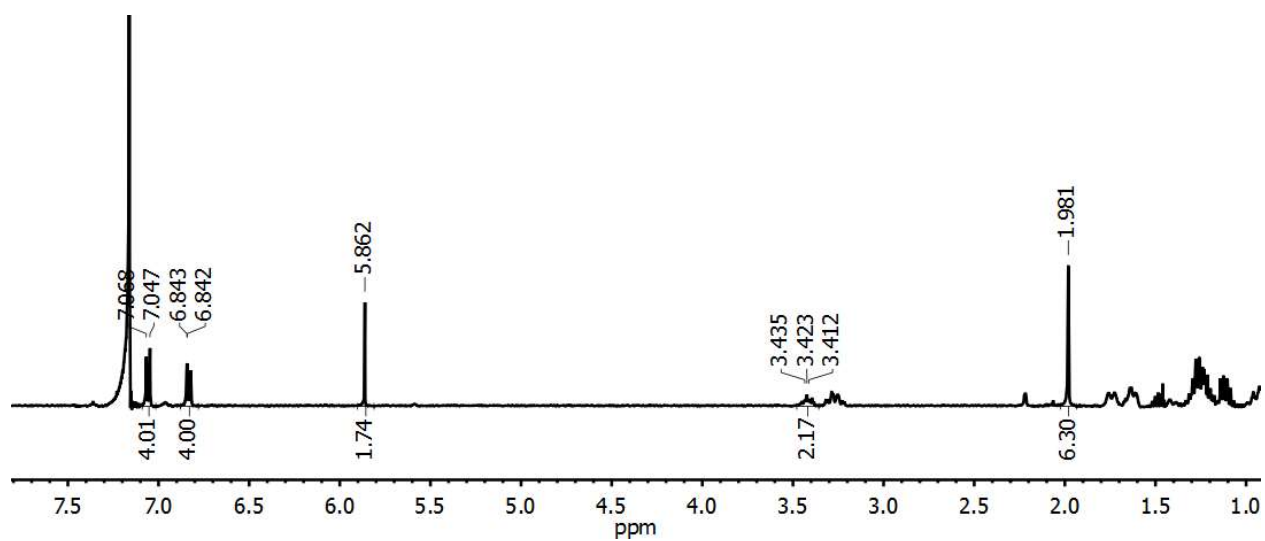


Figure 1A - 6. $^{13}\text{C}\{^1\text{H}\}$ NMR of **1** in C_6D_6 , low signal intensity is due to low solubility of **1**.

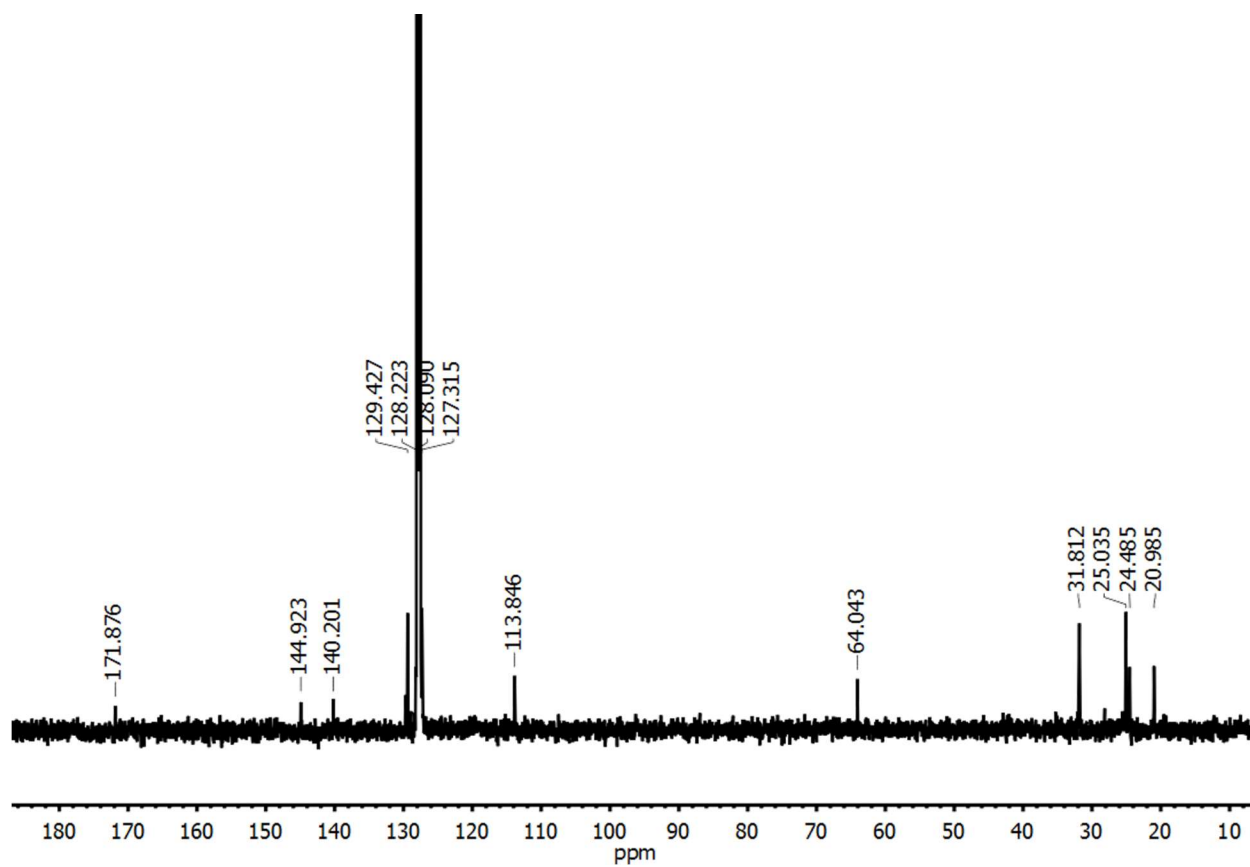


Figure 1A - 7. ^1H NMR of **2** in C_6D_6 .

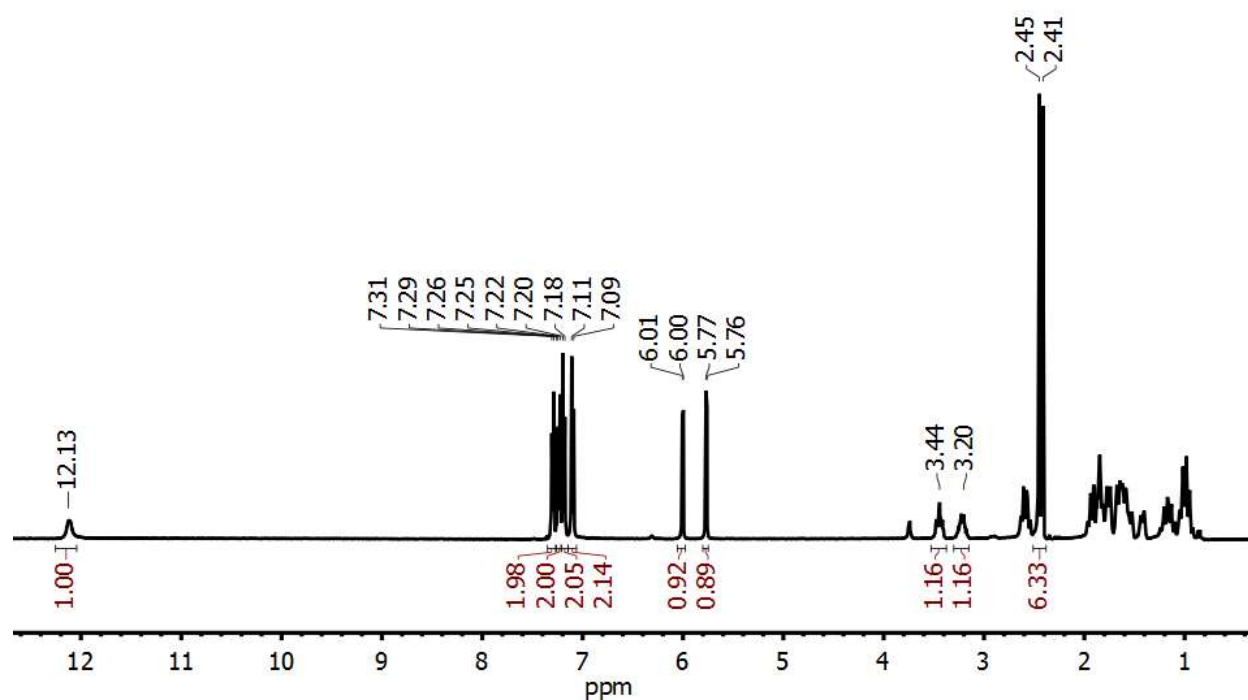


Figure 1A - 8. $^{13}\text{C}\{^1\text{H}\}$ NMR of **2** in C_6D_6 .

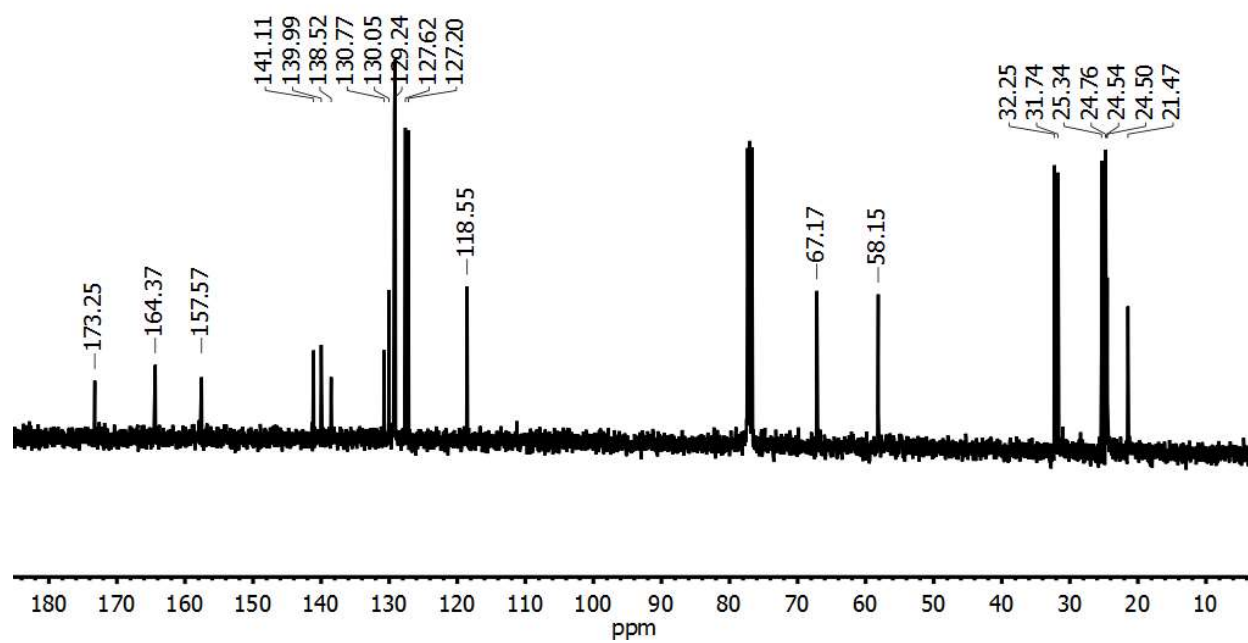


Figure 1A - 9. ^1H NMR of **3** in C_6D_6 .

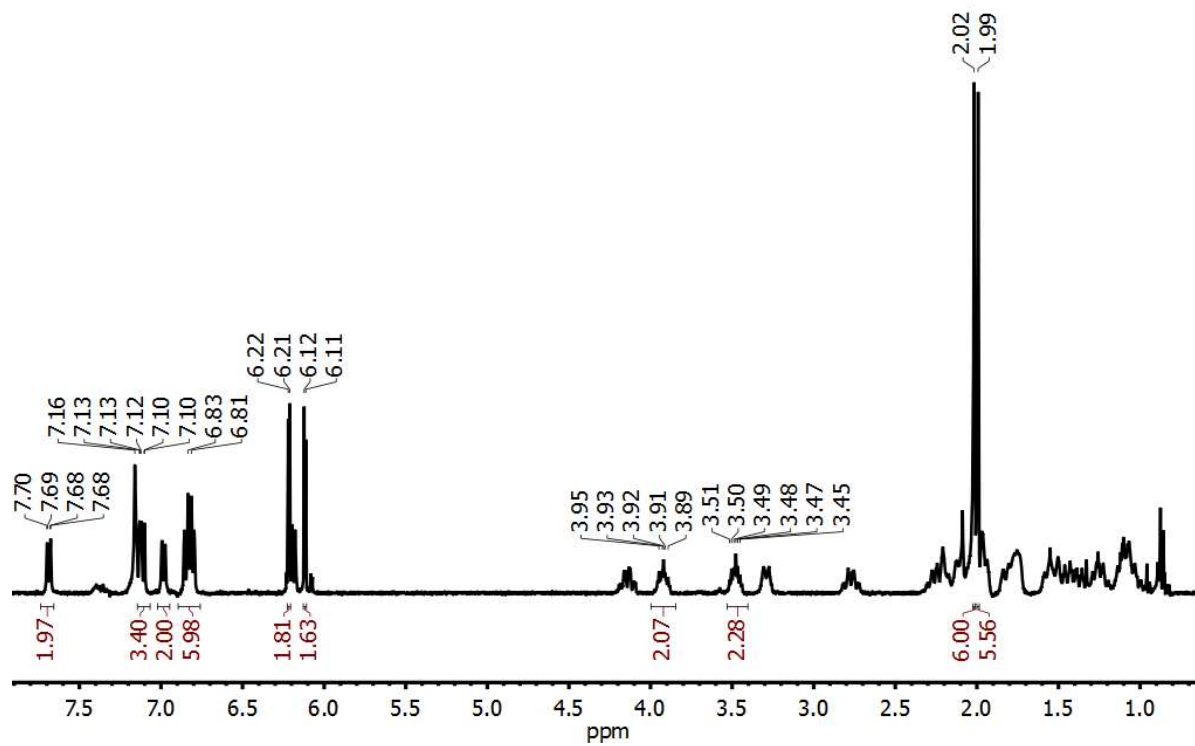


Figure 1A - 10. ^1H NMR of **4** in C_6D_6 .

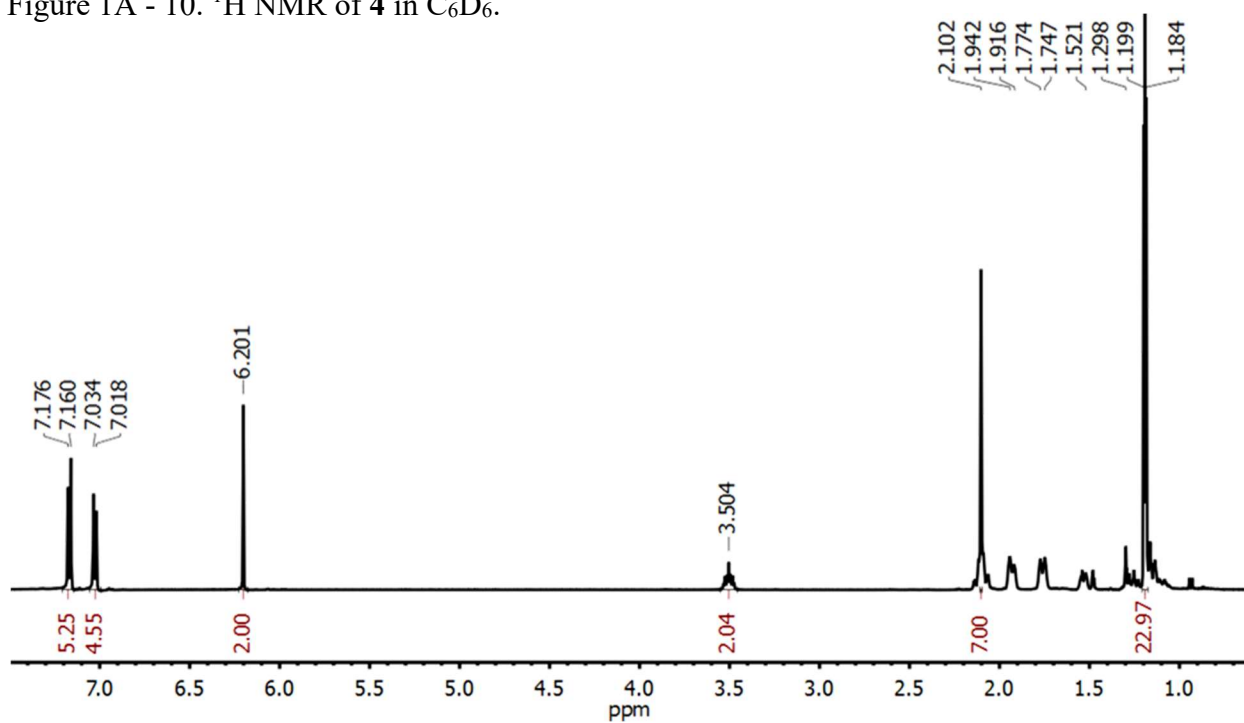


Figure 1A - 11. $^{31}\text{P}\{^1\text{H}\}$ NMR of **4** in C_6D_6 .

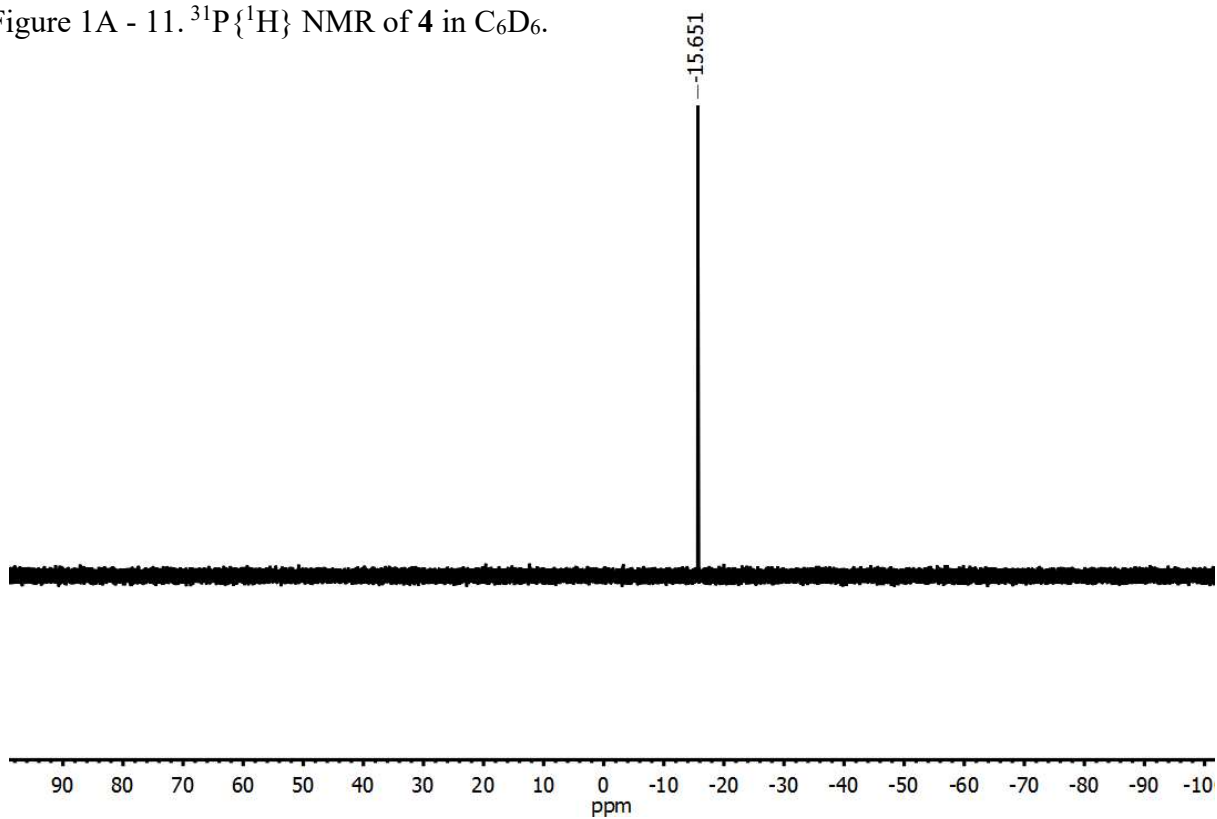


Figure 1A - 12. $^{13}\text{C}\{^1\text{H}\}$ NMR of **4** in C_6D_6 .

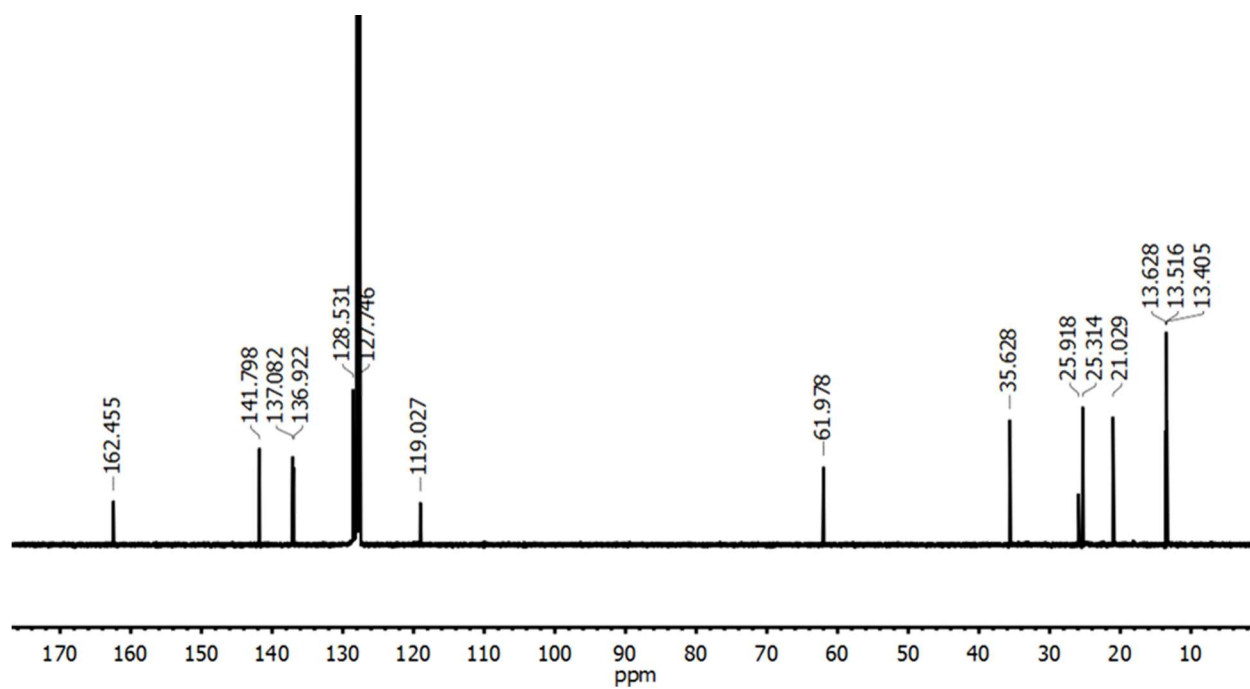


Figure 1A - 13. $^{31}\text{P}\{^1\text{H}\}$ NMR of **4** in THF (bottom), reduction of **4** with Na (middle), and reduction of **4** with Na with an added spike of PMe_3 (top).

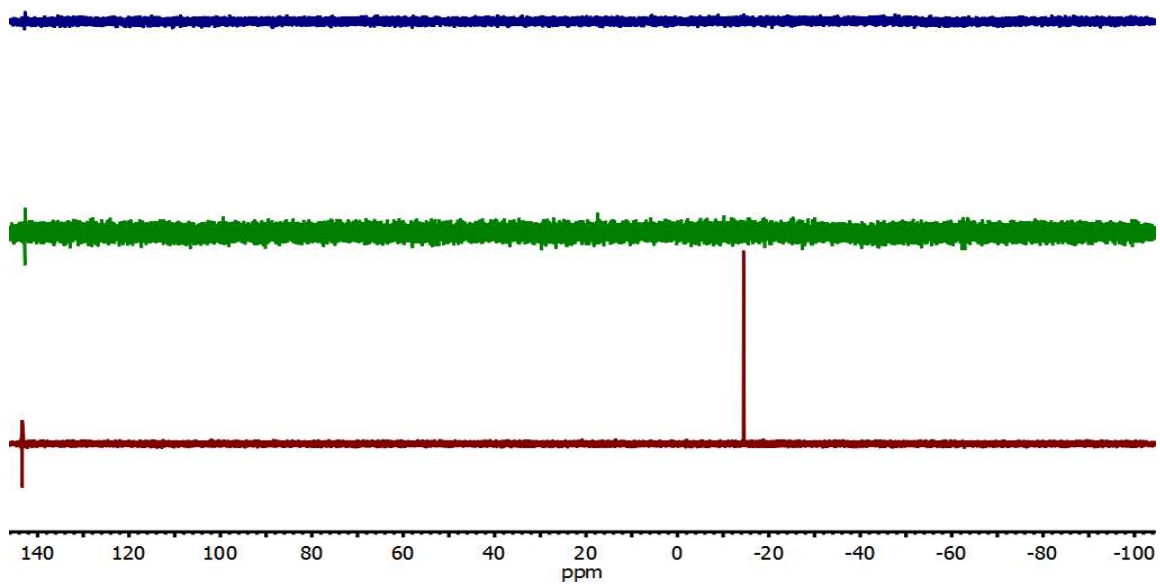


Figure 1A - 14. $^{31}\text{P}\{^1\text{H}\}$ NMR of vacuum distillates from reduction reaction.

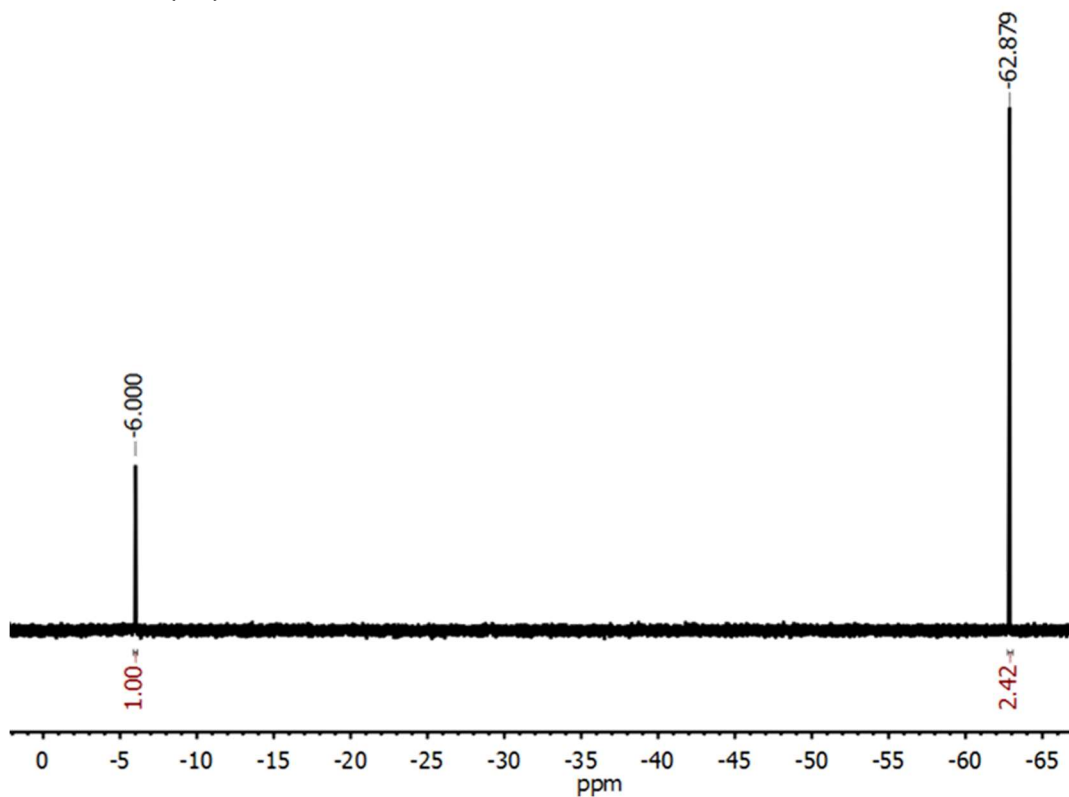


Figure 1A - 15. ^1H NMR of $(^{\text{Tol,Cy}}\text{DIPyH})\text{NiCl}_2$ (**6**) in C_6D_6 .

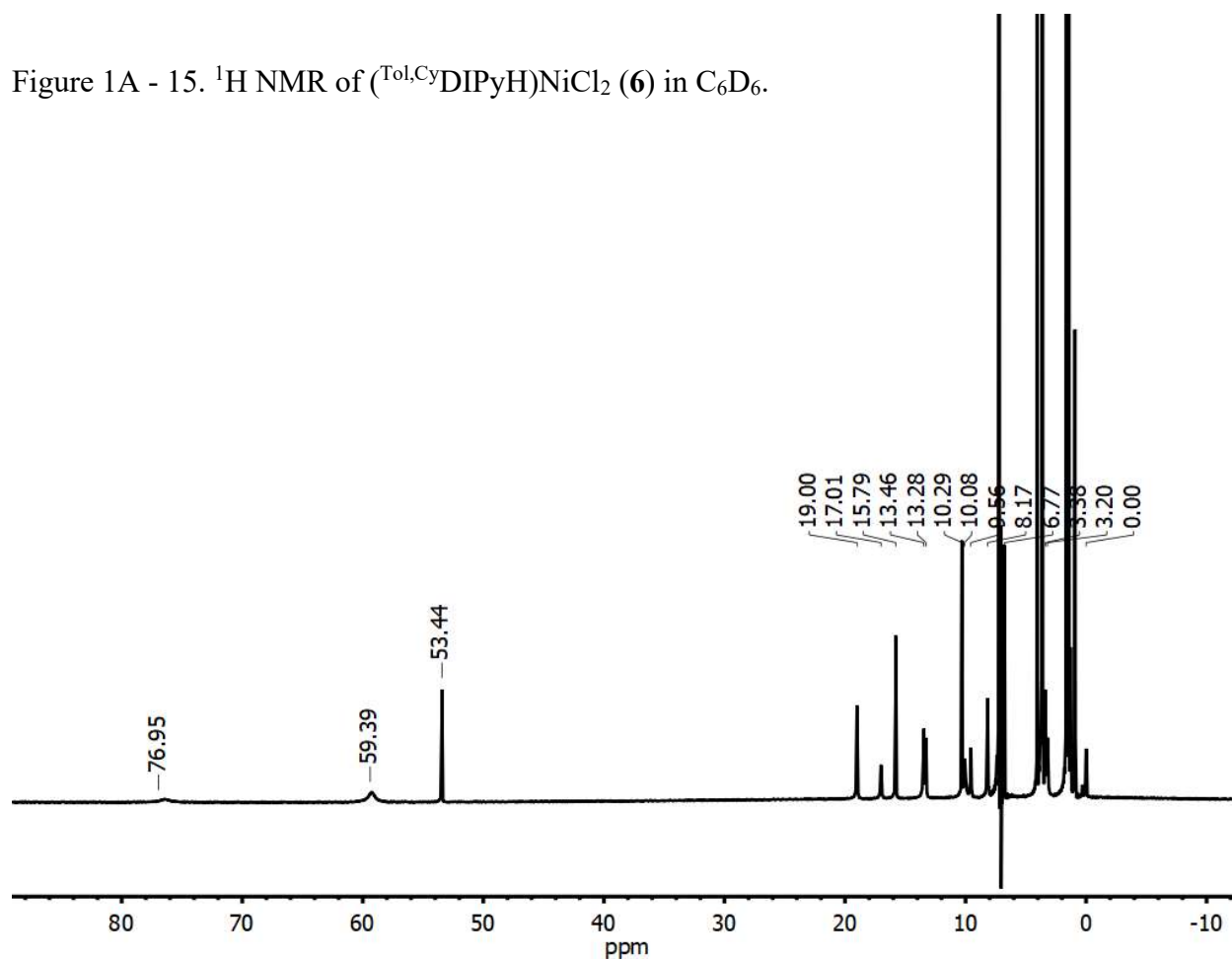


Figure 1A - 16. ^1H NMR of $(^{\text{Tol,Cy}}\text{DIPyH})\text{CoBr}_2$ (**7**) in C_6D_6 .

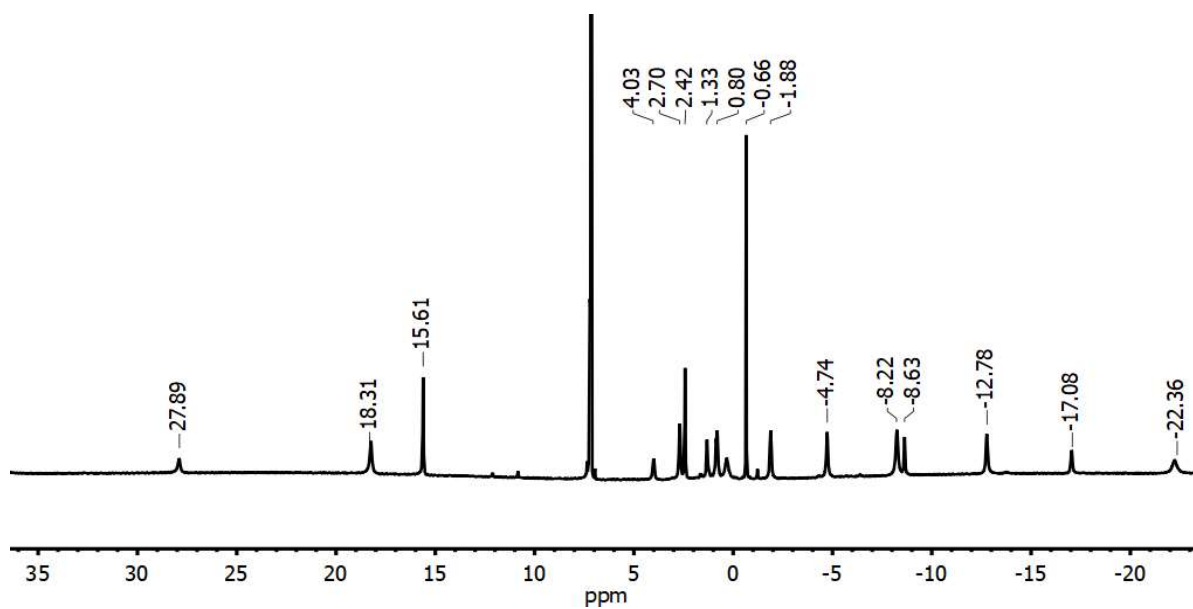
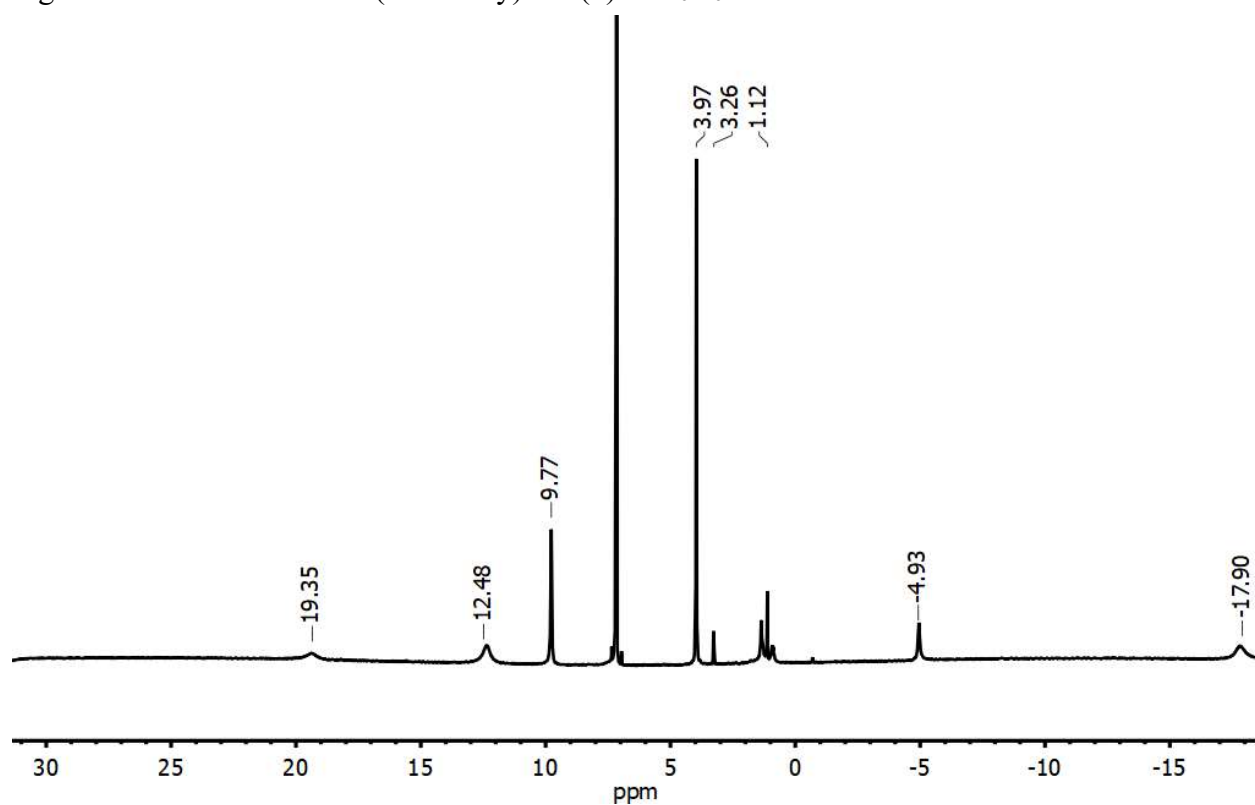


Figure 1A - 17. ^1H NMR of $(^{\text{Tol,Cy}}\text{DIPy})_2\text{Co}$ (**8**) in C_6D_6 .



UV-visible Spectra

Figure 1A - 18. UV-vis trace for decomposition of **5** in THF with linear fit to model first order kinetics.

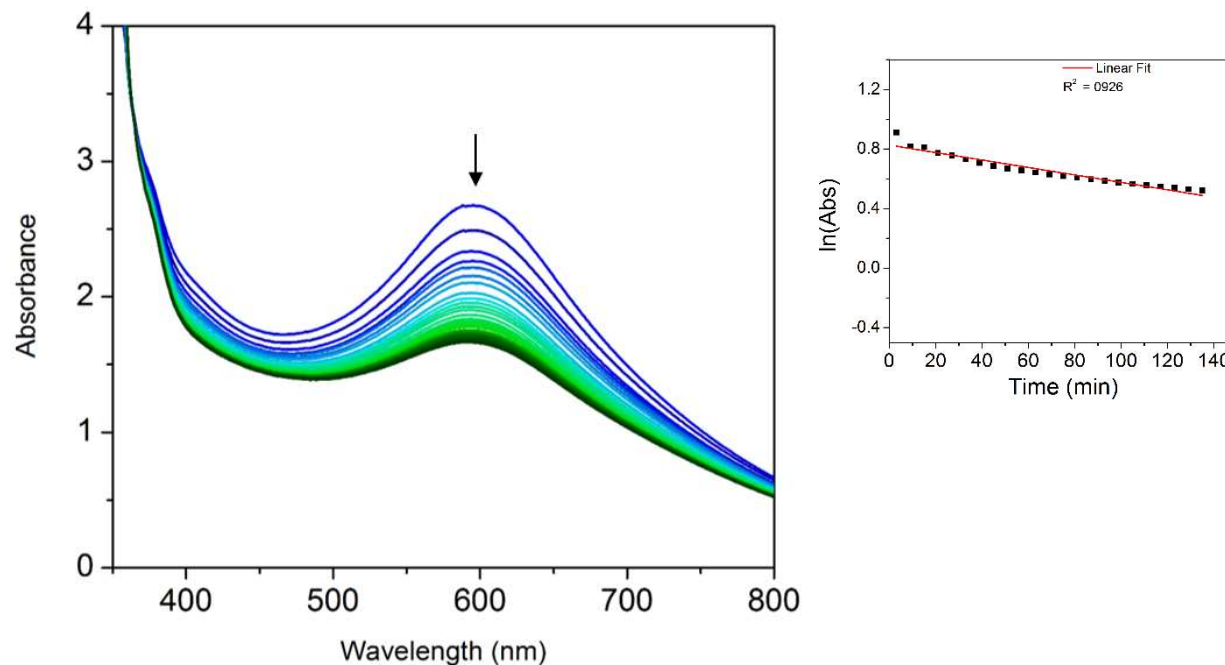
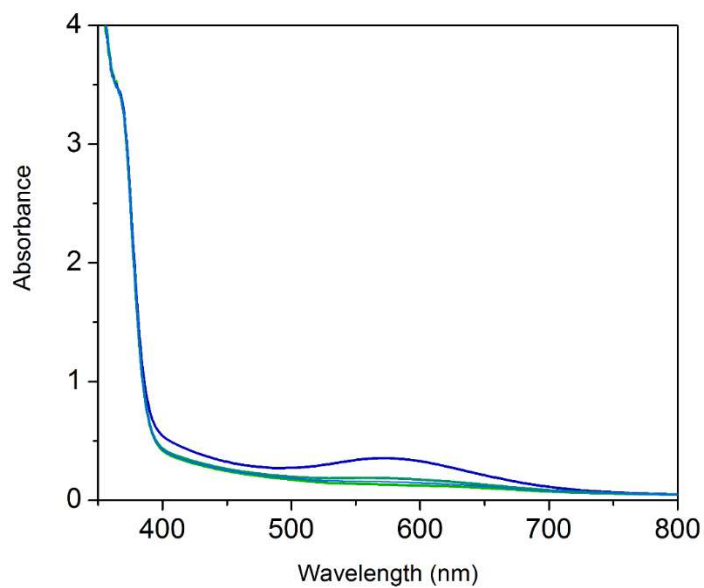


Figure 1A - 19. UV-vis trace of decomposition of **5** in benzene. Note that decomposition was too fast for accurate kinetic data.



IR Spectra

Figure 1A - 20. IR (KBr Pellet) of ^{Tol,Cy}DIPyH. The residual broadness at 3500 cm⁻¹ is due to water in the KBr.

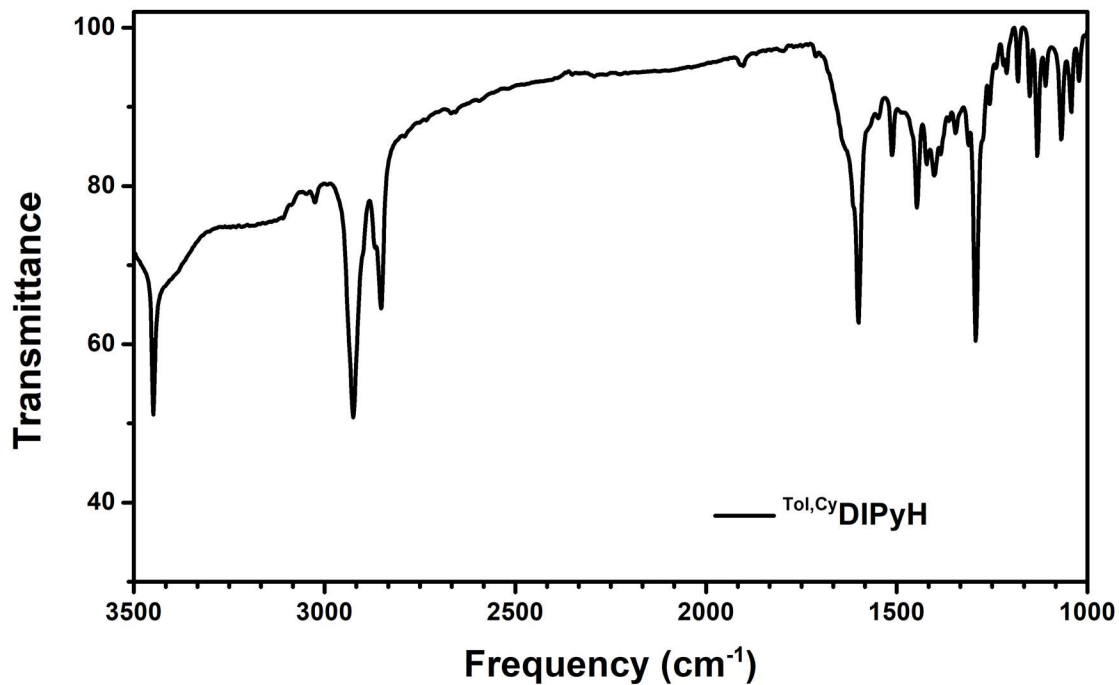


Figure 1A - 21. IR (KBr Pellet) of (^{Tol,Cy}DIPy)PdCl. Residual water causes the features at 3200 cm⁻¹.

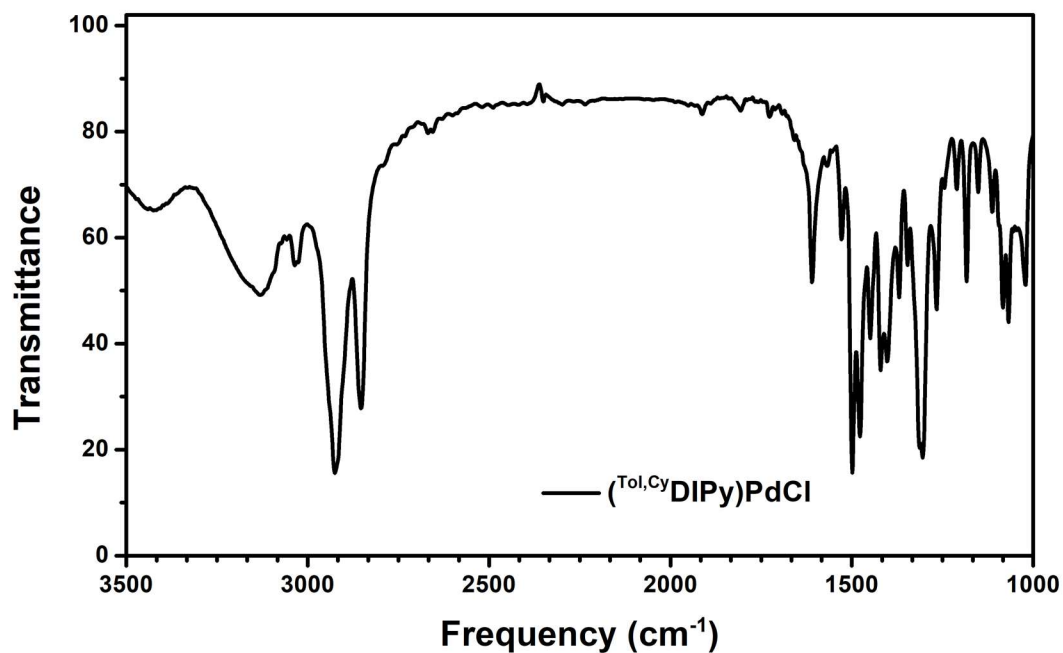


Figure 1A - 22. IR (KBr Pellet) of 2.

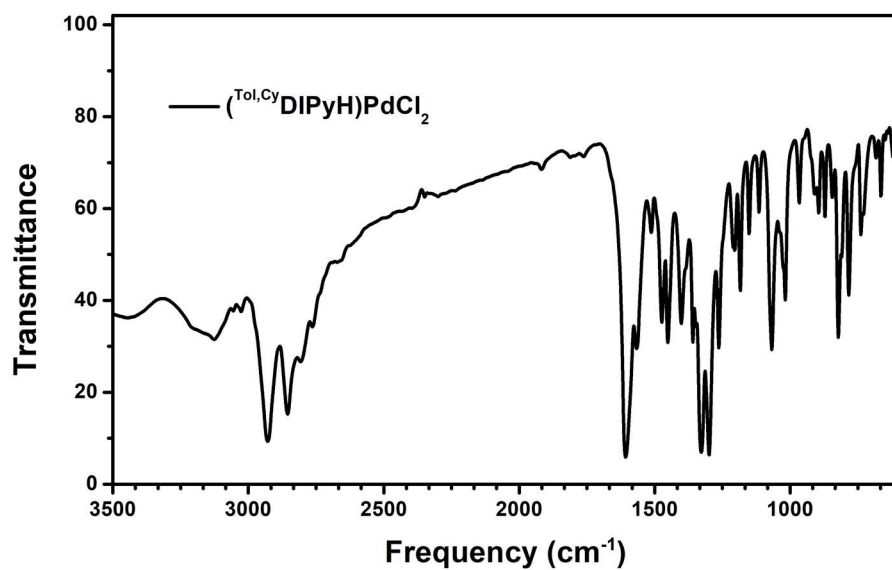


Figure 1A - 23. IR (KBr Pellet) of (Tol,Cy)DIPy)(PMe₃)₂PdCl. Residual water causes the features at 3200 cm⁻¹.

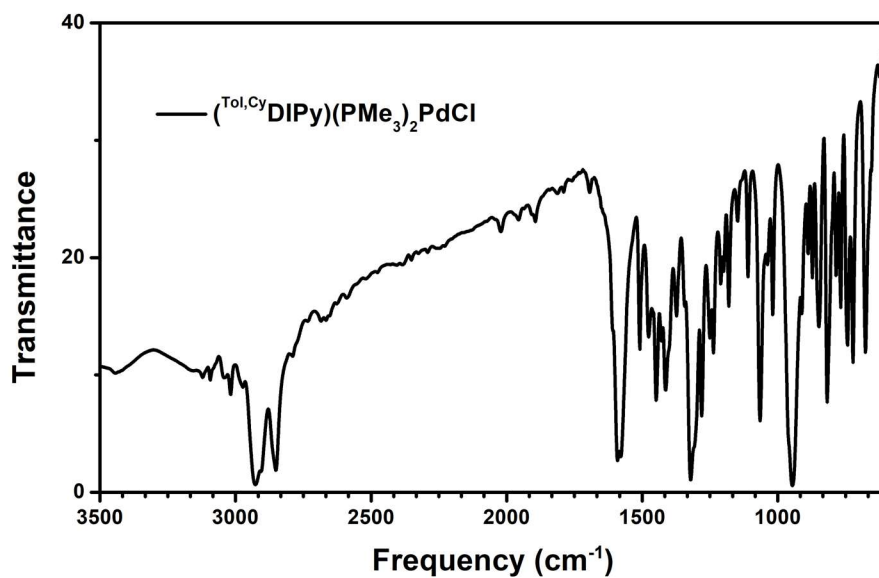
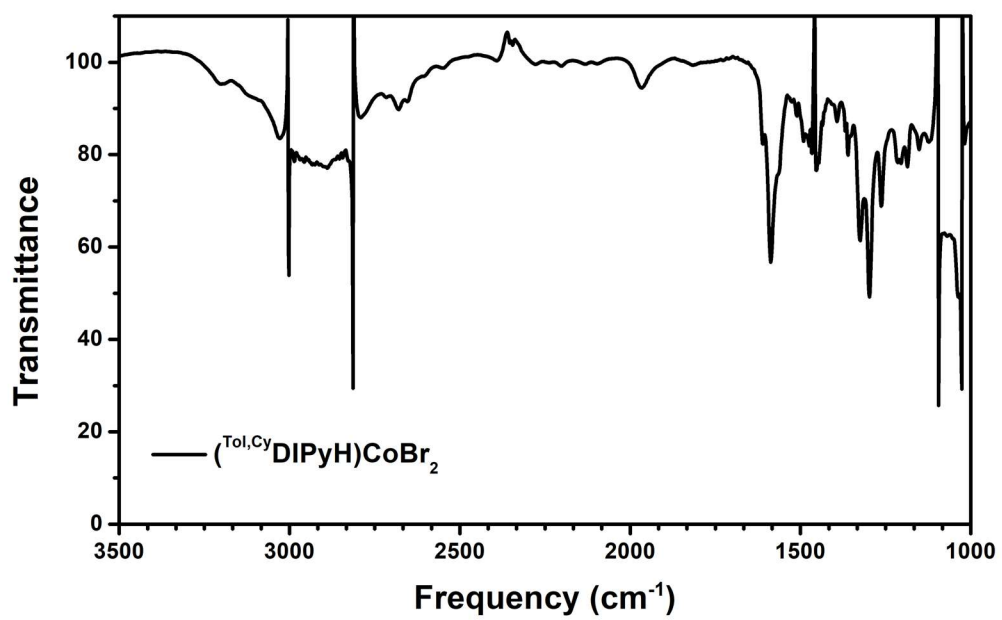


Figure 1A - 24. IR (THF solution) of 7.



Computations

Table 1A - 1. Tabulated results of calculations for energy and EPR parameters for proposed structures of **5**. Geometry Optimization: Gaussian 09, B3LYP, Functional: LANL2DZ (Pd), 6-31G(d,p) (C,N,H,P) EPR Calculation: ORCA B3LYP, Functional: ZORA-def2TZVP (Pd), def2-TZVP (P), EPR-II (C,H,N).

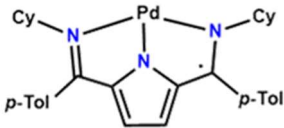
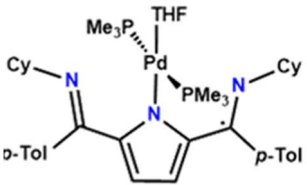
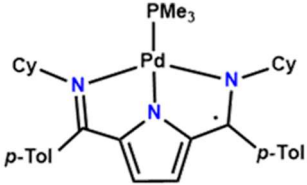
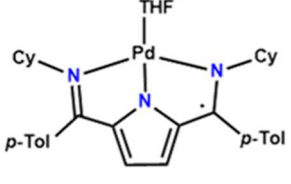
Structure	Energy (ΔG , kcal/mol)	EPR g-value	EPR A_{Pd} (MHz)	Pd Mulliken Spin Population
	-1.2	2.0	9	0.36
	0	1.99	42	0.36
	-16	2.00	15	0.33
	-17	1.99	17	0.36

Figure 1A - 25. Calculated lowest energy structure of **5**.

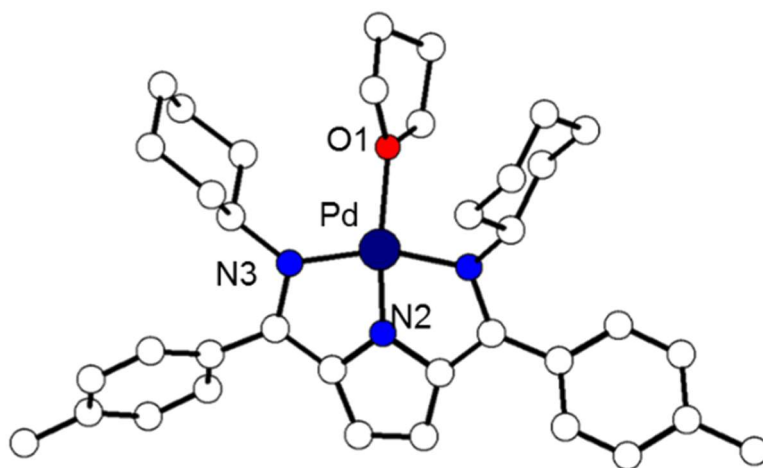


Table 1A - 2. Coordinates of calculated structure of **5**.

Pd	-0.00103	0.34190	-0.04787
O	0.05771	2.29893	-0.71502
N	-0.01047	-1.40352	-0.03141
C	1.14288	-2.21390	-0.11940
C	-6.30066	-3.12860	0.11558
C	-1.16976	-2.20410	-0.12081
C	-2.30630	-1.34729	-0.02899
N	1.90488	0.00637	0.01954
C	-0.72149	-3.56753	-0.25838
H	-1.37045	-4.44359	-0.34451
C	6.29833	-3.10238	-0.20855
C	-3.70453	-1.90588	0.03029
C	0.67994	-3.57234	-0.27399
H	1.31886	-4.45342	-0.37821
C	3.97922	-3.12049	0.59642
H	3.18762	-3.59756	1.18879
C	2.29019	-1.36495	-0.05926
N	-1.91399	0.01815	0.02098
C	-5.38805	-3.42963	-0.92529
H	-5.68130	-4.13761	-1.71243
C	-4.11721	-2.83504	-0.96664
H	-3.42469	-3.08131	-1.78257
C	-5.89036	-2.22255	1.11966
H	-6.57277	-1.99037	1.94855

C	-7.69291	-3.78191	0.15068
H	-8.27304	-3.51783	-0.74967
H	-7.60907	-4.88118	0.18226
H	-8.25634	-3.45109	1.03556
C	-4.61732	-1.62528	1.08430
H	-4.31619	-0.95586	1.90007
C	3.68492	-1.90916	-0.09602
C	6.01202	-1.90769	-0.90908
H	6.79828	-1.43574	-1.51382
C	4.73508	-1.32380	-0.85994
H	4.53820	-0.41700	-1.44438
C	5.25559	-3.69990	0.54148
H	5.45115	-4.63086	1.09091
C	7.70167	-3.73055	-0.24643
H	8.27754	-3.34937	-1.10310
H	8.26262	-3.49239	0.67447
H	7.63856	-4.82754	-0.32445
C	-3.07208	0.99781	0.15650
H	-4.01624	0.42540	0.13873
C	3.00451	0.92255	0.54770
H	3.90645	0.30947	0.72676
C	-3.00685	1.75799	1.52802
H	-3.01939	1.02097	2.34925
H	-2.05161	2.30630	1.59941
C	-3.14343	2.01256	-1.03642

H	-2.20928	2.59076	-1.08271
H	-3.24184	1.45182	-1.98173
C	2.59007	1.54080	1.93076
H	1.66444	2.13020	1.80886
H	2.36644	0.72091	2.63434
C	3.40823	2.06005	-0.45501
H	3.72990	1.61381	-1.41144
H	2.53655	2.69793	-0.66165
C	3.72353	2.44312	2.51352
H	3.38409	2.90326	3.45788
H	4.59894	1.81285	2.74792
C	4.55786	2.93659	0.13311
H	5.45764	2.31173	0.26822
H	4.81619	3.74053	-0.57829
C	-4.20176	2.74898	1.68810
H	-5.14200	2.17335	1.74334
H	-4.09893	3.30697	2.63515
C	-4.35376	2.98341	-0.86731
H	-4.37214	3.70587	-1.70209
H	-5.29215	2.40394	-0.91096
C	-4.28406	3.74598	0.49158
H	-5.17283	4.39078	0.60394
H	-3.39644	4.40276	0.49875
C	4.14964	3.55419	1.50576
H	3.31087	4.25686	1.35648

H	4.99348	4.13152	1.92158
C	0.02643	3.63410	-0.05302
C	-0.17156	4.67563	-1.19371
C	0.52336	4.00193	-2.41726
C	0.29807	2.47549	-2.17765
H	0.98735	3.79422	0.48183
H	-0.80090	3.62554	0.68428
H	0.28635	5.64352	-0.93382
H	-1.24533	4.82886	-1.39043
H	1.60102	4.23279	-2.42654
H	0.08266	4.32179	-3.37478
H	1.17278	1.85528	-2.46046
H	-0.59884	2.09761	-2.71269

Electrochemistry

Figure 1A - 27. CV of **1** in THF with 0.1 M NBu₄PF₆ electrolyte. Scan rate = 100mV/sec.

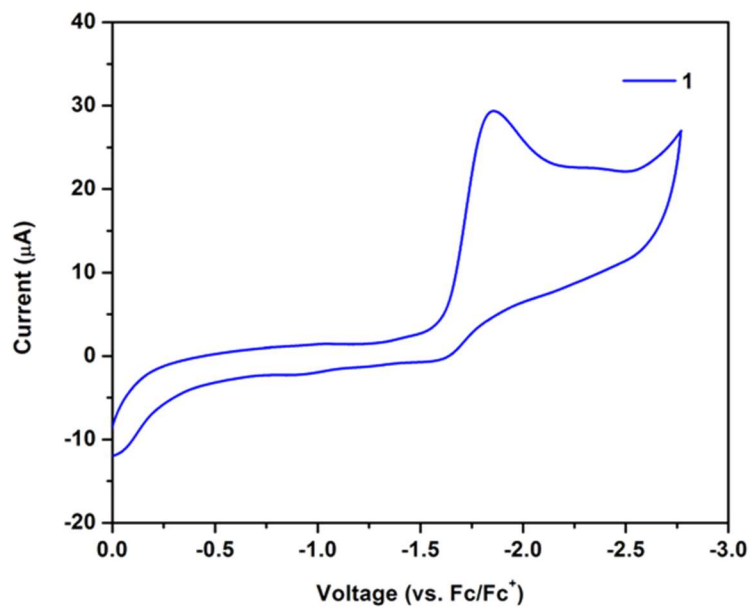


Figure 1A - 26. CV of **4** THF with 0.1 M NBu₄PF₆ electrolyte. Scan rate = 100mV/sec.

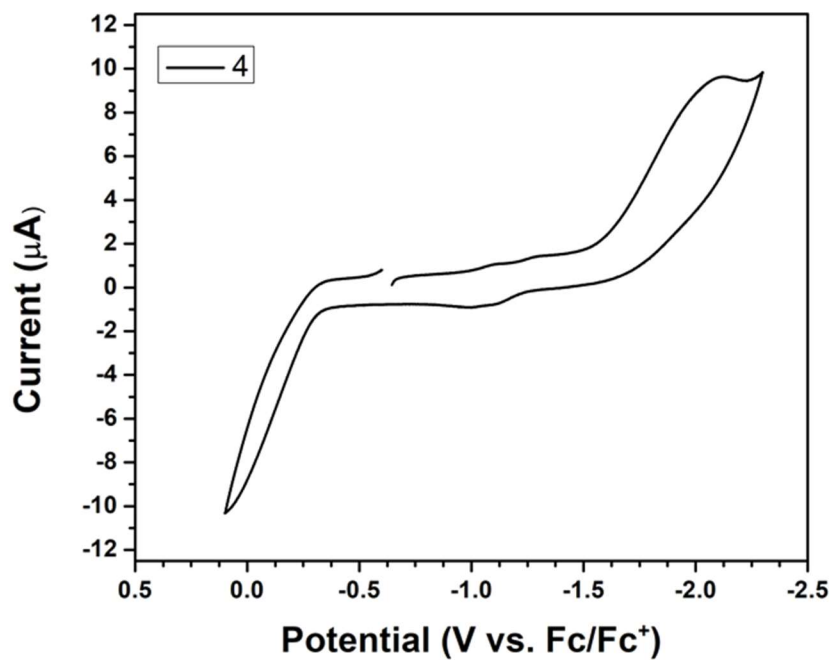


Figure 1A - 29. CV of **5** in THF with a glassy carbon working electrode, scan rate 100 mV/sec, 0.1 M NBu₄PF₆.

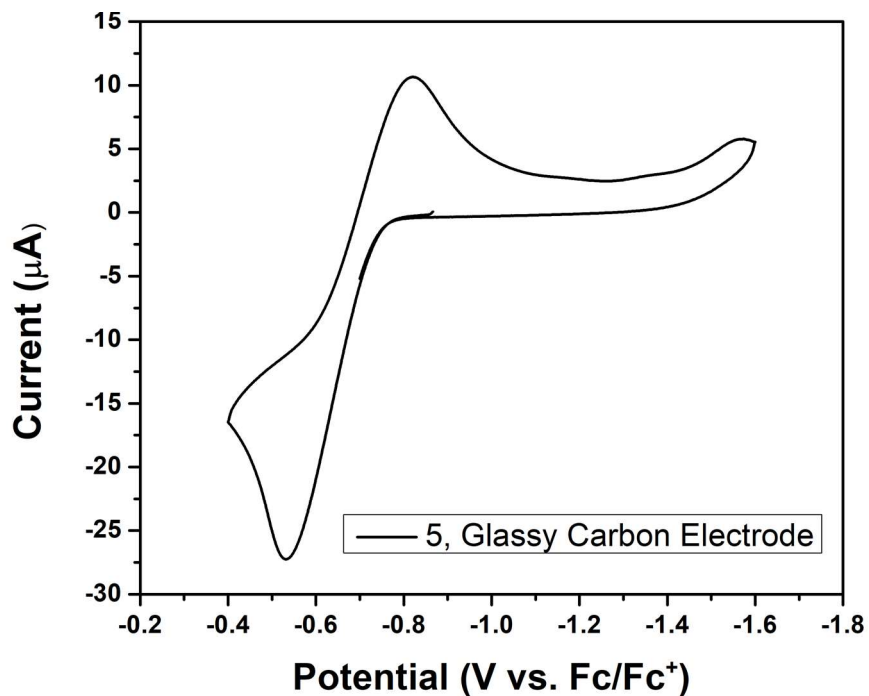
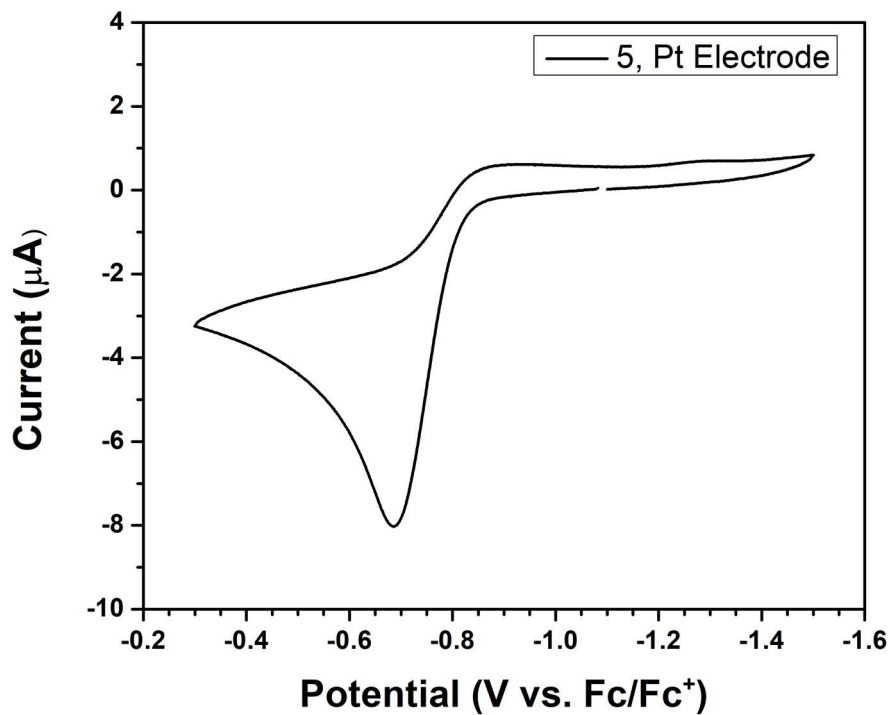
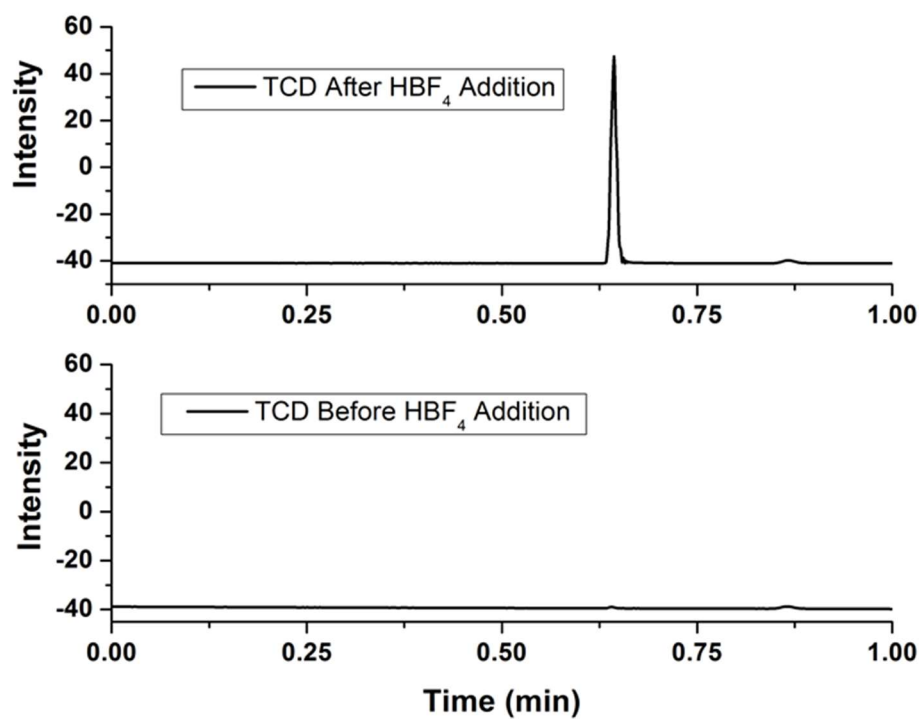


Figure 1A - 28. CV of **5** in THF with a Pt working electrode, scan rate 100 mV/sec, 0.1 M NBu₄PF₆.



GC Data

Figure 1A - 30. GC of the headspace of a sealed solution of **5** before and after addition of HBF_4 . The peak observed is due to gaseous H_2 .



X-Ray Structure Determination

Figure 1A - 31. SXRD structure of **2**.

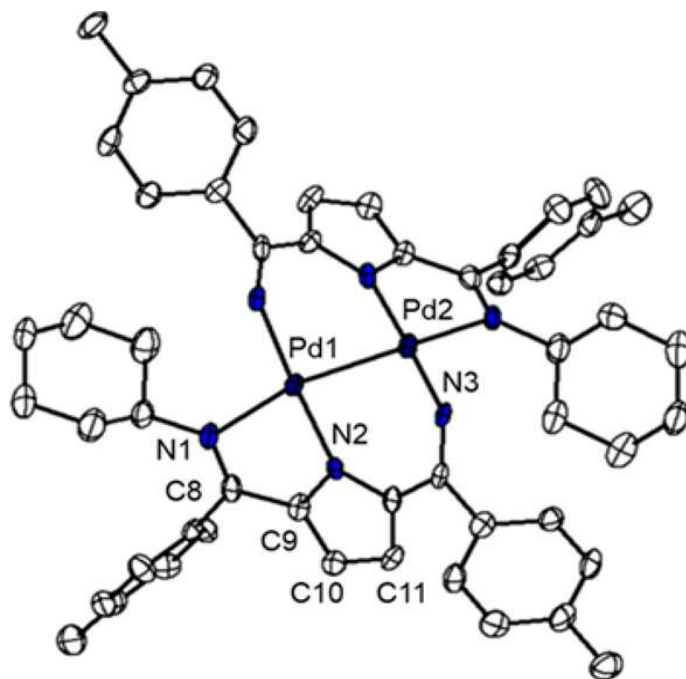


Figure 1A - 32. SXRD structure of **8**.

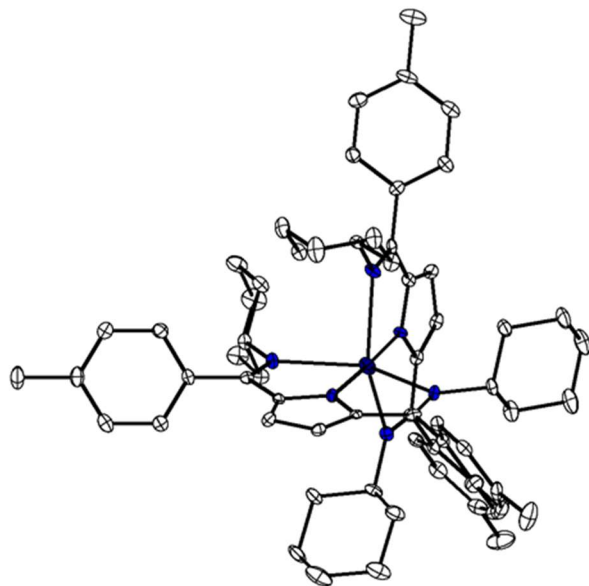


Table 1A - 3. Structural refinement parameters of structures.

Compound #	1	2	3	4
Formula	PdC ₃₂ H ₃₈ N ₃ Cl	PdC ₃₂ H ₃₉ N ₃ Cl ₂	Pd ₂ C ₆₄ H ₇₆ N ₆	PdC ₃₈ H ₅₆ ClN ₃ P ₂
Crystal System	Monoclinic	Monoclinic	Monoclinic	Monoclinic
Space Group	C2/c	C2/c	C2/c	C2/c
a, Å	13.2443(8)	19.3940(18)	20.8643(16)	9.3839(8)
b, Å	19.7556(12)	16.2257(18)	12.7816(16)	19.7195(16)
c, Å	13.1309(12)	13.5072(4)	20.8387(18)	21.1724(17)
α, deg	90	90	90	90
β, deg	109.816(2)	112.154(4)	102.458(4)	98.975(3)
γ, deg	90	90	90	90
V, Å ³	3232.2(3)	3929.9(7)	5426.4(9)	3869.9(6)
Z	4	4	4	4
Radiation (λ, Å)	Mo-Kα, 0.71073	Mo-Kα, 0.71073	Mo-Kα, 0.71073	Mo-Kα, 0.71073
ρ (calcd.), g/cm ³	1.248	1.083	1.398	1.302
μ (Mo Ka), mm ⁻¹	0.680	0.627	0.709	0.660
Temp, K	100	100	100	100
θ max, deg	27.204	25.790	25.337	28.803
data/parameters	21.2	20.2	13.9	24.4
R ₁	0.0408	0.0815	0.0450	0.0393
wR ₂	0.0771	0.1639	0.0907	0.0681
GOF	1.084	1.100	1.080	1.050

Compound #	6	7
Formula	NiC ₃₂ H ₃₉ Cl ₂ N ₃	CoC ₃₂ H ₃₉ Br ₂ N ₃
Crystal System	Monoclinic	Monoclinic
Space Group	P2 ₁ /c	P2 ₁ /c
a, Å	12.1298(11)	9.4381(5)
b, Å	9.1081(7)	11.9319(6)
c, Å	27.019(2)	26.8846(12)
α, deg	90	90
β, deg	90.341(3)	93.124
γ, deg	90	90
V, Å ³	2985.0(4)	30.23.1
Z	4	4
Radiation (λ, Å)	Mo-K _α , 0.71073	Mo-K _α , 0.71073
ρ (calcd.), g/cm ³	1.325	1.502
μ (Mo K _α), mm ⁻¹	0.855	3.236
Temp, K	100	100
θ max, deg	25.09	26.42
data/parameters	14.6	17.2
R ₁	0.0590	0.0446
wR ₂	0.1356	0.0898
GOF	1.227	1.054

Appendix 2. Supporting Data for Chapter 2.

NMR spectra

Figure 2A - 1. ^1H NMR of $^{\text{Tol,FPPh}}$ DHP in CDCl_3 .

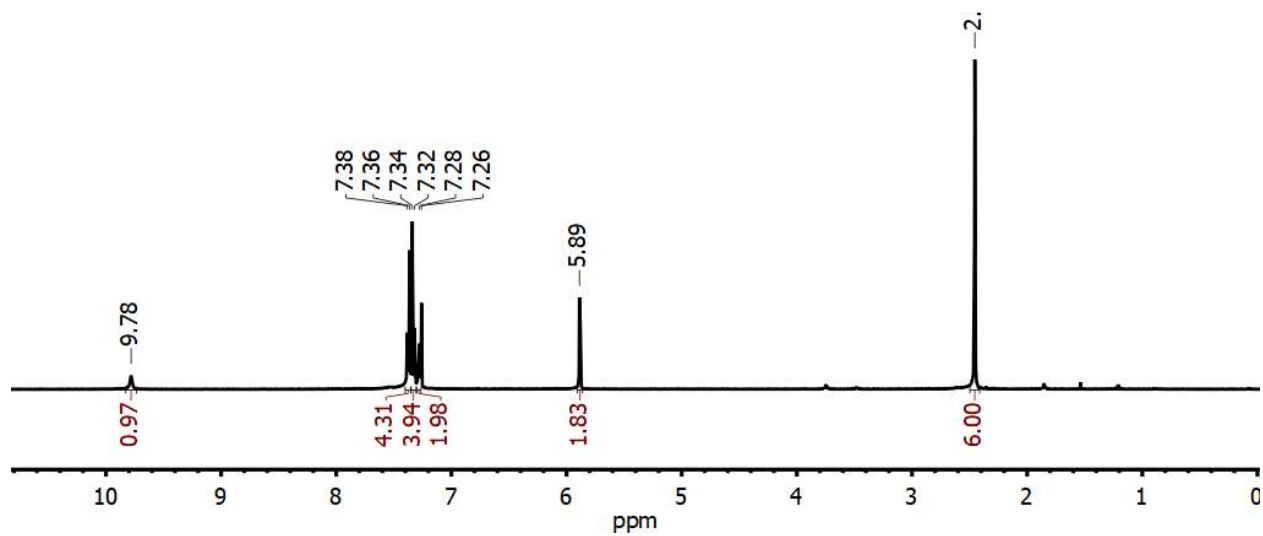


Figure 2A - 2. $^{13}\text{C}\{^1\text{H}\}$ NMR of $^{\text{Tol,FPPh}}$ DHP in CDCl_3 .

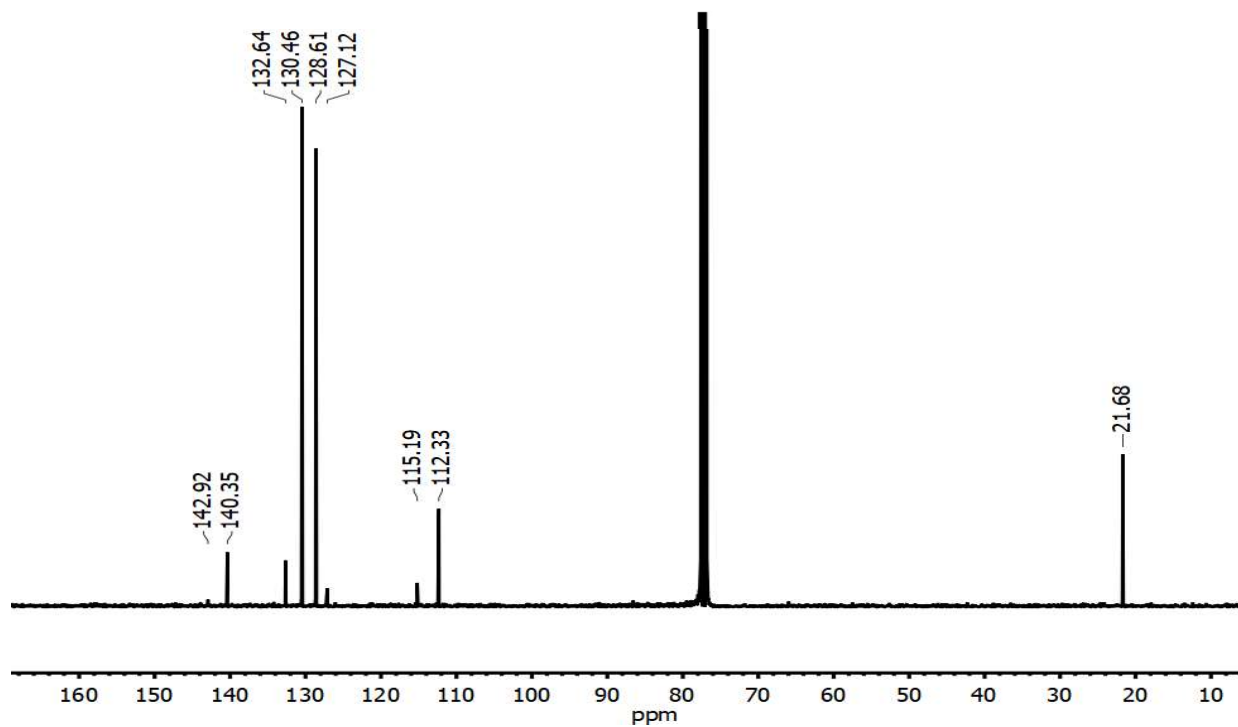


Figure 2A - 3. $^{19}\text{F}\{^1\text{H}\}$ NMR of symmetrical $^{\text{Tol,FPPh}}$ DHP in CDCl_3 . Small impurities result from a small amount of mono-condensed product.

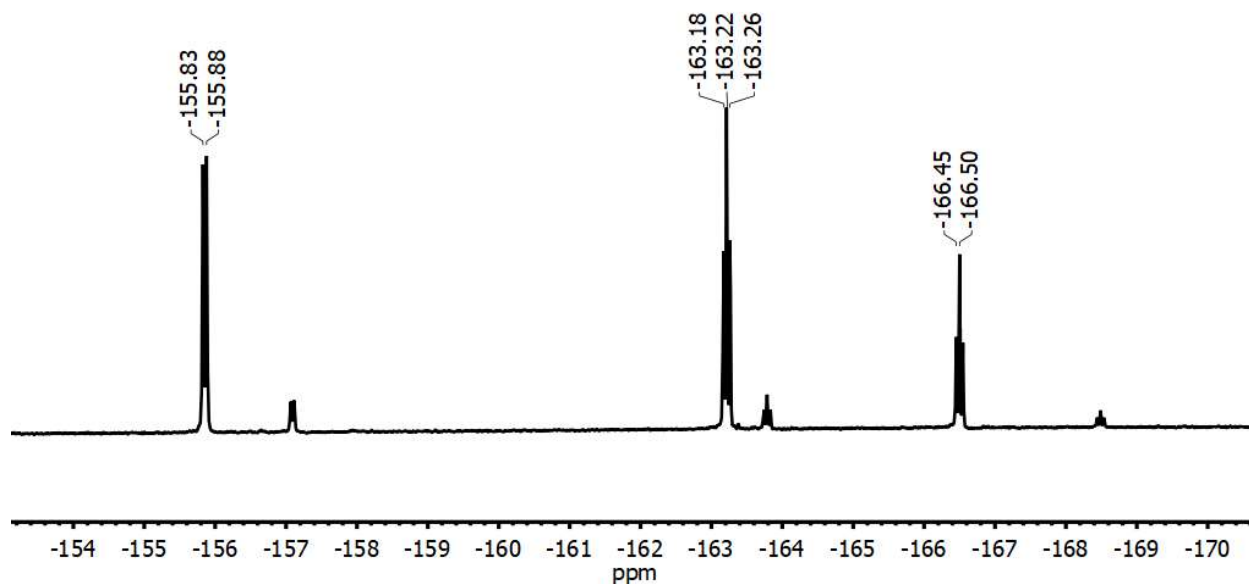


Figure 2A - 4. ^1H NMR of $^{\text{Tol,FPPh}}$ DHP in CDCl_3 after sitting at RT for 2 days, leading to appearance of isomerized DHP.

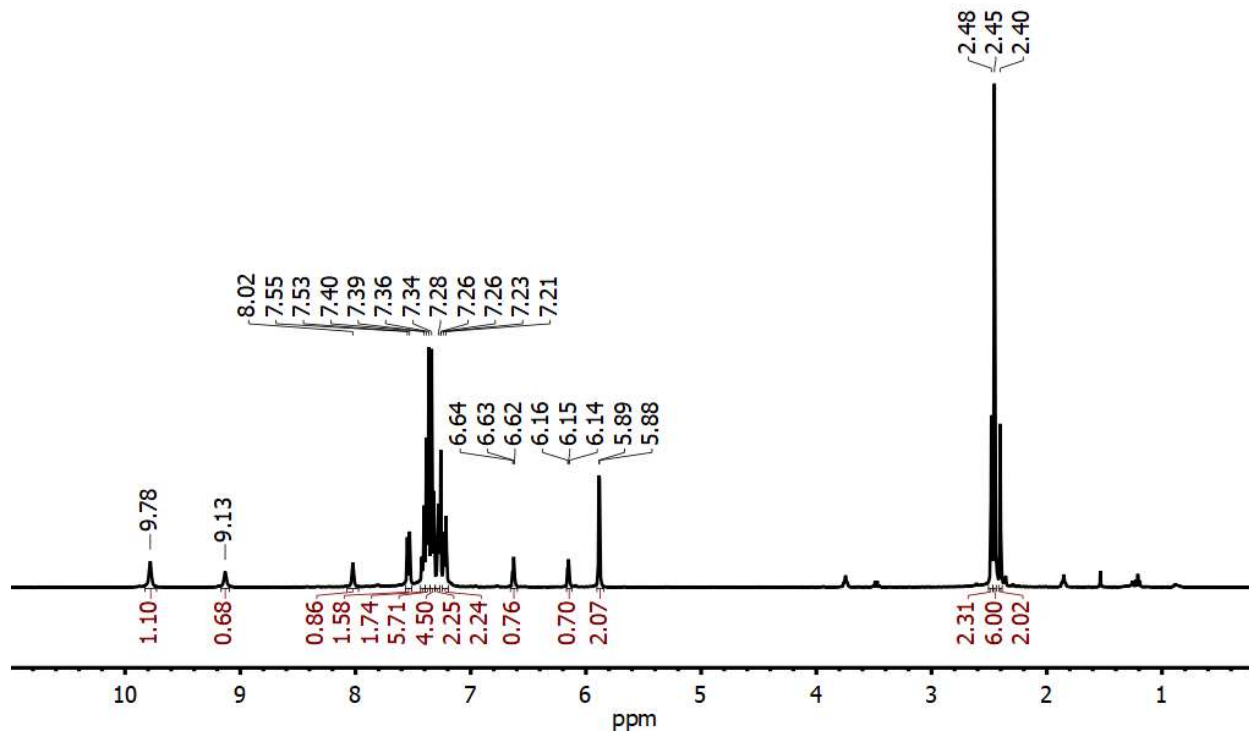


Figure 2A - 5 $^{19}\text{F}\{^1\text{H}\}$ NMR of $^{\text{Tol,FPPh}}$ DHP in CDCl_3 after sitting at RT for 2 days, leading to appearance of isomerized DHP.

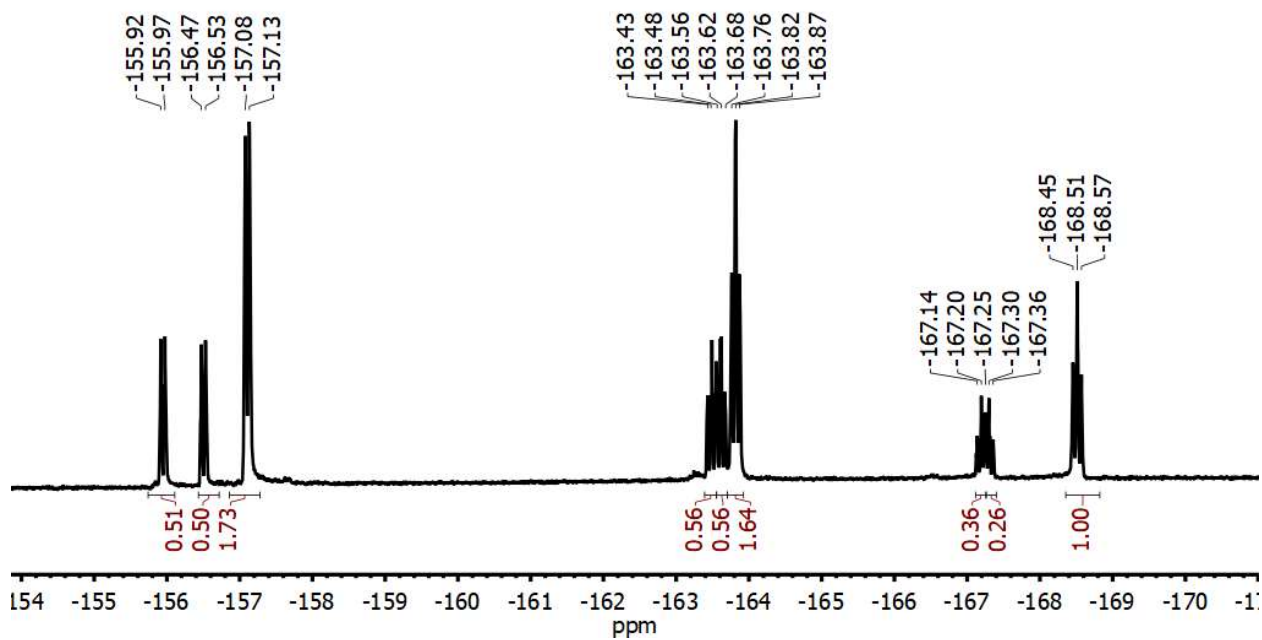


Figure 2A - 6. ^1H NMR of **1** in C_6D_6 .

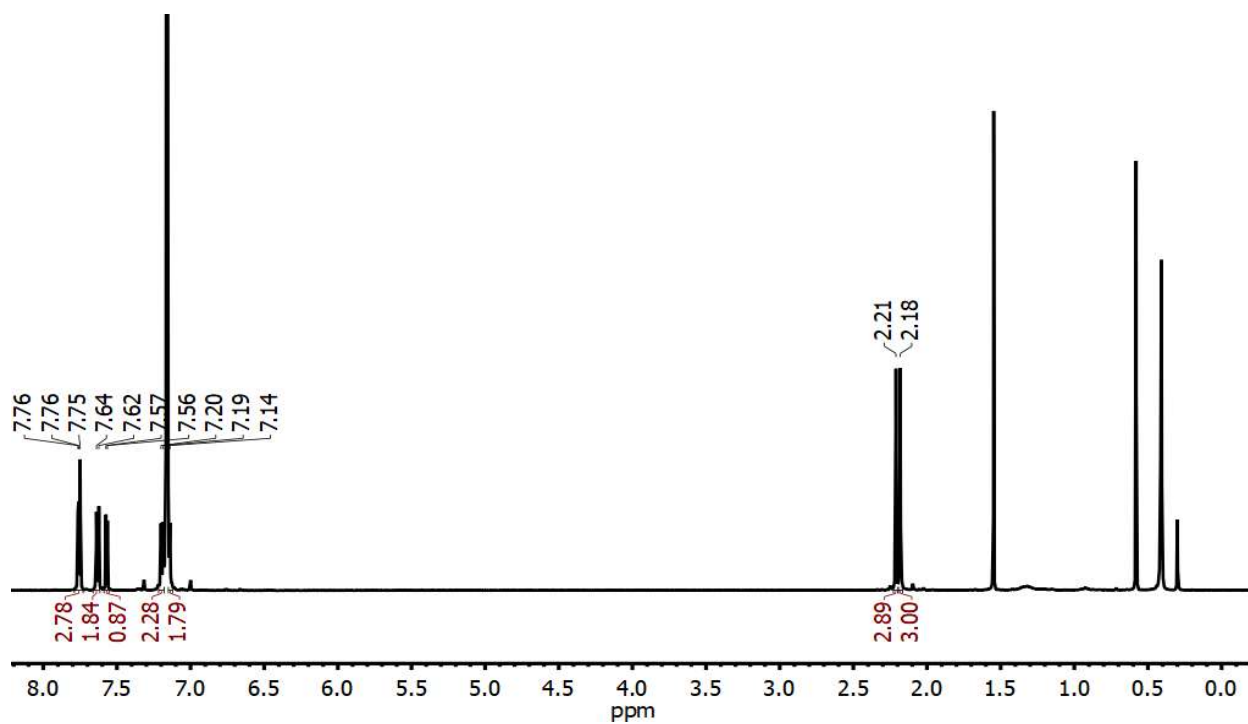


Figure 2A - 7. $^{19}\text{F}\{^1\text{H}\}$ NMR of **1** in C_6D_6 .

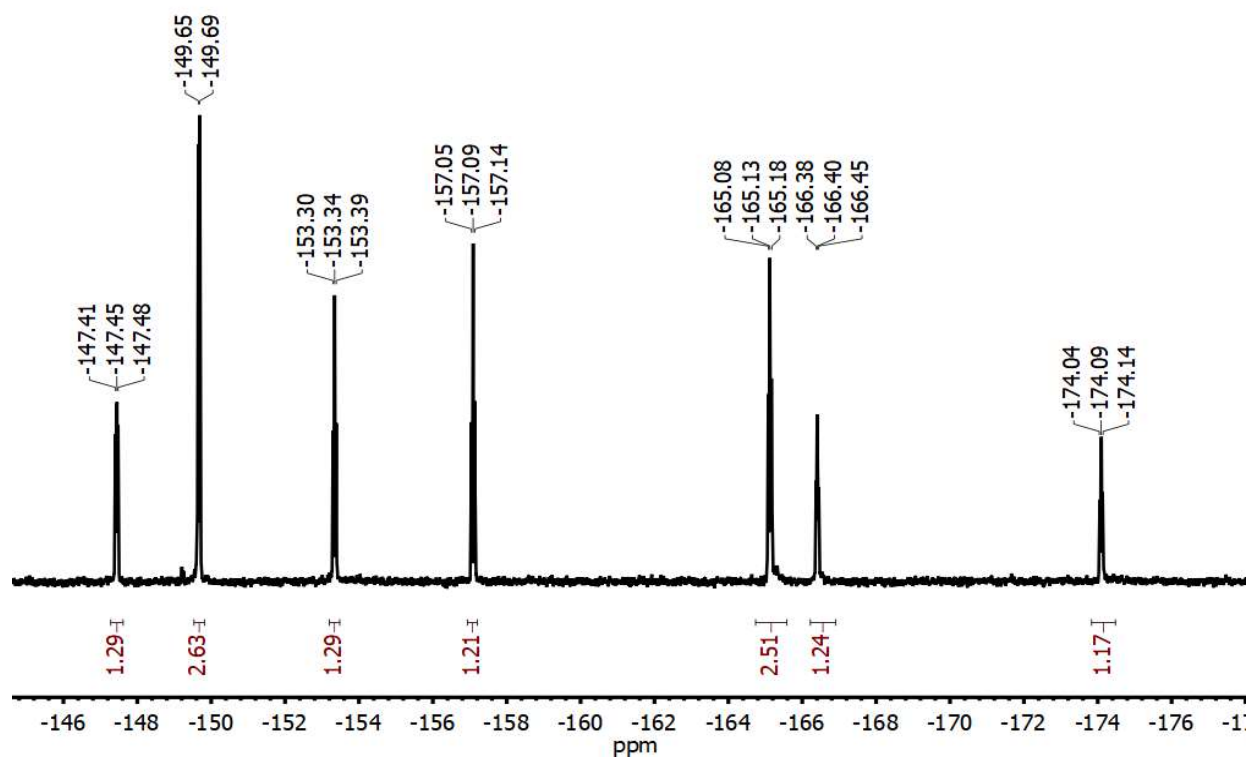


Figure 2A - 8. $^{19}\text{F}\{^1\text{H}\}$ NMR in C_6D_6 of reaction to form **1**, showing appearance of fluorosilicates at -79 ppm.

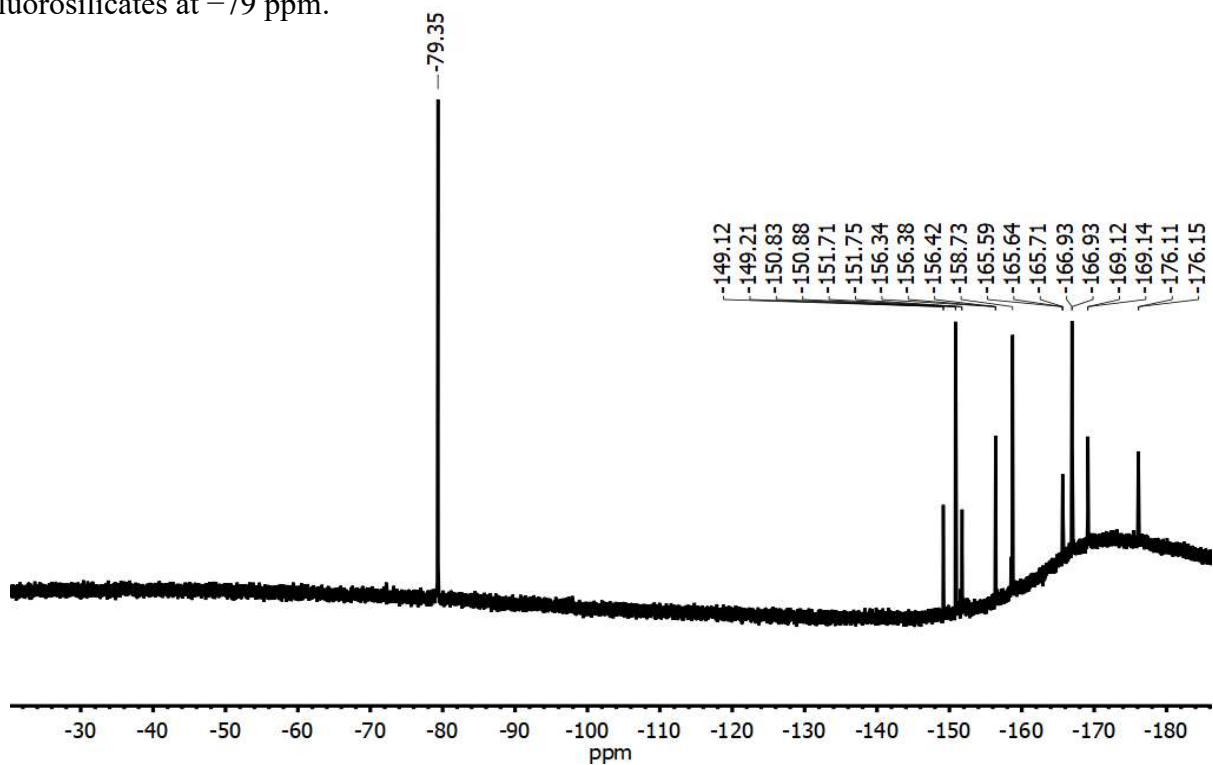


Figure 2A - 9. ^1H NMR of $t\text{BuTolDHP}\cdot 2\text{HCl}$ in CDCl_3 .

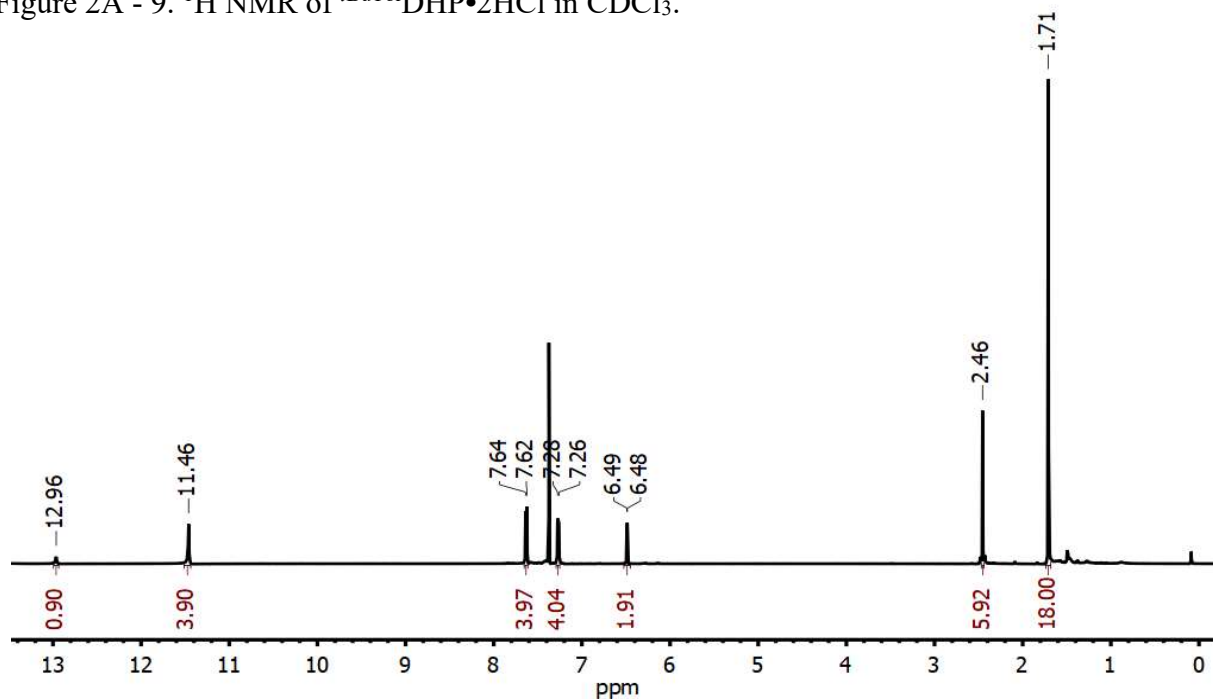


Figure 2A - 10. ^1H NMR of $t\text{Bu,TolDHP}\cdot 2\text{HCl}$ in CDCl_3 .

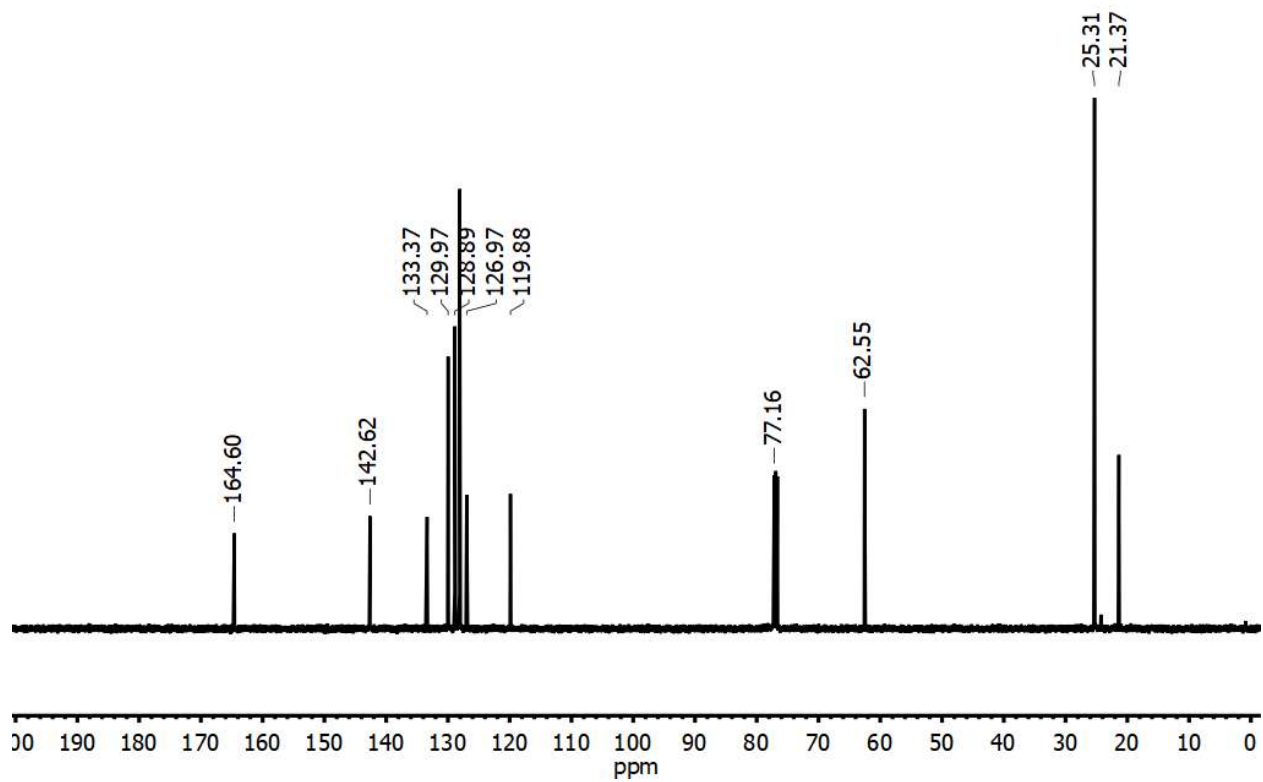


Figure 2A - 12. ^1H NMR of ($t^{\text{Bu,Tol}}$ DHP)Ni (**2**) in C_6D_6 .

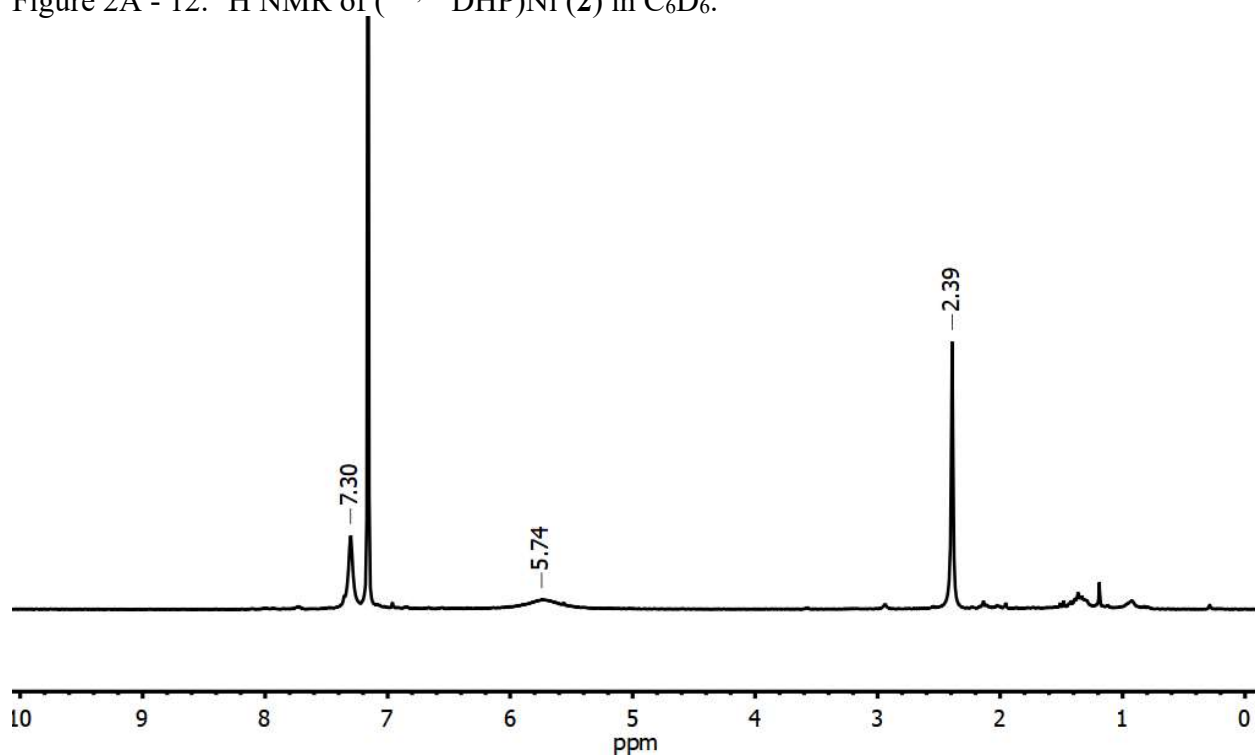


Figure 2A - 11. ^1H NMR of ($t^{\text{Bu,Tol}}$ DHP)NiOTf in C_6D_6 .

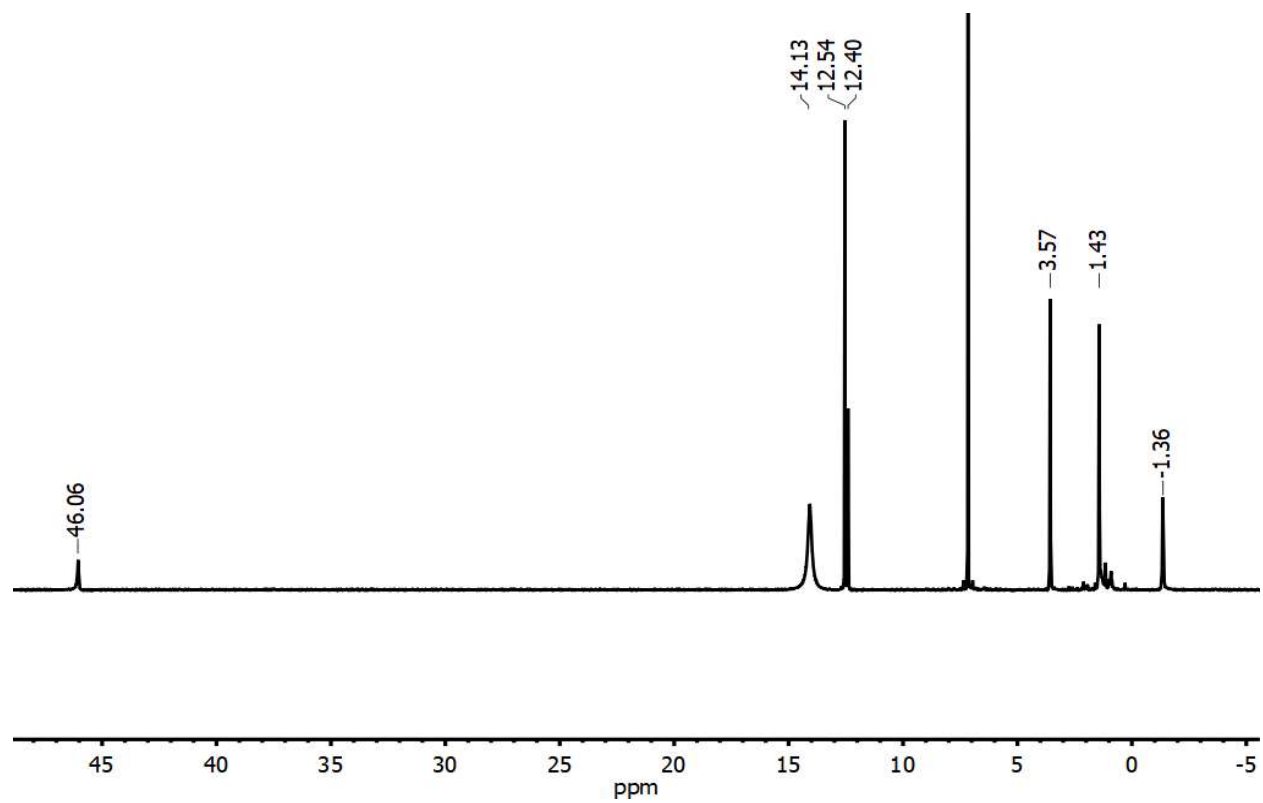


Figure 2A - 13. $^{19}\text{F}\{^1\text{H}\}$ NMR of $(^{t\text{Bu,Tol}}\text{DHP})\text{NiOTf}$ in C_6D_6 .

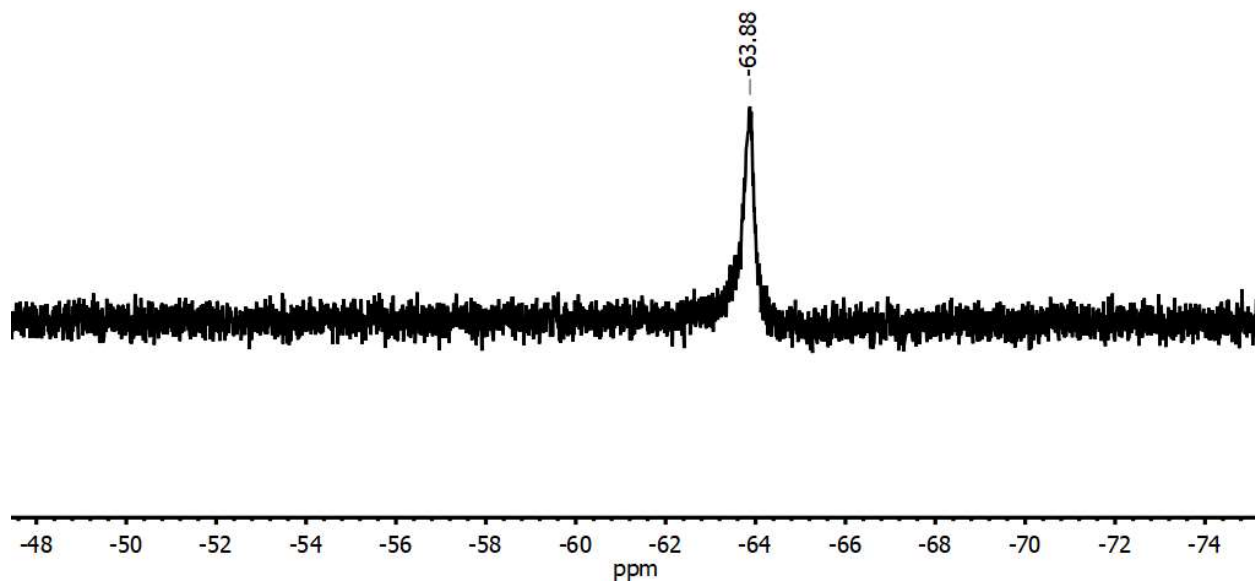


Figure 2A - 14. ^1H NMR of $(^{t\text{Bu,Tol}}\text{DHPH}_2)\text{NiCl}$ in C_6D_6 .

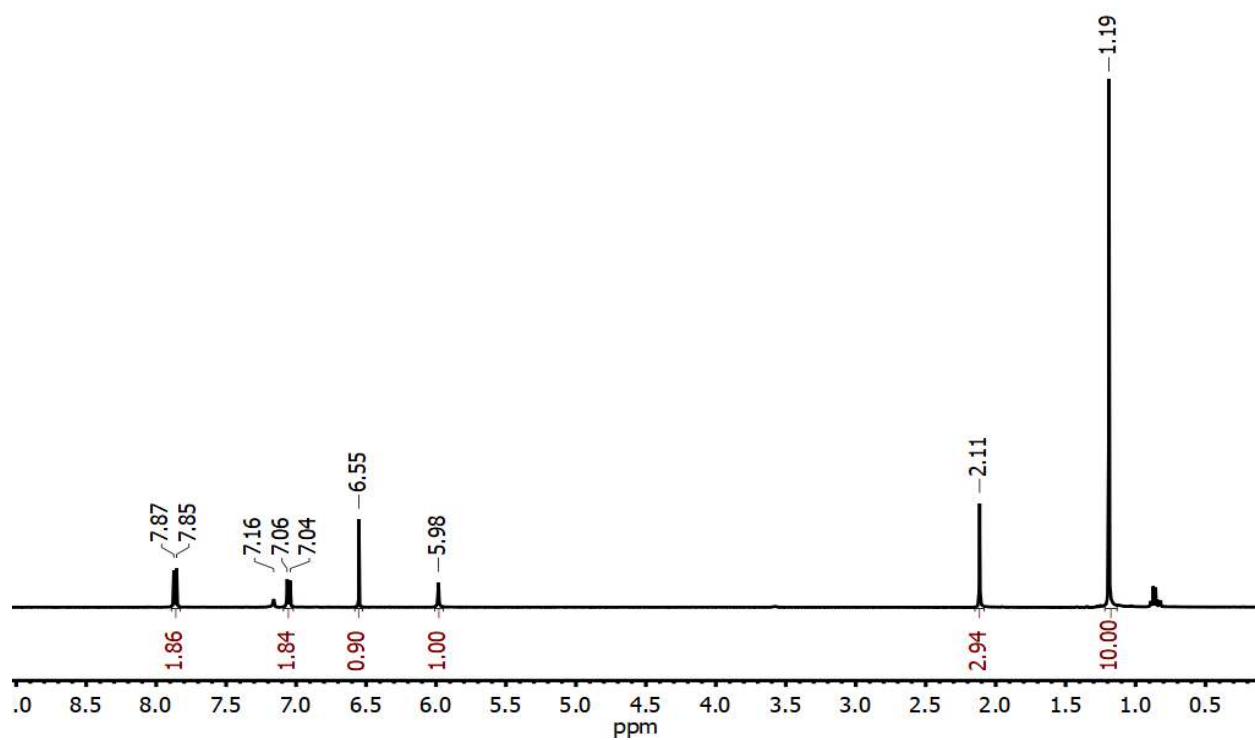


Figure 2A - 15. $^{13}\text{C}\{^1\text{H}\}$ NMR of $(^{\text{tBu,Tol}}\text{DHPH}_2)\text{NiCl}$ (**5**) in C_6D_6 .

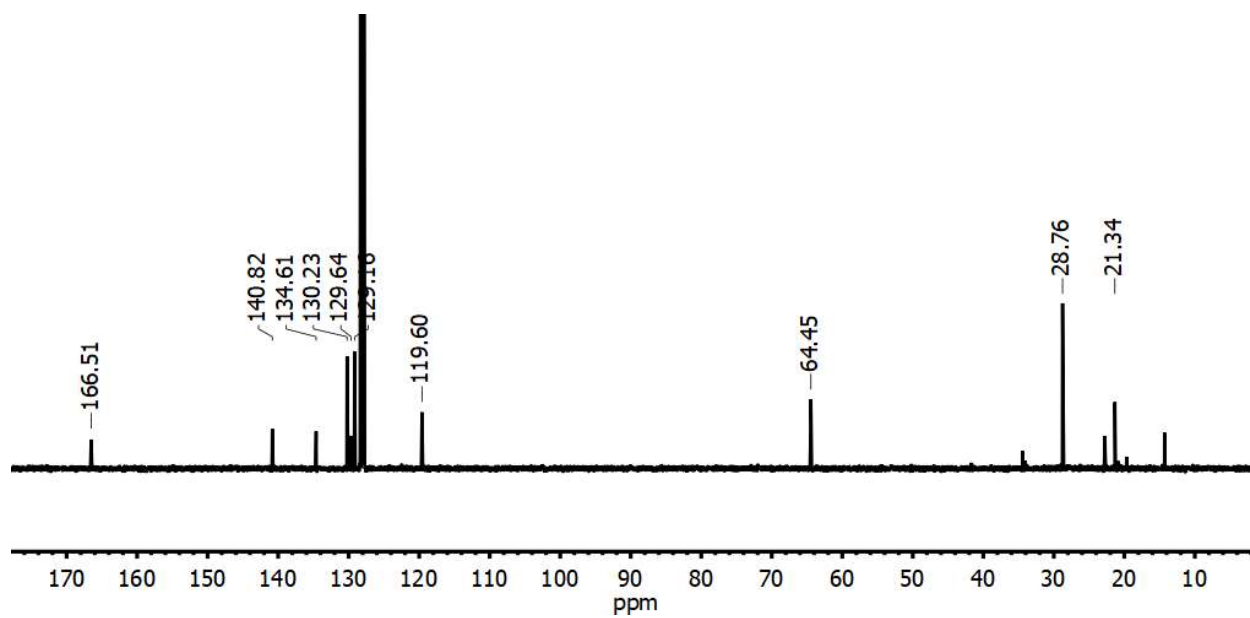


Figure 2A - 16. ^1H NMR of $[(^{\text{tBu,Tol}}\text{DHPH}_2)\text{Ni}]\text{OTf}$ (**6**) in C_6D_6 .

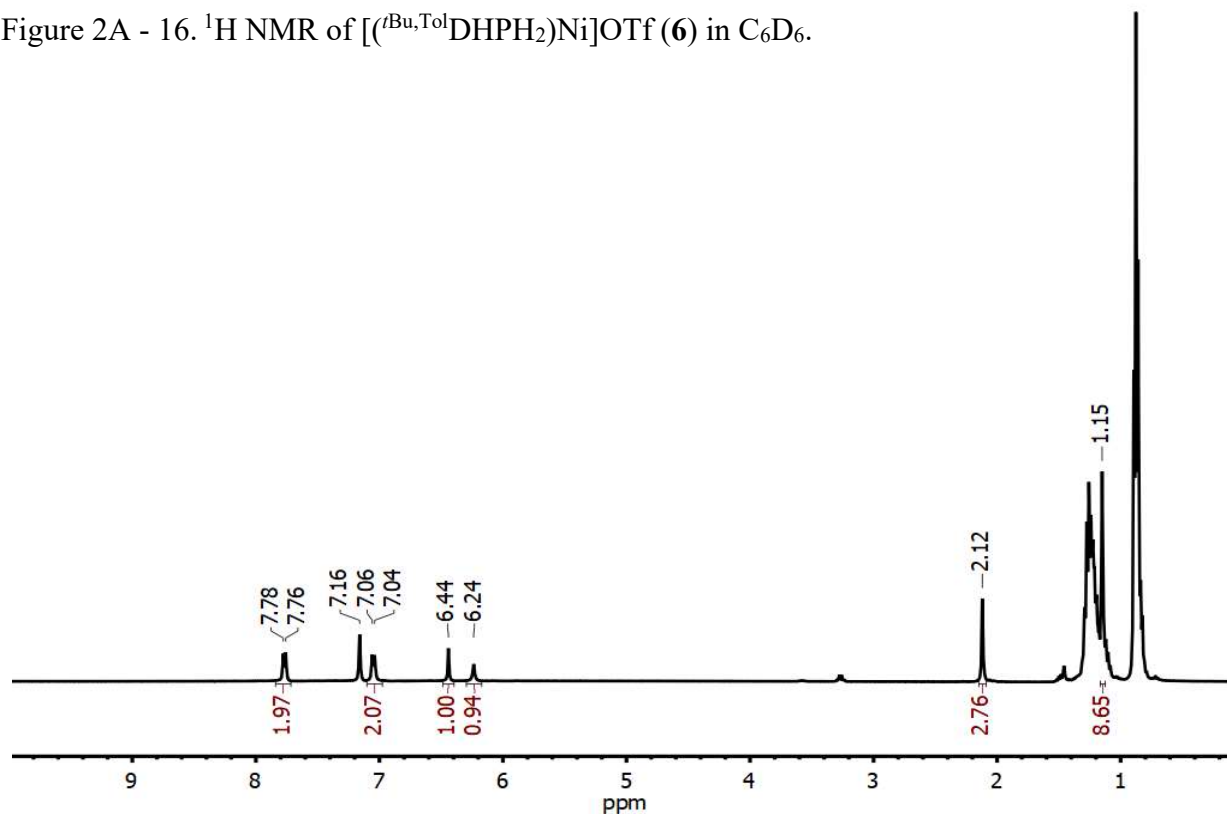
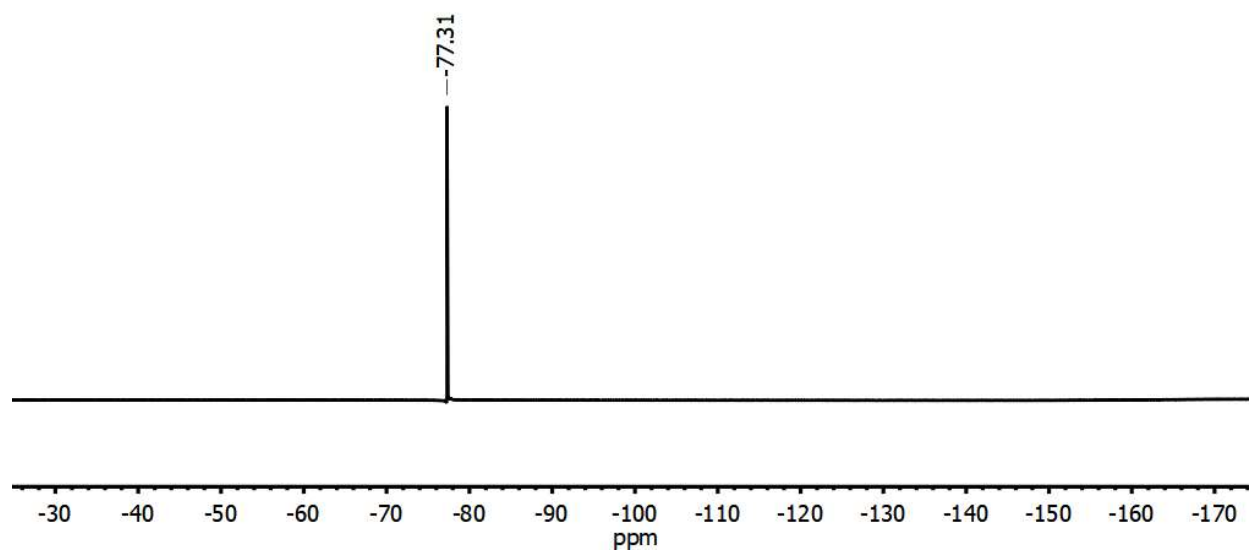


Figure 2A - 17. $^{19}\text{F}\{^1\text{H}\}$ NMR of $[(^t\text{Bu,Tol})\text{DHPH}_2]\text{Ni}]\text{OTf}$ (**6**) in C_6D_6 .



EPR Spectra

Figure 2A - 18. X-band EPR of 1 mM **2** in toluene/petroleum ether at 15 K, MW frequency = 9.628 GHz, MW power = 2.0 mW. Simulation parameters: $g_{x,y,z} = 2.24, 2.12, 2.12$, HStrain = 400, 275, 275 Hz.

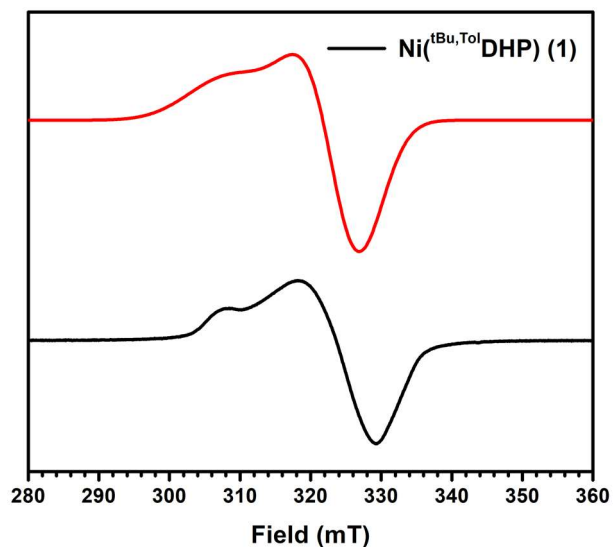


Figure 2A - 19. X-band EPR of 1 mM **2** in frozen THF at 15 K. MW power = 2 mW, MW freq = 9.630 GHz.

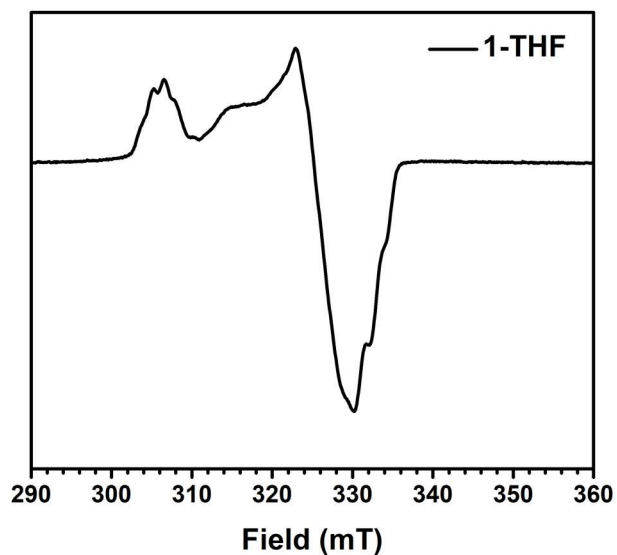


Figure 2A - 20. X-Band EPR of 10 mM **4** in THF at 15 K, MW frequency = 9.631 GHz, MW power = 0.06 mW. Simulation parameters: $g_{x,y,z} = 2.23, 2.10, 2.07$. HStrain = 125, 70, 130 Hz. *S = $\frac{1}{2}$ impurity.

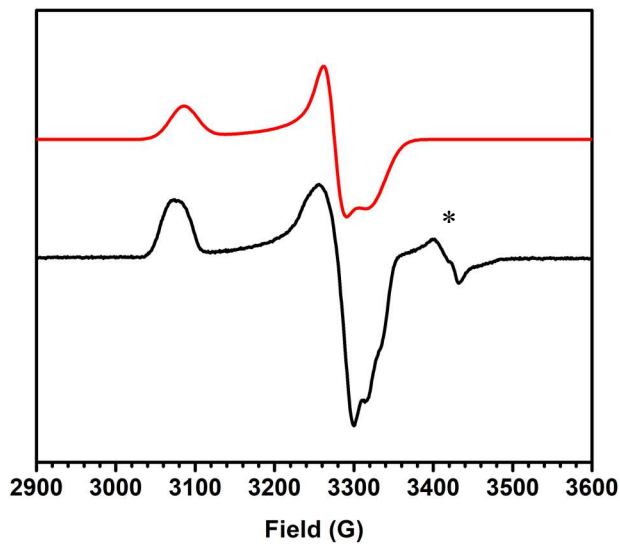


Figure 2A - 21. X-Band EPR of 1 mM **4** in benzene at 15 K. MW frequency = 9.629 GHz, MW power = 2.0 mW. Simulation parameters: $g_{x,y,z} = 2.23, 2.10, 2.07$. HStrain = 125, 70, 130 Hz. *S = $\frac{1}{2}$ impurity.

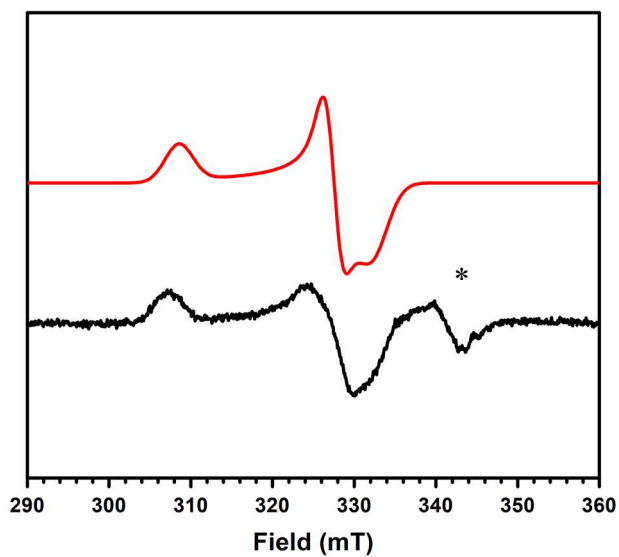


Figure 2A - 23. Comparison of the EPR of **2** and **4** in benzene. Intensities have been normalized for comparison.

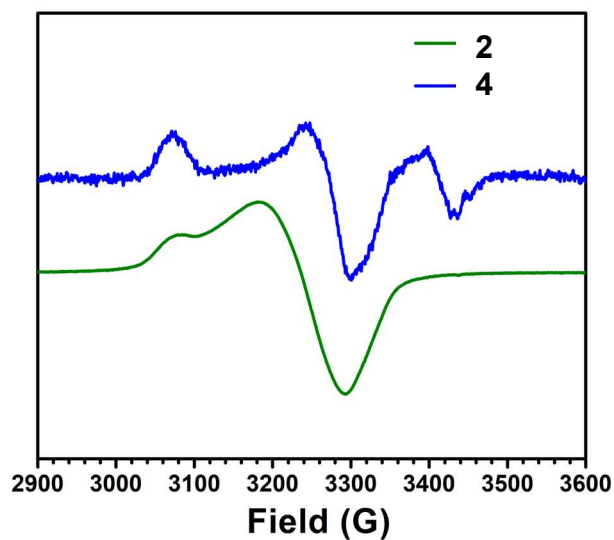


Figure 2A - 22. Comparison of the EPR of **2** and **4** in THF. Intensities have been normalized for comparison.

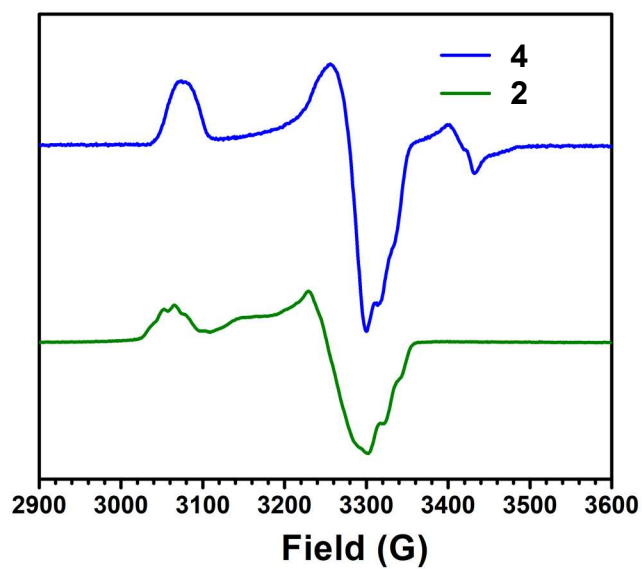
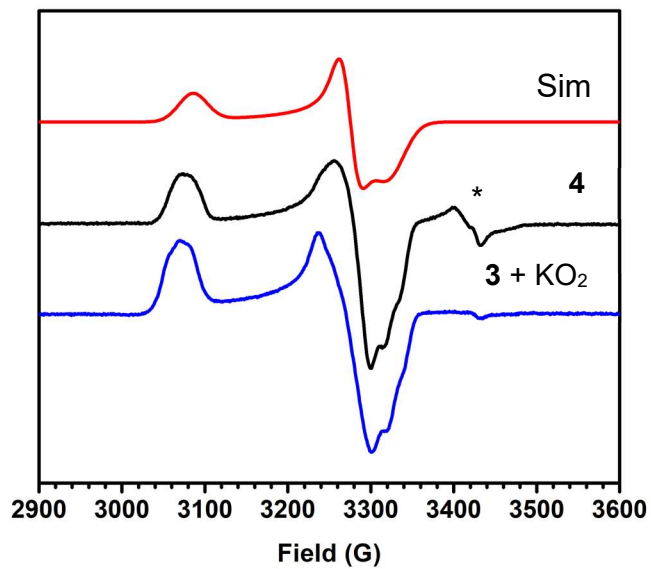


Figure 2A - 24. X-band EPR of **3** in frozen THF compared with EPR of **3** generated from **2** at 15 K. MW power = 0.002 mW, MW freq = 9.630 GHz. *S = ½ impurity. Intensities have been normalized for comparison.



UV-visible Spectra

Figure 2A - 25. UV-visible spectrum of 0.5 mM **2** in benzene at room temperature, with an inset of the low energy feature.

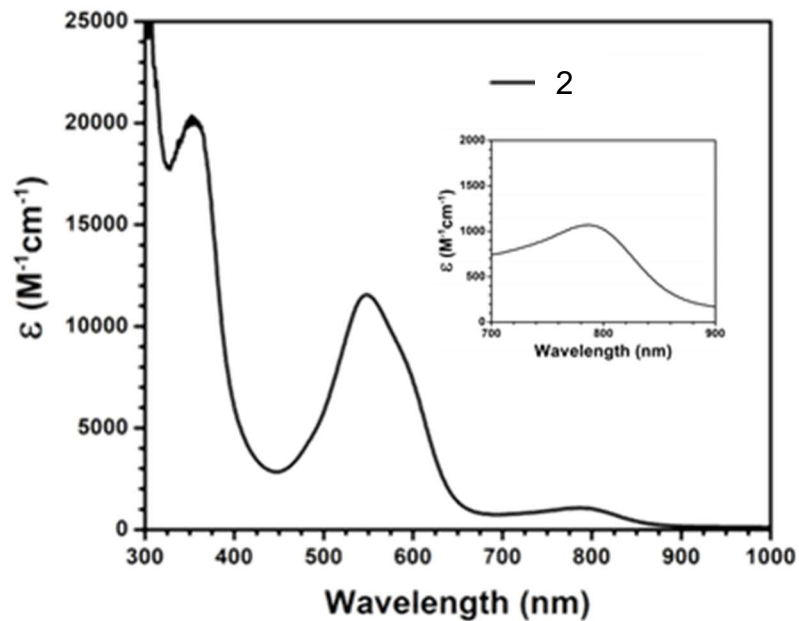


Figure 2A - 26. UV-visible spectra of 0.25 mM **3** in THF at room temperature.

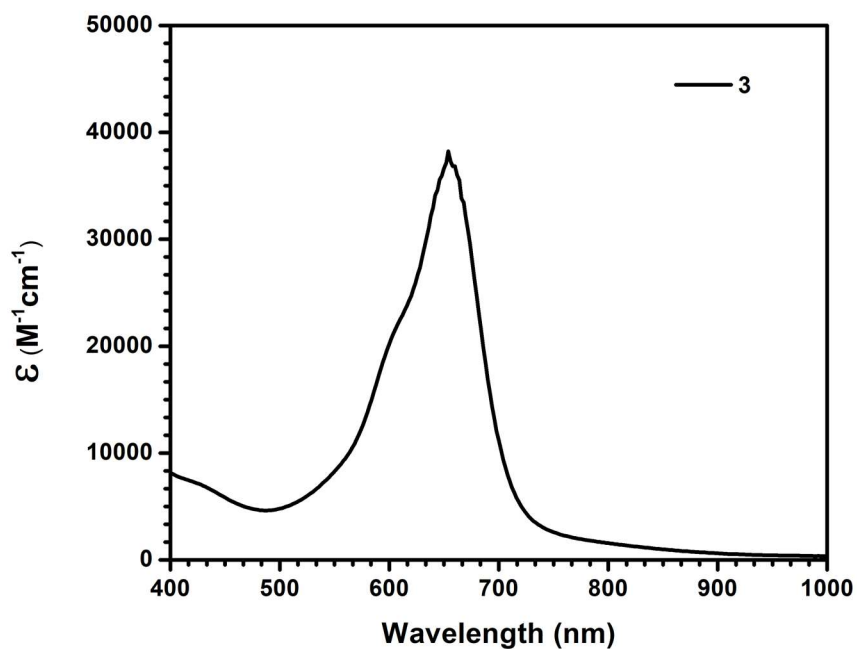


Figure 2A - 28. UV-visible spectrum **3** (1 mM in Ni) in benzene at room temperature.

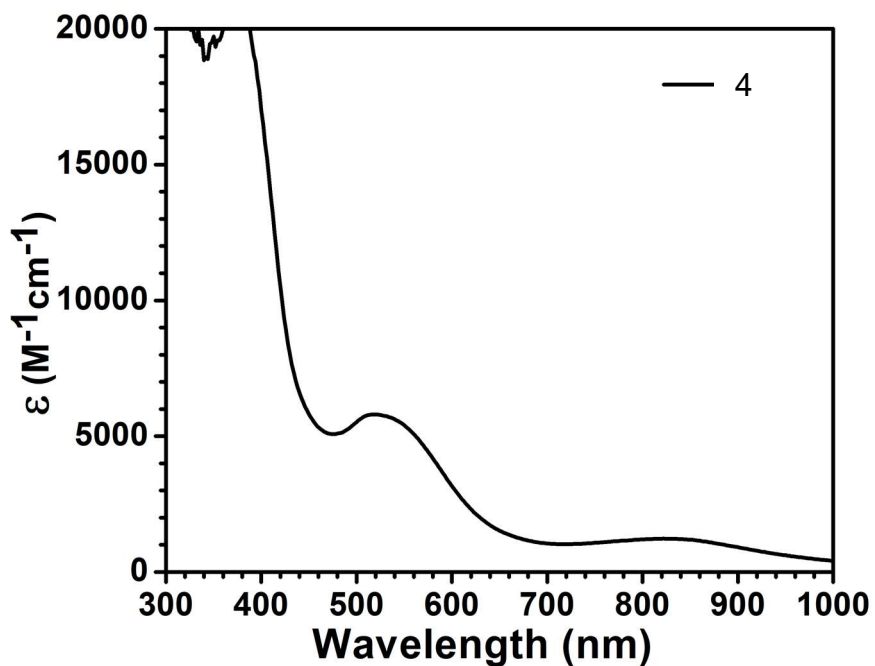


Figure 2A - 27. UV-visible spectra of conversion of 0.5 mM **2** to **4** in benzene after injection of an excess of ambient air, with scans taken every 52 seconds. The feature at 400 nm is cut off due to overloading the detector.

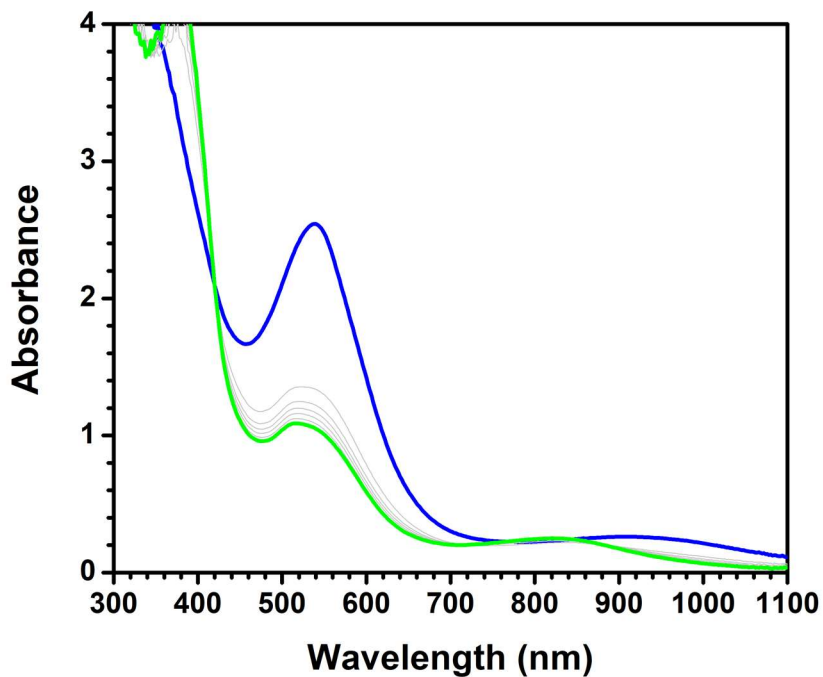


Figure 2A - 29. Conversion of 0.5 mM **1** to **3** by exposure of **1** to O₂ at room temperature in THF, with an inset showing isosbestic conversion at the low energy feature, with scans every 15 seconds. Note that the low energy feature exhibits some solvent dependence.

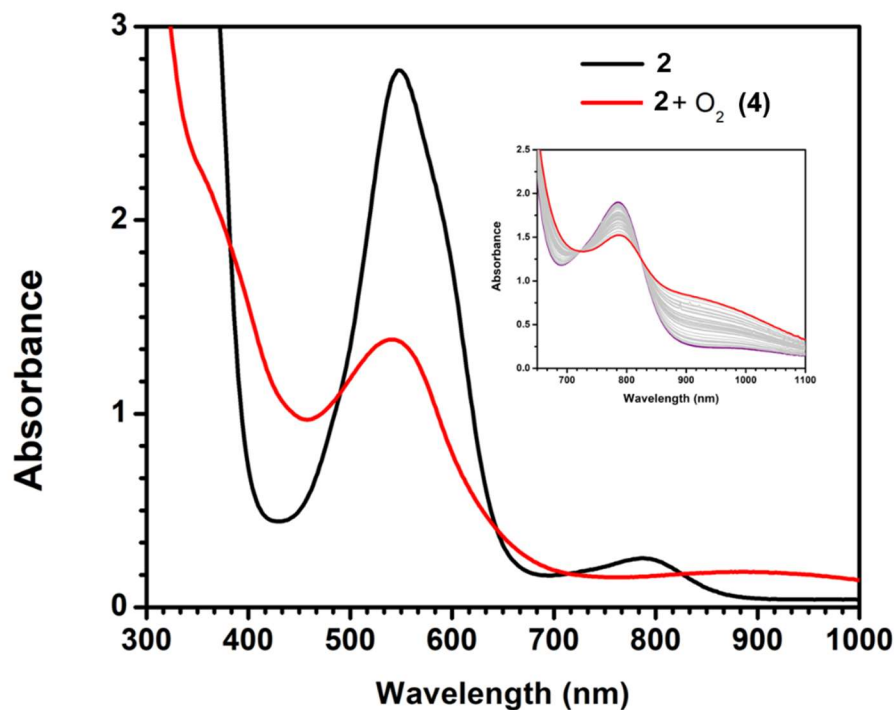


Figure 2A - 30. Conversion of **3** (0.5 mM in Ni) to **2** by addition of AgOTf at room temperature in THF.

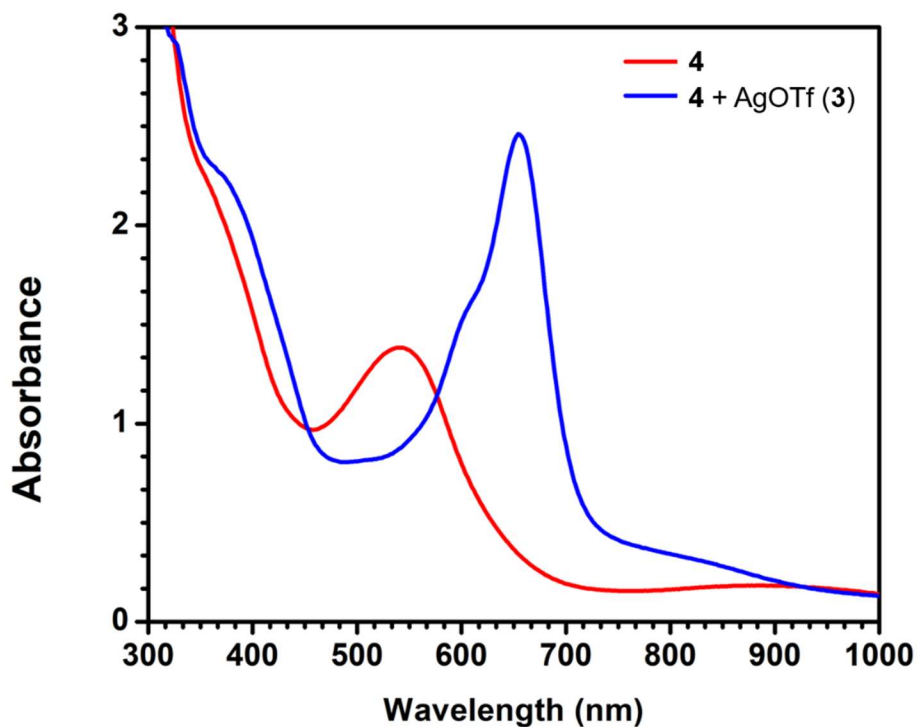


Figure 2A - 32. Conversion of 0.1 mM **3** to **4** with KO_2 at room temperature in THF. *The feature at 650 nm is residual **2** that has not fully reacted.

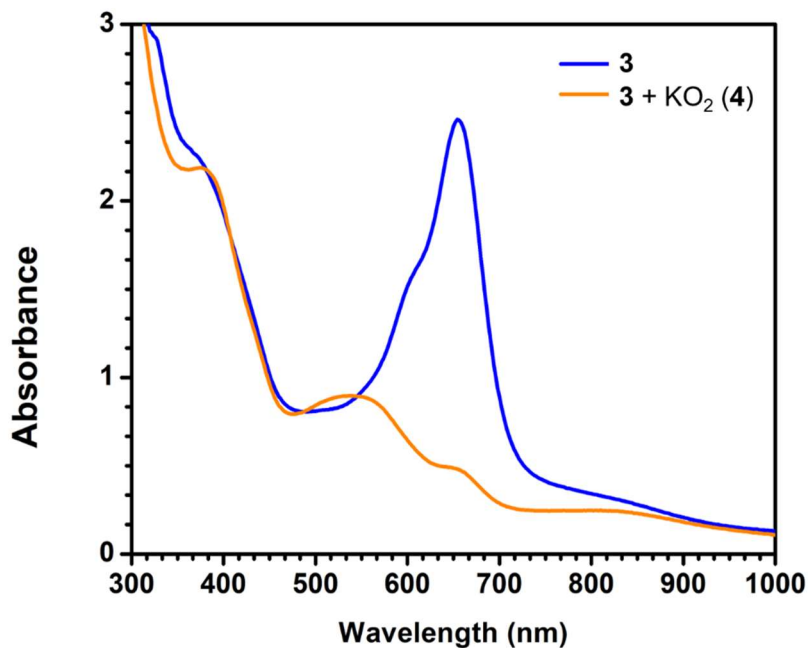


Figure 2A - 31. UV-Vis comparison of **4** generated via two different methods. The presence of residual **2** is responsible for the extra features in the orange spectrum.

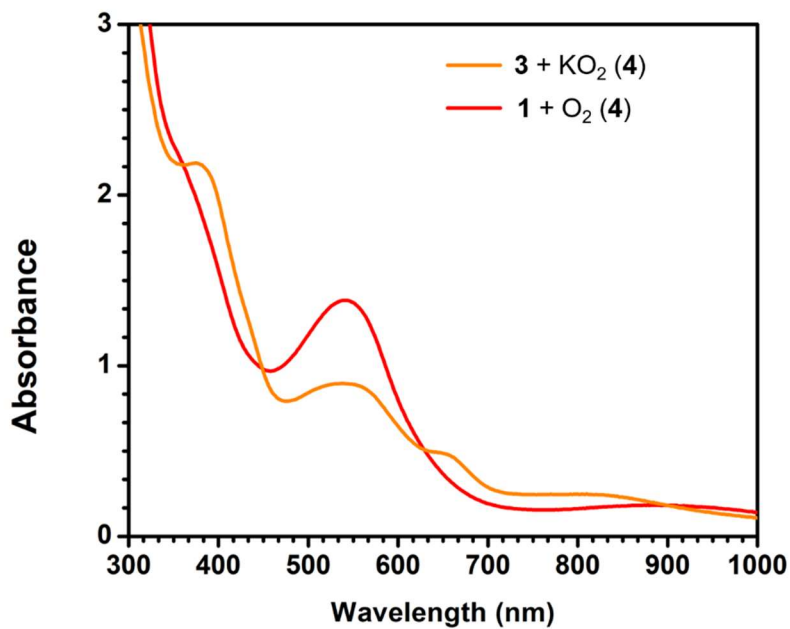


Figure 2A - 33. UV-visible spectra of the reaction of **4** with benzyl alcohol (30 eq) in benzene at 50 °C in C₆H₆ with scans every 2 minutes.

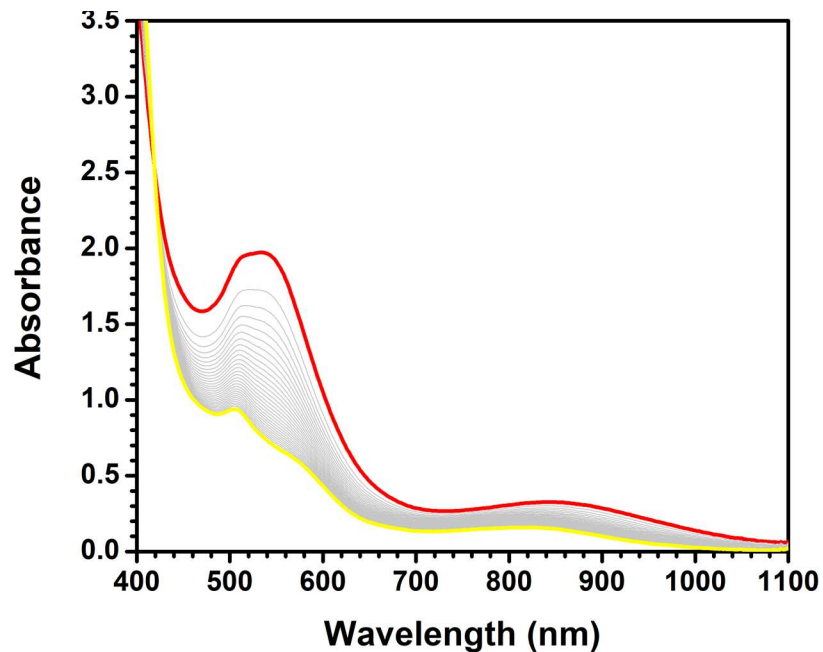


Figure 2A - 34. Linear fit to 1/[**4**] (left) and non-linear fit of absorbance vs. time (right). Rate constant from non-linear fit: -0.0011 sec^{-1} . The data was fit to $A = A_{\text{inf}} + (A_0 - A_{\text{inf}})/(1+kT)$. R^2 of Fit: 0.99.

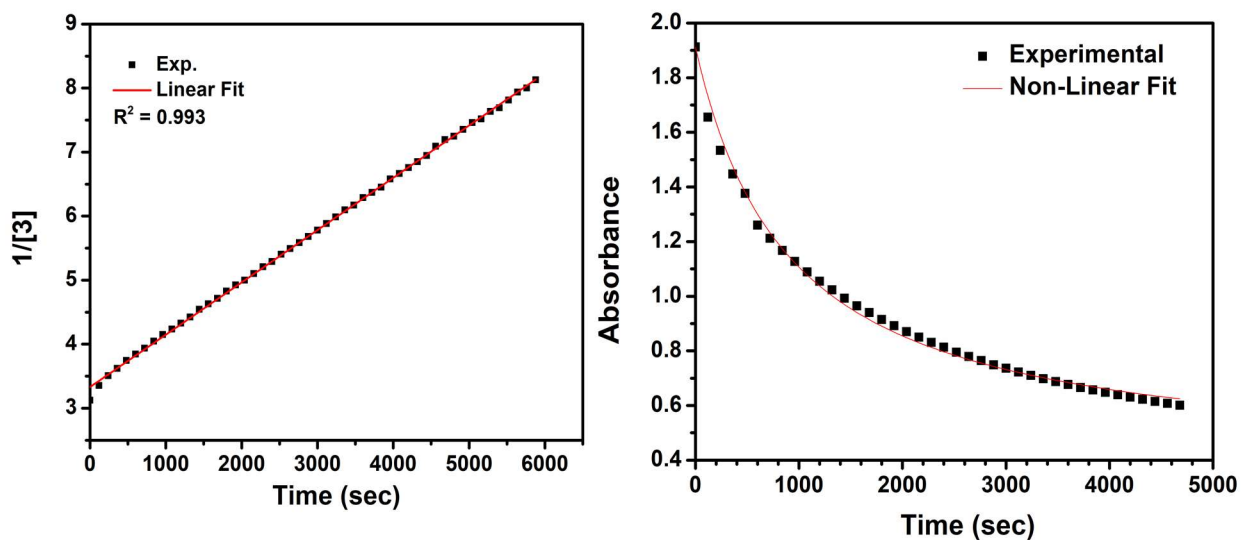


Figure 2A - 35. UV-visible spectra of decay of **4** at 50° C in benzene, with scans taken every 2 minutes.

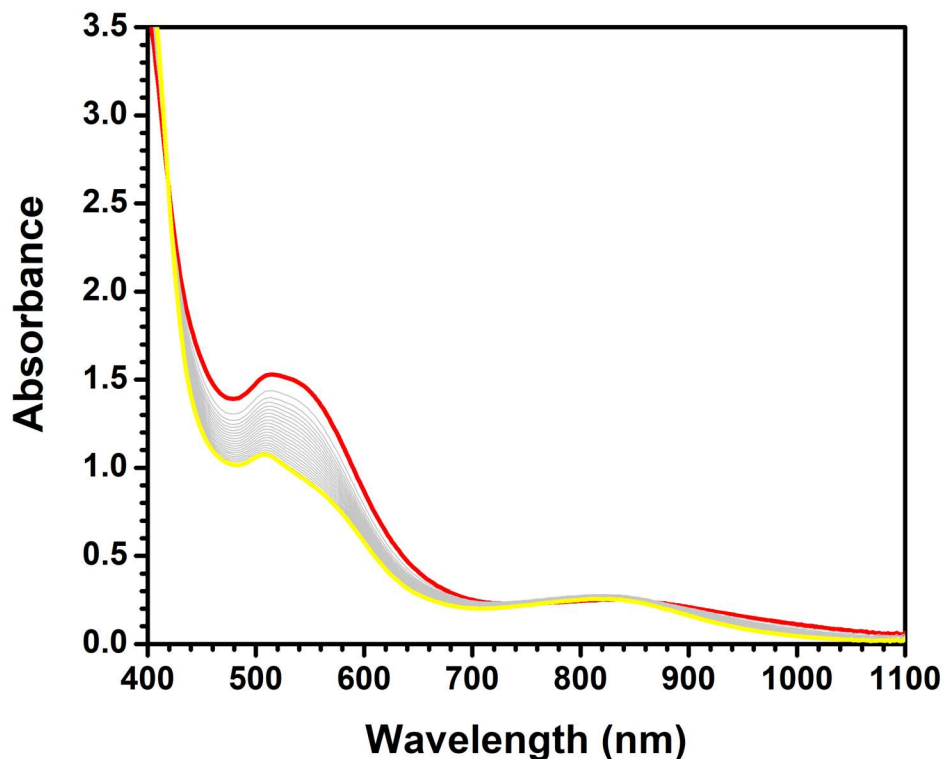
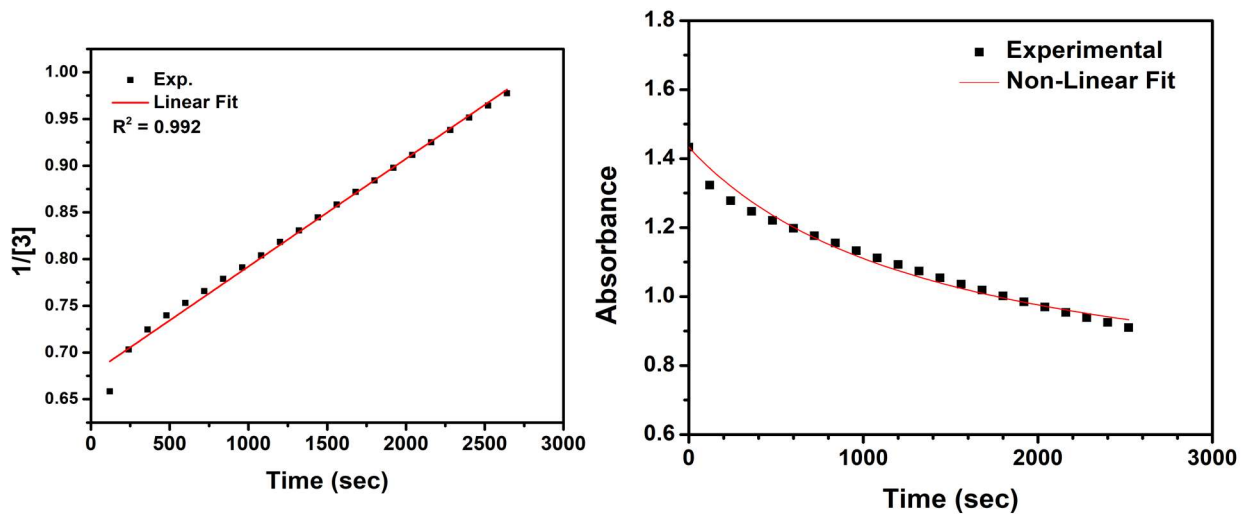


Figure 2A - 36. Linear fit to $1/[4]$ (left) and non-linear fit of absorbance vs. time (right) Rate constant from non-linear fit: 6.9×10^{-4} . The data was fit to $A = A_{inf} + (A_0 - A_{inf})/(1+kT)$. R^2 of fit: 0.97.



Electrochemistry

Figure 2A - 37. Cyclic voltammogram of 1 mM **2** in 0.1 M NBu₄PF₆ in THF with 100 mV/sec scan rate.

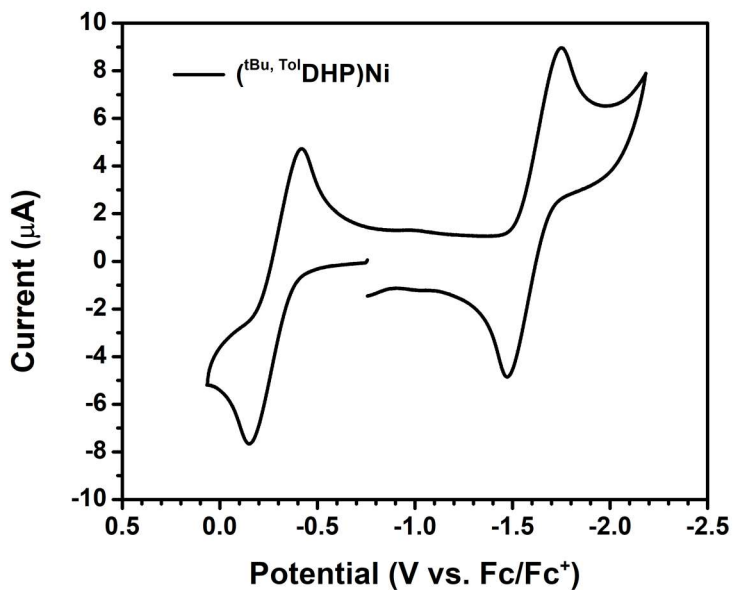


Figure 2A - 38. Cyclic voltammogram of 1 mM **4** in 0.1 M NBu₄PF₆ in THF with 100 mV/sec scan rate.

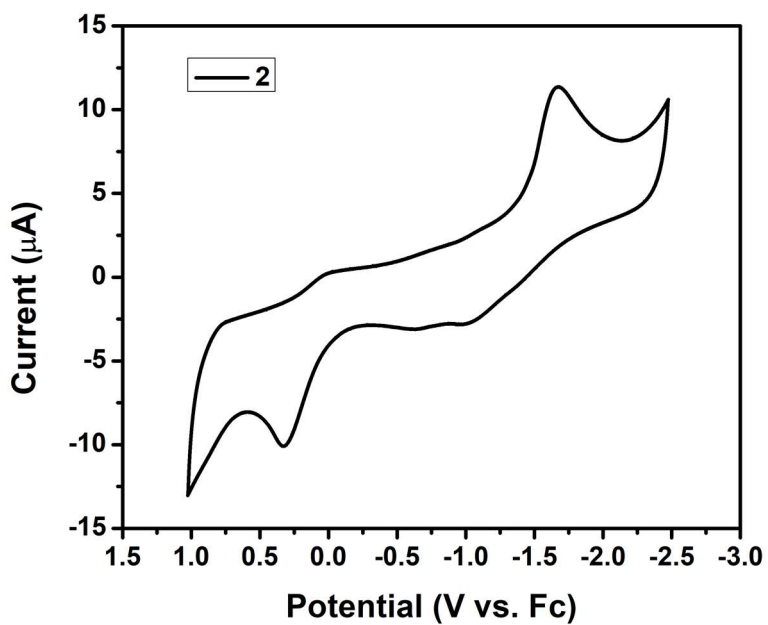
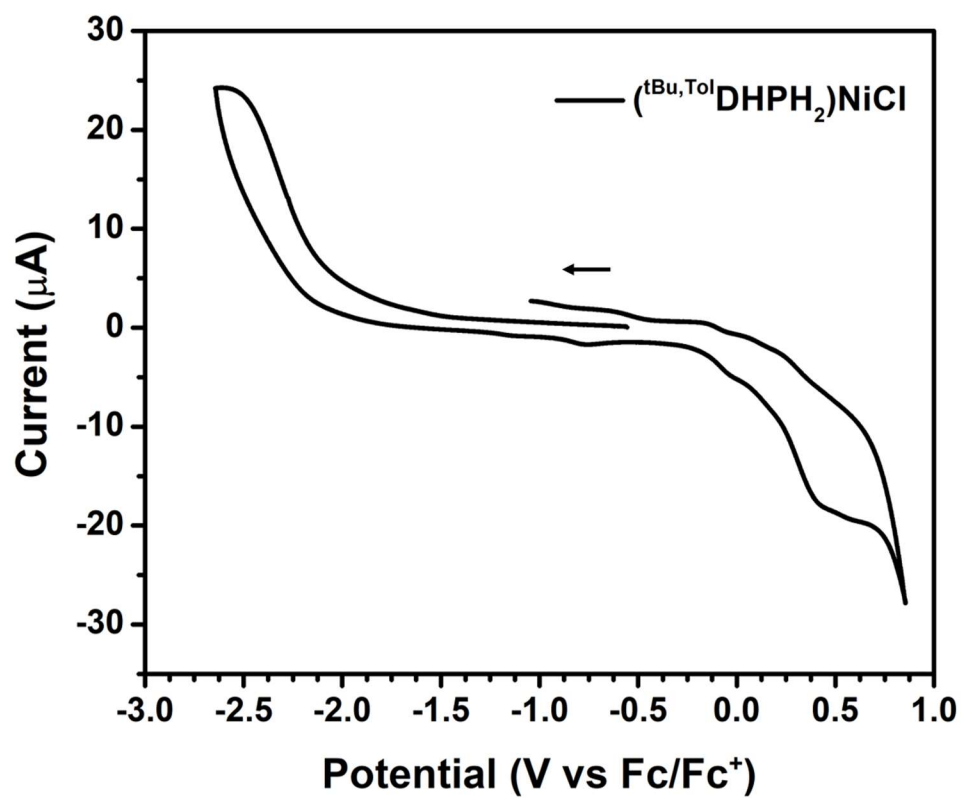


Figure 2A - 39. CV of 2 mM **5** in THF with 0.1 M NBu₄PF₆ electrolyte, and 100 mV/sec scan rate.



IR Spectra

Figure 2A - 40. IR (THF solution) of ^{Tol,Ph}DHP

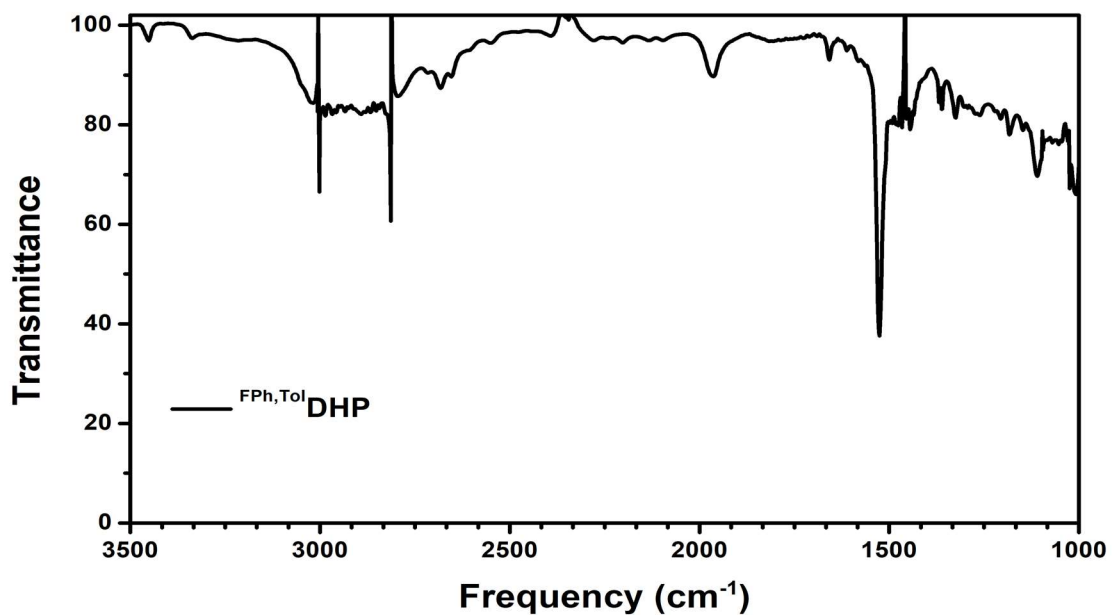


Figure 2A - 41. IR (nujol mull) of ^{tBu,Tol}DHP•2HCl. The intense features from 3000-2500 and 1500 cm⁻¹ are from the nujol.

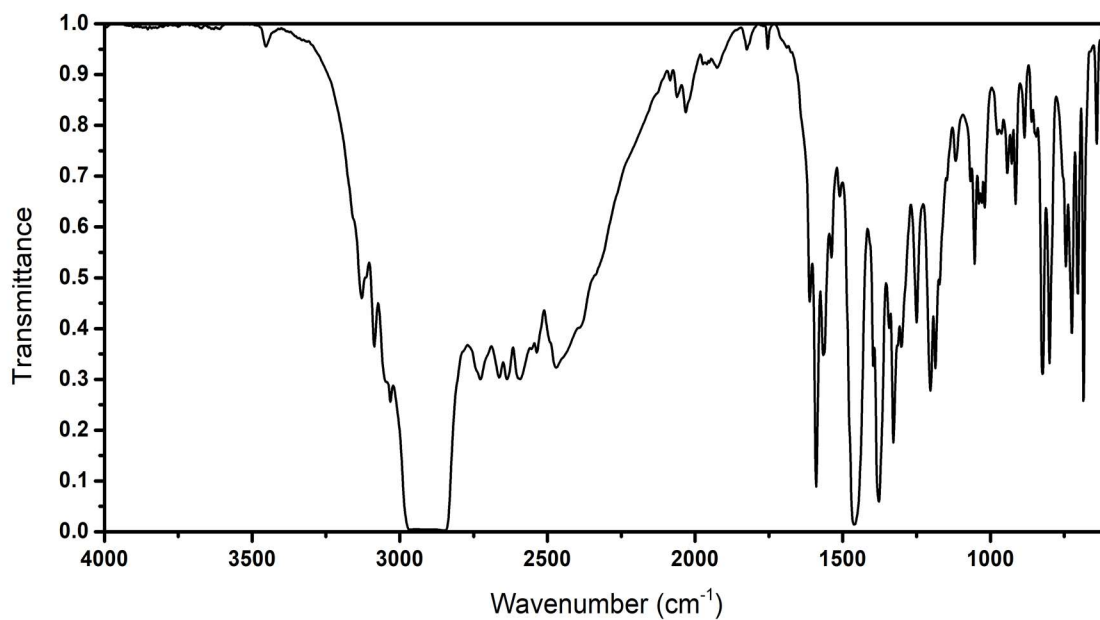


Figure 2A - 42. IR (KBr Pellet) of **2**. The broad feature at 3500 cm^{-1} is due to residual water in the KBr.

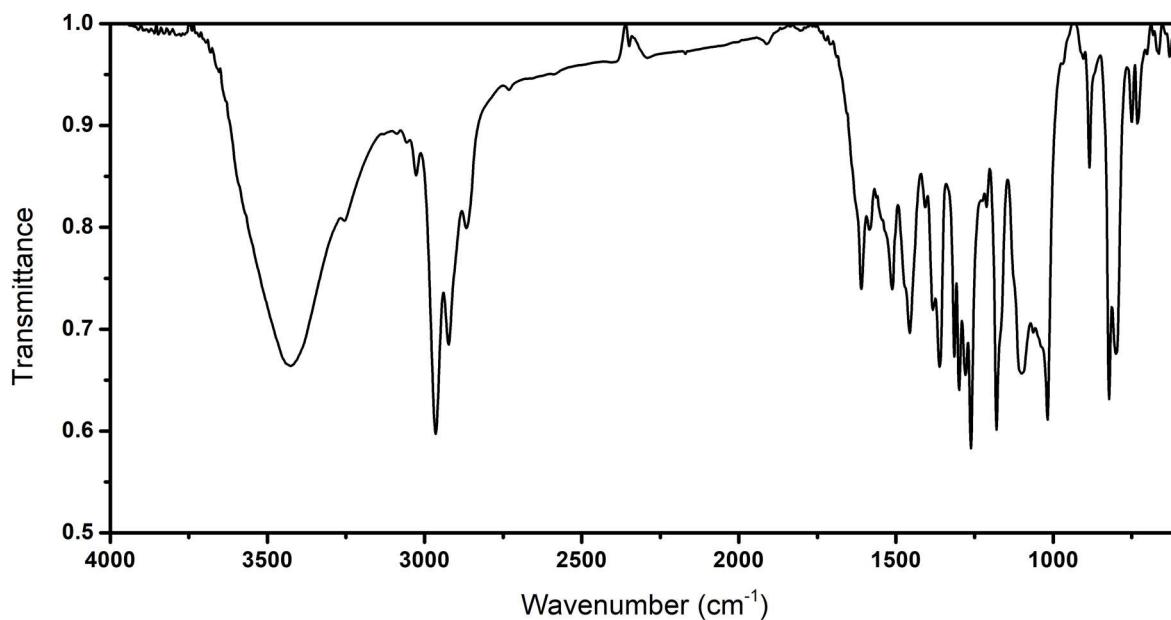


Figure 2A - 43. IR (KBr Pellet) of **3**. The broad feature at 3500 cm^{-1} is due to residual water in the KBr.

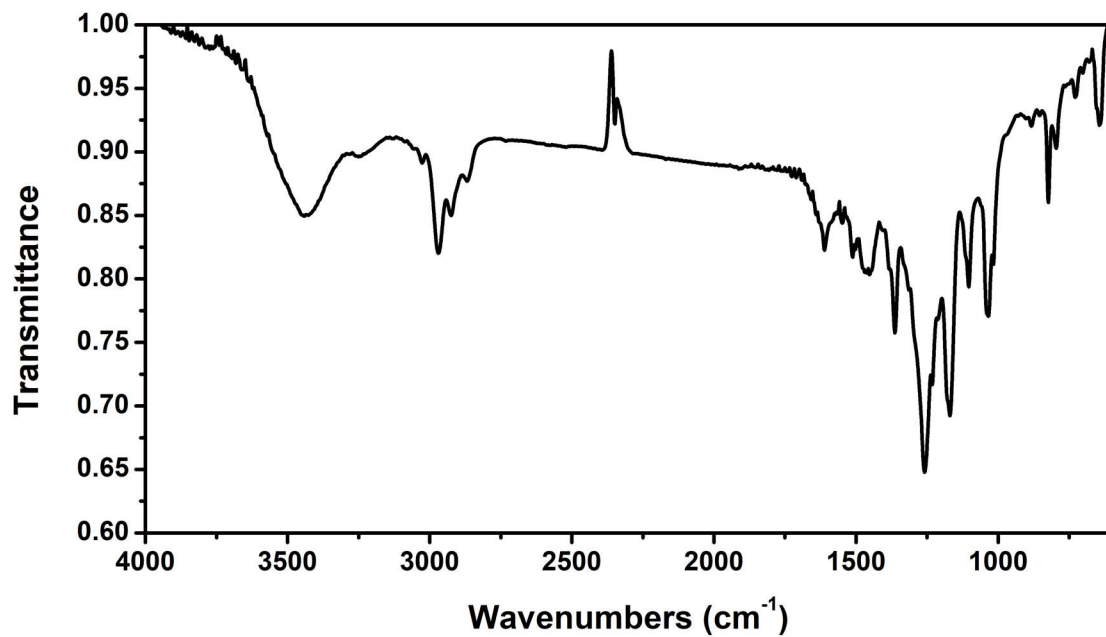


Figure 2A - 44. IR (KBr Pellet) of **4**. The broad feature at 3500 cm^{-1} is due to residual water in the KBr.

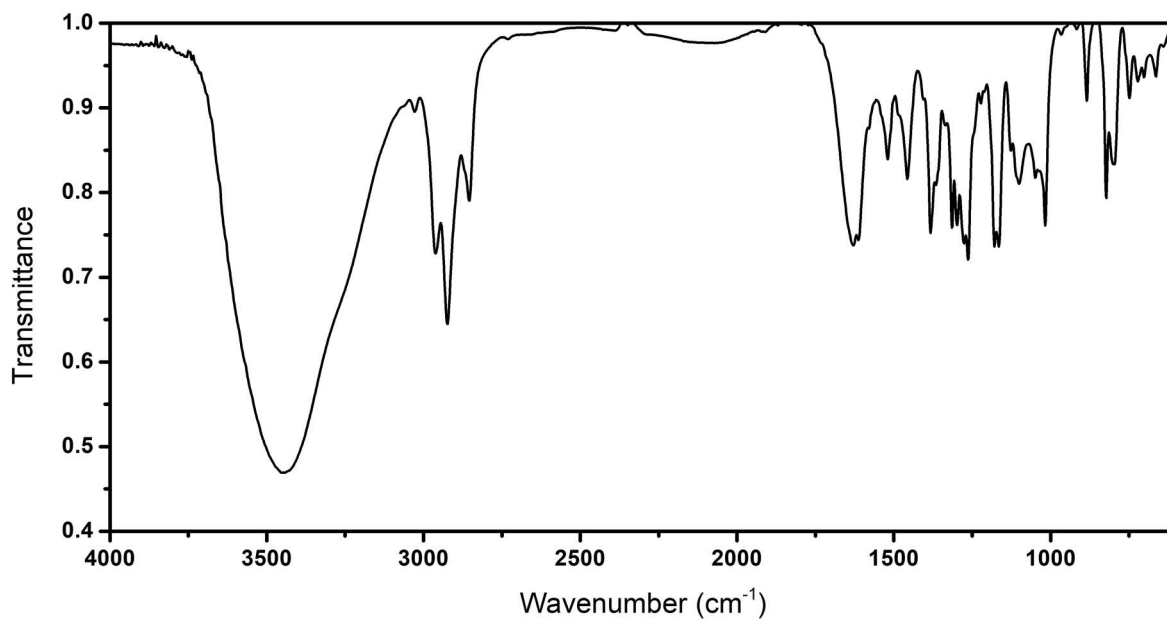


Figure 2A - 45. IR (THF solution) of $(^t\text{Bu,Tol})\text{DHPH}_2\text{NiCl}$ (**5**).

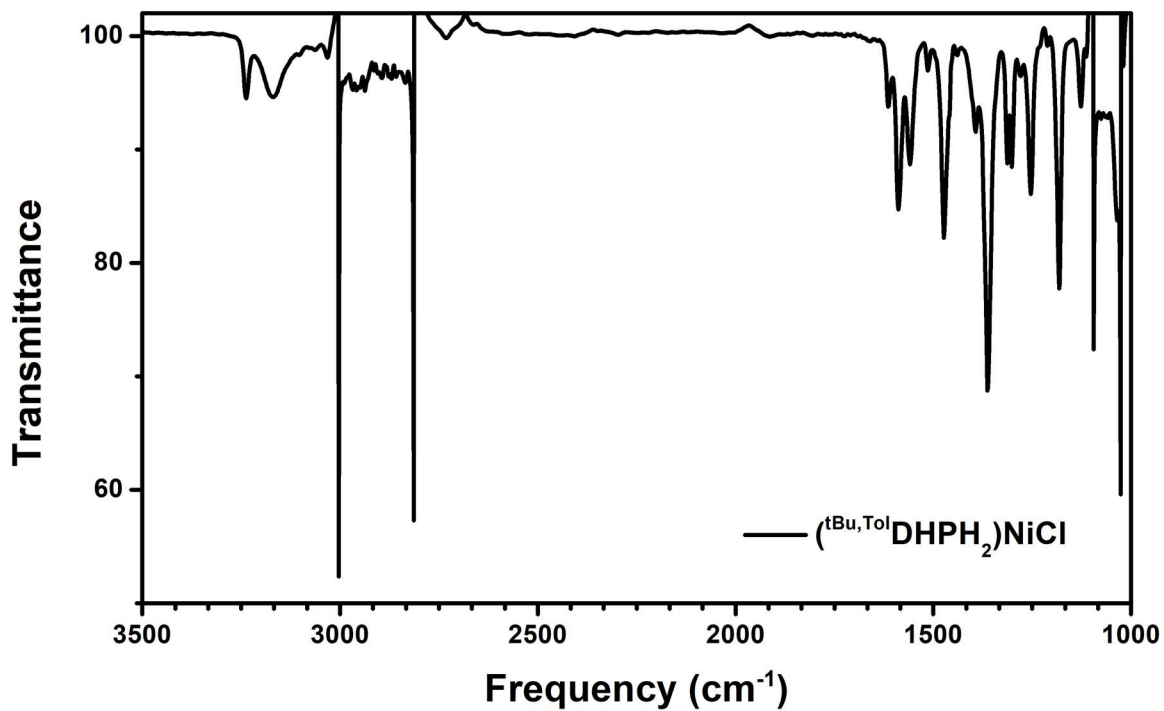


Figure 2A - 46. IR (KBr Pellet) of **4** with ^{16}O (dotted line) overlaid with the IR (KBr Pellet) of **4** with ^{18}O (solid line). Predicted shift: 64 cm^{-1} Actual: 60 cm^{-1} .

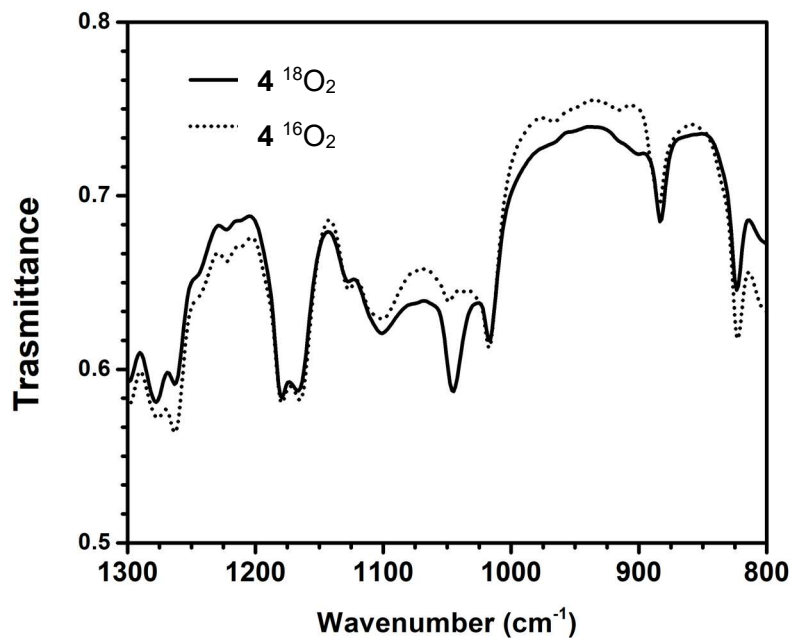
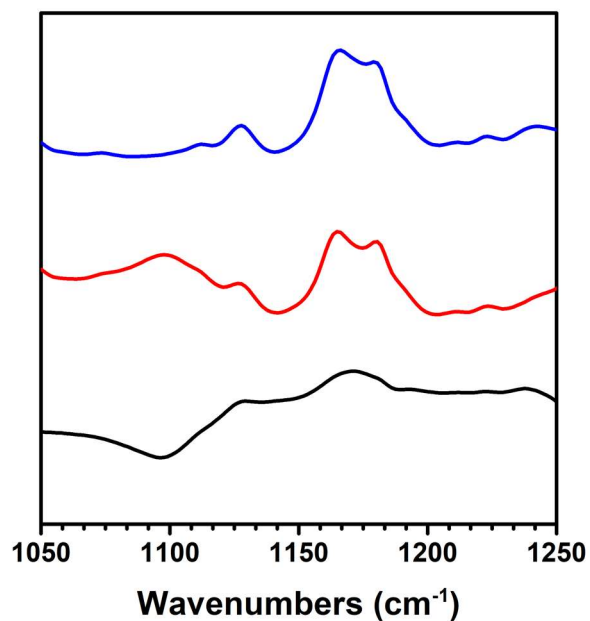


Figure 2A - 47. IR (C_6H_6 solution) of **4**, with ^{16}O in blue (top), ^{18}O in red (middle), and the subtraction in black (bottom).



GC/MS

Figure 2A - 48. GC trace of oxidation of toluene with **4** showing appearance of benzaldehyde at 4.7 minutes. Inset: Calibration curve for benzaldehyde.

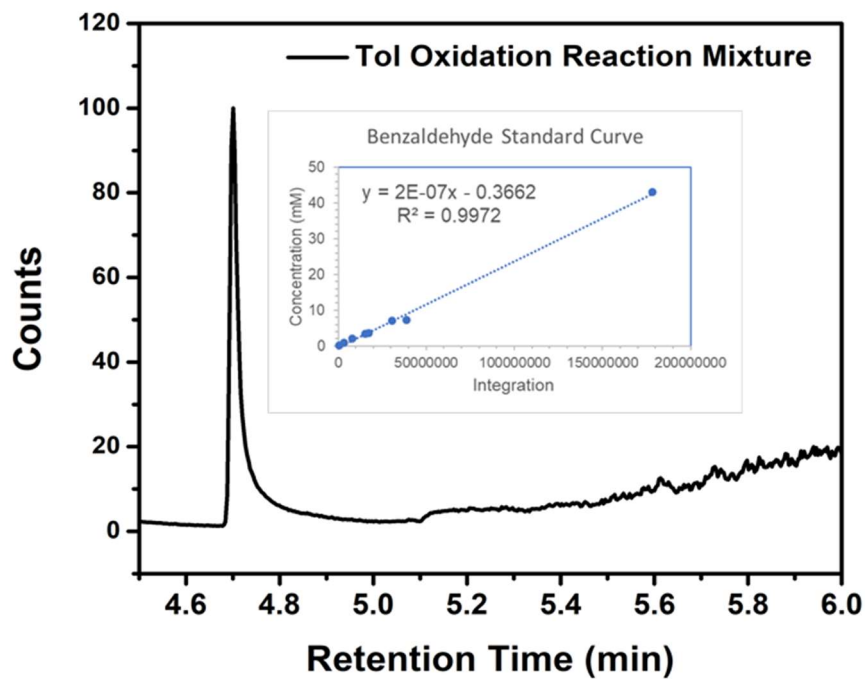


Figure 2A - 49. MS of benzaldehyde from oxidation of toluene by **4**.

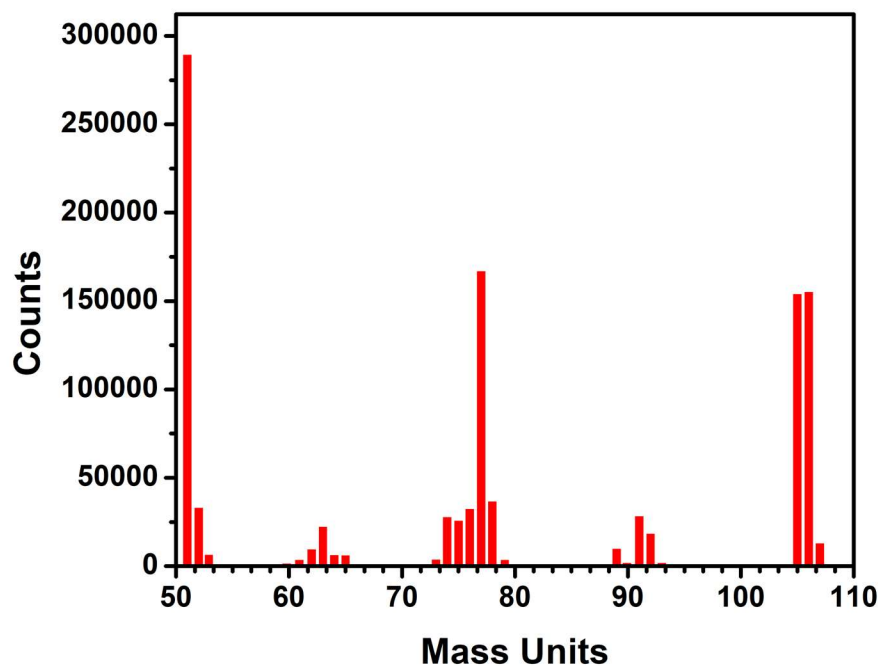


Figure 2A - 51. GC trace of reaction of 4 with toluene under $^{18}\text{O}_2$.

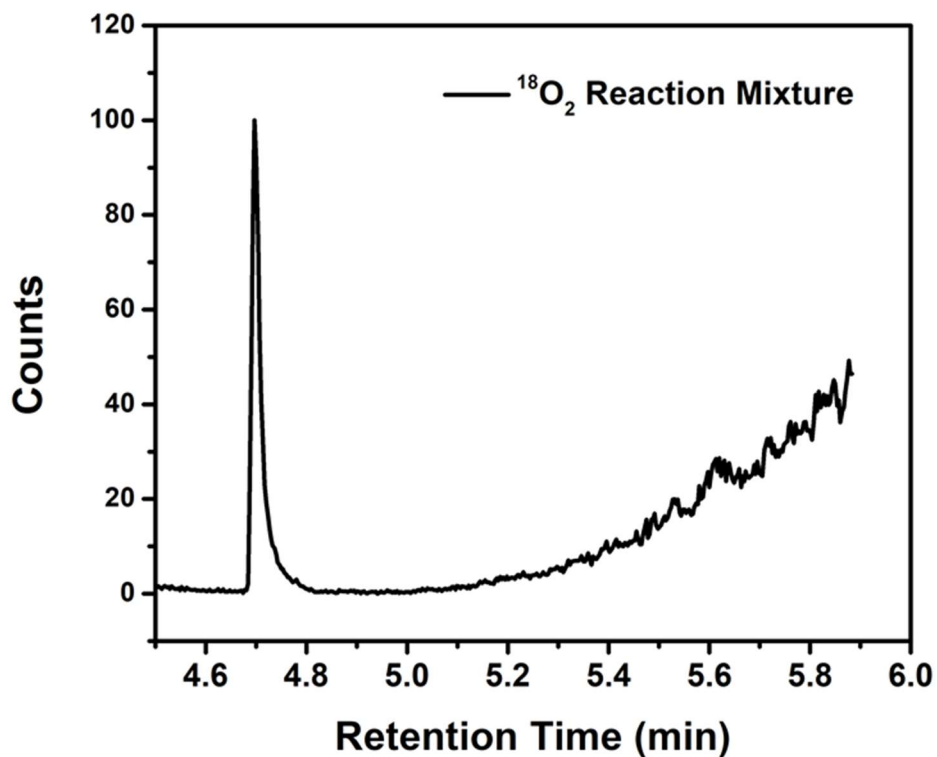


Figure 2A - 50. MS comparison between ^{16}O benzaldehyde and ^{18}O enriched benzaldehyde from toluene oxidation. Residual ^{16}O benzaldehyde is from exchange with natural abundance water in the reaction.

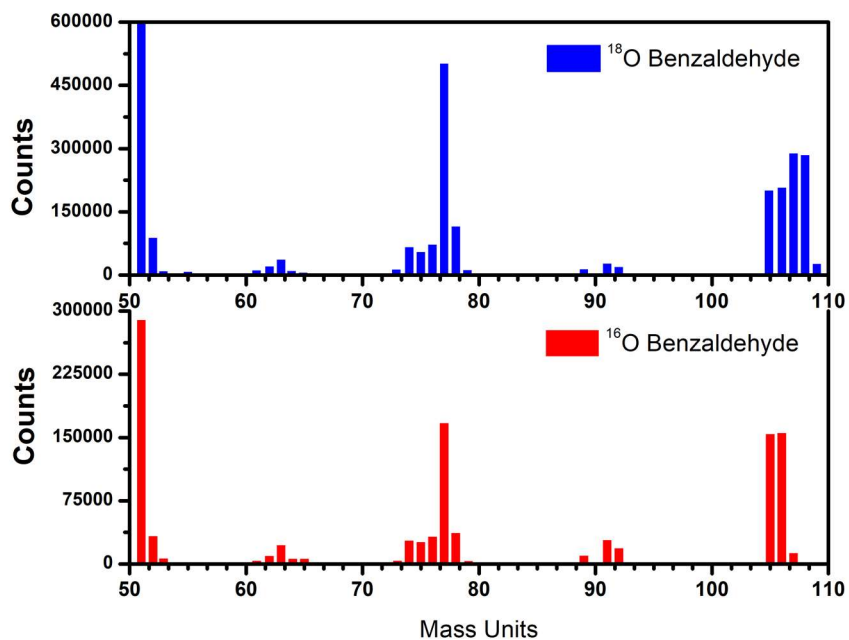
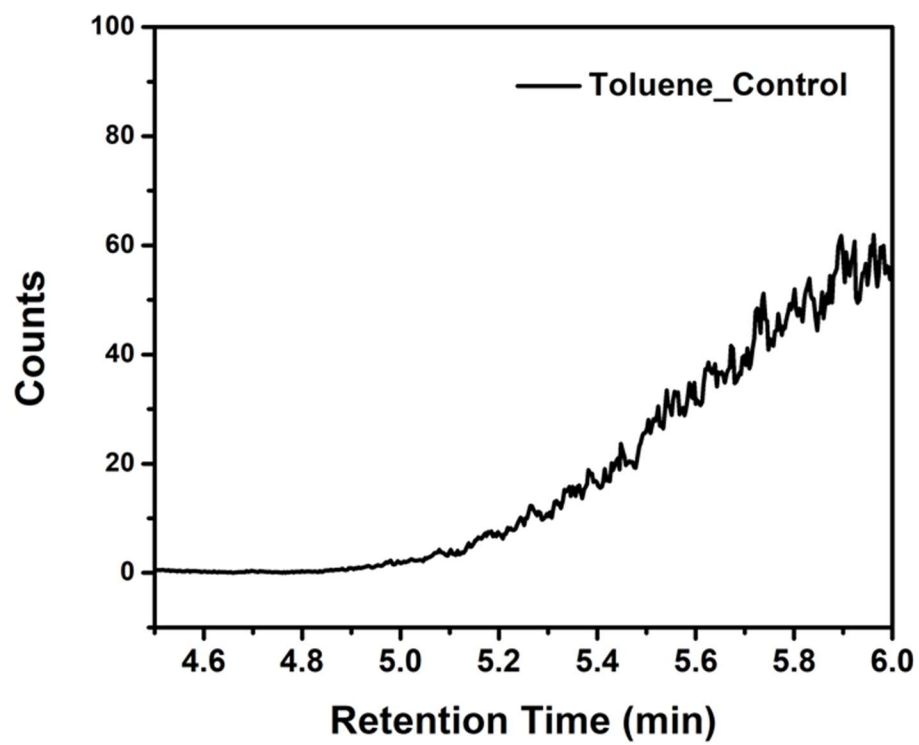


Figure 2A - 52. GC trace of the control reaction of toluene heated to 70 °C in air for 3 hours.



DFT Calculations.

General considerations: Geometry optimization calculations were performed with ORCA¹ software suite using density functional theory (DFT). Geometries were fully optimized starting from coordinates generated from a molecular model built in Avogadro. The B3P functional was used with a basis set of def2-SVP on H, def2-TZVPP on Ni, O, and N, and def2-TZVP on C atoms. The resulting structures were confirmed to be minima on the potential energy surface by frequency calculations using ORCA¹⁰. Frequency calculations were also conducted using the B3P functional and previously listed basis sets for each atom type. Final spin density plots and Mulliken spin densities were generated from these geometry optimization calculations. Single point broken symmetry calculations using flipspin were also run, but the broken symmetry calculations gave no difference in spin density so those results are not included. Time Dependent DFT (TDDFT) calculations were undertaken using the PBE0 functional and def2-TZVPP basis set on Ni and def2-TZVP on all other atoms. Furthermore, an effective core potential of SDD was used on Ni. The input file used was the previously optimized geometry for **4** that was optimized using B3P and the previous basis sets.

Figure 2A - 53. Calculated Structure of **2**.

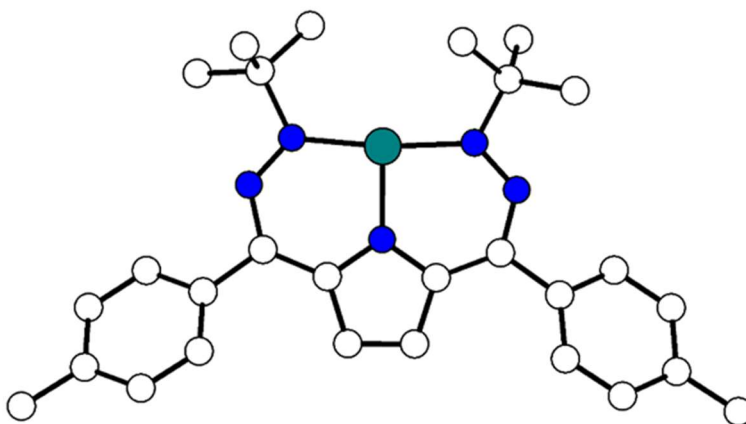


Figure 2A - 54. Spin density map of **2**.

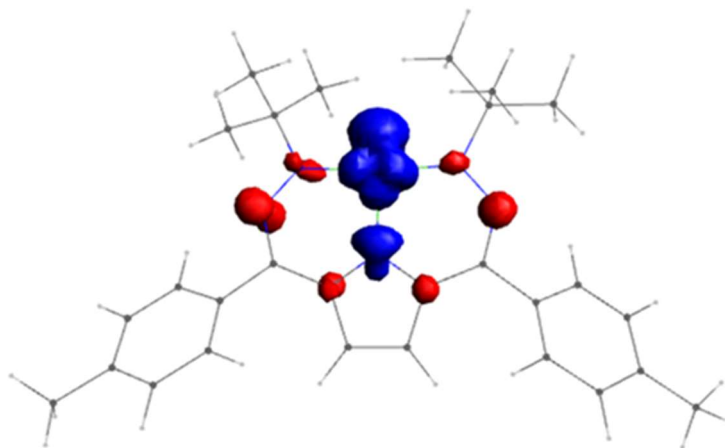


Table 2A - 1. Coordinates of calculated structure of **2**.

C	-1.13252322139551	0.76588619144505	-0.00179052748438
C	0.24115790531312	0.76816647670773	0.01003045893462
C	0.66297859626679	2.10800270297869	0.25495659691713
C	-1.56119836316437	2.10810507420334	0.21621632526716
C	-2.87305475220965	2.66017956678554	0.16024836152371
C	1.97617609057733	2.65093185743722	0.30604765476697
C	3.14879708944328	1.79129345412847	0.01223983925147
N	-3.16912326374698	3.94933733763283	0.04261126914468
N	-0.45330924857889	2.88382346278263	0.37212532216143

N	2.30219035421600	3.91509980880582	0.54938823427201
N	1.44289008941987	4.86252518203587	0.78826164247542
N	-2.29615639933584	4.91359286925548	0.03817868096182
Ni	-0.45863418308734	4.75835171611407	0.55755636952991
C	-2.90885431105221	6.24793473711268	-0.21117899287958
C	-4.15137681575656	6.14300886942155	-1.08954715457167
H	-3.92175299620523	5.61111527885107	-2.01766736071197
H	-4.49958996289060	7.14807744764360	-1.34604530347010
H	-4.95498037415075	5.60985982427256	-0.58116670752921
C	2.09382303438402	6.14128204197897	1.18610430185403
C	3.36391377500522	5.89604096011895	1.99744758754720
H	3.15561126334823	5.25683798635180	2.86004396936792
H	3.75419852665772	6.85180338338186	2.36096115548317
H	4.12770691920050	5.40527383641120	1.39432471779228
C	-1.85842001737180	7.08819414377102	-0.93201718903394
H	-1.60881465816724	6.64822613719345	-1.90165005706570
H	-0.93459184508419	7.16552818234958	-0.34485280832555
H	-2.22214323384998	8.10629985148326	-1.09534096952738
C	2.42358469246146	6.94703283869236	-0.07143598754990
H	3.10987528057478	6.38071308934157	-0.70641086125076
H	2.89833511927366	7.89723593598493	0.19344061189350
H	1.52143767373670	7.16591151629517	-0.65140514299065
C	1.08627376730653	6.89167352250071	2.05084459903514

H	1.47507341540870	7.87054195362868	2.34318781131332
H	0.85888849483644	6.32869491064642	2.96157795393418
H	0.14621270549301	7.07408690159295	1.51140982754338
C	-3.26797046944026	6.87981481314948	1.13541077319251
H	-3.98501348216276	6.24780870117207	1.66646008715965
H	-3.71418368410118	7.86961250045973	0.99539935193263
H	-2.38015157071543	6.99731190955840	1.76663212154814
C	3.35624975203286	0.55118824294788	0.61995642152095
C	4.45947190753095	-0.22441230243844	0.29536002459559
C	5.39315155735458	0.20191015729160	-0.64907005295700
C	5.20137883357612	1.45517256547117	-1.22755704152815
C	4.10443128011784	2.23614078114196	-0.90290342457481
C	6.54814705502290	-0.66724407050628	-1.05191684257120
H	7.32377872560986	-0.08705753135339	-1.55846606232055
H	6.21977067293606	-1.45304778656061	-1.74240201477811
H	6.99882246051168	-1.16345137997403	-0.18673240548819
C	-4.18645748680249	0.62014403923967	0.87416710291768
C	-5.34242629274002	-0.15069651604210	0.82296700954555
C	-6.42020502666957	0.20960498503895	0.01957560376258
C	-6.29886655050713	1.37525014371226	-0.74030743787239
C	-5.15132800321632	2.14383841685910	-0.69668352419597
C	-7.67883428757471	-0.60692472260641	-0.02698539494403
H	-7.58259752276628	-1.51946364673380	0.56560690553288

H	-7.92969284454377	-0.89446827498673	-1.05317708688132
H	-8.52885169468630	-0.03897547173457	0.36797098286131
H	-7.12031603042191	1.68475506228946	-1.38238974975413
H	3.97187680859376	3.20735656635316	-1.36740194088453
H	2.65721756732573	0.20024783977533	1.37256467873496
H	4.59883411293197	-1.18235116648666	0.78964531362522
H	5.92258221362343	1.82361825399096	-1.95319538790112
C	-4.06719578703490	1.78483925006322	0.11361940591528
H	-5.07823156473166	3.04483607200089	-1.29447612625257
H	-5.40910456483921	-1.04736704187147	1.43333909283684
H	-3.37968190163305	0.32447275112644	1.53691474105242
H	-1.77767266520601	-0.07774914057912	-0.19485026362163
H	0.89064833574894	-0.07580604910519	-0.16520908878815

Figure 2A - 55. Calculated Structure of 4.

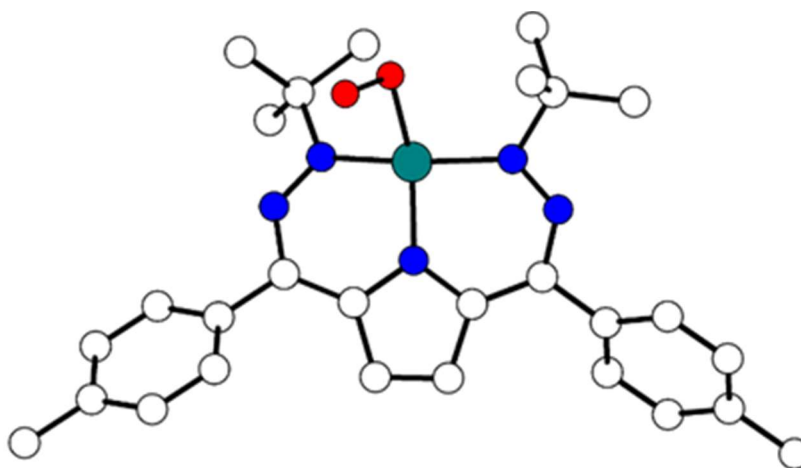


Figure 2A - 56. Spin density map of **4**, with isovalues set to 0.005.

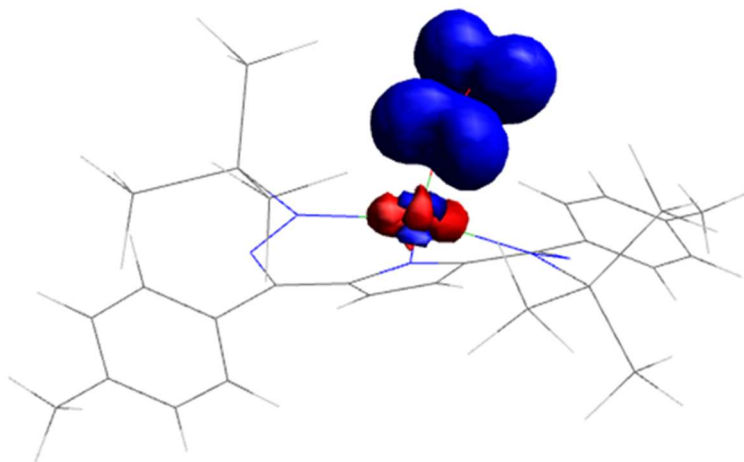


Table 2A - 2. Coordinates of calculated Structure of **4**.

C	-1.12169265656318	0.85449870271526	-0.06416967432390
C	0.24476172391915	0.83345693607253	-0.12899015175641
C	0.69552738538338	2.20617103673519	-0.05167193792143
C	-1.51918170458032	2.24310929117849	0.04359684836631
C	-2.81344351846670	2.79565773486569	0.05248626631069
C	2.01489850108951	2.68617842682286	0.06327744247487
C	3.19639375010932	1.86890821974831	-0.26831463854705
N	-3.08416478386416	4.10179212434468	-0.16982868226024
N	-0.40096924360202	3.02412928040473	0.05336130600828
N	2.26972373969855	3.88920119665291	0.62657165769039
N	1.41625110211827	4.83712877870317	0.72867205471513
N	-2.21821962155428	5.03849335343823	-0.36815742861305
Ni	-0.31915026253031	4.89321186932138	-0.10258417984563

C	-2.94884437423002	6.35483008484578	-0.70576946796642
C	-4.47161986652610	6.21086000931959	-0.56461472465680
H	-4.88688850110733	5.48437219196748	-1.27334539376472
H	-4.91763592120996	7.19418593175458	-0.77710012831333
H	-4.76559397219641	5.90299491493807	0.44716803651945
C	1.92394874489058	5.92782095718773	1.67502019688013
C	2.51491426074521	5.26907483129894	2.93276055411045
H	1.75847753866423	4.65556985333811	3.44575388627080
H	2.84395289618782	6.05731503343466	3.62579642595902
H	3.37501331928609	4.63407204852731	2.68937396186169
C	-2.63203371953303	6.70344892791627	-2.17078065859405
H	-2.97034794648984	5.89594673194607	-2.83678713029615
H	-1.56505283598440	6.87450455555232	-2.34069573270696
H	-3.17480063914596	7.62074098081222	-2.44619169926302
C	2.99915208187941	6.73485726136902	0.93084356545354
H	3.83809690961721	6.08288969217143	0.65087713595416
H	3.37816401941672	7.53484767373409	1.58536826464419
H	2.59081866420411	7.19160353519259	0.02031637016938
C	0.75582361620541	6.82494269566093	2.09273454074611
H	1.09226035547529	7.49261375611681	2.90006849452309
H	-0.08495924431796	6.22712791235678	2.47514022844384
H	0.40214925922320	7.44951291294405	1.26565597232253
C	-2.48943498353671	7.45290031647577	0.26533857500313

H	-2.67301929886949	7.14847867342605	1.30623940730474
H	-3.07552118441175	8.36402216099658	0.07302451966171
H	-1.43246714876938	7.70678362989809	0.14344360659024
O	0.87006108263291	6.30473908490863	-1.85038803226109
O	0.09410074324592	6.57101810240011	-0.83564458568267
C	3.18810152503754	1.00938331236559	-1.38174956048942
C	4.31066338883608	0.24726591749428	-1.70730615300746
C	5.48575520089989	0.31803337760773	-0.94681167899063
C	5.49762294255635	1.19295161798646	0.15364016386712
C	4.38289224073567	1.95477823031700	0.48739498022278
C	6.69712623266120	-0.50819053245531	-1.29153257124822
C	-4.01948534874774	0.92894241024430	1.24069894535711
C	-5.15934532809898	0.15744354603473	1.45817394586680
C	-6.34095356320083	0.38146378124520	0.73393670728292
C	-6.33548056676334	1.41387293929908	-0.21584392295432
C	-5.19946577688765	2.18926010866753	-0.43926244527787
C	-7.57344865723401	-0.44810663622978	0.98517277395429
H	-7.24069806105476	1.61184172239114	-0.79608198920875
H	4.41447840875300	2.62102691856667	1.35035260925650
H	2.30403598961379	0.96464418871896	-2.02055933181560
H	4.27741835338127	-0.40133708941023	-2.58641992580944
H	6.40136616770367	1.27360749024726	0.76433260885334
C	-4.01229631608591	1.95717499567088	0.27806773756519

H	-5.21850249505007	2.98605231676971	-1.18391060176867
H	-5.13586246925905	-0.62585580507699	2.22106787360346
H	-3.12999257694529	0.75587367761918	1.84964943729700
H	6.55394233007756	-1.05504607976317	-2.23359274040351
H	6.91182553866728	-1.24596772513938	-0.50132868184222
H	7.59386187098743	0.12270161908816	-1.39571526157153
H	-8.38048694858457	-0.18329756724349	0.28838337936188
H	-7.95070792412660	-0.29993815813538	2.01022837772193
H	-7.36303327116620	-1.52354377454909	0.87136283957385
H	-1.79762988621496	0.00583706459690	-0.10615554651696
H	0.89158073300630	-0.03622327842151	-0.19664704009052

Table 2A - 3. Orbital Contributions in **2** and **4**.

Complex MO	NiL-rad 2 alpha 131	NiLO ₂ 4 alpha 142
3dz ²	0.018358	0.014669
3dxz	-0.02569	0.05018
3dyz	0.013521	0.040462
3dx ² y ²	-0.13023	0.161115
3dxy	0.006357	-0.03144
4pz	0.010037	-0.01848
4px	0.002705	0.013367
4py	0.075705	-0.01398
% p character	0.088447	-0.0191
% d character	-0.11768	0.234988

Figure 2A - 57. Calculated structure of hydroperoxo.

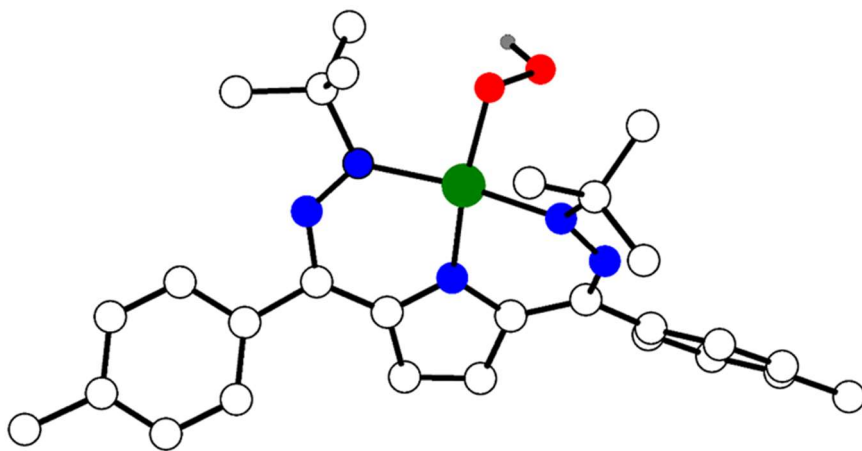


Table 2A - 4. Coordinates of calculated structure of hydroperoxide.

C	-1.10533597856450	0.78240898942854	0.05737356014129
C	0.24626869895660	0.75992433794550	-0.02331750186244
C	0.69688451341491	2.13224046795793	0.02576035358750
C	-1.50124297695312	2.17390133827943	0.12295668110518
C	-2.78159621701123	2.71915646126632	0.06889221725178
C	2.00048374213627	2.60450695160969	0.12146044246700
C	3.20086266131919	1.83532667484701	-0.22470607201949
N	-3.02848912753031	4.00994392603471	-0.22951824114925
N	-0.39171648505275	2.94884942703255	0.12460105674850
N	2.25229565630367	3.80425425891136	0.69520500089568
N	1.41921307005062	4.73700153314167	0.79590253078582
N	-2.17271329488539	4.92425296249491	-0.43523796422343
Ni	-0.29778483468470	4.80452521662750	-0.04588150143092
C	-2.88298856554647	6.21534931498631	-0.81804306373019
C	-4.39462661187235	6.01995013149489	-0.90578548968033
H	-4.66482374387236	5.28563010484751	-1.66665757054762
H	-4.83500016001761	6.98049561727851	-1.19055932196112
H	-4.82898954704726	5.69864036692084	0.04200939884370
C	1.92554880174786	5.82776416490166	1.71720594766153
C	2.81258810794172	5.22511611334852	2.80591012443812
H	2.29782696840579	4.42051579792887	3.34015120174814
H	3.05452223230989	6.01357605910715	3.52423296056323

H	3.74538863891915	4.83278887163010	2.40103757235474
C	-2.39838542663018	6.65156142996395	-2.20281514189267
H	-2.49350430450228	5.82671332863385	-2.91584062044706
H	-1.36841504996643	6.99823387330298	-2.16488776152532
H	-3.02441109019812	7.47465388180906	-2.55872369023991
C	2.73533838211551	6.82603569996736	0.89127848439795
H	3.54593577184513	6.31134212592382	0.36830233554858
H	3.17609459392220	7.56812225963577	1.56502427348587
H	2.10367391800669	7.32887525955476	0.16029102986018
C	0.72652214038603	6.49340746501797	2.37741660387065
H	1.08446466226688	7.23761670720722	3.09501442396541
H	0.12338031566168	5.76004692359217	2.92339987704064
H	0.10367375419614	7.00080321322899	1.64236871119493
C	-2.60032951787875	7.26439445836273	0.25696989957324
H	-2.94637170890227	6.90561560157157	1.23144270782377
H	-3.15406660194006	8.17801618420464	0.01906138590345
H	-1.54162085388009	7.51381684882796	0.31410287839134
O	1.00669584633509	6.25861652715745	-1.67362979600675
O	0.06903220823822	6.52157046642981	-0.61032565672858
C	3.22737254320305	0.98151070346160	-1.33117485177389
C	4.39839752075106	0.33527461399055	-1.70143654772678
C	5.58184249681877	0.51924367599836	-0.98918676053601
C	5.55129810174589	1.37397807609420	0.11445530471220

C	4.39054027970866	2.02093247264303	0.49116363488313
C	6.85080319228125	-0.18131363968506	-1.37382537078497
C	-4.11853834551087	0.93468043857427	1.24926993429851
C	-5.32809690161776	0.29666622290934	1.48389974420092
C	-6.47756717655193	0.63491203913844	0.76854297568656
C	-6.36514724034731	1.61891497405499	-0.21087951082947
C	-5.16214326304615	2.25574863333293	-0.45269480502369
C	-7.80239881066887	-0.00665226691982	1.05253982202677
H	-7.24348396181128	1.90277530089194	-0.78413739839731
H	4.39157894255751	2.68645278963965	1.34639338176578
H	2.33458888389347	0.85959876319727	-1.93660706155097
H	4.39501493055369	-0.30471471086553	-2.57988685195509
H	6.46220435033600	1.54124966044019	0.68339568896731
C	-4.01395840354229	1.93576396119216	0.27746449595570
H	-5.10313360562586	3.03089652019585	-1.20692216757746
H	-5.38504959023671	-0.45883699782926	2.26412342241456
H	-3.25834754547831	0.68595256134825	1.86326019955246
H	6.82330059945726	-0.52053637455211	-2.41237343304777
H	7.01710558593324	-1.06208358861131	-0.74389567771401
H	7.71633718039863	0.47595256809277	-1.24692438452316
H	-8.59410217268556	0.45409043990293	0.45849787688935
H	-8.07111863785816	0.09846014916117	2.10962284311898
H	-7.78905892685647	-1.07771024429906	0.81962604535656

H	-1.78079974900093	-0.06010671501975	0.04834318667250
H	0.89191429502524	-0.10432706253213	-0.07936173622758
H	0.43773284063170	6.29847569364061	-2.46087426503630

Table 2A - 5. Tabulated Energies for the calculation of O–H BDE.

	NiLOO· (4)	TEMPOH	→ NiLOOH	TEMPO	Reaction Energy	O–H BDE = Reaction energy – 70 kcal/mol (TEMPOH BDE)
Energy (hartree s)	-3019.54	-484.133	-3020.15	-483.53	0.011	0.10
Energy (kcal/m ol)	-1894761	-303793	-1895144	-303415	-7.25	63

Figure 2A - 58. TD-DFT predicted UV-vis spectrum of **4**. 2000 cm^{-1} line broadening was applied. Inset shows the low-energy feature.

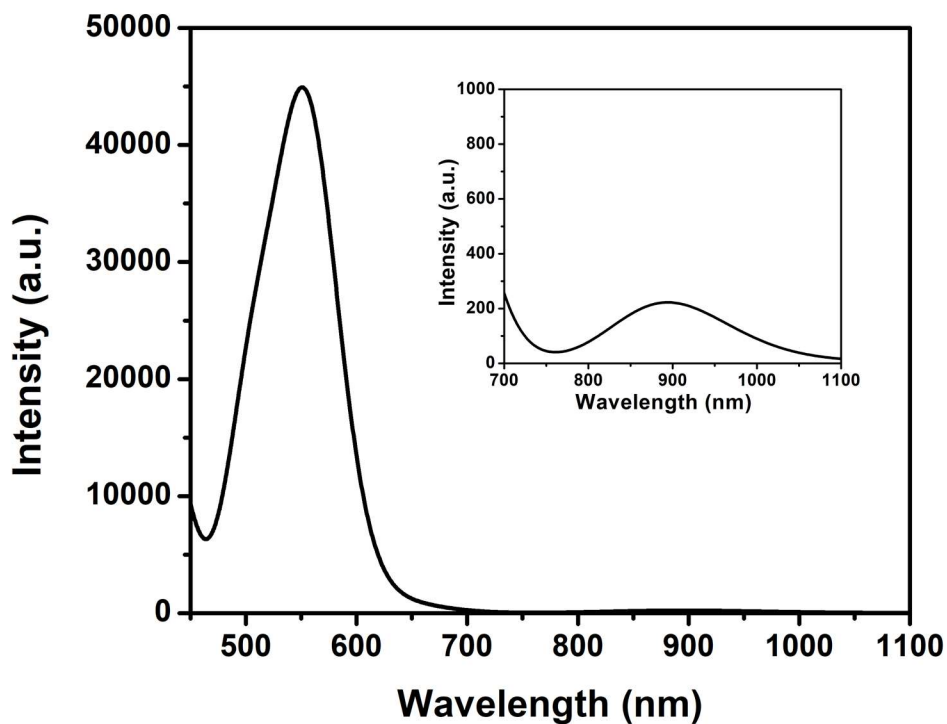


Table 2A - 6. Wavelength and intensities of transitions of **4** calculated by TD-DFT.

Wavelength (nm)	Intensity (au)
933.6196	9.1903
911.1119	70.896
885.3161	146.0343
766.2071	10.2842
647.5551	474.347
626.8452	409.527
620.5321	12.011
557.5503	38981.518

531.6914	3904.827
513.9327	1174.971
510.1364	15775.096
501.4693	1577.0208
492.1235	1691.643
488.7370	133.889
478.2812	1420.766
444.0261	1585.1
439.5624	2018.025
432.1465	2132.674
431.4194	7024.7875
417.765	2626.557
410.3254	284.9424
408.8976	4827.142

Figure 2A - 59. TD-DFT calculated UV-vis transitions of and the experimental collected UV-vis of **4** (red).

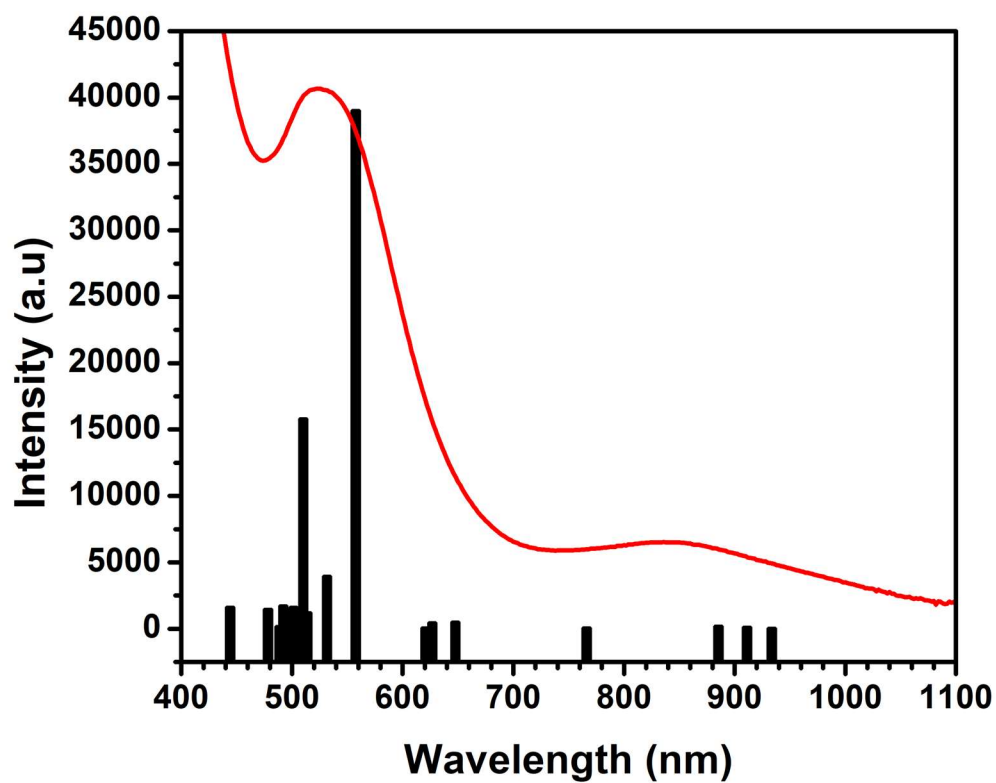


Figure 2A - 60. Calculated structure of **6**.

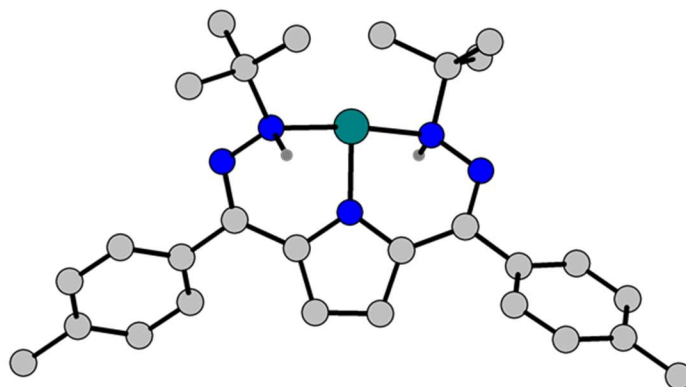


Table 2A - 7. Coordinates of the calculated structure of **6**.

N	-1.47368979453448	0.11123463615405	-0.23276580348059
C	-2.55914746095404	-0.72955073696077	-0.21765099235042
C	-2.08896719561558	-2.05219812422366	-0.02587305794752
C	-0.70085546839267	-1.98599286870223	0.08484480554559
C	-0.32758747745483	-0.62668391794009	-0.07539699913384
H	-0.01266573927900	-2.81744934267169	0.20502696932592
H	-2.71291315077631	-2.93726034032887	0.05723359489586
Ni	-1.54630167120524	1.91488560340249	-0.54637473593150
C	0.99889235897531	-0.04476580941371	-0.16898146544326
N	1.26514921434377	1.13087815564686	-0.70073430855538
N	0.19127857325656	1.77433655816950	-1.36181689899738
C	0.46063186884833	3.23476375691004	-1.70059952338034
C	1.27684904145023	3.88570980857998	-0.58542093761004
H	0.81382180156739	3.73130630321945	0.40088768481181
H	1.34090048970078	4.96668584017545	-0.77540928699331
H	2.29121303123046	3.47283878857326	-0.55061868984143
C	-0.97254521206399	3.79802428629029	-1.72881394058748
H	-1.49263906616397	3.69372176856966	-0.71647812060692
H	-1.58914870803528	3.39476003779794	-2.54794161305430
H	-0.98095416527513	4.89511392413513	-1.81977003880497
C	1.15606822932715	3.35278152908082	-3.05529991664438
H	2.13886039856435	2.86343148726422	-3.02155708686856

H	1.31108606485715	4.41059891071359	-3.31202805480986
H	0.56068656424339	2.89547164239314	-3.86158626383366
N	-3.28843109802710	1.85640196216530	0.41429739024740
N	-4.25630197331934	1.02680578361818	-0.22849041487747
C	-3.90694497956853	-0.22385905784696	-0.42390112740362
C	-4.96690258498352	-1.12445828825096	-0.92707991670719
C	2.16539337967316	-0.77136279987243	0.37498437963217
C	-6.29451720280326	-0.95742758341068	-0.49539959641233
C	-7.30687070677399	-1.78269774753307	-0.97682785295546
C	-7.03972467384332	-2.79605323713992	-1.91135681755134
C	-5.71283095668051	-2.95183699443247	-2.34806521562262
C	-4.69193806905446	-2.13852458083719	-1.86525036043934
H	-6.52370617705991	-0.18090828654885	0.23536780267308
H	-8.32807088522191	-1.64315030654419	-0.61521706115638
H	-5.47703330673742	-3.72244111896586	-3.08640658065690
H	-3.67652499941183	-2.27035293764974	-2.24235504716172
C	-8.13029446682165	-3.69389820636727	-2.42803388896383
H	-9.11344415780197	-3.39882714196522	-2.03956765923087
H	-7.94867573825955	-4.74098162958502	-2.13645763940771
H	-8.17257738311227	-3.66945182442978	-3.52837208078936
C	3.40882101333296	-0.69454414672396	-0.27715759610065
C	4.52409892421664	-1.34240305748649	0.24583873497576
C	4.44691289976335	-2.07746587017844	1.44002945551958

C	3.20386905972400	-2.14062906734478	2.09365775505103
C	2.07968802720851	-1.50730234476243	1.57288544090322
H	3.48749708873439	-0.13182173690553	-1.20801211969555
H	5.47742066373535	-1.28128860199382	-0.28381722386189
H	1.13539202785840	-1.55272776347202	2.11757593715530
H	3.11989992400696	-2.68873736895065	3.03480376452488
C	-3.95766317011028	3.13955771700985	0.92190329996396
C	-2.91046412665474	3.89277312973225	1.74852779864556
H	-2.55162287358010	3.28799978160290	2.59657298848728
H	-3.35748600011328	4.80658486597095	2.16211284225824
H	-2.03638144840319	4.19873743447151	1.15419793283460
C	-4.45436253987118	3.95537827671747	-0.27049157255830
H	-3.62882777990427	4.30538726390438	-0.90656907575532
H	-4.99202616050564	4.84168425963897	0.09302924442714
H	-5.14171770311250	3.35879693336878	-0.88462551467581
C	-5.13323702479614	2.74548263370352	1.82966627664689
H	-4.80405594789690	2.08133373169210	2.64404342244144
H	-5.91858373832992	2.23705823301607	1.25760650737334
H	-5.56028190996232	3.65015411319833	2.28460997697764
C	5.64908044623645	-2.78517138478999	2.00237247357782
H	6.56463410358410	-2.51758453023812	1.45931683170356
H	5.52439997448901	-3.87875990344989	1.93762100272841
H	5.79285068459280	-2.53983984833788	3.06560021760528

H	-2.95064567015516	1.36395323792202	1.26193942503253
H	-0.01258029089424	1.26312111144617	-2.23867685910646

Figure 2A - 61. Coordinates of the calculated structure of **3**.

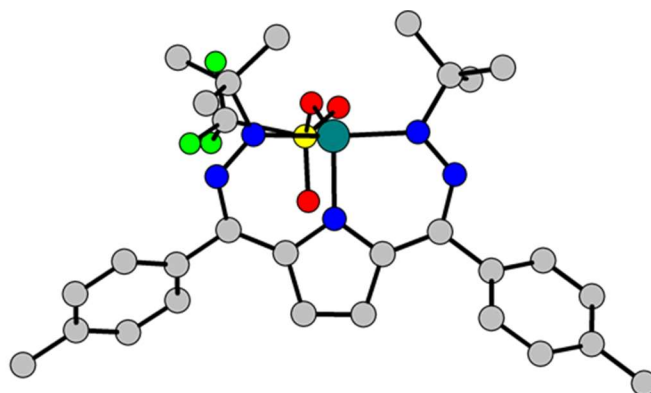


Table 2A - 8. Coordinates of the calculated structure of **3**.

N	-1.83972750435741	0.36991039791393	-0.23953993501305
C	-2.89318970733355	-0.49007621302985	-0.37579185187572
C	-2.38682330827005	-1.84692219593675	-0.40310482613494
C	-1.02507955274014	-1.76792037618245	-0.31111350804689
C	-0.68462357224906	-0.36103278727992	-0.21214046374915
Ni	-1.97549614918906	2.25169839910267	-0.49318612909170
C	0.58937241925865	0.23964830112085	-0.14440444868840
N	0.84269015309871	1.56040768980064	-0.33678468243887
N	-0.05504021502330	2.47278392383121	-0.48943687922599
C	0.61334967287564	3.80063806360824	-0.84594131353584
C	1.75174612021443	4.08789927836635	0.14453333194014
H	1.37318967805233	4.11522027612225	1.17748053936387
H	2.19006268425801	5.07020871125208	-0.08682334815382
H	2.53713136987885	3.32508671702129	0.08186076395252
C	-0.42620173374677	4.91654591293963	-0.76837271248832
H	-0.78419736777156	5.05518005093116	0.26153827638869
H	-1.27496367674533	4.72167102914073	-1.43886749836655
H	0.03622929834706	5.86186644975527	-1.08666031270460
C	1.14995757222501	3.67106156645020	-2.28167531334617
H	1.88671510860188	2.85744726366737	-2.34075904560019
H	1.64191387384724	4.61030443903391	-2.57563660996172

H	0.33964079845673	3.46796472534241	-2.99604913340920
N	-3.83818970533772	2.19227172699971	0.14070887029068
N	-4.61142199946946	1.17644771256522	0.06367625071738
C	-4.23192371495915	-0.04837155590543	-0.38787799343642
C	-5.34269689225254	-0.93296807743362	-0.78005973573726
C	1.80747872739781	-0.56251928417341	0.10262963184365
C	-6.57492918534984	-0.90959757534202	-0.10130227899191
C	-7.62148127704448	-1.73717880271083	-0.50174709457919
C	-7.48890959369583	-2.60559917254129	-1.59661531153569
C	-6.26357112110190	-2.60988656313084	-2.28438103449263
C	-5.20932689023236	-1.79023451615391	-1.89109641219876
H	-6.69757987302533	-0.24479677908147	0.75451902336854
H	-8.56497624726791	-1.71259573149193	0.04942029748373
H	-6.14060159971020	-3.25162096446458	-3.16060582865299
H	-4.28647975904370	-1.77157585389742	-2.47310703569496
C	-8.62223240973037	-3.49611800639980	-2.03364639219099
H	-9.50814324475885	-3.35837279391217	-1.39877013931838
H	-8.33288028000404	-4.55866954365670	-1.98899481885244
H	-8.91332517869264	-3.28544852725398	-3.07489688613798
C	3.00306403828794	-0.27500780486162	-0.58111339877018
C	4.15887219552435	-1.01451189701379	-0.34285046056097
C	4.17719171266543	-2.06040445380741	0.59238814801509
C	2.98856352418440	-2.33361943644362	1.28874448035536

C	1.82674178267856	-1.60248909686246	1.05245627263878
H	3.00986765575442	0.53354023459273	-1.31323746926767
H	5.06961883612763	-0.77690680196866	-0.89839275419948
H	0.93077574035903	-1.81383954261572	1.63933341489654
H	2.97682513738384	-3.12579857847195	2.04246632062730
C	-4.53317480102945	3.36048207264765	0.81787698336490
C	-3.50726265162831	4.47836332546923	0.98588288103408
H	-2.64905411634277	4.14449276405863	1.58998122553703
H	-3.96901770548076	5.33312647821816	1.50075201388510
H	-3.14556979022048	4.83345167871556	0.01118563808710
C	-5.66963625858332	3.82120379924085	-0.11061939568473
H	-5.27522397707957	4.09548101737666	-1.09903478462645
H	-6.16550555832506	4.70161139749494	0.32444953299976

X-Ray Absorption Studies

Figure 2A - 62. Calculated structure of **4** with atom labels.

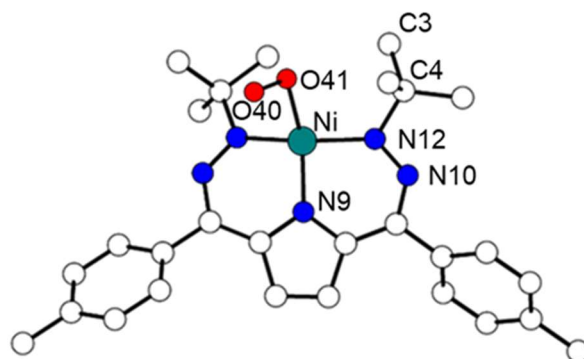


Table 2A - 9. EXAFS Fit Parameters for **4**.

Complex 4	N	R (Å)	σ^2 (Å ²)	R-factor	Reduced chi-square
Ni-N9	1	1.873(6)	0.0022(9)	0.0080	20.6
Ni-N12	2	1.920(6)	0.0022(9)		
Ni-O41	1	2.08(1)	0.0009(5)		
Ni-O40	1	2.70(1)	0.0009(5)		
Ni-N10	2	2.870(6)	0.0022(9)		
Ni-C3	1	3.05(3)	0.009(4)		
Ni-C4	1	3.09(3)	0.009(4)		

$\Delta E_0 = -2.4$ eV; $S_0^2 = 0.74$; Independent Points: 13.9; Fitting Range: k: 1-11.5 Å⁻¹; R: 1.0-3.1 Å

N, Coordination numbers; R, interatomic distances; σ^2 , Debye-Waller factors (the mean-square deviations in interatomic distance). The values in parentheses are the estimated standard deviations; ΔE_0 , change in the photoelectron energy; S_0^2 , amplitude reduction factor.

Table 2A - 10. Comparison of EXAFS and DFT calculated bond lengths of **4**.

Complex 4	N	DFT model	XAFS R (Å)
Ni-N9	1	1.8770	1.873(6)
Ni-N12	2	1.8774	1.920(6)
Ni-O41	1	1.9241	2.08(1)
Ni-O40	1	2.5420	2.70(1)
Ni-N10	2	2.8739	2.870(6)
Ni-C3	1	2.8727	3.05(3)
Ni-C4	1	2.9128	3.09(3)

Figure 2A - 64. EXAFS spectrum (black) and fits (red) in k-space at the Ni K-edge absorption of 4.

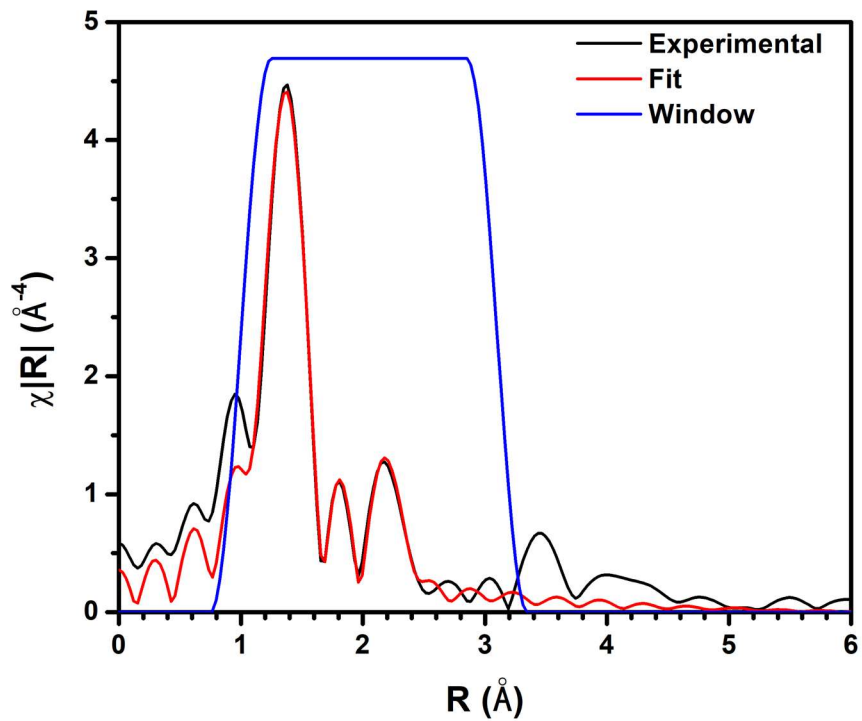


Figure 2A - 63. EXAFS spectrum (black) and fits (red) in k-space at the Ni K-edge absorption of 4.

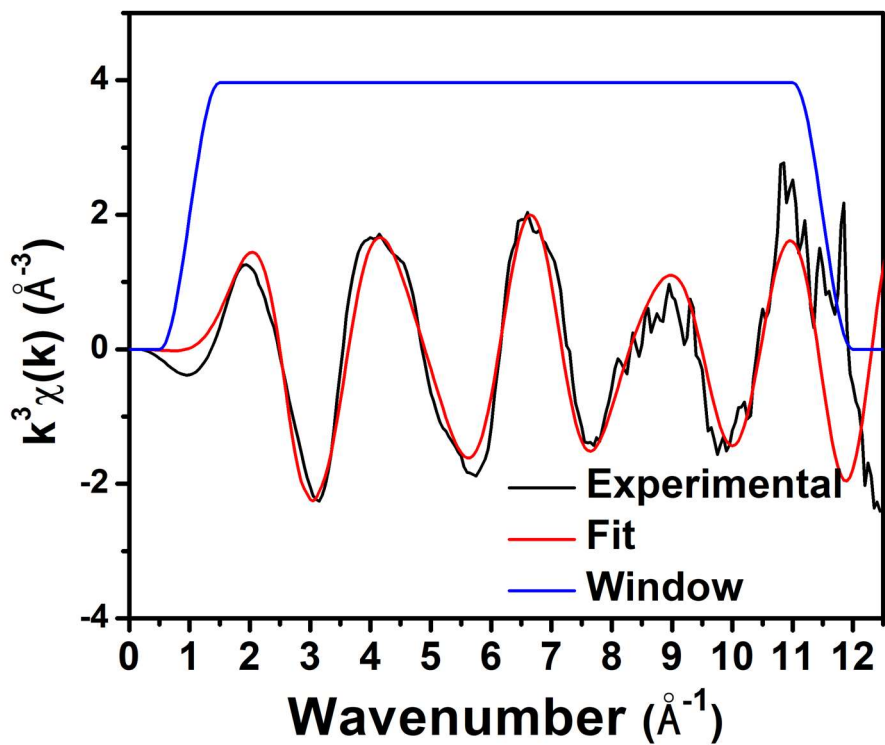


Table 2A - 11. EXAFS fit parameters of pathways with or without O40 (second O).

Fit parameters	ON ₃ C ₂ O	ON ₃ C ₂	
O41	$\Delta R(\text{\AA})$	0.20(1)	0.20(3)
	$\sigma^2 (\text{\AA}^2)$	0.0005(9)	-0.001(3)
N	$\Delta R(\text{\AA})$	-0.004(6)	-0.002(3)
	$\sigma^2 (\text{\AA}^2)$	0.0022(9)	0.002(2)
C	$\Delta R(\text{\AA})$	0.18(3)	0.20(4)
	$\sigma^2 (\text{\AA}^2)$	0.009(4)	0.002(5)
O40	$\Delta R(\text{\AA})$	0.16(1)	
	$\sigma^2 (\text{\AA}^2)$	0.0009(5)	
ΔE_0 (eV)	-1.4(8)	0(2)	
S_0^2	0.74(8)	0.7(2)	
R-factor	0.0080	0.0747	
Reduced chi-square	20.6	160.2	

X-ray Crystallography

Table 2A - 12. Crystal structure and refinement data.

Identification code	(1)	(2)	(3)
Empirical formula	C ₃₄ H ₁₉ F ₉ N ₆ NiO	C ₂₈ H ₃₄ N ₅ Ni	C ₅₈ H ₆₈ F ₆ N ₁₀ Ni ₂ O ₆ S ₂
Formula weight	734.25	499.31	1296.76
Temperature/K	100(2)	100(2)	100(2)
Crystal system	Monoclinic	monoclinic	Triclinic
Space group	C2/c	C2/c	P-1
a/Å	35.170(3)	51.354(6)	12.197(6)
b/Å	12.6182(10)	5.7125(7)	15.166(8)
c/Å	13.9741(11)	17.328(2)	21.970(11)
α/°	90	90	71.701(12)
β/°	100.927(4)	93.198(4)	76.170(11)
γ/°	90	90	69.672(13)
Volume/Å ³	6089.0(9)	5075.5(10)	3579(3)
Z	8	8	2
ρ _{calc} /g/cm ³	1.541	1.307	1.203
μ/mm ⁻¹	0.726	0.790	0.649
F(000)	2896.0	2120.0	1352.0
Crystal size/mm ³	0.34x0.11x0.09	0.36 × 0.21 × 0.17	0.36 x 0.24 x 0.22
Radiation	MoKα (λ = 0.71073)	MoKα (λ = 0.71073)	MoKα (λ = 0.71073)
2Θ range for data collection/°	4.392 to 52.996	4.708 to 50.328	4.292 to 37.618
Index ranges	-44 ≤ h ≤ 44, -15 ≤ k ≤ 15, -17 ≤ l ≤ 17	-60 ≤ h ≤ 59, -6 ≤ k ≤ 6, -20 ≤ l ≤ 20	-10 ≤ h ≤ 11, -13 ≤ k ≤ 13, -19 ≤ l ≤ 19
Reflections collected	63378	40928	18028
Independent reflections	6136 [R _{int} = 0.0647, R _{sigma} = 0.0467]	4486 [R _{int} = 0.0850, R _{sigma} = 0.0449]	5349 [R _{int} = 0.0758, R _{sigma} = 0.0739]
Data/restraints/parameters	6136/0/463	4486/351/407	5349/1703/883
Goodness-of-fit on F ²	1.087	1.078	1.045
Final R indexes [I ≥ 2σ (I)]	R ₁ = 0.0411, wR ₂ = 0.0897	R ₁ = 0.0672, wR ₂ = 0.1602	R ₁ = 0.1592, wR ₂ = 0.3329
Final R indexes [all data]	R ₁ = 0.0743, wR ₂ = 0.0913	R ₁ = 0.0851, wR ₂ = 0.1703	R ₁ = 0.1917, wR ₂ = 0.3534
Largest diff. peak/hole / e Å ⁻³	0.40/-0.44	0.72/-0.76	1.48/-0.99

Identification code	(5)
Empirical formula	C ₃₃ H ₄₈ ClN ₅ Ni
Formula weight	608.92
Temperature/K	100(2)
Crystal system	triclinic
Space group	P-1
a/Å	10.3991(5)
b/Å	11.3467(5)
c/Å	15.9639(8)
α/°	90.377(2)
β/°	106.279(2)
γ/°	115.5700(10)
Volume/Å ³	1613.26(13)
Z	2
ρ _{calc} /cm ³	1.254
μ/mm ⁻¹	0.714
F(000)	652.0
Crystal size/mm ³	0.59 × 0.47 × 0.34
Radiation	MoKα (λ = 0.71073)
2θ range for data collection/°	4.498 to 52.874
Index ranges	-13 ≤ h ≤ 13, -14 ≤ k ≤ 14, -19 ≤ l ≤ 19
Reflections collected	34504
Independent reflections	6628 [R _{int} = 0.0325, R _{sigma} = 0.0278]
Data/restraints/parameters	6628/0/371
Goodness-of-fit on F ²	1.049
Final R indexes [I ≥ 2σ (I)]	R ₁ = 0.0445, wR ₂ = 0.1135
Final R indexes [all data]	R ₁ = 0.0555, wR ₂ = 0.1197
Largest diff. peak/hole / e Å ⁻³	1.50/-0.72

Appendix 3. Supporting Data for Chapter 3. NMR spectra

Figure 3A - 1. ^1H NMR of K1 in DMSO-d_6 .

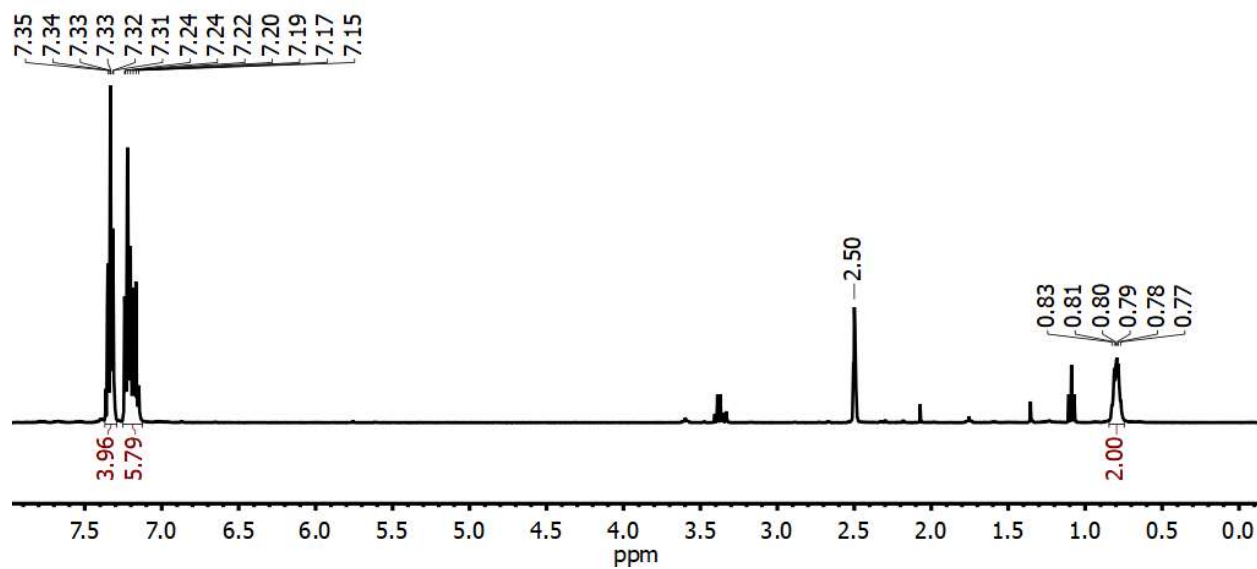


Figure 3A - 2. $^3\text{P}\{^1\text{H}\}$ NMR of K1 in DMSO-d_6 .

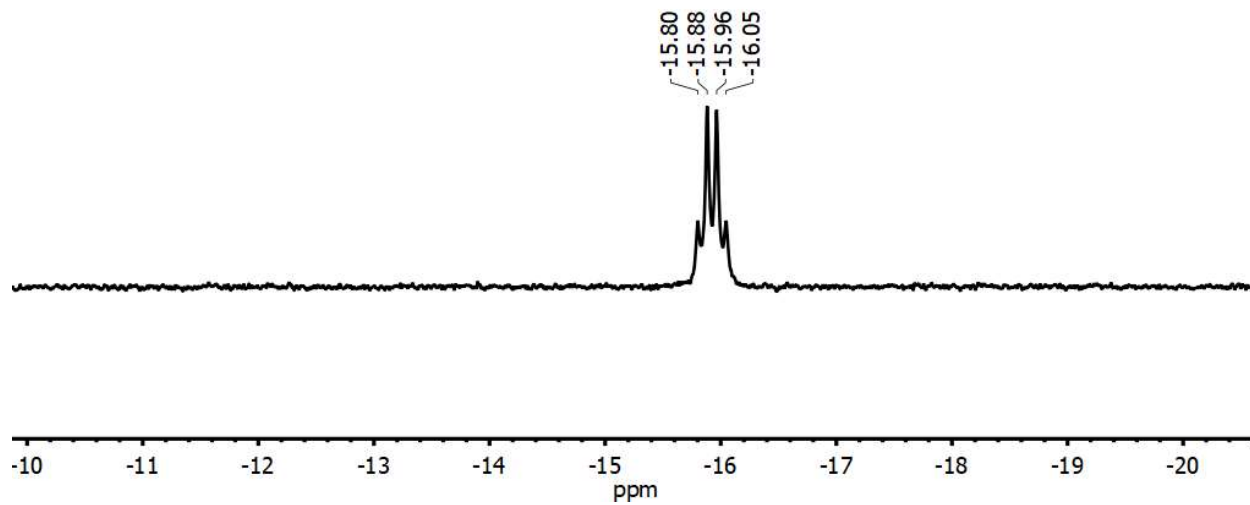


Figure 3A - 3. $^{11}\text{B}\{^1\text{H}\}$ NMR of K1 in DMSO-d_6 .

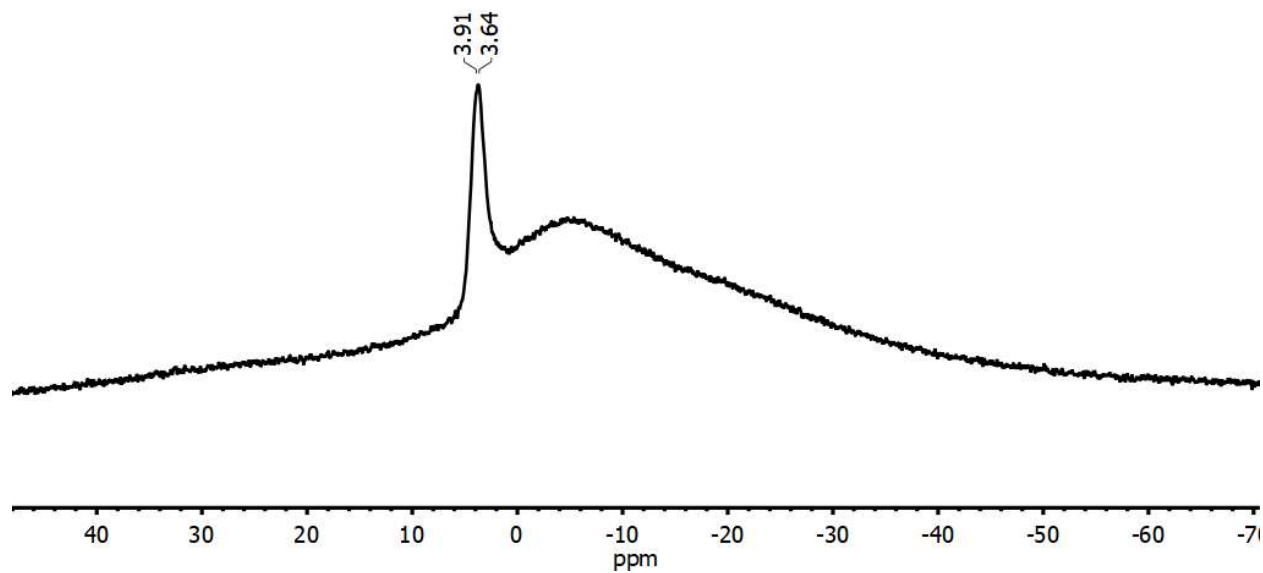


Figure 3A - 4. $^{31}\text{P}\{^1\text{H}\}$ NMR of $\text{PPh}_4\text{I}^{\text{Se}}$ in CDCl_3 .

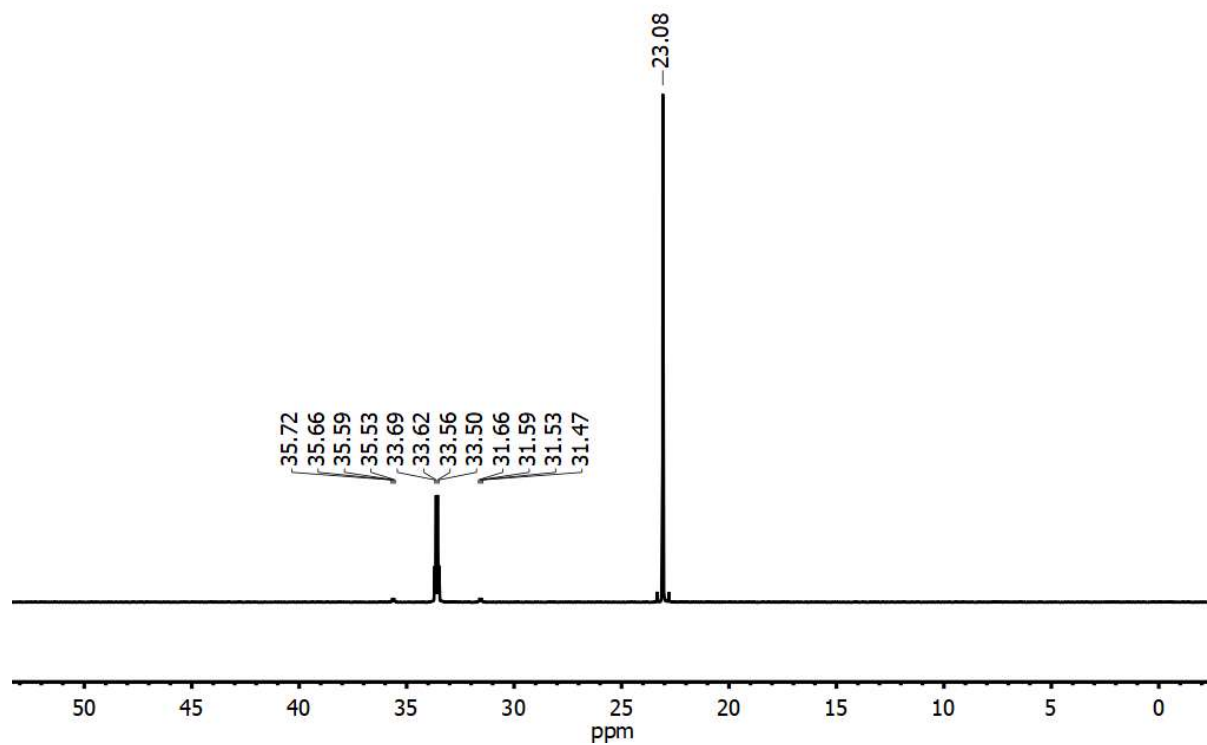


Figure 3A - 5. $^{19}\text{F}\{^1\text{H}\}$ NMR of $\text{PPh}_4\text{I}^{\text{Se}}$ in CDCl_3 .

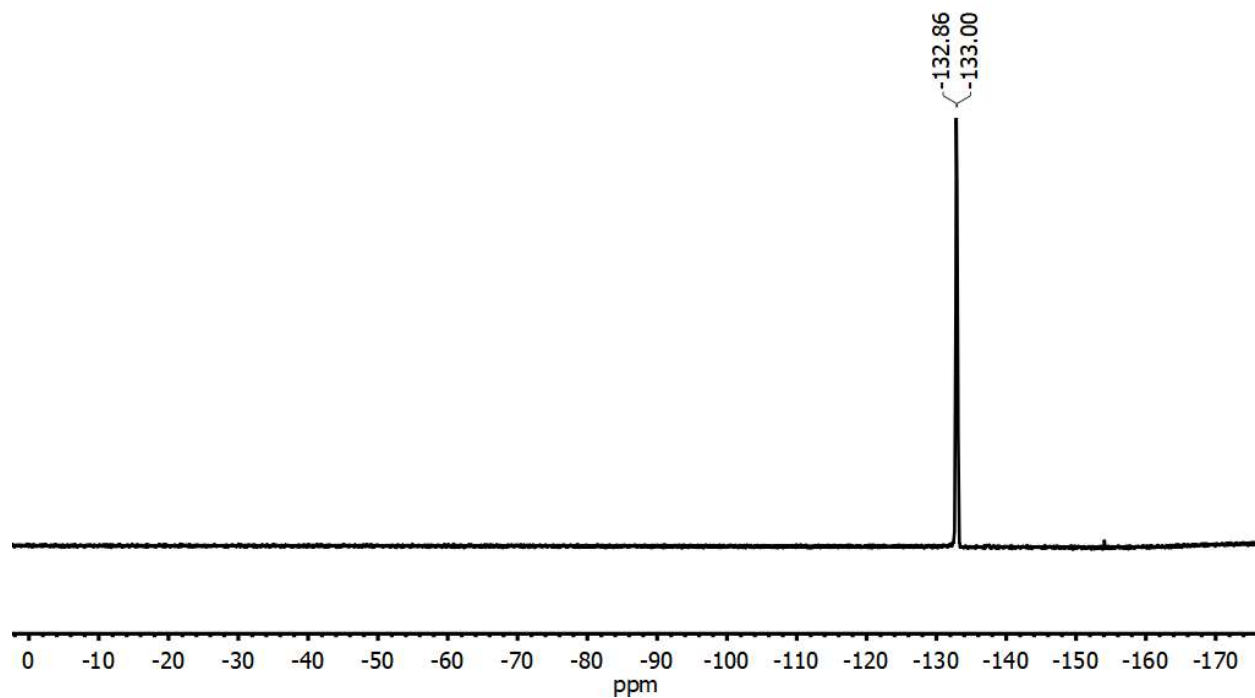


Figure 3A - 6. ^1H NMR of $\text{PPh}_4\text{I}^{\text{Se}}$ in CDCl_3 .

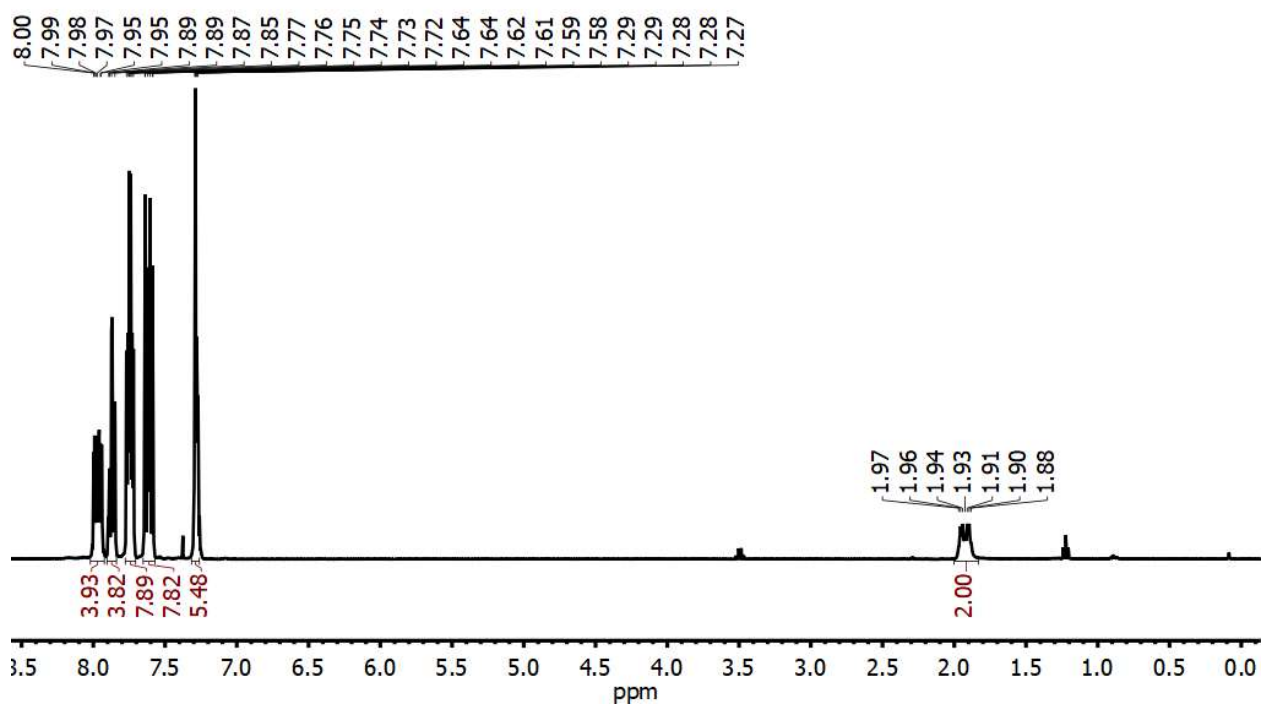


Figure 3A - 7. $^{11}\text{B}\{^1\text{H}\}$ NMR of $\text{PPh}_4\text{I}^{\text{Se}}$ in CDCl_3 .

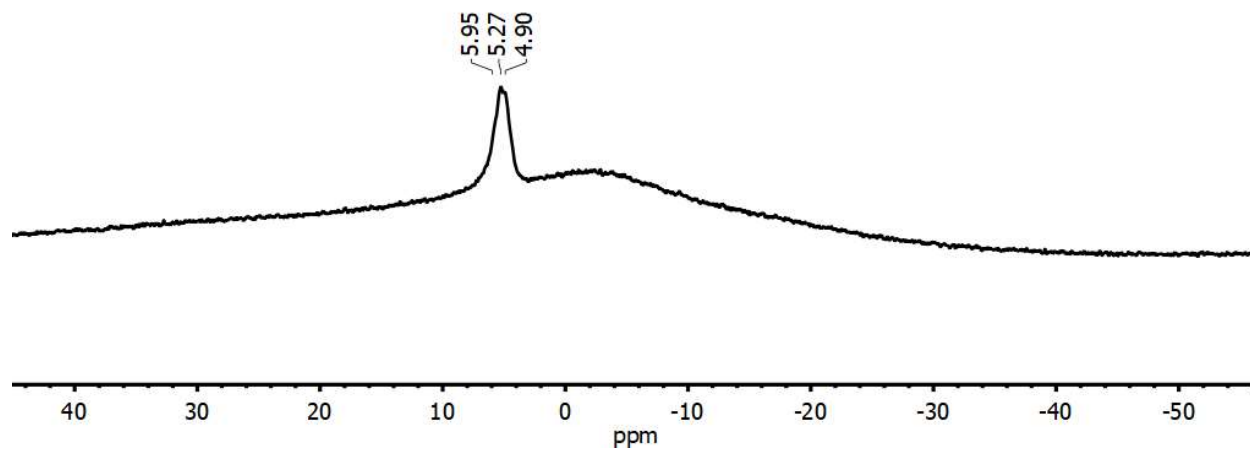


Figure 3A - 8. $^{13}\text{C}\{^1\text{H}\}$ NMR of $\text{PPh}_4\text{I}^{\text{Se}}$ in CDCl_3 .

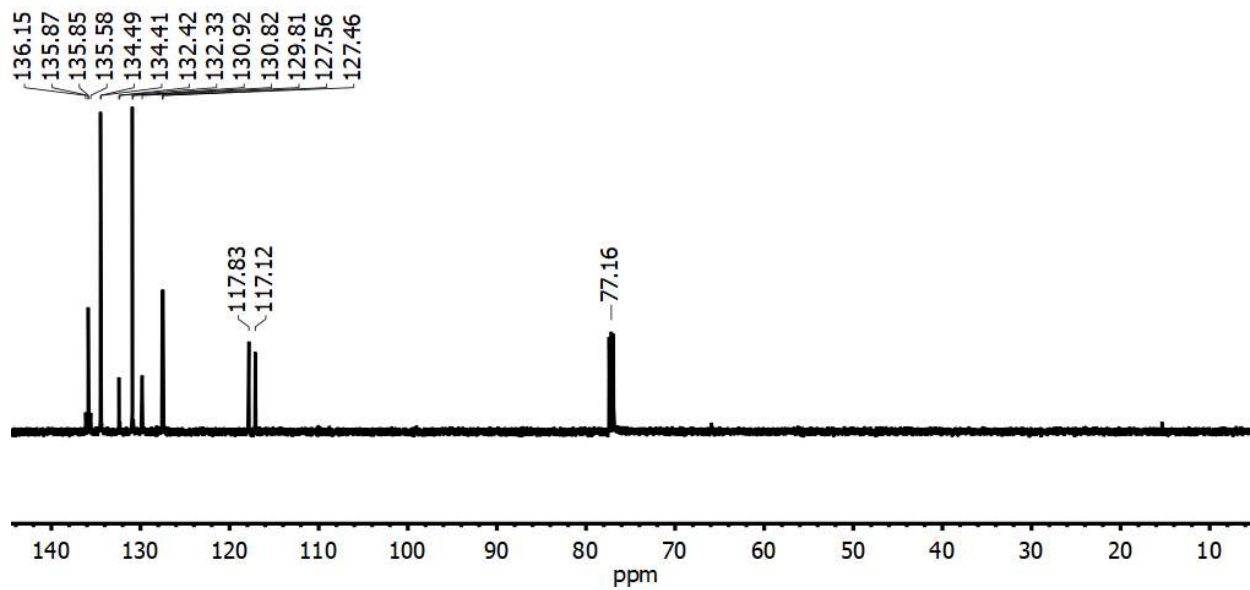


Figure 3A - 9. ^1H NMR of **2** in CDCl_3 . Peaks at 3-4 and 1.2 are from THF and Et_2O .

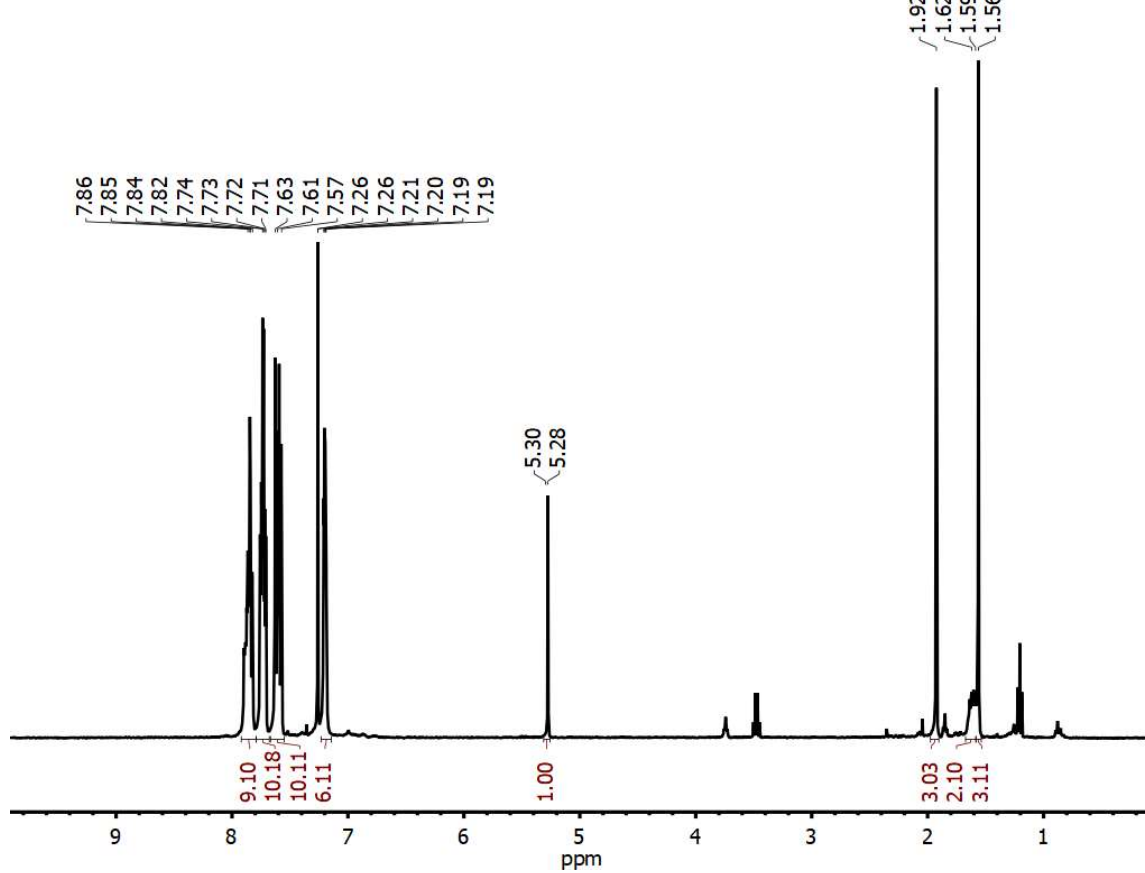


Figure 3A - 10. $^{31}\text{P}\{^1\text{H}\}$ NMR of **2** in CDCl_3

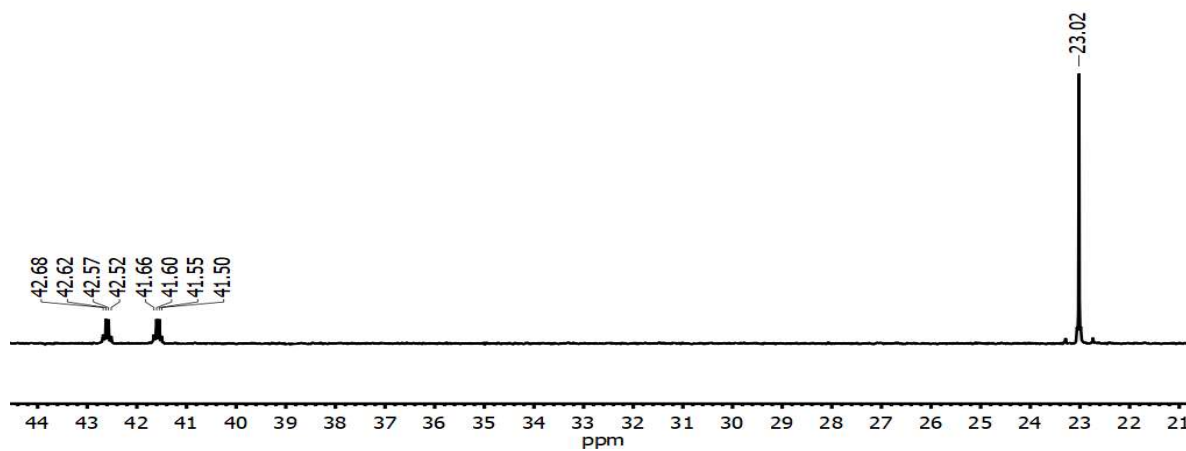


Figure 3A - 12. ^{19}F $\{^1\text{H}\}$ NMR of **2** in CDCl_3

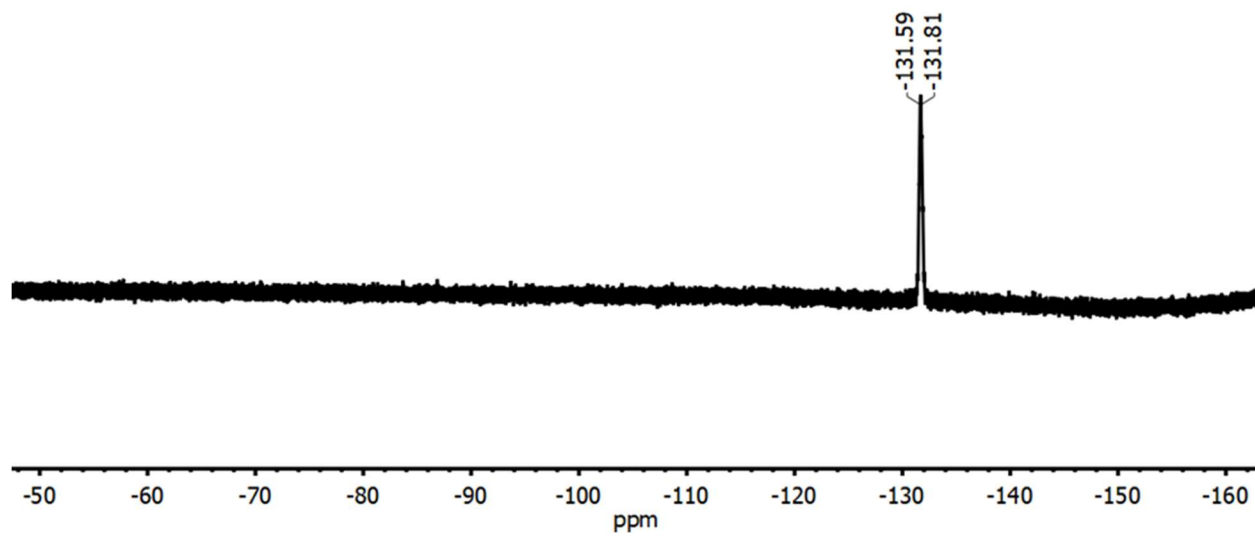


Figure 3A - 11. ^{13}C $\{^1\text{H}\}$ NMR of **2** in CDCl_3

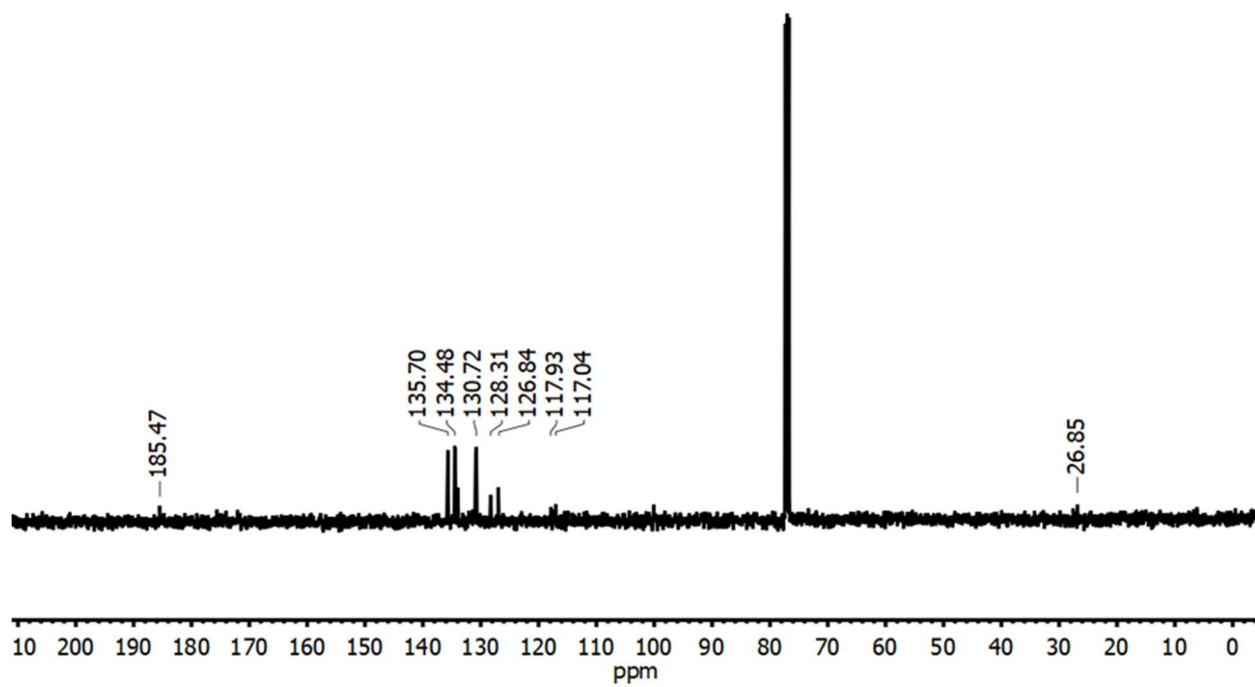
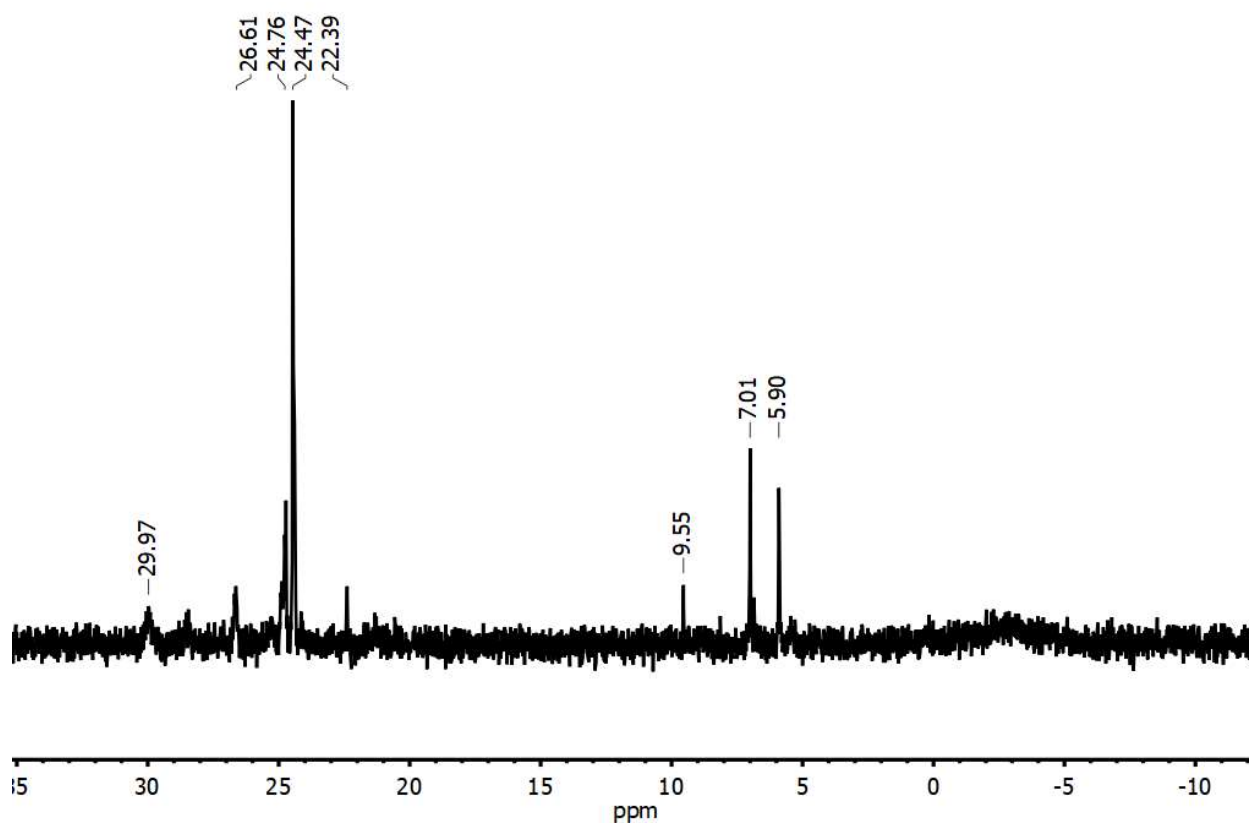


Figure 3A - 13. $^{31}\text{P}\{^1\text{H}\}$ NMR of the reaction mixture of the Heck coupling of styrene and chlorobenzene with PPh_4I and $\text{Pd}(\text{dba})_2$.



GC/MS

Figure 3A - 14. Representative GCMS trace for the Heck Coupling of styrene and chlorobenzene.

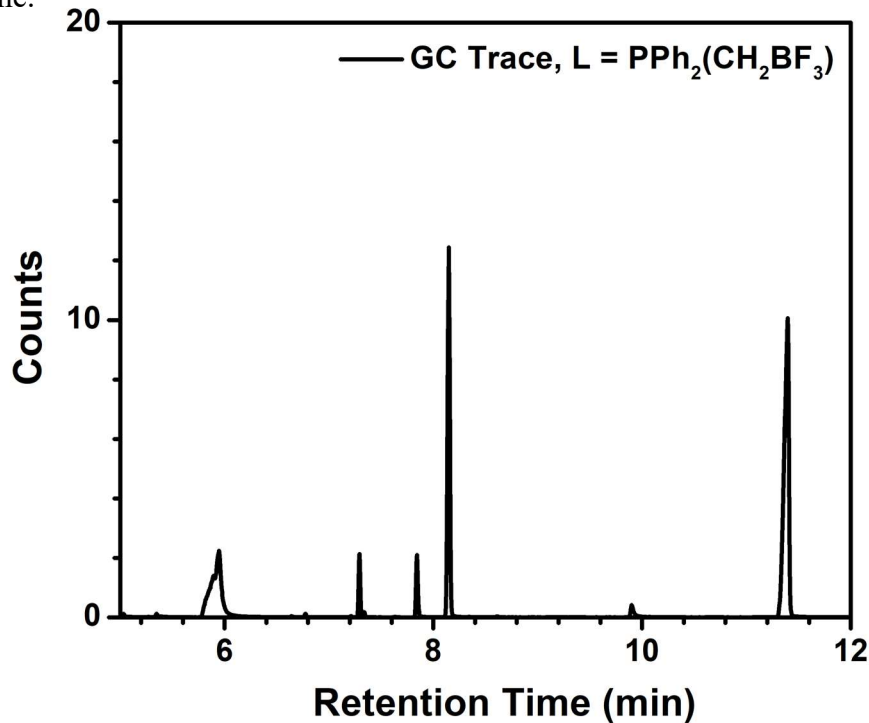


Figure 3A - 15. Comparison of GCMS trace for the Heck coupling of 1-hexene and chlorobenzene for PCy_3 and **1**. Additional peaks are various dba degradation products.

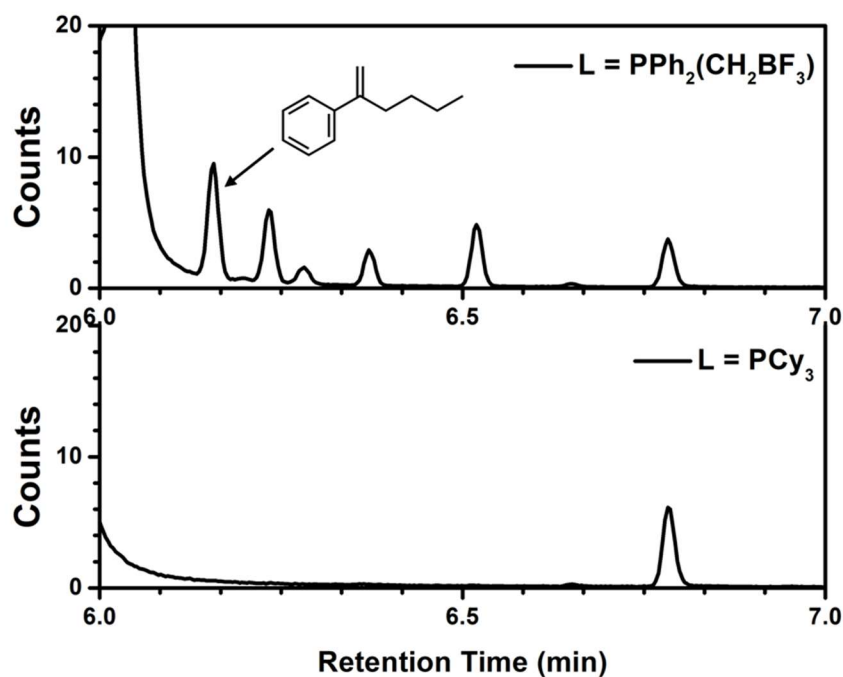
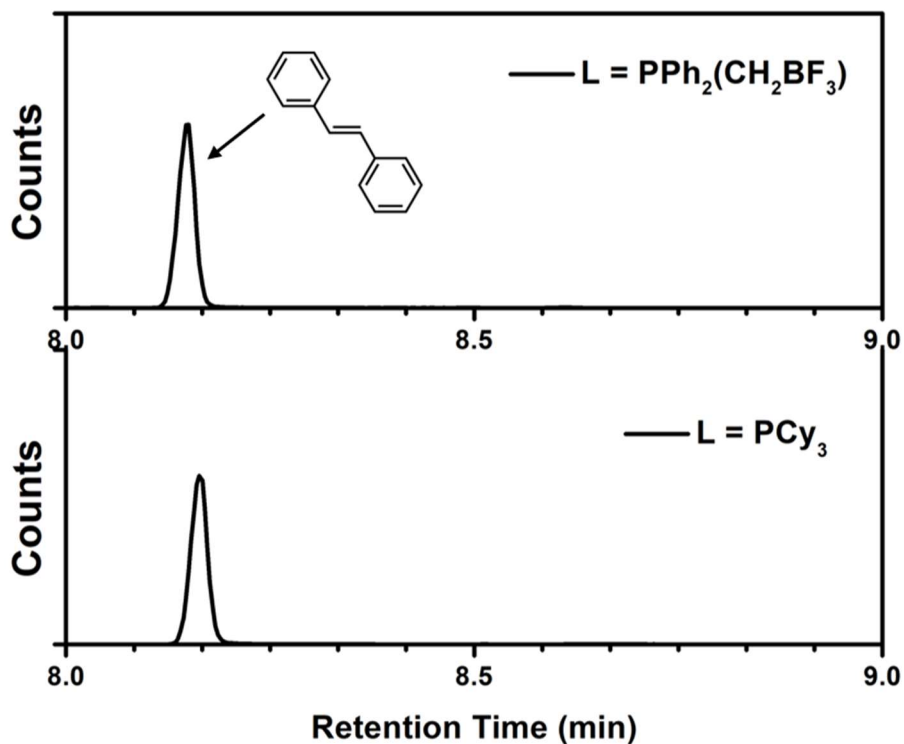


Figure 3A - 16. Comparison of GCMS trace of Heck coupling of styrene and chlorobenzene with PCy₃ or 1.



Scheme 3A - 1. Heck coupling of styrene and chlorobenzene.

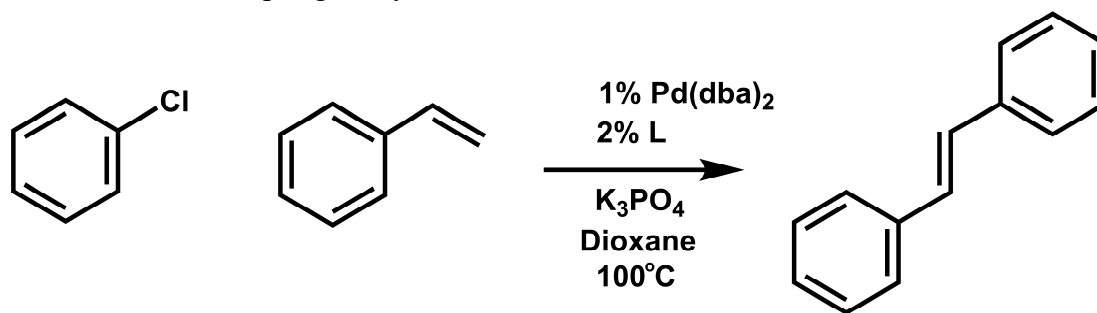


Table 3A - 1. Percent conversion of Heck reaction of chlorobenzene and styrene at different timepoints.

L	Conversion after 3 hr	Conversion after 24 hr
1	1%	10%
PCy ₃	0.5%	8%

Scheme 3A - 2. Heck coupling of chlorobenzene and 1-hexene.

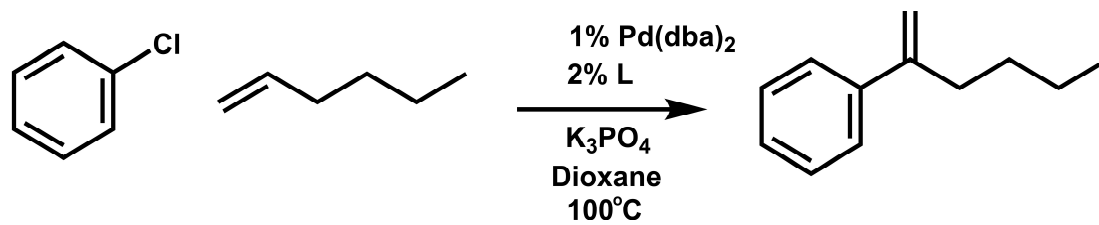


Table 3A - 2. Conversion of chlorobenzene and 1-hexene.

L	Conversion after 24 hr
1	Trace
PCy ₃	0

IR Spectra

Figure 3A - 17. IR (DCM solution) of **2**

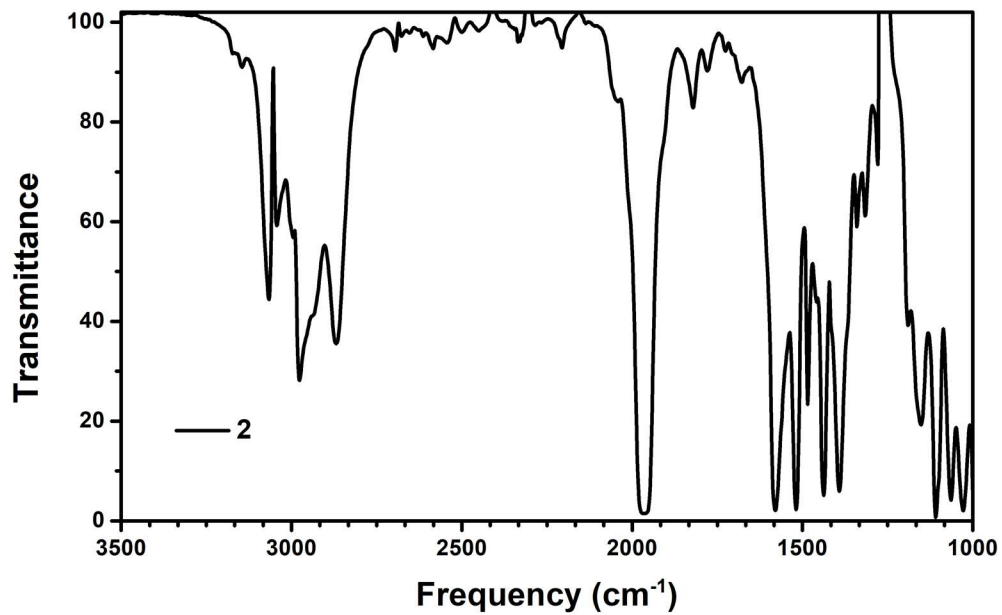
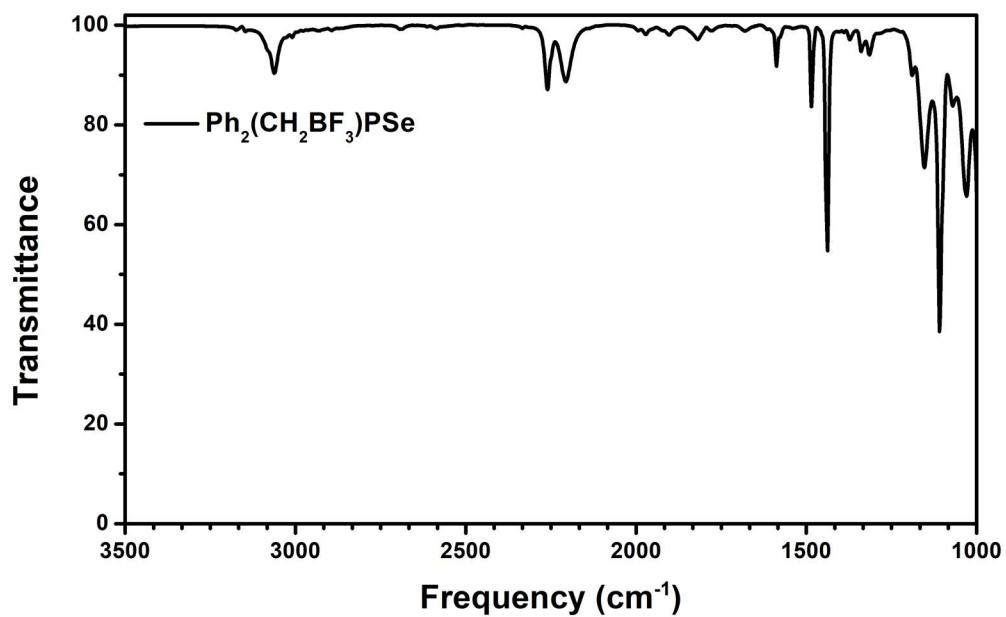


Figure 3A - 18. IR (DCM solution) of PPh₄1Se



X-Ray Structure Determination

Table 3A - 3. Refinement data for X-ray structures.

Identification code	2
Empirical formula	$C_{43}H_{39}BF_3O_3P_2Rh$
Formula weight	836.40
Temperature/K	100(2)
Crystal system	triclinic
Space group	P-1
a/Å	9.1533(6)
b/Å	13.0253(9)
c/Å	33.273(2)
$\alpha/^\circ$	83.172(2)
$\beta/^\circ$	88.634(2)
$\gamma/^\circ$	79.181(2)
Volume/Å ³	3868.8(4)
Z	4
ρ_{calc}/cm^3	1.436
μ/mm^{-1}	0.578
F(000)	1712.0
Crystal size/mm ³	0.47 × 0.26 × 0.17
Radiation	MoK α ($\lambda = 0.71073$)
2 Θ range for data collection/ $^\circ$	4.266 to 48.298
Index ranges	-10 ≤ h ≤ 9, -14 ≤ k ≤ 14, -37 ≤ l ≤ 38
Reflections collected	43104
Independent reflections	12046 [$R_{int} = 0.0802$, $R_{sigma} = 0.0838$]
Data/restraints/parameters	12046/0/967
Goodness-of-fit on F ²	1.026
Final R indexes [$I \geq 2\sigma(I)$]	$R_1 = 0.0425$, $wR_2 = 0.0751$
Final R indexes [all data]	$R_1 = 0.0842$, $wR_2 = 0.0853$
Largest diff. peak/hole / e Å ⁻³	0.72/-0.52

Appendix 4. Further H₂ Donor Ligand Research Titanium Templated Condensation with Hydrazides

To further explore the boundaries of 2,5-pyrrole pincer ligands, condensation of *t*-butyl hydrazide with the acylpyrrole was targeted. The hydrazide arms would have more binding sites for metals/hydrogens, and could accommodate a wide variety of redox/protonation states on the ligand. Direct condensation with the acyl pyrrole with acid catalysis, sieves, a Dean-Stark apparatus, and high temperature were unsuccessful in all cases, so templated synthesis was targeted.

Strong Lewis acids are widely used for difficult condensation reactions and often result in binding of the template to the ligand. TiCl₄ is a strong Lewis acid which can template the condensation but then decompose to HCl and insoluble TiO₂ upon reaction with the water produced from the condensation. Reaction of the ditolylacylpyrrole with two equivalents of *t*-butyl hydrazide and TiCl₄ in acetonitrile at 80 °C resulted in formation of an asymmetrical product by ¹H NMR in

Figure 4A- 1. SXR D Structure of **1**

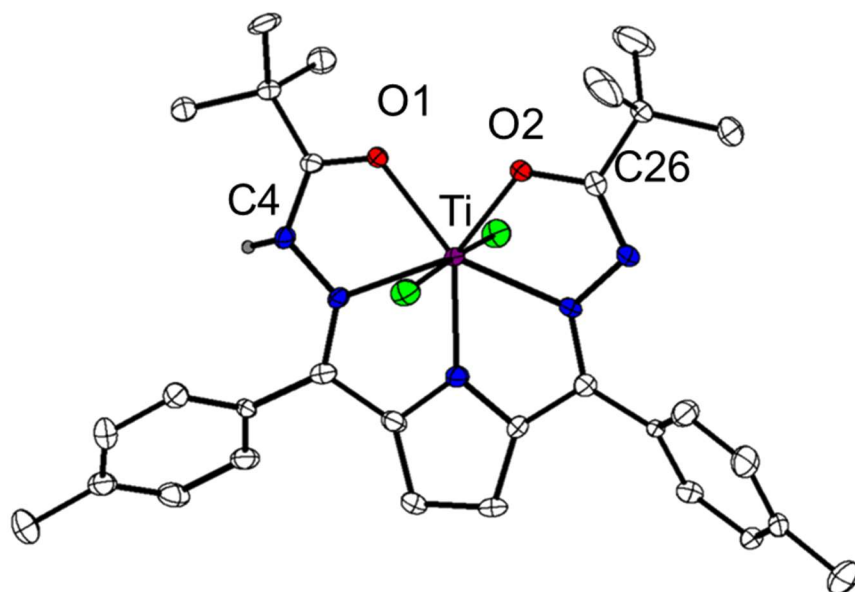
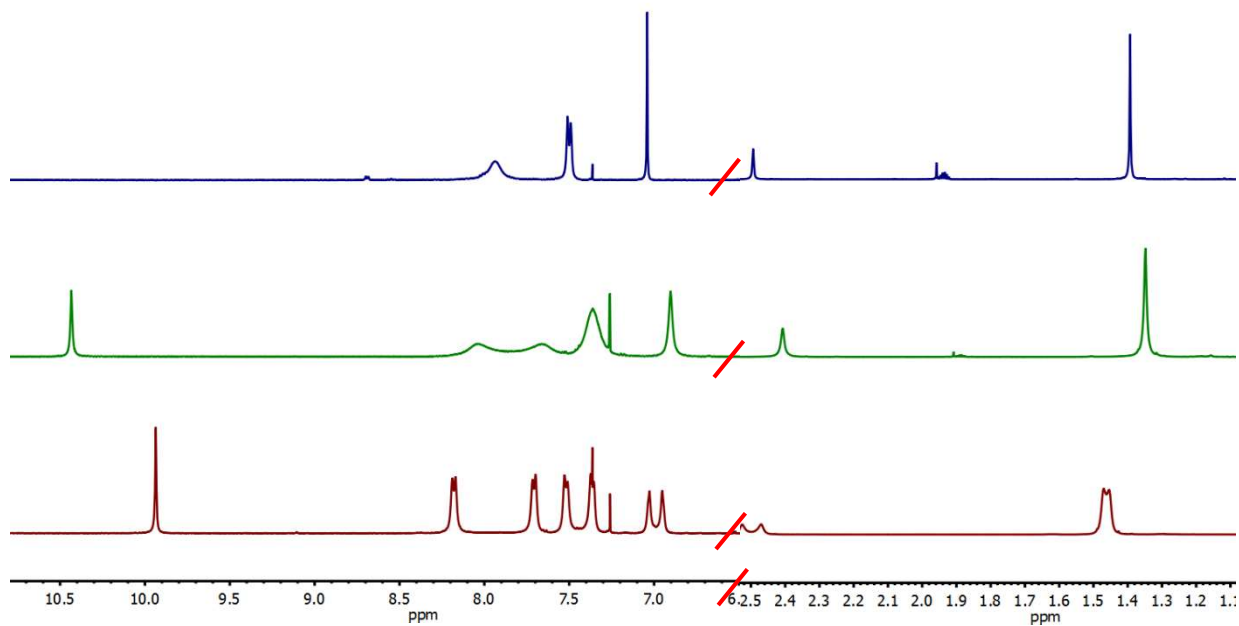
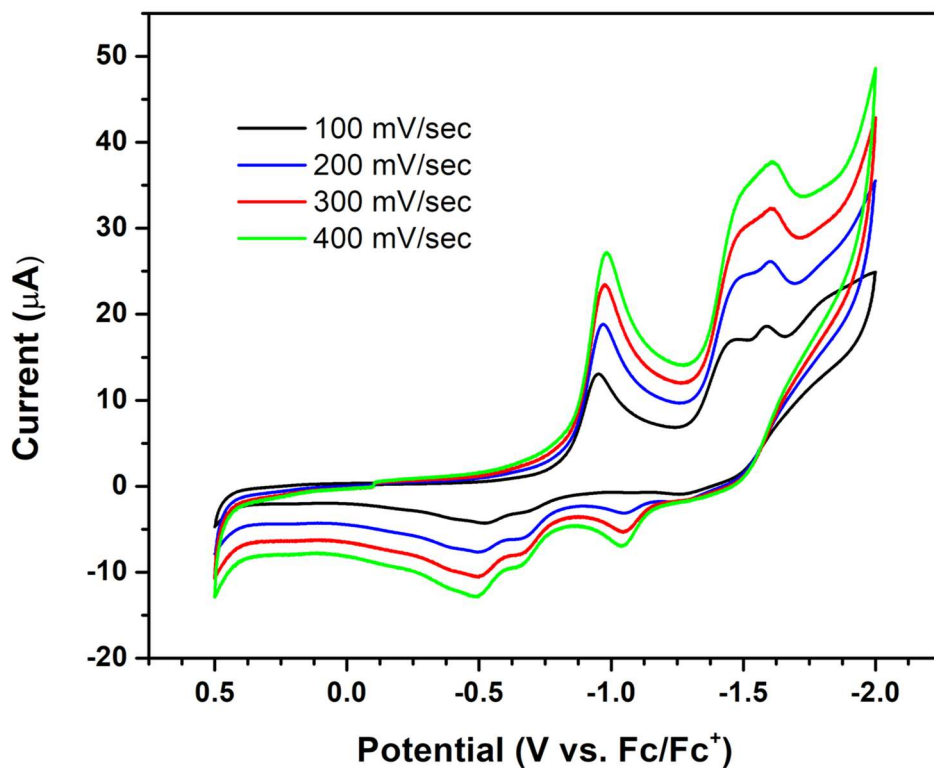


Figure 4A- 2. Symmetrization of ^1H NMR of **1** upon switching from CDCl_3 (bottom) to CDCl_3 with a drop of CD_3CN (middle) to only CD_3CN (top).



CDCl_3 which appeared symmetrical when the NMR was recorded in CD_3CN . Crystallization by vapor diffusion of petroleum ether into benzene resulted in isolation of single crystals of **1**, a templated pyrrole-dihydrazone bound to Ti through the alpha-nitrogens of the hydrazone and the oxygens of the hydrazone carbonyl, with two chlorides bound to Ti to balance the charge on the Ti(IV). Significant bond lengths differences were observed in the solid-state structure between the two sides of the ligand, with one C-O bond lengthened along with a significantly shortened C-N bond, indicating a tautomerization where one nitrogen was protonated. Packing in the solid state also confirms the protonation, as hydrogen bonding interactions between the hydrogen and a neighboring chloride help give two-dimensional structure. The symmetrization of the NMR in MeCN likely resulted from rapid proton exchange between the two ligand arms, whereas this process was much slower in CDCl_3 so the structure appeared asymmetric. Ti(IV) is very stable and difficult to reduce, but redox-inactive metals have been used as Lewis acids in support of redox-active ligands, so cyclic voltammetry was recorded to investigate the redox activity of the ligand scaffold.

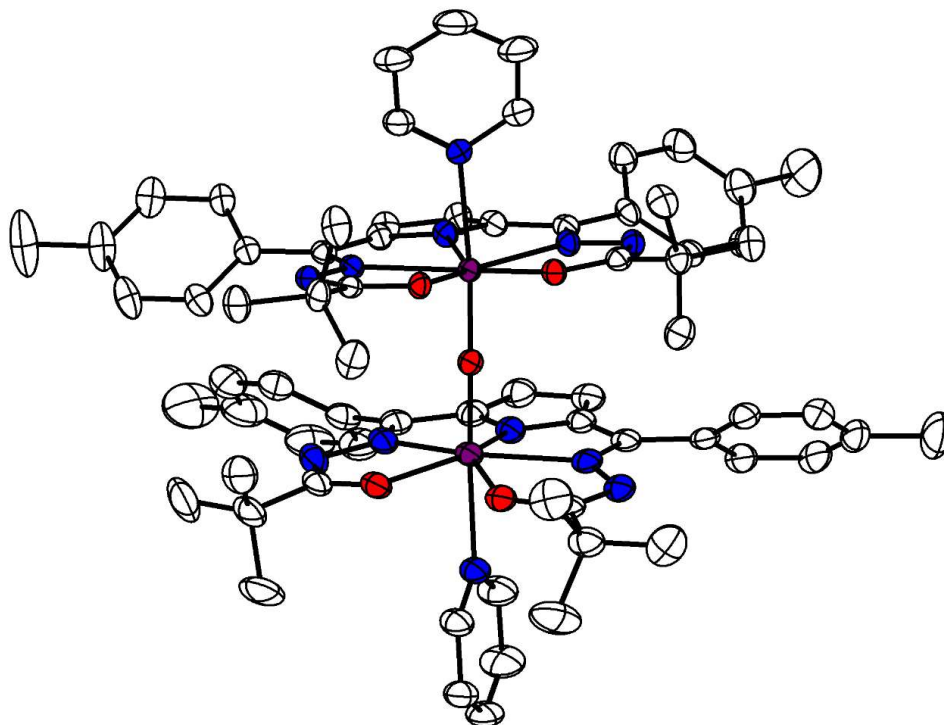
Figure 4A- 3. CV of 5 mM **1** in THF with 0.1 M NBu₄PF₆ electrolyte, at variable scan rates.



Cyclic voltammetry of **1** in THF showed many irreversible reduction waves at mild potentials, with reversibility increasing upon higher scan rates, indicating either loss of Cl⁻ or loss of a proton. This was briefly studied for its proton reduction reactivity, and though the current was much more intense upon addition of acid, bulk electrolysis did not indicate a high level of H₂ formation.

Reactivity was also studied via deprotonation of **1** with NaH. The deprotonation proceeds cleanly to a newly symmetric product, likely due to deprotonation and loss of NaCl to form **3**.

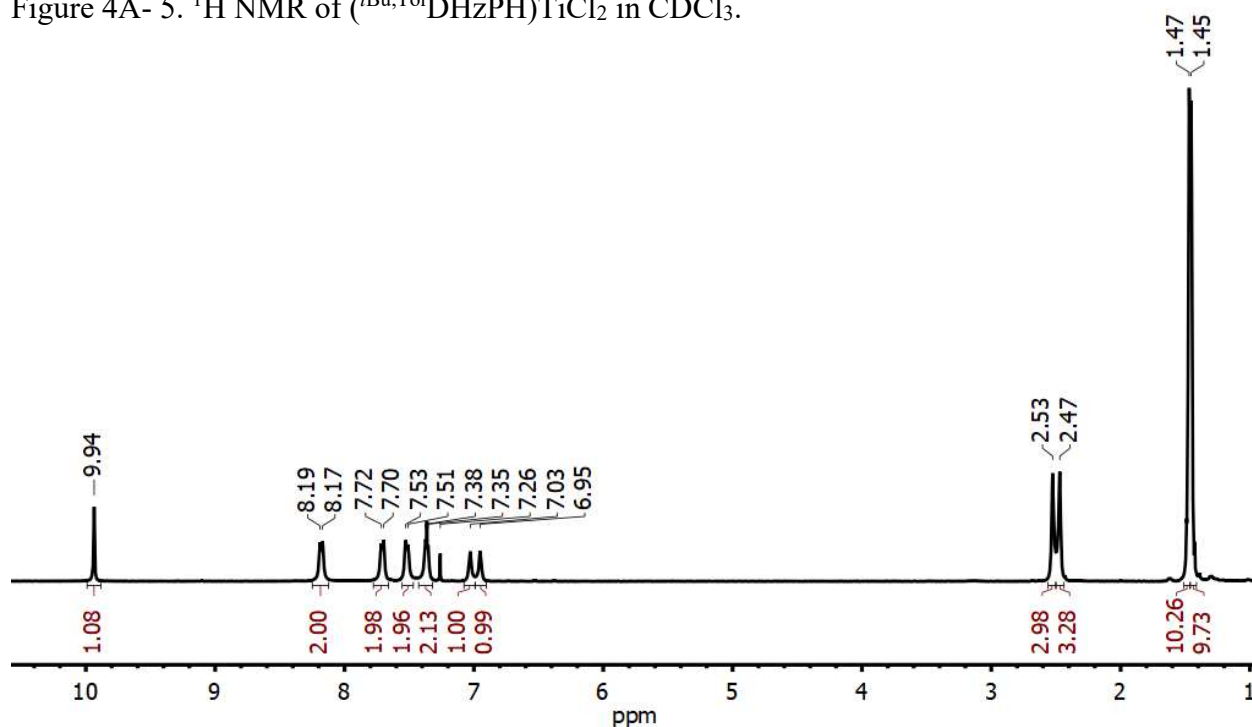
Figure 4A- 4. SXRDR Structure of **4**



Compound **3** was significantly more unstable than **1** or **2**, likely due to loss of a chloride, and therefore was not structurally characterized, though the ^1H NMR indicated clean conversion. Reactivity of **3** with H_2O and pyridine resulted in conversion to **4**, a novel dimeric structure bridged by an oxygen atom. The proposed pathway to form this product is water binding and deprotonation, which resulting in a titanium-hydroxide, which can then bind to another equivalent of **3** and become deprotonated, resulting in the oxide bridge and two protonated ligands. Then the protonated ligands are deprotonated by the hydroxide ions in solution, resulting in loss of two equivalents of NaCl , which then binds pyridine to stabilize the complex. Complex **4** was characterized both by ^1H NMR, showing a clearly symmetric ligand environment with one pyridine per ligand, and SXRDR.

Synthesis of (*t*^{Bu},Tol)DH₂PH)TiCl₂ (1). ¹H NMR (CDCl₃, 400 MHz, 25 C) δ = 9.94 (s, 1H, N–H), 8.18 (d, *J* = 8 Hz, 2H, Tol C–H), 7.71 (d, *J* = 8 Hz, 2H, Tol C–H), 7.52 (d, *J* = 8 Hz, 2H, Tol C–H), 7.36 (d, *J* = 8 Hz, 2H, Tol C–H), 7.03 (broad s, 1H, Pyrrole C–H), 6.95 (broad s, 1H, pyrrole C–H), 2.53 (s, 3H, Tol-CH₃), 2.477 (s, 3H, Tol-CH₃), 1.47 (s, 9H, *t*Bu), 1.45 (s, 9H, *t*Bu).

Figure 4A- 5. ¹H NMR of (*t*^{Bu},Tol)DH₂PH)TiCl₂ in CDCl₃.



Synthesis of (*t*^{Bu},Tol)DH₂P)Ti(Py)₂O. ¹H NMR (C₆D₆, 400 MHz, 25° C) δ = 7.72 (d, *J* = 8 Hz, 8H, Tol C–H), 7.43 (broad s, 4H, o-Py), 7.23 (t, *J* = 8 Hz, 2H, p-Py), 6.96 (d, *J* = 8 Hz, 8H, Tol C–H), 6.74 (t, *J* = 8 Hz, 4H, m-Py), 6.07 (s, 4H, Pyrrole C–H), 2.30 (s, 12H, Tol-CH₃), 1.16 (s, 36H, *t*Bu)

Figure 4A- 6. ^1H NMR of ($^t\text{Bu,Tol}$ DHzP)Ti(Py) $_2$ O in C_6D_6 .

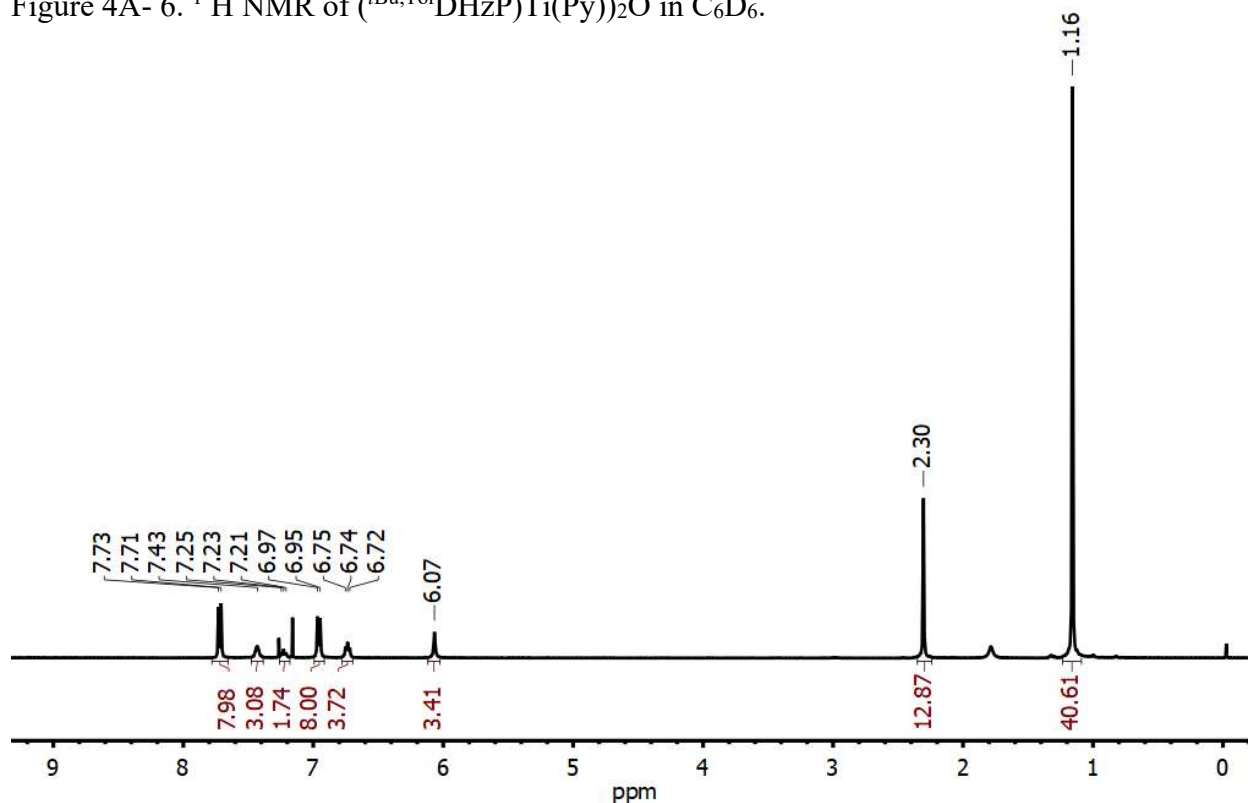


Table 4A - 1. Refinement data for

Identification code	PyDimer	AM_Ti_Hyzd
Empirical formula	$\text{C}_{70}\text{H}_{79}\text{N}_{12}\text{O}_5\text{Ti}_2$	$\text{C}_{30}\text{H}_{35}\text{Cl}_2\text{N}_5\text{O}_2\text{Ti}$
Formula weight	632.12	
Temperature/K	100(2)	100(2)
Crystal system	triclinic	Orthorhombic
Space group	P-1	Pbca
a/Å	12.7490(7)	20.8841(13)
b/Å	15.4403(8)	29.3744(19)
c/Å	20.4203(11)	30.7069(19)
α /°	76.485(2)	90
β /°	83.320(2)	90
γ /°	86.476(2)	90
Volume/Å 3	3879.4(4)	18837(2)
Z	4	25
$\rho_{\text{calc}}/\text{g}/\text{cm}^3$	1.082	1.306
μ/mm^{-1}	0.256	0.477

F(000)	1334.0	774.0
Crystal size/mm ³	0.64 × 0.34 × 0.27	0.194 x 0.177 x 0.118
Radiation	MoK α (λ = 0.71073)	MoK α (λ = 0.71073)
2 Θ range for data collection/ $^{\circ}$	4.172 to 46.628	4.14 to 46.712
Index ranges	-14 \leq h \leq 14, -17 \leq k \leq 17, -22 \leq l \leq 22	-23 \leq h \leq 22, -32 \leq k \leq 32, -34 \leq l \leq 33
Reflections collected	89987	335043
Independent reflections	11181 [R _{int} = 0.0543, R _{sigma} = 0.0311]	13674 [R _{int} = 0.0911, R _{sigma} = 0.0310]
Data/restraints/parameters	11181/3/881	13674/1117
Goodness-of-fit on F ²	1.028	1.053
Final R indexes [I \geq 2 σ (I)]	R ₁ = 0.0444, wR ₂ = 0.1102	R ₁ = 0.0393, wR ₂ = 0.0827
Final R indexes [all data]	R ₁ = 0.0600, wR ₂ = 0.1182	R ₁ = 0.0643, wR ₂ = 0.0926
Largest diff. peak/hole / e \AA^{-3}	0.37/-0.33	0.65/-0.73